

ONERA

THE FRENCH AEROSPACE LAB

r e t u r n o n i n n o v a t i o n

FINAL REPORT

Development of a predictive discharge numerical model on solar panels - Final Report

Contract n° 22048/09/NL/AT

Authors: J.-CH. MATÉO-VÉLEZ, P. SARRAILH,
J.-F. ROUSSEL

SPACE ENVIRONMENT DEPARTMENT

FR 10/14511 DESP - December, 2010

UNCLASSIFIED

ONERA

THE FRENCH AEROSPACE LAB

Toulouse Center
B.P. 74025 - 2, Avenue E. Belin
F-31055 TOULOUSE CEDEX 4
Phone (33) 5.62.25.25.25 - Fax 5.62.25.25.69
<http://www.onera.fr/desp/>
French National Aerospace Research Establishment

DÉPARTEMENT SPACE ENVIRONMENT

Final Report FR 10/14511 DESP

Development of a predictive discharge numerical model on solar panels - Final Report

Contract n° 22048/09/NL/AT

December, 2010

Authors

J.-CH. MATÉO-VÉLEZ, P. SARRAILH,
J.-F. ROUSSEL

Approved by :

J.-F. ROUSSEL

Head of

Space Environment Department

DESP-T n° c 118/2010

UNCLASSIFIED



UNCLASSIFIED

IDENTIFICATION SHEET of ONERA document # FR 10/14511 DESP

Issuing department: Space Environment	Contracting party: ESTEC	Contract references: 22048/09/NL/AT
	Program record # : 202.T	Date: December, 2010
Title: <i>Development of a predictive discharge numerical model on solar panels - Final Report</i> Contract n° 22048/09/NL/AT		
Authors: J.-CH. MATÉO-VÉLEZ, P. SARRAILH, J.-F. ROUSSEL		
PROTECTION Level:	PROTECTION Release:	
Title : Sans Mention de Protection	Title : not applicable	
Sheet : Sans Mention de Protection	Sheet : not applicable	
Document : Sans Mention de Protection	Document : not applicable	

Author abstract

The "Development of a Predictive Discharge Numerical Model on Solar Panels" contract, ESTEC contract No. 22048/09/NL/AT, aimed at developing a SPIS-based numerical tool capable to simulate the electrostatic discharge (ESD) triggering at triple points on spacecraft solar panels. A second application of this contract consisted in proposing and testing a new concept of ESD monitor on spacecraft solar panels. The main result of this activity was an upgrade of the SPIS code, delivered to the community as usual in open source form through SPINE web site (<http://www.spis.org>), including code documentation. These major enhancements led to a new version: SPIS-ESD (release candidate in December 2010). This activity also led to the assessment of the ESD monitor concept and to possible spacecraft integration solutions.

Keywords

UNCLASSIFIED

DISTRIBUTION LIST of ONERA document # FR 10/14511 DESP

Document only

- *Outside ONERA*
 - ESA/ESTEC
 - D. RODGERS
 - Postbus 299 2200 AG Noordwijk, The Netherlands 1 ex.
 - CDROM + 5 ex.
 - ESA/ESTEC
 - COMMUNICATION PRODUCTION OFFICE
 - Postbus 299 2200 AG Noordwijk, The Netherlands 1 ex.
 - CDROM + 2 ex.
 - ARTENUM
 - J. FOREST
 - 24 rue Louis Blanc 75010 Paris 1 ex.
 - ASTRIUM
 - M. SEVOZ
 - 31 rue des Cosmonautes 31402 Toulouse Cedex 4 1 ex.
- *Inside ONERA*
 - DCT/CID 1 ex.
 - Adjoint(s) de Gestion 1 ex.
 - DESP-Toulouse: J.-CH. MATÉO-VÉLEZ 1 ex.

Identification sheet only

- *Outside ONERA*
- *Inside ONERA*
 - E. ROSENCHER (DSB/TIS) - CID Toulouse
- *Systematic distribution*
 - No distribution
- *Electronic distribution*
 - No distribution

Toulouse Center
B.P. 74025 - 2, Avenue E. Belin
F-31055 TOULOUSE CEDEX 4
Phone (33) 5.62.25.25.25 - Fax 5.62.25.25.69
<http://www.onera.fr/desp/>
French National Aerospace Research Establishment

Final Report

December 2010

Contributors

Jean-Charles Matéo-Vélez
Pierre Sarrailh
Jean-François Roussel
Bernard Dirassen

ONERA/DESP
 2 Av. Edouard Belin
 31055 Toulouse cedex
 France

Julien Forest

Artenum SARL
 24 rue Louis Blanc
 75010 Paris
 France

Marc Sévoz
Patrice Péliou

ASTRIUM SAS
 31 rue des cosmonautes
 31400 Toulouse
 France

Document Status Sheet			
Document Title:			
Issue	Date	Author(s) of document/change	Reason of change
1.0	15/12/2010	JCMV	First issue

CONTENTS

1. INTRODUCTION	15
1.1. Objectives	15
1.2. This Report Structure	15
1.3. Acronyms	16
1.4. Reference Documents	17
2. LITERATURE STUDY	21
2.1. The Context	21
2.2. Geostationary Spacecraft Charging	22
2.2.1. The Geosynchronous Plasma Environment	22
2.2.2. Absolute Charging	23
2.2.3. Differential Charging	25
2.2.4. Spacecraft Charging at GEO	26
2.3. Discharges on Solar Panels	33
2.3.1. Discharge Process at Triple Points	33
2.3.2. Specific Issues for ESD Hazard Modelling and Experiments	43
2.4. Conclusion	47
3. USER REQUIREMENTS	48
3.1. The Context	48
3.2. User Requirements Formulation	49
3.2.1. UR1: IPG Situation	49
3.2.2. UR2: Metals	49
3.2.3. UR3: Dielectrics	49
3.2.4. UR4: Electron Avalanche	50
3.2.5. UR5: Time scales	50
3.2.6. UR6: Post Processing	50
3.2.7. UR7: Interface and Control	51
3.2.8. UR8: Requirements Originating from Software Development Process	51
4. SOFTWARE REQUIREMENTS	52
4.1. SR1: IPG Situation	52
4.1.1. SR1.1 Triple Point Geometry	52
4.1.2. SR1.2 Boundary Conditions	53
4.1.3. SR1.3 Microscopic Structures	53
4.1.4. SR1.4 Interaction with the Environment	54
4.1.5. SR1.5 Dimension of the Problem	54
4.2. SR2: Metals	54
4.2.1. SR2.1 Work Function	54

4.3.	SR3: Dielectrics	54
4.3.1.	SR3.1 Dielectric Properties	54
4.3.2.	SR3.2 Dielectric Thickness	54
4.4.	SR4: Electron Avalanche.....	55
4.4.1.	SR4.1 Electron Creation	55
4.4.2.	SR4.2 Electron Trajectory	55
4.4.3.	SR4.3 Electron Interaction with Materials	55
4.5.	SR5 Time Scales.....	55
4.6.	SR6: Post Processing	55
4.6.1.	SR6.1 ESD Hazard	55
4.6.2.	SR6.2 Electron Trajectories.....	55
4.6.3.	SR6.3 Electric Field.....	55
4.7.	SR7: Interface and Control	56
4.7.1.	SR7.1 Ease of Use	56
4.8.	SR8: Requirements Originating from Software Development Process.....	56
4.8.1.	SR8.1 Computing Structure and Code Development	56
4.8.2.	SR8.2 Platform Operational Requirements	56
4.8.3.	SR8.3 Documentation.....	56
4.8.4.	SR8.4 Data Hosting	57
4.9.	Electric Field Enhancement by Microscopic Structures.....	57
4.10.	Capacitive and Conductive Coupling of Thick Dielectrics	57
4.11.	Equivalent Circuit.....	58
4.12.	Pre-Defined Models Wizards.....	59
5.	SOFTWARE VERIFICATION AND VALIDATION PLAN	60
5.1.	Verification Plan	60
5.2.	Validation Plan	61
6.	ARCHITECTURE DESIGN.....	67
6.1.	General Overview of the Model	67
6.2.	IPG Situation and Inputs for the Tool.....	68
6.2.1.	Geometrical Mockup	68
6.2.2.	Boundary Conditions	72
6.2.3.	Material Inputs.....	73
6.2.4.	Environment Inputs	74
6.3.	ESD Prediction Scenario and NUM Development.....	74
6.3.1.	SPIS-NUM Development Overview	74
6.3.2.	ESD Prediction Scenario	75
6.3.3.	Tip Model and ESD Triggering Condition.....	76
6.3.4.	Spacecraft Circuit Solver.....	77
6.4.	Wizard Creation and Project Configuration	79
6.4.1.	Standard Project Configuration in SPIS-UI.....	79
6.4.2.	Pre-Defined Models Wizards	79

7. DETAILED DESIGN	81
7.1. Simulation.....	81
7.1.1. ESDRiskScenario	81
7.1.2. SimulationFromUIParamsESD	82
7.2. SC/Plasma Interactions.....	82
7.2.1. FowlerNordheimWithTipAreaSurfDistrib	82
7.2.2. TipRecession	82
7.2.3. RLCSCforESD	85
7.3. Current Scalers for the Implicit Circuit Solver.....	86
7.3.1. CurrentScalerFromCurrentVariation	86
7.3.2. CurrentScalerFromLocalCurrentVariation	86
7.3.3. FNCurrentScaler.....	86
7.3.4. FNWithTipAreaCurrentScaler.....	87
7.4. SPIS-ESD User Interface / User Manual.....	88
8. TEST REPORT	89
8.1. Triple Point Configurations	89
8.1.1. Configurations Originating from SVVP.....	89
8.1.2. Sample Manufacturing.....	93
8.1.3. Extra Configurations.....	94
8.1.4. Configurations to be Tested.....	96
8.2. Experimental Setup.....	96
8.2.1. Experimental Facility	96
8.2.2. Inverted Potential Gradient using V-UV photons	98
8.2.3. ESD Test Procedure.....	103
8.3. ESD Tests Results.....	104
8.3.1. Nominal Case	104
8.3.2. Photon Incidence Angle.....	107
8.3.3. Metal vs. Dielectric Length	109
8.3.4. Dielectric Material.....	111
8.3.5. Metal.....	112
8.3.6. Co-planar Triple Point.....	114
8.4. Test Report Conclusion	117
9. SOFTWARE VERIFICATION AND VALIDATION	118
9.1. ESD Prediction Tool.....	118
9.1.1. SPIS ESD Tool Overview	118
9.1.2. IPG Situation	121
9.1.3. Nominal Case	122
9.1.4. ESD Triggering Model.....	124
9.2. ESD Materials Database (xml SPIS format).....	128
9.2.1. Index Names in the xml File.....	128
9.2.2. AluminumForESD.....	129
9.2.3. GoldForESD	130

9.2.4.	Teflon FEP (BOL)	131
9.2.5.	CMX	133
9.3.	Software Verification.....	135
9.3.1.	Potential Evolution	135
9.3.2.	Emitted and Collected Currents.....	136
9.3.3.	Time Step Adaptation.....	138
9.3.4.	Tip Evolution.....	138
9.3.5.	Electrons Density in Volume: Space Charge Effect?	141
9.3.6.	Verification Phase Conclusion	141
9.4.	Software Validation	142
9.4.1.	Nominal Case	142
9.4.2.	Geometry Effect.....	143
9.4.3.	Surface Resistivity at the Dielectric Edge	144
9.4.4.	Tip Material Effect	145
9.4.5.	Planar Configuration.....	146
9.5.	Results Analysis and Possible Code Improvements	148
10.	ESD MONITOR CONCEPTUAL DESIGN AND ASSESSMENT	149
10.1.	ESD Monitor Concept	149
10.2.	ESD Monitor Assessment.....	153
10.2.1.	Physical Considerations.....	153
10.2.2.	Numerical Simulation.....	155
10.2.3.	Numerical Model.....	155
10.2.4.	Results	158
10.2.5.	Experiments	165
10.2.6.	Discussion.....	168
10.3.	Conclusion	168
11.	APPENDIX 1 - ESD MONITOR CONCEPTUAL DESIGN – SPACECRAFT INTEGRATION	170
12.	APPENDIX 2 – SPIS-ESD USER MANUAL.....	170

FIGURES

Figure 1 - Secondary emission yield for kapton®.....	24
Figure 2 - Absolute charging of a spacecraft.....	25
Figure 3 - Absolute and differential charging of a spacecraft	26
Figure 4 - MUSCAT simulation of spacecraft charging in GEO [15]; isopotential lines	29
Figure 5 - MUSCAT simulation of spacecraft charging in GEO [14]	30
Figure 6 - NASCAP simulation of spacecraft charging in GEO [RD6, RD7]	30
Figure 7 - IPG situation on a GEO spacecraft (typical isopotential lines represented).....	31
Figure 8 - Schematic of solar cell assembly in typical IPG situation.....	32
Figure 9 - Inverted potential gradient situation obtained in plasma (left) and electrons (right) during experiments; the dense plasma neutralizes the dielectric surfaces; low energy electrons produces secondary electron emission yield greater than 1	35
Figure 10 - Global localizations of ESDs on solar cell assemblies	36
Figure 11 - Edge of a solar cell after a single ESD [23].....	36
Figure 12 - Typical experimental setup for the triggering of electrostatic discharges on solar cell coupons; (1) represents the solar cell coupons in vacuum chamber; (2) is the external circuit representing the spacecraft absolute capacitance; (3) simulates the solar array and provides power to secondary arcs ...	37
Figure 13 - Typical blow-off, flash-over and secondary arc current waveforms experimentally observed....	38
Figure 14 - Simplified test setup used for ESD triggering on a solar cell; the secondary arc is not simulated; the flash-over can be adapted by using several interconnected cells.....	39
Figure 15 - Model of the vacuum arc cathode spot [33].....	40
Figure 16 - potential profile through and out of a conductor submitted to a large electric field at its right (left)	41
Figure 17 - Mechanisms of electron avalanche from surface micro irregularities	42
Figure 18 - The two proposed configurations of IPG at triple point: co-planar (left) and perpendicular (right); during phase 2.....	45
Figure 19 - Accuracy criterion for tests and simulations.....	47
Figure 20 - Pre-defined CAD models, given as a first approach; the exact relevant geometries should rather be determined later from testing them with the operational code.	53
Figure 21 - Simple version of a spacecraft equivalent circuit, with continuous components (all small capacitors and resistors spread on top of each super node, one per surface element) and absolute capacitance C_{sat} . Here C_{sat} is distributed over all super nodes and results in three capacitors C_i , $i = 0, 1, 2$, relating them to the plasma ground at the bottom, with capacitances proportional to their areas A_i , of sum A_{tot} . Other discrete components can be plugged by the user between super nodes (resistors, capacitors, inductances and bias).....	58
Figure 22 - Schematics of CEDRE chamber	61
Figure 23 - Schematic of the sample used to demonstrate the photon setup capability	62
Figure 24 - Evolution of the surface potential on the sample of Figure 23 when using the photon setup for the IPG building.....	62
Figure 25 - IPG in flight and means to obtain it in ground tanks	64
Figure 26 - Schematics of the two geometrical configurations of triple points foreseen for the experiments	65
Figure 27 - Campaign with the photon setup.....	65

Figure 28 - Campaign with the electron setup.....	66
Figure 29 – Overview of the model of the IPG situation at triple point in GEO.....	68
Figure 30 - CAD model visualization from GMSH of the geometrical mockup for the ESD prediction tool.....	69
Figure 31- Zoom X 50 of the figure 2 – Schema of the dielectric trench as a function of angle α : (a) $\alpha = \pi/2$ – perpendicular case, (b) $\alpha = \pi/4$ and (c) $\alpha = 0$ – planar case.....	70
Figure 32 - Zoom X 20 of Figure 31. Schema of the Fowler-Nordheim emission site.....	70
Figure 33 - Schema of the general overview of SPIS-NUM.....	75
Figure 34 - Schema of the ESD risk scenario.....	76
Figure 35 - Simple version of a spacecraft equivalent circuit, with continuous components (all small capacitors and resistors spread on top of each super node, one per surface element) and absolute capacitance C_{sat} . Here C_{sat} is distributed over all super nodes and results in three capacitors C_i , $i = 0, 1, 2$, relating them to the plasma ground at the bottom, with capacitances proportional to their areas A_i , of sum A_{tot} . Other discrete components can be plugged by the user between super nodes (resistors, capacitors, inductances and bias).....	78
Figure 36 - Tip geometry.....	83
Figure 37 - Capacitive coupling.....	85
Figure 38 - Conductive coupling.....	85
Figure 39 - Side view of the two triple point configurations used during the experiments.....	90
Figure 40 - Top view of the two triple point configurations used during the experiments.....	90
Figure 41 - SEY of Teflon.....	92
Figure 42 - SEY of CMX-AR coverglass.....	92
Figure 43 – Design of the samples used for the co-planar configuration.....	93
Figure 44 – Design of the samples used for the perpendicular configurations.....	94
Figure 45 - Influence of the photon incidence angle. On the left side, the dielectric edge is fully irradiated ($\alpha=15^\circ$). On the right side, the dielectric edge is not irradiated ($\alpha=-15^\circ$).....	95
Figure 46 - The two configurations used to study the influence of the metal length.....	95
Figure 47 - Schematic view of CEDRE chamber.....	97
Figure 48 - Bias voltage circuit.....	98
Figure 49 - Relative intensity of L7293 lamp, from Hamamatsu data sheet.....	98
Figure 50 - Relative intensity of L7293 lamp, from ONERA measurements.....	99
Figure 51 - Photo current density measured on copper, at the sample holder location.....	100
Figure 52 - Picture of the nominal configuration sample.....	100
Figure 53 - Detailed view of the nominal configuration.....	101
Figure 54 - Schematic view of the nominal triple point with the UV protection mask permitting to select the region irradiated by the UV source.....	101
Figure 55 - Principle of the IPG obtained with UV photons.....	102
Figure 56 - Typical IPG situation obtained with the UV method.....	102
Figure 57 – ESD test procedure diagram.....	103
Figure 58 - Design principle of the nominal configuration TP.....	104
Figure 59 - Picture of an ESD in the nominal configuration. The white lines represent the irradiated zone of the sample; the dashed arrows represent the triple point location.....	105
Figure 60 - Peak current vs. ESD voltage threshold in the nominal configuration. The arrows refer to the order of appearance of ESDs.....	105
Figure 61 - Blow-off current of the ESDs obtained in the nominal configuration.....	106
Figure 62 - Bias voltage of the ESDs obtained in the nominal configuration (some ESD bias voltage measurements are missing).....	106
Figure 63 - Design principle of the photon incidence angle configuration.....	107

Figure 64 - Picture of an ESD in the photon incidence angle configuration.....	107
Figure 65 - Peak current vs. ESD voltage threshold in the photon incidence angle configuration. The two events at 1000 V could not be detected by the video camera. As a result, we do not consider them as ESD events.....	108
Figure 66 - Blow-off current of the ESDs obtained in the photon incidence angle configuration.....	108
Figure 67 - Design principle of the Metal vs. Dielectric length configuration.....	109
Figure 68 - Peak current vs. ESD voltage threshold in the Metal vs. Dielectric length configuration. The first event was detected by the video camera but not by the oscilloscope.	110
Figure 69 – Schematics of typical iso potential lines in two configurations of metal length. On the right side, the local barrier of potential due to the long metallic gap provokes a high local recollection of the photo electrons. The potential gradient at the vicinity of the triple point is lower than on the left side.	110
Figure 70 - Peak current vs. ESD voltage threshold in CMX-AR configuration. The 2nd ESD has been localized with the video camera but the current measurement is missing.....	111
Figure 71 - Blow-off current of the ESDs obtained in the CMX-AR configuration.....	112
Figure 72 - Peak current vs. ESD voltage threshold in the gold configuration.....	113
Figure 73 - Blow-off current of the ESDs obtained in the gold configuration.....	113
Figure 74 - Bias voltage during ESDs obtained in the gold configuration.....	114
Figure 75 - Design principle of the co-planar configuration.....	115
Figure 76 - Peak current vs. ESD voltage threshold in the co-planar configuration.....	115
Figure 77 - Blow-off current of the ESDs obtained in the co-planar configuration.....	116
Figure 78 – Summary of the ESD thresholds.....	117
Figure 79 - SPIS-ESD model of the IPG situation at triple point in GEO. The triple point can be perpendicular, angular or co-planar.....	119
Figure 80 –General overview of SPIS-NUM.....	119
Figure 81 – Schema of the ESD risk scenario.....	120
Figure 82 – Geometrical mock-up of the IPG situation.....	121
Figure 83 - IPG design principle of the nominal triple point configuration used during experiments.....	123
Figure 84 - Mechanisms of electron avalanche from surface micro irregularities.....	125
Figure 85 - tip geometry.....	126
Figure 86 – Barrier of potential imposed by the SPIS ESD tool as a function of time.....	135
Figure 87 – Emitted photoemission and Fowler-Nordheim currents (in Log scale) as a function of time. For photoemission: emission from all surfaces. For Fowler-Nordheim emission: emission from the tip...	136
Figure 88 – Current collected on the metallic part, the emission zone and the dielectric (in Log scale) as a function of time.....	137
Figure 89 – Simulation time step as a function of time.....	138
Figure 90 - Tip temperature evolution.....	139
Figure 91 - Neutral pressure evolution.....	139
Figure 92 - Tip length evolution.....	140
Figure 93 - Amplification factor evolution.....	140
Figure 94 – Electron density during the first ESD: a) Fowler-Nordheim electron and b) secondary emission electron.	141
Figure 95 – Comparison of experimental and numerical results in the nominal configuration.	142
Figure 96 – Comparison of experimental and numerical results changing the incidence angle of UV to -15° (+15° in the nominal case).....	143
Figure 97 – Comparison of experimental and numerical results changing the metal length to 15mm compared to 3mm in the nominal case.	144

Figure 98 – Comparison of experimental and numerical results as a function of the surface resistivity at the dielectric edge.....	145
Figure 99 – Comparison of experimental and numerical results as a function of the metal material	146
Figure 100 – Comparison of experimental and numerical results in the planar configuration.	147
Figure 101 - Basic schematic of the ESD monitor concept; example with 5 metallic plates.....	149
Figure 102 - Electrical connection of the ESD monitor	150
Figure 103 - Evolution of potential during charging and discharges; example of the flash-over represented in Figure 101; near the metallic plate #1	151
Figure 104 - Equivalent circuit of the dielectric sheet during transient currents.....	152
Figure 105 - Surface potential homogenization by recollection of photoelectrons.....	153
Figure 106 - Equivalent electric circuit of the ESD monitor.....	154
Figure 107 - CAD model of the patch of the spacecraft.....	156
Figure 108 - Surface meshing at spacecraft length scale.....	156
Figure 109 - Surface meshing at patch length scale	157
Figure 110 - Evolution of the potentials on the spacecraft in the case of $R_M = 10^{12} \Omega$	159
Figure 111 - Potential map around the spacecraft with $R_M = 10^{12} \Omega$	160
Figure 112 - Potentials in the cutting plane of the metallic plate with $R_M = 10^{12} \Omega$	160
Figure 113 – Potential on the top surface of the solar array.....	161
Figure 114 – Potential Y-profile on top of the solar array at location $Z = 1$ m from the patch.....	161
Figure 115 Evolution of the currents on the metallic plate in the case of $R_M = 10^{12} \Omega$	162
Figure 116 - Evolution of the potentials on the spacecraft in the case of $R_M = 10^9 \Omega$	163
Figure 117 - Evolution of the currents on the metallic plate in the case of $R_M = 10^9 \Omega$	164
Figure 118 - Sample used during the experiments	165
Figure 119 - Potential profile on top of the sample; bias voltage is -1000 V.....	166
Figure 120 – Photoemission current setup.....	167
Figure 121 – Experimental setup for the validation of the ESD monitor concept	167
Figure 122 – Equilibrium potential profile upon the patch for different insulating resistors.....	168

TABLES

Table 1 - Typical plasma parameters at geostationary orbit.....	22
Table 2 - ECCS-E-10-04A Worst-case bi-Maxwellian environment for outer magnetosphere.....	23
Table 3 - User modifiable parameters in the geometrical mockup file	69
Table 4 - Fixed parameters in the geometrical mockup file	72
Table 5 - Dielectric properties measured during the MCPIA campaign ⁽¹⁾ [1], in the frame of these study ⁽²⁾ , or given by the material manufacturer ⁽³⁾	91
Table 6 - Sample dimensions.....	94
Table 7 - TP configurations to be tested.....	96
Table 8 - Global parameters configuration concerning the SPIS-ESD scenario	120
Table 9 - Group editor configuration.....	121
Table 10 - Global parameters configuration for the photoemission	122
Table 11 - Modifiable global parameters configuration for UV incidence angle.....	123
Table 12 - User modifiable parameters in the geometrical mockup file	123
Table 13 - Global parameters configuration for the Fowler-Nordheim emission	125
Table 14 - Global parameters configuration for the secondary emission by electrons.....	125
Table 15 - Time integration configuration for all the secondary electrons	126
Table 16 - Tip recession configuration in SPIS UI.....	128
Table 17 - 19 NASCAP properties in the xml SPIS file.....	128
Table 18 - SPIS extended properties in the xml SPIS file	129
Table 19 - High resistors supporting high voltage from SRT Resistor Technology	155
Table 20 - Environment for SPIS simulation of outer magnetosphere.....	158
Table 21 - ECSS-E-10-04A Worst-case bi-Maxwellian environment for outer magnetosphere	164

1. INTRODUCTION

1.1. Objectives

The "Development of a Predictive Discharge Numerical Model on Solar Panels" contract, ESTEC contract No. 22048/09/NL/AT, aimed at developing a SPIS-based numerical tool capable to simulate the electrostatic discharge (ESD) triggering at triple points on spacecraft solar panels. A second application of this contract consisted in proposing and testing a new concept of ESD monitor on spacecraft solar panels.

The main result of this activity was an upgrade of the SPIS code, delivered to the community as usual in open source form through SPINE web site (<http://www.spis.org>), including code documentation. These major enhancements led to a new version: SPIS-ESD (release candidate in December 2010). This activity also led to the assessment of the ESD monitor concept and to possible spacecraft integration solutions.

1.2. This Report Structure

This final report gathers first the amount of work and documents that were produced in, or around, the process of code development. They successively involve a review of physics, requirements, verification and validation plan, software design, test report, validation report.

The state of the art of charging and discharge mechanisms on spacecraft solar panels was oriented towards the development of a new version of SPIS dedicated to the triggering of ESDs on solar array triple points. For general charging/discharges discussions, other documents exist, as e.g. ECSS 10-06. The state of the art permits to define the prerequisites to next sections on modeling requirements. User Requirements aimed at gathering all the necessary improvements of SPIS from the user point of view. It was followed by the Software Requirements, and the Verification and Validation Plan. The Software Architecture Design gave the details of the implementation of the numerical routines. Ground test results were presented in the Test Report. The Software Verification and Validation report compared the updated SPIS code with the test results and also presented code improvements for the future. The software User Manual was finally provided.

This final report also gathers the ESD monitor conceptual design report which assessed the capability of a new method to measure ESD occurrence and Flash-Over expansion on spacecraft solar panels.

1.3. Acronyms

AD	Architecture Design
AU	Astronomic Unit, the distance between Earth and the Sun
BO	Blow-off current
BOL	Beginning of Life
ECSS	European Cooperation for Space Standardisation
EOL	End of Life
ESA	European Space Agency
ESD	ElectroStatic Discharge
FEE	Field-Effect Emission
FN	Fowler-Nordheim
FO	Flash-over current
GEO	Geostationary Earth Orbit
GMSH	Mesh generator (and object modeller) used in SPIS
IPG	Inverted Potential Gradient
LEO	Low Earth Orbit
MOL	Middle of Life
ONERA	Office National d'Etudes et de Recherches Aérospatiales
ONERA/DESP	Office National d'Etudes et de Recherches Aérospatiales, Département Environnement SPatial
PIC	Particle-In-Cell
RD	Reference Document
RIC	Radiation induced conductivity
SA	Solar Array
SAS	Solar Array Simulator
S/C	Spacecraft
SEEE	Secondary Electron Emission from Electron impact
SEY	Secondary Electron Emission Yield
SOW	Statement Of Work
SPIS	Spacecraft Plasma Interaction Software
SPIS-ESD	SPIS Electrostatic Discharge Tool
SR	Software Requirements
UR	User Requirements
TN	Technical Note
TP	Triple Point
TR	Test Report
UV	Ultra Violet
WP	Work Package
w.r.t.	with respect to

1.4. Reference Documents

- [ITT] Invitation to tender AO/1-5849/08/NL/AT - Development of a Predictive Discharge Numerical Model on Solar Panels
- [PROP] Proposal for the Development of a Predictive Discharge Numerical Model on Solar Panels, in response to AO/1-5849/08/NL/AT, Onera, Ardenum, Astrium
- [ITT-FO] Invitation to tender AO/1-6058/09/NL/GLC– Flash- Over Evaluation on Large Solar Panels.
- [RD1] L. Girard, D. Payan, J.-F. Roussel, F. Severin, "SPIS modelling of electrostatic discharge triggering in a solar cell gap", 10th Spacecraft Charging Technology Conference, Biarritz, France, 2007.
- [RD2] ECSS-E-10-04A Space Environment.
- [RD3] D. Payan, F. Severin, J.-P. Catani, J.-F. Roussel, R. Reulet, D.Sarrail, "Electrostatic discharges on solar arrays. Physical model of inverted potential gradient electrostatic discharge", 7th SCTC, Noordwijk, The Netherlands, 2001.
- [RD4] ECSS-E-20-06 Spacecraft Charging.
- [RD5] L. Gaillot, M.-L. Fille, L. Levy, D. Sarrail, "Secondary arcs on solar generators - EMAGS2 test campaign", 9th SCTC, Tsukuba, Japan, 2005.
- [RD6] I. Katz et al., "Mechanism for spacecraft charging initiated destruction of solar arrays in GEO", AIAA Paper 98-1002, 1998.
- [RD7] I. Katz, V. A. David, D. B. Snyder, E. A. Robertson, "ESD initiated failures on high voltage satellites", Space Environments and Effect Flight Experiments Workshop, Huntsville, Alabama, 1998.
- [RD8] J.-F. Roussel, F. Rogier, G. Dufour, J.-C. Mateo-Velez, J. Forest, A. Hilgers, D. Rodgers, L. Girard, D. Payan, "SPIS modelling capabilities, achievements and prospects", 10th SCTC, Biarritz, France, 2007.
- [RD9] SPIS code: <http://dev.spis.org/projects/spine/home>
- [RD10] European Cooperation for Space Standards – Engineering – Software
- [1] D. Hastings and H. Garrett, "Spacecraft-Environment Interactions", Cambridge Univ. Press, New York, 1996.
- [2] C. D. Child, "Discharge from hot CaO," *Phys. Rev.*, Vol. 32, pp. 492, 1911.
- [3] I. Langmuir, "The effect of space charge and residual gases on thermionic currents in high vacuum," *Phys. Rev.*, Vol. 2, pp. 450, 1913.
- [4] I. Langmuir and K. B. Blodgett, "Currents limited by space charge between concentric spheres", *Phys. Rev.*, Vol. 24, pp. 49-59, 1924.
- [5] L. W. Parker, "Plasmasheath-photosheath theory for large space structures," in *Space Systems and Their Interactions with the Earth's Space Environment*, Prog. In Ast. And Aero., Vol. 71, ed. By H.B. Garret and C.P. Pike, 1980.
- [6] D. Bohm, H. E. Burhop, H. S. Massey, "The use of probes for plasma exploration in strong magnetic fields," in *The characteristics of electrical discharges in magnetic fields*, Ed. A. Guthrie and R. K. Wakerling, New York: Mc Graw-Hill, 1949, pp. 13-76.

- [7] J. E. Allen, R. L. Boyd, P. Reynolds, "The collection of positive ions by a probe immersed in a plasma," *Proc. Phys. Soc. B*, Vol. 70, pp. 297-304, 1957.
- [8] H. Mott-Smith, I. Langmuir, "The theory of collectors in gaseous discharges," *Phys. Rev.*, Vol. 28, pp. 727-763, 1926.
- [9] I. B. Bernstein, I. Rabinowitz, "Theory of electrostatic probes in a low-density plasma," *Phys. Fluids*, Vol. 2, pp. 112-121, 1959.
- [10] J. G. Laframboise, "Theory of spherical and cylindrical Langmuir probes in a collisionless, Maxwellian plasma at rest," University of Toronto, Institute of Aerospace Studies Report 100, 1966.
- [11] F. F. Chen, "Numerical computations for ion probe characteristics in a collisionless plasma," *Plasma Phys.*, Vol. 7, pp. 47-67, 1965.
- [12] A. Hilgers, S. Clucas, B. Thiébault, J.-F. Roussel, J.-C. Mateo-Velez, J. Forest, and D. Rodgers, "Modelling of Plasma Probe Interactions with a PIC Code Using an Unstructured Mesh", *IEEE Trans. Plasma Sci.*, Vol. 36, N°5, pp. 2319-2323, Oct. 2008.
- [13] J.-C. Mateo-Velez, J.-F. Roussel, D. Sarrail, F. Boulay, V. Inguibert, D. Payan, "Ground Plasma Tank Modeling and Comparison to Measurements", *IEEE Trans. Plasma Sci.*, Vol. 36, N°5, pp. 2369-2377, Oct. 2008.
- [14] T. Muranaka, S. Hosoda, J.-H. Kim, S. Hatta, K. Ikeda, T. Hamanaga, M. Cho, H. Usui, H. O. Ueda, K. Koga, and T. Goka, "Development of Multi-Utility Spacecraft Charging Analysis Tool (MUSCAT)", *IEEE Trans. Plasma Sci.*, Vol. 36, N°5, pp. 2336-2349, Oct. 2008.
- [15] J.-F. Roussel, F. Rogier, G. Dufour, J.-C. Mateo-Velez, J. Forest, A. Hilgers, D. Rodgers, L. Girard, D. Payan, "SPIS Open Source Code: Methods, Capabilities, Achievements and Prospects", *IEEE Trans. Plasma Sci.*, Vol. 36, N°5, pp. 2360-2368, Oct. 2008.
- [16] L. Lévy, T. Paulmier, B. Dirassen, C. Inguibert, M. Van Eesbeek, "Aging and prompt effects on space material properties", *IEEE Trans. Plasma Sci.*, Vol. 36, N°5, pp. 2228-2237, Oct. 2008.
- [17] B. G. Herron, J. R. Bayles, J. D. Worden, "High-voltage solar array technology", *J. Spacecraft*, Vol. 10, N°7, pp. 457-462, 1973.
- [18] N.T. Grier, N.J Stevens, "Plasma interaction experiment (PIX) flight results", *Spacecraft Charging Technology-1978*, NASA CP-2071, pp. 295-314, 1978.
- [19] D. E. Hastings, G. Wyle, D. Kaufman, "Threshold voltage for arcing on negatively biased solar arrays," *Journal of Spacecraft and Rockets*, Vol. 27, No 5, pp. 539-544, 1990.
- [20] J.-C. Mateo-Velez, V. Inguibert, J.-F. Roussel, D. Sarrail, L. Levy, F. Boulay, E. Laffont, D. Payan, "ESDs on Solar Cells - Degradation, Modeling, and Importance of the Test Setup", *IEEE Trans. Plasma Sci.*, Vol. 36, N°5, pp. 2395-2403, Oct. 2008.
- [21] T. Okumura, S. Ninomiya, H. Masui, K. Toyoda, M. Imaizumi, M. Cho, "Solar cell degradation due to ESD for international standardization of solar array ESD test", 10th SCTC, Biarritz, France, 2007.
- [22] B. Vayner, D. C. Ferguson, J. T. Galofaro, "Emission spectra of arc plasmas", *IEEE Trans. Plasma Sci.*, Vol. 36, N°5, pp. 2219-2227, Oct. 2008.

- [23] D. Payan, D. Schwander, J.-F. Roussel, V. Inguibert, D. Sarrail, J.-C. Mateo-Velez, "CNES-ONERA recommended test set-up to qualify solar array design against sustained arc triggered by an electrostatic discharge", 8th Eur. Space Power Conf., Konstanz, Germany, Sept. 2008.
- [24] E. Amorim, "Electrostatic and secondary discharges on solar arrays: common characteristics with vacuum arcs", Proc. 52th Int. Astronautical Congress, Toulouse, France, Oct. 2001.
- [25] T. Ose, H. Masui, K. Toyoda, M. Cho "Experimental investigation of secondary arc plasma on solar array in GEO environment by spectroscopy", 10th SCTC, Biarritz, France, 2007.
- [26] B. Vayner, J. Galofaro and D. Ferguson, "Interactions of high-voltage solar arrays with their plasma environment: ground tests", J. Spacecraft and Rockets, Vol. 41, No. 6, 2004.
- [27] V. Inguibert, D. Sarrail, J.-C. Mateo-Velez, R. Reulet, L. Levy, F. Boulay, D. Payan, "Electrostatic discharge and secondary arcing on solar array - flashover effect on arc occurrence", IEEE Trans. Plasma Sci., Vol. 36, N°5, pp. 2404-2412, Oct. 2008.
- [28] D.E. Parks, G. A. Jongeward, I. Katz, V. A. Davis, "Threshold-determining mechanism for discharges in high-voltage solar arrays," Journal of Spacecraft and Rockets, Vol. 24, No 4, pp. 367-371, 1987.
- [29] D. E. Hastings, M. Cho, H. Kuninaka, "The arcing rate for a high voltage solar array: theory, experiment and predictions", Journal of Spacecraft and Rockets, Vol. 29, No 4, pp. 538-554, 1992.
- [30] M. Cho, D. E. Hastings, "Computer particle simulation of high voltage solar array arcing onset", Journal of Spacecraft and Rockets, Vol. 30, No 2, pp. 189-201, 1993.
- [31] D. Payan, F. Séverin, J.-P. Catani, J.-F. Roussel, R. Reulet, D. Sarrail, "Electrostatic Discharges on Solar arrays. Physical Model of Inverted Potential Gradient Electrostatic Discharge," 7th Spacecraft Charging Technology Conference, Noordwijk, the Netherlands, 2001.
- [32] B. Jüttner, V. F. Puchkarev, E. Hantzsche, I. Beilis, "Cathode spots," in *Handbook of vacuum arc science and technology, Fundamentals and applications*, R. L. Boxman, P. J. Martin, D. M. Sanders, Ed. New Jersey: Noyes Publications, 1995, pp. 73-281.
- [33] I. I. Beilis, "State of the theory of vacuum arcs", IEEE Trans. Plasma Sci., Vol. 29, N° 5, pp. 657-670, Oct. 2001.
- [34] D. Payan, "Vacuum electrostatic discharges", in *Space Environment: prevention of risks related to spacecraft charging*, Ed. Toulouse: Cépaduès, 2002, pp. 317-366.
- [35] H. C. Miller, "Anode phenomena," in *Handbook of vacuum arc science and technology, Fundamentals and applications*, R. L. Boxman, P. J. Martin, D. M. Sanders, Ed. New Jersey: Noyes Publications, 1995, pp. 308-364.
- [36] M. Belhaj, T. Tondu, V. Inguibert, "Experimental investigation of the effect of the internal space charge accumulation on the electron emission yield of insulators submitted to e-irradiation: application to polycrystalline MgO", J. Phys. D: Appl. Phys. 42 (2009).
- [37] Handbook of Chemistry and Physics, CRC Press, 62nd edition, 1981-1982.
- [38] Material Characterization for Plasma Interaction Analysis, ESA Co 17446/03/NL/CH.
- [39] J.C. Matéo-Vélez et al., "ESDs on solar cells – Degradation, Modeling and importance of the test setup", IEEE Trans. Plasma Sci., Vol. 36, N°5, 2008

DECEMBER 2010

SMP

- [40] D W Williams and W T Williams, "Effect of electrode surface finish on electrical breakdown in vacuum", J. Phys. D: Appl. Phys. (5), 1972.
- [41] Paola Rossetti, Fabrizio Paganucci, and Mariano Andrenucci, "Numerical Model of Thermoelectric Phenomena Leading to Cathode-Spot Ignition", IEEE TRANSACTIONS ON PLASMA SCIENCE, VOL. 30, NO. 4, AUGUST 2002.

2. LITERATURE STUDY

2.1. The context

Satellites and spacecraft in the outer magnetosphere, including geostationary orbit, are subjected to high level of electrical charging, which can attain several thousands of kilovolts during substorms. Large dielectric coverings exposed to the environment are also susceptible to charge differentially w.r.t. the spacecraft structure up to many hundreds of volts. This situation can lead to electrostatic discharges on solar arrays. Two types of discharges are possible on solar panels, depending on the voltages of adjacent conductive parts and dielectric covering. The inverted potential gradient situation (in opposition to the normal potential gradient situation), in which the dielectrics are less negative than conductors, is thought to be the more common and hazardous in orbit.

ESD can generate three types of defects or damages to a satellite. They can induce upsets in electronic components due to the transient currents flowing during the discharge. Then, degradation of cells has been observed during ground test campaign. Finally, ESDs sometimes initiate secondary arcs, causing loss of power on satellites. These arcs are obtained when a part of the solar panel power is dissipated through the discharge. This latter mechanism led to the failure of complete strings on the Tempo-2 and PanAmSat-6 satellites causing a power loss of around 20% ([RD7]).

Means of prevention exist (ECSS-E-20-06 [RD4]) and an international standard of solar panels qualification and characterization is currently being drafted (ISO/DIS 11221 "Space Systems – Space Solar Panels – Spacecraft Charging Induced Electrostatic Discharge Test Methods"). For instance, [RD4] defines a series of requirements that spacecraft constructors may respect. The main requirements with respect to ESD hazard is the maximum permitted voltage between components. In the situation of normal potential gradient, *i.e.* when the dielectric is more negative than the conductor, the maximum differential voltage between a dielectric and an adjacent conductor should not reach 1000 V. Moreover, the electric field within the dielectric shall not exceed 10^7 V/m. In the inverted potential gradient situation, *i.e.* when the dielectric is less negative than the conductor, the maximum differential voltage between a dielectric and an adjacent conductor exposed to vacuum should not reach 100 V. If these requirements can not be fulfilled, the first objective of manufacturers is to avoid sustained secondary arcs, which occur when the arc is powered by solar panels. This approach does not consist in trying to eradicate the emergence of ESDs but rather in preventing their most dangerous consequence: the secondary arcing. Then, the second objective of satellite manufacturers is to estimate the power loss caused by ESDs (without transition to secondary arcs) during the spacecraft lifetime. Indeed, ESD can damage the solar cells by deteriorating their current-voltage characteristics. Cumulative ESD tests have shown that the energy released during the discharge has a serious impact on cells efficiency.

In this context, it is clear that a numerical tool aiming at predicting ESDs on solar panels is extremely interesting. Such a tool, which could simulate the build up of differential potential between surface elements as well as the triggering phase of an ESD, would be a decisive guide for determining the risks associated to a particular design and for giving information on the end of life power margins of solar panels.

2.2. Geostationary Spacecraft Charging

Spacecraft charging results from the possibility of electric charge exchange with the environment. Absolute and differential spacecraft charging are well understood. The environment can charge the space vehicle structure, which constitutes the electric ground reference of embedded electronic components: this is absolute charging. Environment can also charge covering dielectrics relative to the structure: this is differential charging.

In this section a short description of the geosynchronous plasma environment is given in paragraph 2.2.1. Then, the important phenomena that lead to the build up of absolute and differential charging are presented in 2.2.2 and 2.2.3. The global spacecraft charging is finally presented in 2.2.4.

2.2.1. The Geosynchronous Plasma Environment

A spacecraft at GEO is generally outside the plasmopause. Generally, such a spacecraft is surrounded by a relatively cool, tenuous plasma characteristic of the outer magnetosphere. However, sudden injections of high energy plasma (typically a mean energy of a few tens of kilovolts) can occur due to substorms believed to result from a complex interaction between the solar wind plasma and magnetic field and the magnetosphere. Typical plasma parameters at geostationary orbit are represented in Table 1 in normal conditions and during substorms.

Table 1 - Typical plasma parameters at geostationary orbit

	Density (cm ⁻³)	Ion temperature	Electron temperature
Quiet	10	1eV - 1 keV	1eV - 1 keV
Substorm	1	10 keV	10 keV

ECCS-E-10-04A "Space Environment" [RD2] defines a worst case environment for the determination of surface charging, to be used as input to a spacecraft charging simulation or calculation, applicable to the outer magnetosphere environment, including GEO environment. This is a dynamic region in terms of plasma density and temperature and for most engineering purposes, worst case environments are the most important consideration. The worst case of Table 2 is a double Maxwellian fit to an extremely severe event observed by the SCATHA spacecraft on 24 April 1979, when the spacecraft charged to -8 kV in sunlight.

Table 2 - ECCS-E-10-04A Worst-case bi-Maxwellian environment for outer magnetosphere

	Electron density (cm ⁻³)	Electron temperature (keV)	Ion density (cm ⁻³)	Ion temperature (keV)
Population 1	0.2	0.4	0.6	0.2
Population 2	1.2	27.5	1.3	28.0

This kind of environment generally creates high negatively biased absolute potential. The way the different surface materials interact not only with this environment but also with photons produces differential potentials. This is explained in the following paragraphs.

2.2.2. Absolute Charging

The physical law governing the equilibrium potential of a surface immersed in plasma is that electric exchanges with it are globally zero. The current density resulting from such a surface is then:

$$0 = J_e - J_i - J_{sec} - J_{ph} + J_{rec} \quad (1)$$

- with
- $J_e =$ environment electron current density:
 - this is a decreasing function of the negative potential V_a of the collecting surface $J_e = J_e(V_a)$,
 - in condition of extreme substorms: $J_e(0) = 0.8 \text{ nA/cm}^2$.
 - $J_i =$ environment ion current density:
 - for a plasma constituted of electrons and protons at thermodynamic equilibrium $J_i \approx J_e/40$ for a surface at plasma potential ($V = 0$).
 - $J_{sec} =$ backscattered electrons and secondary emission of electrons (SEE) current density:
 - backscattered electrons are electrons reflected back from the surface with some loss of energy. Typically they have half the energy of incident electrons and about 20-30 % of the incident flux. We can take account of them simply by reducing the incident flux.
 - SEE current is more efficient under electron impact and $J_{sec} = \gamma \cdot J_e$ with $\gamma = \gamma(E)$
 - γ_e is the rate of secondary emission under electron impact which depends on the incident energy and on the material. γ_e can be greater or lower than unity. The following law can be used for electron impact with energy E and under incidence angle θ [1]:
$$\gamma(E, \theta) = \gamma_{max} \frac{E}{E_{max}} \exp\left(2 - 2\sqrt{E/E_{max}}\right) \exp(2 - 2\cos\theta) \quad \text{where } \gamma_{max} \text{ and } E_{max} \text{ are}$$

respectively the maximum SEE yield for electron impact and primary electron energy that produces maximum SEE yield. An example is given for kapton® in Figure 1 for a normal incidence.
 - $J_{ph} =$ photoemission current density:
 - In the absence of a barrier, photons impacting normally a kapton® surface extract a saturation current $J_{ph} = J_{ph,sat} = 2 \text{ nA/cm}^2$.

- Photo electrons can be represented by a Maxwellian distribution of equivalent temperature T_{ph} .

J_{rec} = recollected electron current density:

- photoelectron and secondary electron energy is low (some electron-volts). That makes them very sensitive to barriers of potentials. As a result they can be recollected. The barrier of potentials can result from S/C geometry (potentials on surfaces) and from space charge effects.

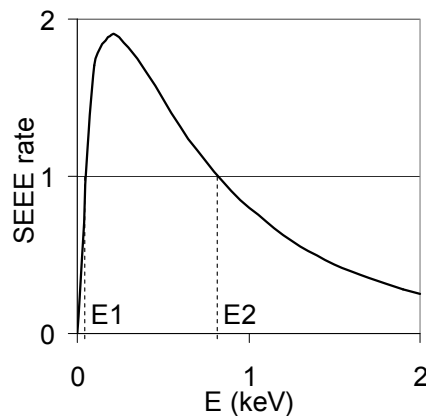


Figure 1 - Secondary emission yield for kapton®

The accumulation of charges on a satellite leads to the change of its potential w.r.t. the neutral ambient plasma. The potential adapts so as to reduce the flow of attracted species and increase the flow of repelled specie, until equilibrium is reached. The potential leading to this equilibrium is called the floating potential. This theoretical view of current collection assumes that no artificial sources, such as plasma thrusters, ion engines or electron emitters for instance are present on the spacecraft.

Finally, the spacecraft is equivalent to a capacitor whose frames are the structure surface and the plasma sheath. This capacitance C_a is charged under the difference of potentials between the structure potential V_a , which results from (1), and the plasma potential (= 0 V) at some Debye lengths. Depending on satellite size and on the geometry (sphere, cylinder, etc.), values of C_a range from about 50 pF to almost 200 pF.

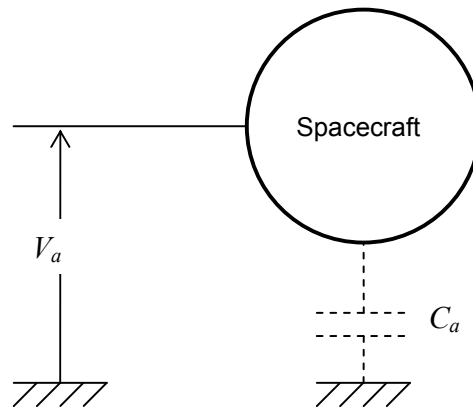


Figure 2 - Absolute charging of a spacecraft

Remark: in a dense LEO plasma, the spacecraft absolute capacitance ranges from some nF to tens of nF.

2.2.3. Differential Charging

Spacecraft are often covered with dielectrics in order to control their thermal equilibrium. Their inner surfaces are generally metallized and set to the absolute potential of the spacecraft. Their outer surfaces are exposed to the environment and can charge differentially in comparison to the structure. The dielectric characteristics of the materials are of course important. This insulating property permits differential voltages if the resistivity of the material is sufficiently high (or equivalently, if the conductivity is sufficiently low). Conductivity depends on the material, on its temperature and on the electric field across the material thickness. Polymers conductivity is generally higher under radiation (energetic electrons and ions, gamma rays). The radiation induced conductivity consists in exciting electrons into the conduction band, which generates charge carriers in direct proportion of the energy absorption rate, *i.e.* dose rate. It might also be pointed out that many experimental setups are currently used to determine the expected important influence of parameters such as temperature and aging.

As a result, the equilibrium equation of these surfaces can be written as:

$$0 = J_e(V_s) - J_i(V_s) - J_{\text{sec}}(V_s) - J_{ph} - J_{\text{rec}}(V_s) - J_C(V_s - V_a) - J_{\text{RIC}}(V_s - V_a) \quad (2)$$

with V_s = surface potential of the considered dielectric (in comparison to plasma potential)

V_a = structure potential (in comparison to the same reference)

J_C = bulk conduction current density: $J_C = \sigma(V_s - V_a)/e$ where σ is the conductivity of the material (in $\Omega.m$) and e the material thickness (m)

J_{RIC} = radiation induced current density: $J_{\text{RIC}} = k \left(\frac{dD}{dt} \right)^\Delta \left(\frac{V_s - V_a}{e} \right)$ where k is the coefficient of

RIC, D is the dose rate and Δ the RIC power (generally between 0.5 and 1). In opposition to RIC, bulk conductivity is also called dark conductivity.

Remark: in the case of heterogeneous dielectric surface charging, surface conductivity also occurs.

Remark: Worst-case environment for absolute charging, *i.e.* environment leading to greatest negative potentials of the structure, is not necessarily a worst-case environment in term of differential charging since the radiation induced conductivity due to energetic electrons can possibly increase the dielectric material conductivity.

Finally, dielectrics are equivalent to a capacitor whose frames are the spacecraft structure and the external dielectric surface, charged under a difference of potentials $V_d = V_s - V_a$. Differential charging is ruled by coating capacitors. For example, the solar cell cover glasses capacitance is about 200 to 300 nF/m².

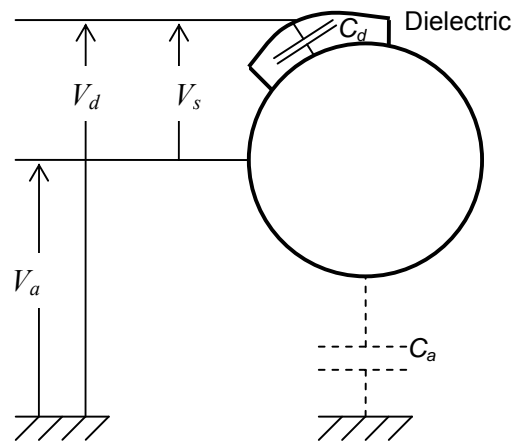


Figure 3 - Absolute and differential charging of a spacecraft

2.2.4. Spacecraft Charging at GEO

In this section, we first introduce the analytical models that can be used to have a first estimation of spacecraft absolute potential in 2.2.4.1. More realistic simulations of spacecraft charging presented in 2.2.4.2 show a rapid view of both absolute and differential voltages obtained on geostationary spacecraft. Finally, charging at the solar cell triple point level is presented in 2.2.4.3.

2.2.4.1. Analytical Models

Due to the large number of involved physical phenomena, spacecraft charging is a complicated problem. Nevertheless, in some simplified cases, spacecraft absolute potential can be analytically estimated. It is the case if we consider the spacecraft only collects electron and ion current from the environment without emitting any particle.

In a non perturbed plasma composed of species following a Maxwellian distribution:

$$f(v) = 4\pi N \left(\frac{m}{2\pi kT} \right)^{\frac{3}{2}} v^2 \exp\left(\frac{-mv^2}{2kT} \right),$$

the current I collected by a surface A related to each species is written as:

$$I = qNA \sqrt{\frac{kT}{2\pi m}} \quad (3)$$

For repelled Maxwellian species, and when the geometry surface is symmetric enough, the current collected is simply:

$$I = qNA\sqrt{\frac{kT}{2\pi m}} \exp\left(-\frac{qV}{kT}\right) \quad (4)$$

For attracted species, the collection depends on the sheath thickness. Well known analytical models exist for simplified geometries such as planes or spheres of conductive material. For a spherical probe immersed in non-flowing Maxwellian plasma, the important parameter is α the Debye ratio between the probe radius and the Debye length. Orbital motion limited models can be used for $\alpha \ll 1$ ('thick sheath') while radial motion (or space charge limited) models are more adapted for $\alpha \gg 1$ ('thin sheath'). None of these two theories is generally adapted to the case $\alpha \approx 1$.

2.2.4.1.1. Thin sheath model - Space charge limited model

Radial motion models are correct if the spacecraft/probe radius is large compared to the sheath of thickness S . This sheath thickness represents the region of area A over which charge is collected. Every particle entering the sheath is assumed to be collected by the probe. The resolution of Poisson's equation together with the equation on energy conservation leads to the determination of S . The Child Langmuir model for a plane ([2]-[3]) was adapted by Langmuir and Blodgett to the case of a spherical probe [4]. This case was fitted by Parker [5] which proposed an expression for A . The current collected is written as:

$$I = J_0 A = qNA\sqrt{\frac{kT}{2\pi m}} \quad \text{for the attracted specie} \quad (5)$$

where $A = 4\pi(R_0 + S)^2$, R_0 being the probe radius

The attracted specie must satisfy the Bohm criterium [6]. A presheath develops between the neutral plasma and the sheath so as to accelerate the attracted specie and permit it to enter the sheath. Allen extended Bohm's theory and proposed for ion collection [7] :

$$I_i = 0.61eN_i A \sqrt{\frac{kT_e}{m_i}} \quad \text{if } T_i \ll T_e \quad (6)$$

2.2.4.1.2. Thick sheath - Orbital motion limited model

In the GEO environment, the sheath is large compared to the spacecraft/probe radius and particles can have orbital motions and miss it. OML current is the maximum current that can be collected if all trajectories in phase space are filled ([8]-[11]). OML theory ignores the sheath and space charge, which practically signifies that the Debye length and the sheath thickness are much larger than the spacecraft/probe radius. That leads to the well known expressions of current collection in attractive and repulsive cases, in the case of spherical symmetry and a Maxwell-Boltzman distribution:

Electrons

$$J_e = J_{e0} e^{-e|V|/kT_e} \quad V < 0 \text{ repelled} \quad (7)$$

$$J_e = J_{e0} (1 + eV/kT_e) \quad V > 0 \text{ attracted} \quad (8)$$

where J_{e0} is the ambient electron current density outside the sheath $J_{e0} = -eN_e \sqrt{\frac{kT_e}{2\pi m_e}}$

Ions

$$J_i = J_{i0} e^{-eV/kT_i} \quad V > 0 \text{ repelled} \quad (9)$$

$$J_i = J_{i0} \left(1 + e|V|/kT_i\right) \quad V < 0 \text{ attracted} \quad (10)$$

where J_{i0} is the ambient ion current density outside the sheath $J_{i0} = eN_i \sqrt{\frac{kT_i}{2\pi m_i}}$

In the spherical symmetry assumption, the potential of a GEO spacecraft can be approximated by the balance between the ion and electron currents. As electrons are much more mobile than ions, the spacecraft potential is negative so as to reduce the electron current. Equation (7) and (10) then lead to the equation ($V < 0$):

$$J_{net} = J_{e0} \exp(-e|V|/kT_e) + J_{i0} \left(1 + e|V|/kT_i\right) \quad (11)$$

The saturated potential V_a is given by $J_{net} = 0$:

$$V_a = -\frac{kT_e}{e} \ln \left[\sqrt{\frac{T_i}{T_e} \frac{m_e}{m_i}} \left(1 - eV_a/kT_i\right) \right] \quad (12)$$

For protons, $\sqrt{m_i/m_e} \approx 43$, and for $T_e \approx T_i$, the solution for V_a is $V_a \approx -2.5 kT_e/e$. The absolute spacecraft charging in GEO is mainly controlled by energetic electrons that impose a negative potential of some kilovolts to the structure. This is due to the mobility of electrons in comparison to ions. Electron current being 40 times greater than ion current (for a spacecraft at plasma potential), electrons are first collected and the spacecraft gets negative, which in turn reduce the electron collection. The equilibrium is then reached when the structure potential is of the order of $-kT_e/e$. This suggests that a spacecraft surface in darkness at GEO may achieve potentials of the order of -10 000 V.

2.2.4.1.3. Photoelectron emission

Let us consider now the GEO environment completed with photons. The current density of photo electrons J_{ph} depends on the surface potential. If photo electrons are represented by a Maxwellian distribution of equivalent temperature T_{ph} then, following [1]:

$$\text{For } V \leq 0: \quad J_{ph} = J_{ph,sat} \quad (13)$$

$$\text{For } V > 0: \quad J_{ph} = J_{ph,sat} \left(1 + \frac{eV}{kT_{ph}}\right) \exp\left(-\frac{eV}{kT_{ph}}\right) \quad (14)$$

If we neglect the effect of barriers of potential, it can be shown that the surface will float to a positive potential $V_s \approx kT_{ph}/e$. Indeed, the photo current is generally one order of magnitude greater than ambient current. As a consequence, the spacecraft tends to float positively so as to enhance ambient electron collection. The floating potential must rise to the order of magnitude of the emitted electron energy, about +2 to +5 V. However, this result must be carefully taken into account because barrier effects inhibiting photoelectrons escape are neglected. As described in the next paragraph, it is usually not true.

2.2.4.2. Global Spacecraft Charging Numerical Models

The analytical models above are useful to obtain a first estimation of the spacecraft potential in orbit. Numerical simulations are yet more adapted to realistic geometries.

Numerical codes aiming at determining the interaction between spacecraft and plasma can calculate the current collection by simple objects; see for example the results of [12], [13] and [14]. In more complicated

situations, SPIS, the Spacecraft Plasma Interaction Software, has already shown its capabilities to simulate the spacecraft voltage at different length scales: spacecraft and intercellular gap scales [15]. In this previous work, a spacecraft was immersed in a plasma composed of $3 \times 10^6 \text{ m}^{-3}$ of cold 1 eV electrons, $3 \times 10^6 \text{ m}^{-3}$ of warm 10 keV electrons and $6 \times 10^6 \text{ cm}^{-3}$ of 100 eV protons. The photocurrent was 2 nA/cm^2 . The potential of the solar panels chassis (whose dimension is $2 \times 10 \text{ m}$) is about -3000 V while solar cells cover glasses potential is about -2000 V . As a consequence, the differential voltage between surface components is about 1000 V .

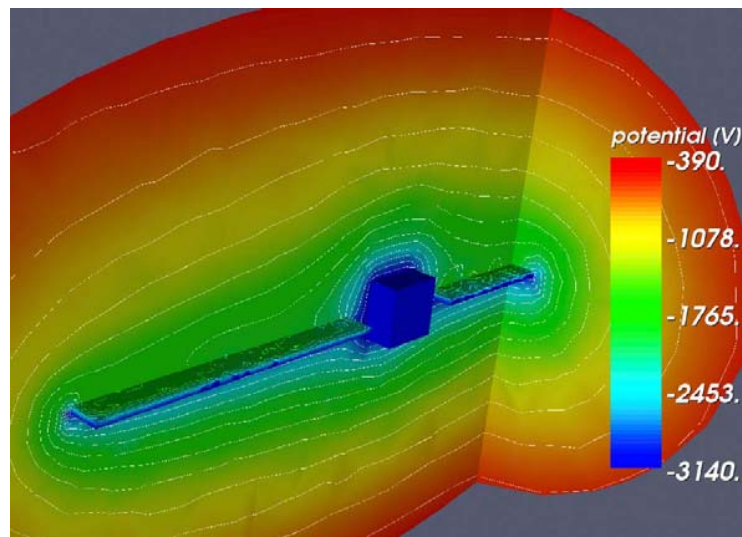


Figure 4 - MUSCAT simulation of spacecraft charging in GEO [15]; isopotential lines

The Multi-Utility Spacecraft Charging Analysis Tool (MUSCAT) was also used to simulate GEO satellite charging in the following conditions: Maxwellian electrons with $N_e = 1 \times 10^7 \text{ m}^{-3}$, $kT_e = 7.5 \text{ keV}$, and ions with $N_i = 0.25 \times 10^6 \text{ m}^{-3}$ and $kT_i = 10 \text{ keV}$ [14]. The differential charging of the coverglass was obtained by high secondary emission yield instead of photoemission. A differential voltage of more than one thousand volts is obtained at a time scale of 60 s.

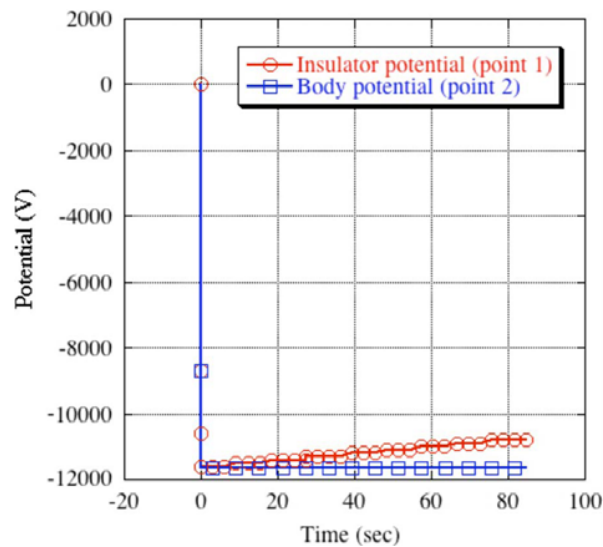


Figure 5 - MUSCAT simulation of spacecraft charging in GE0 [14]

The NASA Charging Analyzer Program (NASCAP) was also used to simulate the time evolution of spacecraft charging using the NASA recommended worst case environment: 12 keV electrons with a density of $1.12 \times 10^6 \text{ m}^{-3}$ and 29.5 keV ions with a density of $2.36 \times 10^5 \text{ m}^{-3}$ [RD6, RD7]. Taking into account the photo current and coverglass resistivity, a differential charging rate of 3 V/s was obtained, cf. Figure 6. After several minutes, a differential voltage of about one thousand volts is obtained.

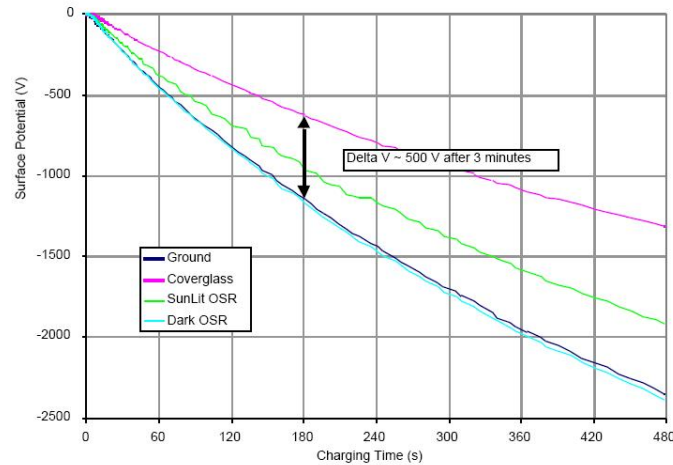


Figure 6 - NASCAP simulation of spacecraft charging in GE0 [RD6, RD7]

These three typical simulations are good illustrations of the so-called inverted potential gradient (IPG) situation. In GEO, the spacecraft absolute voltage is of the order of magnitude of $-kT_e/e$, as explained before because of energetic electrons. Photoemission causes electron emission from sunlit surfaces. Combined with secondary emission, that tends to make dielectrics more positive than the structure, the large Debye length allows the influence of the more negative potential of the array rear side (usually grounded) to spread on top of the sunlit side. Emitted electrons are then prevented from escaping towards infinity once the dielectric surface potential has reached a value slightly more positive than the barrier (emitted electron energy is about

1 to 2 eV), see Figure 7. It is estimated that a 5 V barrier already blocks around 90% of the photo electrons. The balance is reached when the net emitted electron current (around 10 % of photo electrons) compensates the energetic electron current collected by the spacecraft. The surface potential adjusts itself locally so that the normal electric field is very close to zero. It is important to note that the barrier of potential depends on the location on the front side. The situation in which the spacecraft structure is negatively charged and sunlit covering dielectrics positive in comparison to the structure is called inverted potential gradient situation in comparison to the normal gradient situation in which the metallic grounded parts are less negative than dielectric surfaces.

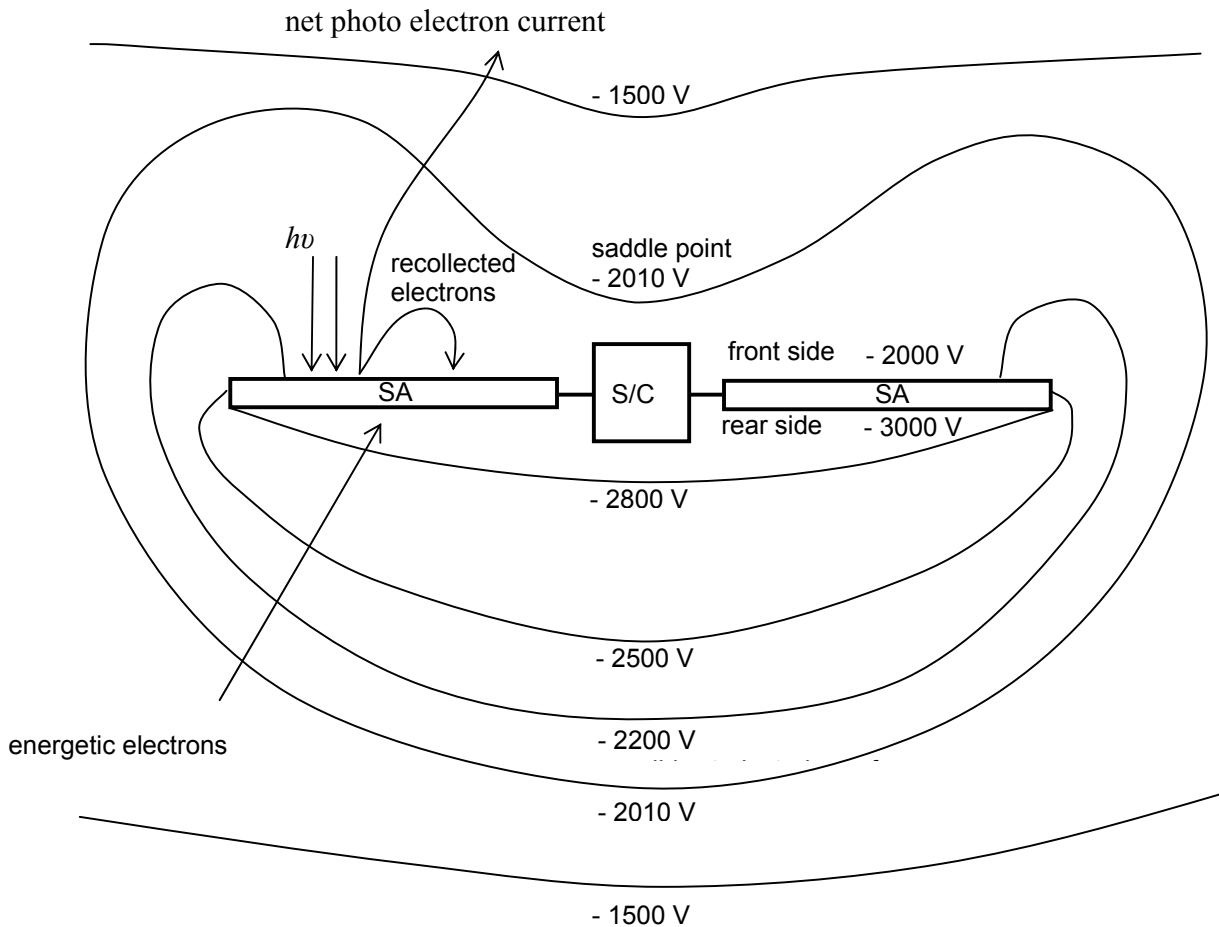


Figure 7 - IPG situation on a GEO spacecraft (typical isopotential lines represented)

It is worth noticing that the phenomena involved in absolute and differential charging are completely 3-dimensional effects. For instance, the way secondary electrons and photoelectrons are recollected depends on the local potentials. In the same way, the collection of ambient particles will depend on geometrical characteristics. As a consequence, the IPG situation will depend both on environment conditions but also on all the characteristics of the spacecraft (geometry, dimensions, material properties, etc.)

2.2.4.3. Charging at Solar Cells Triple Points

Cover glasses represent the main dielectric surfaces on the sunlit face and the surface potential is quite uniform. Combined with the glue that fixes them on the solar cells, they are very resistive and the situation depicted in Figure 7 is possible. The inverted potential gradient is yet not uniform at the intercellular gap

level, represented in Figure 8. The solar cell voltage is close to the structure potential since cells strings are generally charged under less than 100 V. The gap surface is usually coated with Kapton[®], assumed to be photo conductive (enough for the potential difference through the Kapton to be negligible, *i.e.* a bulk conductivity roughly above $10^{-11} \Omega^{-1} \cdot \text{m}^{-1}$). Then the gap area potential is close to the structure potential too. The potential at the top of the coverglass is significantly positive in comparison to the solar cell due to the global IPG situation. Depending on surface conductivity and first of all on the way photoelectrons are blocked, a gradient of potential is created between the top of the coverglass and the solar cell. Roussel *et al.* showed that this gradient region can extend over a few millimetres [15].

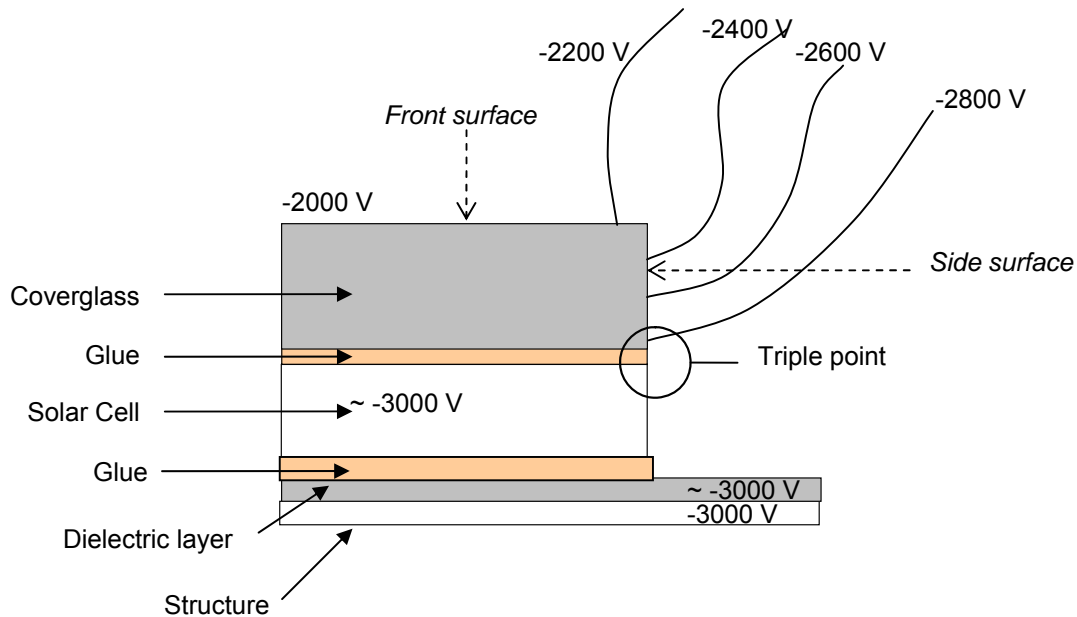


Figure 8 - Schematic of solar cell assembly in typical IPG situation

It is interesting to notice that materials can be more or less conductive depending on the ambient temperature. In general, it is very difficult to estimate the conductivity of covering surface assemblies since they are composed of the cover glass itself but also the glue. In such a layered assembly, the material with the smallest conductivity imposes its coefficient of conductivity to the whole assembly. This is important for spacecraft differential charging analysis; especially as radiation induced conductivity can have different effects depending on the material. The effective conductivity (dark conductivity + RIC) of space materials is still under research. Lévy *et al.* showed that for most materials like polyimide (Kapton), cover glass and adhesives, the RIC helps decreasing the differential potential [16]. They also showed that polymer films such as Kapton, Teflon and Upilex exhibit low dark conductivity and comparatively an enhanced dark conductivity after several days or months of dose. This phenomenon is called delayed RIC (DRIC) since radiations can produce an enhanced dark conductivity. They also put the stress on the fact that other parameters such as temperature or ageing could have a huge effect on dark and RIC conductivity. The passage in eclipse is expected to decrease the material conductivity and to lead to high differential charging. As a consequence, three materials with different potentials can co-exist at solar cell assembly level: metal, dielectric and vacuum. The precise location of the triple point depends on the conductivity of the glue and on the geometry. Conductive glue would shift the triple point to the junction between the glue and the cover glass for example. This situation is known as triple point which is the starting point of electrostatic

discharges on solar cell assemblies in particular, and on every location where resistive dielectrics are adjacent to metallic grounded elements in general.

2.3. Discharges on Solar Panels

An electrostatic discharge can be separated in two phases: the ignition and the propagation. Several types of ignition are possible. The ignition deals with the production of carriers, electrons and ions. This production can be initiated by a wide range of events: micrometeoroid impacts, dielectric breakdown, man-made plasma production, local pressure increase (leading to a Paschen's discharge), or field emission due to an electrical field enhancement in the vicinity of a triple point (conductor-dielectric-vacuum). Field enhancement in the vicinity of a triple point is yet thought to be the predominant mechanism for electrostatic discharge in the inverted potential gradient situation on solar panels.

In 2.3.1, a survey of the experimental evidence and theoretical research on electrostatic discharges on orbit conditions is proposed. That deals with a certain number of additional phenomena (such as field-effect emission for ESD ignition or heat transfer for cathode spot). Finally, the key issues for numerical modelling of the ESD hazard as well as the important parameters to be taken into account during experiments aiming at validating such a tool are presented in 2.3.2.

2.3.1. Discharge Process at Triple Points

The ground experiments developed for the study of ESDs at triple points and in IPG situation are described in 2.3.1.1. The theoretical models proposed to explain the observed phenomena are presented in 2.3.1.2.

2.3.1.1. Observation of ESDs

The first observation of arcing on a negatively biased solar array was made by Herron [17], who biased the solar cells between ± 15 kV and obtained arcing for bias voltage of -6 kV and for a plasma density of 10^8 m^{-3} . In 1978, the NASA plasma interactive experiment (PIX) confirmed that arcing occurs also in space [18]. The experiment consisted in biasing solar cells between ± 1 kV in a 920 km polar orbit and arcing was produced at negative bias voltages greater than -750 V. Then, ground experiments have been extensively and thoroughly performed since electrostatic discharges have been inferred to damage solar arrays. Different kinds of experiments were developed. The first set of experiments consists in the comprehension of the phenomena involved in ESD and secondary arc triggering. The second set consists in determining the threshold for secondary arcing and arc rate. This is generally qualification and characterization tests performed by solar panels constructors from which data are not available.

Remark: normal potential gradient situations in which the dielectric materials are more negative than adjacent metal parts are also responsible for ESD. Nevertheless, as stated in the SOW [ITT], these surface dielectric discharges are believed to be less common than inverted voltage gradient discharges. ECSS requirements on ESD hazard [RD4] are much more constraining for IPG situations (maximum of 1000 V between surface components in the normal gradient situation instead of 100 V in the IPG situation). As a consequence we focus on IPG discharges.

2.3.1.1.1. Experimental Setups

Mainly two kinds of experimental setups have been used to simulate the IPG situation on solar panels. The first setup consists in the use of an electron gun while the second one uses plasma, but both aim at reproducing the IPG situation at triple points.

The plasma setup has been used since the first campaigns whose objective was to determine the arcing onset threshold and arcing rate ([RD6]-[RD7], [19]). The plasma and neutral gas environments in the plasma chambers are typically argon or nitrogen with a pressure range of 10^{-5} to 10^{-3} Pa. The plasma density ranges from 10^3 to 10^6 m^{-3} . The ion energy is typically 1 to 100 eV while the electron thermal energy is about 0.5 to 1 eV. The IPG situation is obtained by biasing the solar cells to high negative voltage w.r.t. ground and in applying a near zero volt potential on the dielectric material by plasma neutralization, *cf.* Figure 9. The bias voltage has the same role as the absolute voltage of the spacecraft V_a . The dielectric sheet behaves as a capacitor C_d charged under the voltage V_a . In comparison to the real situation (ruled by photo emission, secondary electron emission, electron recollection, capacitive coupling), the dense plasma tends to neutralize a bit too efficiently the dielectric surface and in particular the side surface of the cover glasses in contact with the cell. At the triple point vicinity, that leads to an increase in the macroscopic electric field since the potential gradient is greater than normally. The threshold for ESD ignition is then generally lower with the plasma setup than with the electron setup. Concerning secondary arcs now, they depend on the electrical circuit of solar panels and on the possibility to provide the electrostatic discharge with extra power (*i.e.* the solar generator, not the absolute capacitance). Constructors want to ensure that their panels will not produce sustained secondary arcs whatever the origin of the ESD (it could be meteoroids for instance) and the plasma setup is the more comfortable way to obtain ESDs. As a consequence this plasma setup is preferably used for secondary arcing thresholds determination and is often used during solar cells coupons qualification. The EMAGS 2 campaign showed that secondary arcing results obtained in plasma setup are close to the results obtained in electron setup [RD5]. For the assessment of the ESD risk on solar panels (the subject of this study), it is yet necessary to be more precise on the ESD triggering method because the plasma setup will overestimate the ESD hazard. Other means of obtaining the IPG situation must be carried out, in particular the electron setup.

Remark: in the plasma setup, ESDs generally occur on solar cells when the bias voltage is about -500 V, *i.e.* with a differential voltage of about -500 V.

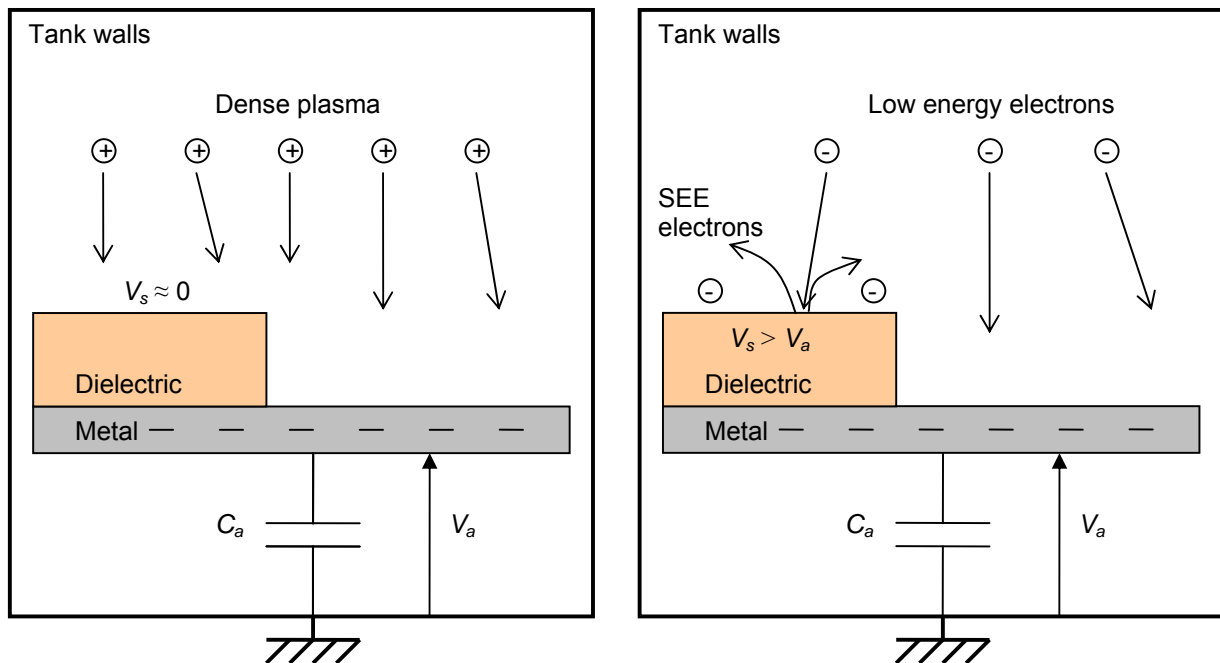


Figure 9 - Inverted potential gradient situation obtained in plasma (left) and electrons (right) during experiments; the dense plasma neutralizes the dielectric surfaces; low energy electrons produces secondary electron emission yield greater than 1

The electron setup consists in using electrons of some thousands electron-volt (with an electron gun) diffused towards the negatively biased coupons. Depending on the biasing voltage and on electron energy, secondary emission of electrons with a yield greater than one is activated. As a result, the potential of the dielectrics slowly increases and the differential voltage too. In this setup, the building of the IPG is more representative of the real one since the IPG is reached by electron emission. In orbit processes of secondary emission exists and we have to consider photo emission too. As photo electrons and secondary emission electrons are emitted with approximately the same energy (about 2 eV), the electron setup during ground experiments is very representative. When electrons collide with the surface, their relative energy $E - eV_s$ must be sufficient to pass the first cross over E_1 (see Figure 1). Then the surface potential will tend to increase towards the equilibrium potential $(E - E_2)/e$. Indeed, if their relative energy passes over E_2 the surface potential gets more negative. Finally, the differential voltage at equilibrium depends on the material, on electron gun energy and on bias voltage of course. The surface potential on top of dielectrics can be measured with non contacting potential probes and the differential voltage necessary for ESD initiation can then be obtained.

Remark: in the electron setup, ESDs generally occur on solar cells when the differential voltage is about -1 kV (surface potential measurements). We do not have access to the potential profile at the triple point vicinity but only to the macroscopic one.

2.3.1.1.2. Experimental Results

The initiation of electrostatic discharges on solar panels is known to occur preferentially on solar cells interconnects and on intercellular gaps (see for example [20]-[22]). Lots of experiments have shown that

damage is also caused by cumulative ESDs produced at solar cell edges, see Figure 10. Pictures of solar cell electroluminescence after ESDs produced on triple junction Arsenic Gallium cells (AsGa) show this kind of damage [21]. This test consists in using the solar cells in an inverse operation mode in which an externally imposed current makes the solar cells emit light (for silicon cells the heating emits in infrared domain while it is visible for AsGa cells). The cell damages are observed in places where the light emission (hence electrical current) concentrates as if short-circuit had occurred. That indicates that something in the solar cell materials and characteristics changes due to ESDs. The ESDs tracks are visible by using adapted devices such as optic microscopes or scanning electron microscope (SEM). The SEM picture of the degradation produced by an ESD obtained on a cell edge with a 500 nF to 1 μ F absolute capacitance is clearly visible in Figure 11 [23]. The coupon was a triple junction AsGa cell and the IPG was obtained with the plasma setup ($V_{bias} \approx -600$ V). The arc track extended over the entire width of the cell, from the glue that fixes it on the kapton® substrate to the junction with the coverglass. The arc completely deteriorates the cell edge. A part of the glue has been removed or evaporated. The solar cell seems to have suffered from melting (see the droplets in Figure 11) and possibly evaporation. The size of the melted area is about 10 to 100 μ m, which agrees with results obtained on zinc samples in the same kind of IPG situation [24]. The current being approximately 1 to 10 A, the current density was about 10^4 to 10^7 A/cm².

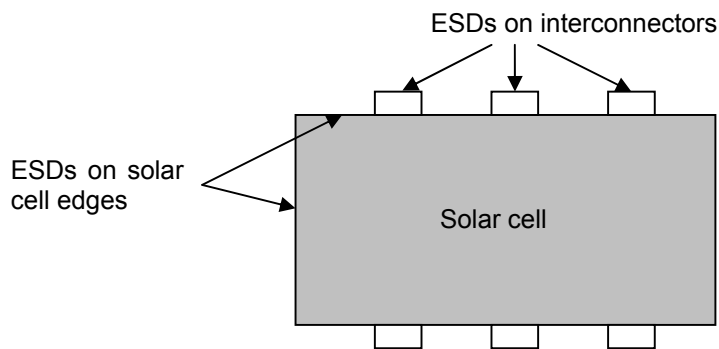


Figure 10 - Global localizations of ESDs on solar cell assemblies

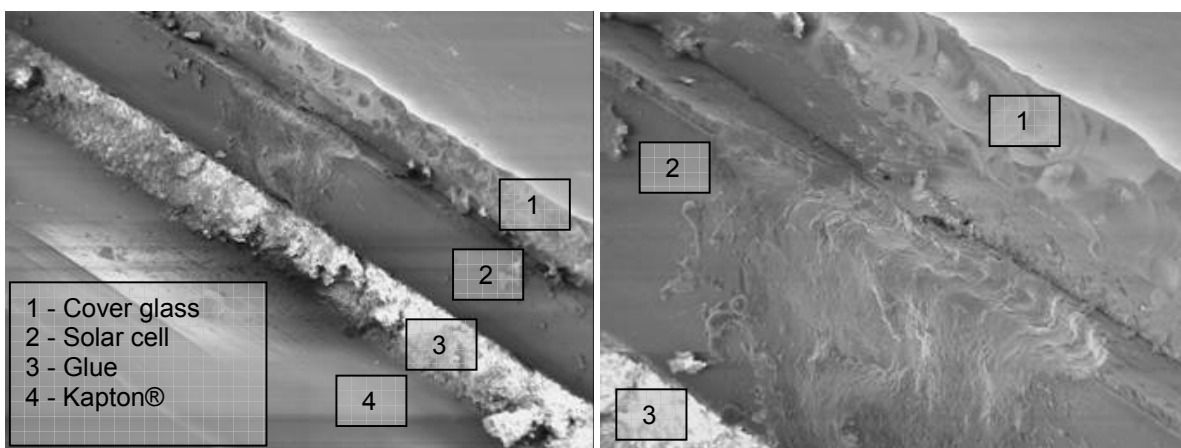


Figure 11 - Edge of a solar cell after a single ESD [23]

Experiments aiming at determining the complete list of the materials involved during the discharges have been conducted since the last few years. It mainly consists in acquiring the spectral emission of light during ESD events ([22], [25]). Discharges are very fast electrical impulsion of about 5 to 50 μs during which the current can attain more than 10 amps. As a consequence, the spectroscopic benches used are thoroughly designed and controlled so as to synchronize the ESD event with its acquisition. The materials ejected from the solar cell assemblies during are: silver, silicon, carbon molecular chains, germanium (which composes 95 % of AsGa cells). It is also worth noticing that hydrogen is observed systematically. Vayner showed that the arcing rate, *i.e.* the number of arcs per unit time, dramatically increases with the residual water vapour partial pressure [26]. As a result, several days of pumping in adequate vacuum chamber are necessary.

Let consider now the electrical signature of the electrostatic discharges. Discharges can be divided in three contributions depending on the way the discharge is powered. The blow-off current is fed by the absolute capacitance C_a charged under the potential V_a and is triggered by the so-called primary discharge described in 2.3.1.2. The flash over is powered by the dielectric covering capacitance C_d in the form of a neutralization wave. Finally the secondary arc (which follows the primary discharge) is powered by the photovoltaic generator or the battery if the solar panel circuitry permits it. The following graph in Figure 12 represents a way to experimentally perform the whole electrical discharges steps on solar cell coupons (see [RD3], [RD4], [22], [23] or [25]).

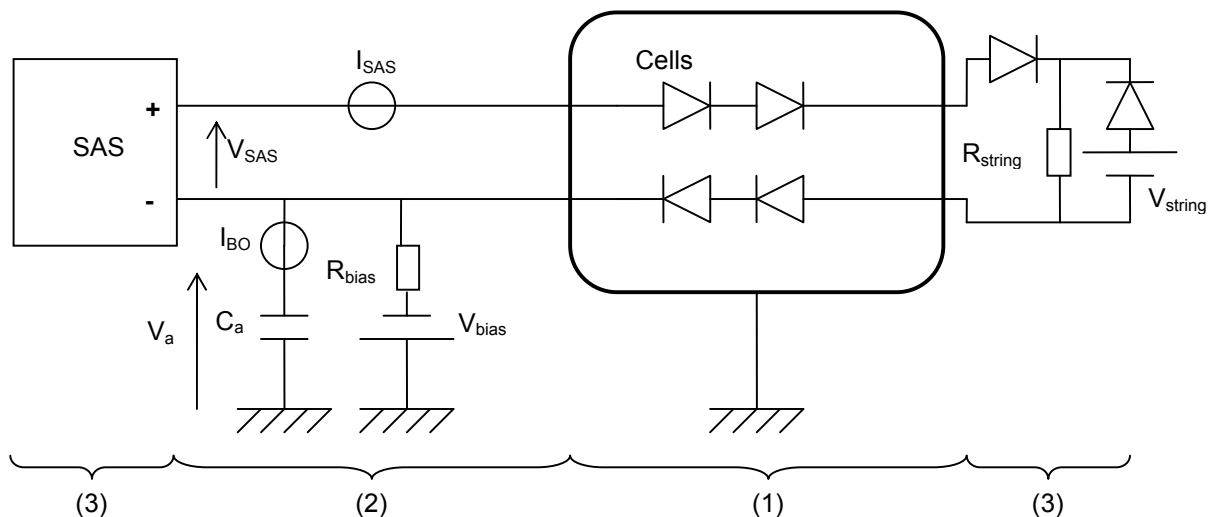


Figure 12 - Typical experimental setup for the triggering of electrostatic discharges on solar cell coupons; (1) represents the solar cell coupons in vacuum chamber; (2) is the external circuit representing the spacecraft absolute capacitance; (3) simulates the solar array and provides power to secondary arcs

Typical waveforms of emitted currents are represented in Figure 13. The blow-off current corresponds to electron emission from the solar cell coupon. Electrons are evacuated to the tank walls and the absolute capacitance discharges. The absolute voltage continuously falls down to zero volts during this short period. In the same time, the flash-over current begins to neutralize the solar cells cover glasses. Measurements of potential profiles show that surfaces of more than 1 m^2 dielectrics surfaces can be discharged [27]. Some experimental setups aim at simulating the cover glasses capacitance by an equivalent capacitor component ([20]-[22]). A more physical and representative dielectric surface aiming at simulating the missing solar cells has been tested at ONERA in collaboration with CNES and discharges of 10 m^2 of dielectric sheet has been

observed [23]. Future works will focus on using real flat panels. Finally, secondary arcing occurs in the gap between adjacent cells if the voltage and if the available string current are sufficient. In that case, discharges powered by the solar array simulator (SAS) can last hundreds of microseconds. If the secondary arcing lasts more than the flash-over, we speak about sustained arcs.

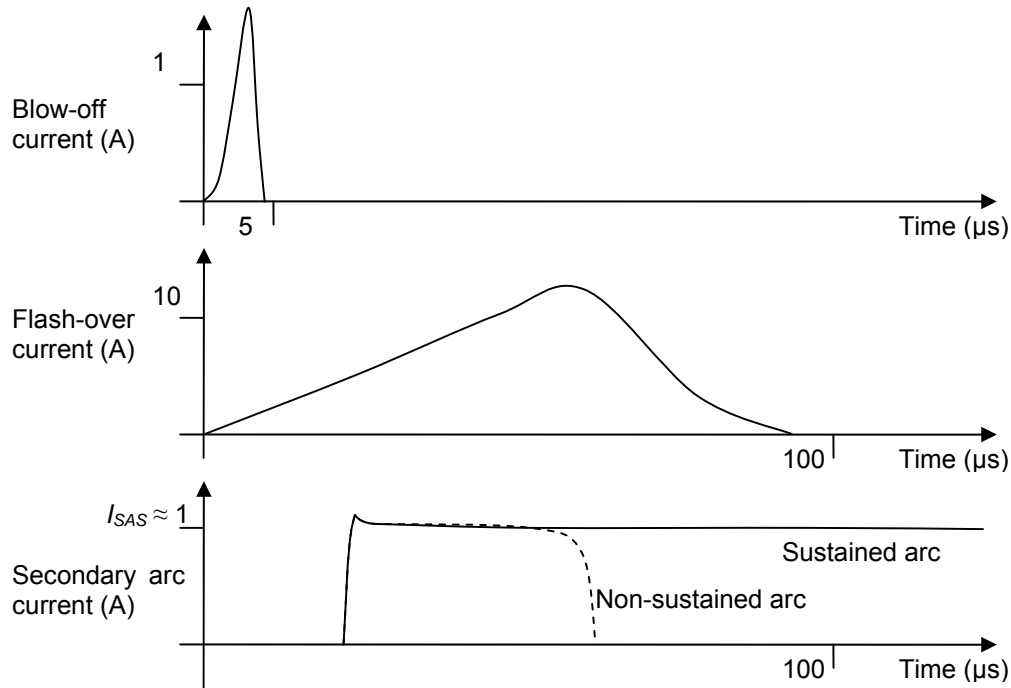


Figure 13 - Typical blow-off, flash-over and secondary arc current waveforms experimentally observed

In the present study we focus on the triggering of ESDs, *i.e.* the very beginning of the electrical phenomena that can finally produce harmful secondary arcing. In this kind of study, a simplified electrical circuitry of solar cells power supply is proposed in the literature, *cf.* Figure 14. The solar array simulator is removed and the solar cells interconnected. The electrostatic discharge gives rise to a transient blow-off current I_{BO} . The resistance R_{bias} is adapted so as to limit the current provided by the power supply during the discharge. As a result, only the absolute capacitance discharges. The dielectrics covering capacitance can also discharge but in the case of a single cell, the flash-over current is negligible.

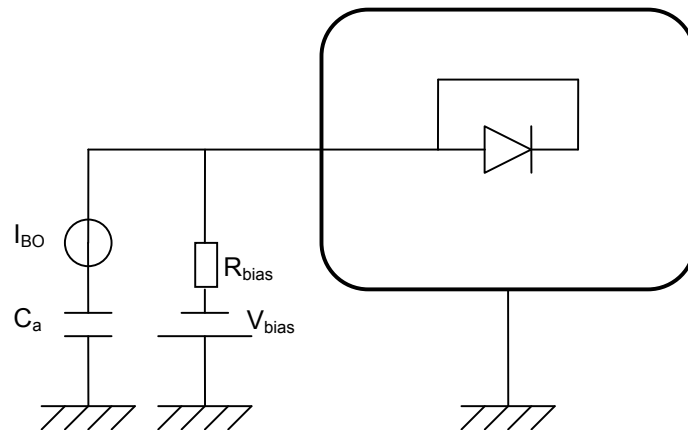


Figure 14 - Simplified test setup used for ESD triggering on a solar cell; the secondary arc is not simulated; the flash-over can be adapted by using several interconnected cells

2.3.1.2. Discharge Model

The breakdown mechanisms leading to discharges on solar panels have been investigated since the late 1980's ([28]-[31]). Theoretical models have been proposed to explain the rise of the current to several amps during the blow-off.

2.3.1.2.1. Cathode Spot

In general terms, an electric arc or discharge may be defined as a discharge between two electrodes in a gas or a vapour in which the voltage drop at the cathode is sufficient to ionize the gas. As a consequence, one could find it difficult to infer electrostatic discharges on orbit. At this stage, several hypotheses can explain the luminous arcs experimentally observed. Hastings *et al.* proposed a first process to explain arcs of several amps ([28]-[30]). They suggested that neutral gas desorbed from the dielectric surface by electron impact could be the medium for a "semivacuum" Paschen discharge. The origin of such electrons is thought to be enhanced field emission of electron (EFEE) and is explained below. The theory of desorbed gas ionization seems in agreement with the experimental results explained before, *i.e.* the fact that arcing rate increases with the residual water vapour partial pressure. The observed microscopic arc tracks also show that the surface materials are completely melted at triple point after an ESD. Erosion is also observed. Moreover the emission spectra demonstrate the presence of a metal vapour/plasma. That clearly signifies that materials are also involved (and not only the desorbed gas). Amorim [24] showed that these discharges have the main characteristics of vacuum arcs ([32]-[33]), in particular in term of crater formation on the cathode. Cathode spot literature indicates spot current densities of 10^5 to 10^8 A/cm² [33] which is in agreement with the current density during primary discharges (estimated with the size of the damaged surfaces and the measured current). When the electron current gets higher (some amps) at the cathode during the EFEE process, Joule effect increases. As the temperature rises, material melting and fusion occur, creating a metallic vapour which becomes the medium of a possible electrical breakdown. Seeding electrons are extracted from the cathode via one of the following processes: field effect, thermionic emission or ion bombardment. A so-called cathode spot is then produced. It has two functions: it provides for the discharge medium by emission of matter in vacuum, and ensures electrical continuity at the cathode by electron emission. In the case of ESDs on solar panels, we speak about aborted vacuum arcs since their development is limited to the charge stocked in the absolute and dielectric covering capacitances. These are the primary discharges experimentally observed.

The structure of cathode spots has been modelled by Beilis [33] and is schematically represented in Figure 15. The cathode spot region may be divided in several regions in which different processes are predominant. The cathode surface is ruled by Joule heating and heat conduction together with electron emission and evaporation. The particles emitted from the cathode flow through the so-called *ballistic zone* which is a collisionless sheath. The strong electric field within this sheath accelerates electrons away from the cathode. A back flow of ion is accelerated towards the cathode which constitutes a significant source of cathode heating. Atoms emitted from the cathode collide with each other and with the back flow in the *heavy particle relaxation zone* which extends a distance a few times the heavy particle mean free path. The accelerated electrons also collide with the neutral flow but as the collision cross section decreases with the electron kinetic energy, the mean free path is longer. The presheath (so-called *electron beam relaxation zone* by Beilis) is then defined as the region in which frequent ionizing collisions occur. A highly ionized plasma is formed and expands until contact with the anode or another solid surface. Once again, it might be said it is theoretical view of the primary discharges since the cathode spots observed during experiments are aborted.

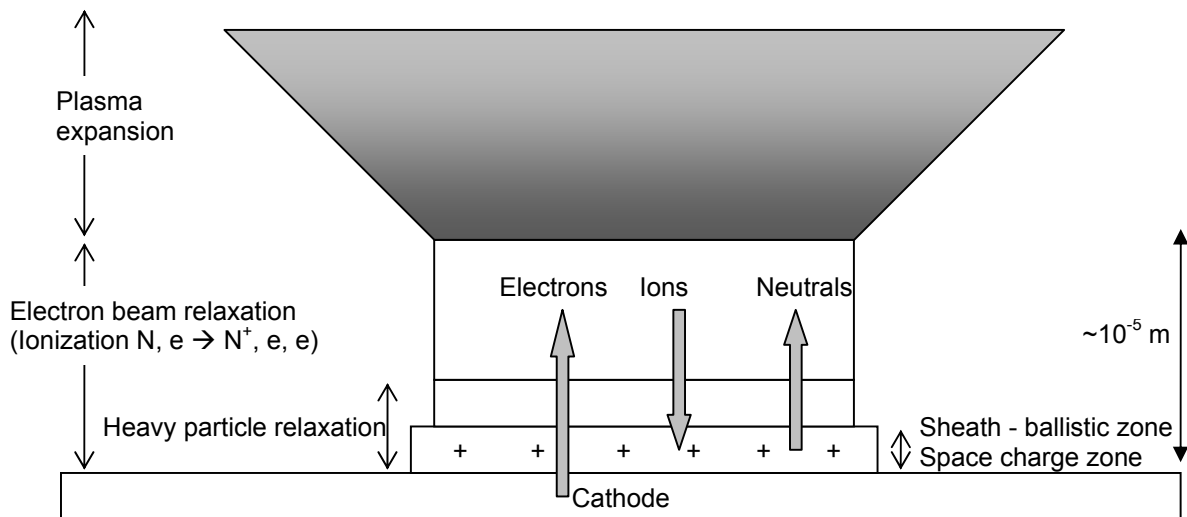


Figure 15 - Model of the vacuum arc cathode spot [33]

2.3.1.2.2. Breakdown Mechanism

Let now focus on the very beginning of the discharge, which is of great interest in the present study, namely the initial electron avalanche that produces cathode heating. Since carrier generation is a key factor in discharges, the important phenomena are emission mechanisms, induced by field or heat. Field emission happens by tunnel effect from conductor submitted to a large external electric field. Pure field effect emission is tunnelling of cold electrons from the metal to the vacuum, *cf.* Figure 16. Without electric field, the barrier of potential is too large for permitting electrons to leave the potential well of the conductor. If a large electric field develops at the surface of the conductor, the barrier has a finite length and the probability of electron escape is no longer null.

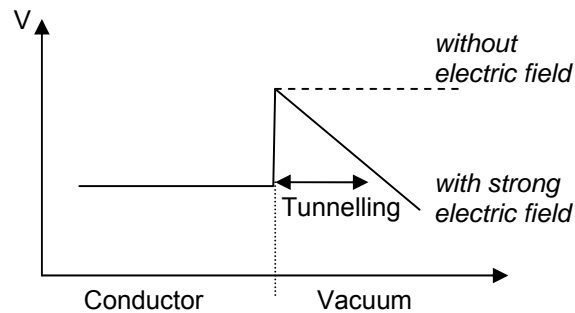


Figure 16 - potential profile through and out of a conductor submitted to a large electric field at its right (left)

There are mainly two types of field enhancement mechanisms. The first one is due to micro structures on the conductor surface such as a micro tips or whiskers. The second one is field enhancement due to a micro dielectric material inclusion on the conductor, as *e.g.* dust. The first mechanism can be responsible for an amplification of the surface electric field of a factor one hundred. The second one can amplify it to a factor of more than one thousand. The mechanism of field effect emission (FEE) can then extract electrons from the conductor with a current density J_{FN} given by the Fowler-Nordheim equation:

$$J_{FN} \sim E^2 \exp\left(-B \phi_w^{3/2} / E\right) \quad (15)$$

where E is the electric field normal to the surface, ϕ_w the metal work function and B a constant.

Thermionic emission is the emission of electrons by a hot conductor. In this case the electrons do not tunnel to leave the potential well of Figure 16 but the most energetic of them get simply enough energy to escape the metal. The so-emitted electron current density is described by the Richardson-Dushman equation:

$$J_T = AT^2 \exp(-\phi_w/kT) \quad (16)$$

where A is a constant.

At the beginning, the thermionic emission can not produce seeding electrons. Moreover, at the triple point vicinity the macroscopic electric field is typically 10^6 to 10^7 V/m, which is not sufficient to produce electron extraction by tunnelling effect. However, at microscopic scales, geometrical irregularities significantly increase the electric field strength and field emission starts. The so-emitted electrons are emitted with an energy close to the material work function, which is close to 4.5 eV for the majority of conductor used in solar cells. Their trajectories are then influenced by local potentials. They are accelerated towards the positive dielectric elements to an energy of several hundreds of volts, which is in the typical range for efficient secondary electron emission, *i.e.* with a yield greater than one. The produced electrons are evacuated to the dielectric-vacuum frontier while keeping a positive charge on the dielectric surface. That immediately amplifies the electric field and so on the field effect emission. The loop is closed and an electron avalanche is triggered. At this stage, the geometrical configuration of the triple point has a huge influence on the electric field enhancement. Some configurations can lead to local barriers of potentials, which prevent secondary electrons from escaping to the plasma. It is also necessary that the emitted electrons collide with the dielectric surfaces. In the case of an intercellular gap, Payan showed that the place of electric field emission is at the upper triple point (between the solar cell and the coverglass), and not at the conjunction of substrate and solar cell [RD3]. Nevertheless, the glue between the solar cell and the substrate was not considered at that time. As a consequence there is still a risk of ESD hazard at the triple point formed at this location if the glue is not conductive enough.

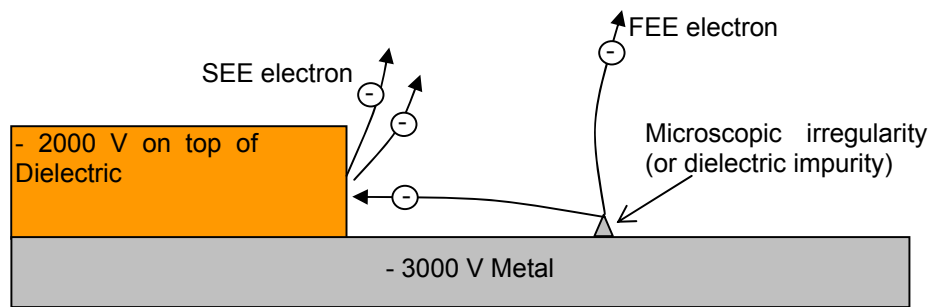


Figure 17 - Mechanisms of electron avalanche from surface micro irregularities

Previous numerical simulations succeeded in calculating the IPG situation at intercellular gap level [RD1]. The electric field amplification was obtained by defining a micro tip of radius $1\ \mu\text{m}$ at the metal surface facing the dielectric coverglass (or resistive glue). We were rather confident that the electron avalanche obtained proved physical divergence. Hastings *et al.* also demonstrated that the combination of field emission and secondary emission at triple point geometry can provide electron avalanche at the earlier stages of the discharge process [29]. The time scale for the development of the electron avalanche is typically some nanoseconds.

Due to Joule effect, cathode temperature increases during the FEE process. As a result, the field-emission current combines with the thermionic current. The combination of the thermo-field emission yield produces a strong non-linear enhancement compared to that of pure thermionic and field emission (more than one hundred) [32]. At this stage melting, vaporization and ionization are intense. The cathode spot is created. To obtain an ESD it is yet necessary that the cathode surface supporting the initial electron avalanche can sustain the heating. To trigger a cathode spot, the metal vapour must be sufficiently dense. If the mean free path for ionization collision is shorter than typical length scale of the triple point, then volume ionization starts which in turn provides the medium with new charge carriers that heat the cathode. That highlights the issue of the temperature equilibrium of the micro structure at the origin of the electron avalanche. If it is big enough, the metal vapour will sustain volume ionization. But it shall not be too large in order to produce adequate enhancement of the electric field. Payan indicates that tips with radius of $0.4\ \mu\text{m}$ can sustain ESDs [34].

2.3.1.2.3. Plasma Expansion and Secondary Arc

Let us now consider the expansion of the plasma created by the cathode spot. It expands from the cathode to a counter electrode: infinity or spacecraft surface. The inter electrode plasma of a vacuum arc serves to conduct the arc current from the cathode to the anode, the anode being possibly any conductor whose potential is greater than the cathode. The plasma is also a medium that interacts strongly with the electrodes. For instance, electrons from the plasma bubble are attracted by the positively charged dielectrics and neutralize these surfaces. This is the physical explanation of the flash over experimentally observed. The plasma expansion velocity is imposed by ion velocity (and the current amplitude too). $10\ \text{eV}$ ions have a velocity of about $10^4\ \text{m/s}$, which is roughly of the order of magnitude of the experimental results.

Once the plasma bubble has reached a collecting electrode such as an adjacent solar cell, important phenomena can occur which can modify the inter electrode plasma. Indeed, the electrical current initially limited by the plasma bubble expansion rises once the plasma connects two cells with a voltage difference supporting at least the cathode drop. This is typically the case in solar cell strings, between which voltages can reach $100\ \text{V}$. An anode spot is obtained when the current density flowing through the counter electrode is about $1\ \text{to}\ 5\ \text{A/mm}^2$, depending on materials [35]. This is typically in the range of the currents measured

during blow-off and flash-over. As denser plasma implies higher conductivity, the current is highly enhanced. If the solar panel electrical circuit permits the flow of such an inrush current, a secondary arc can be triggered which follows the same physics as anode spot. In that case a part of the solar panel power can effectively feed the discharge. Contrarily to blow-off and flash-over, limited to their respective capacitances, a secondary arc is a "real arc", *i.e.* it can last for milliseconds as long as the solar array sustains it.

Remark: the flash-over has a significant impact on secondary arcing. The first is that the flash-over extends the duration of the discharge in comparison to the initial blow-off. As a consequence, it increases the probability to obtain secondary arcs. The second effect influence is the distant arc triggering. If the plasma bubble connects the cathode spot to a solar cell, even at distance greater than 10 cm typically, secondary arcing can occur on that distant cell.

2.3.2. Specific Issues for ESD Hazard Modelling and Experiments

The physics of electrostatic discharges on solar panels is multi-scale and multi-physics. For instance, the global charging state depends on the whole spacecraft interaction with the environment whereas ESDs enhanced field emission of electrons is a micrometric scale process. A huge number of phenomena with very separate time scales are also involved in cathode spots and secondary arcing. As a consequence, an ESD hazard assessment strategy must be developed with regard to the major parameters that influence the onset of ESDs. Dedicated experiments and corresponding simulations must be performed in order to validate any numerical tool aiming at assessing the ESD risk on solar panels. This paragraph deduces from the literature study the key points that must be taken into consideration while neglecting other secondary processes.

The literature study demonstrates the electrostatic discharge risk arises as soon as the inverted voltage gradient situation at triple points is sufficiently pronounced. As a consequence, it is not necessary to simulate the whole discharge process, *i.e.* cathode heating, thermionic current, metal vaporization and ionization, plasma expansion, anode spot, etc., which are far beyond the scope of this study. The risk assessment can be summarized in: *if an electron avalanche occurs on a sufficiently big microscopic structure, there is strong risk of cathode spot initiation.* The situation to simulate is the IPG at triple points leading to electron avalanche.

In the scope of the development of a code aiming at assessing the ESD risk on solar panels, two phases are already clearly identified. Phase 1 corresponds to the delivery of a tool that can be used on a wide range of configurations by users (differing charging means, as *e.g.* photo emission, materials, RIC, etc.). Phase 2 corresponds to the validation of this code by comparison to experiments. During this phase, the code shall simulate as precisely as possible the experimental conditions (charging, materials, triple point geometry, etc.) which shall be as representative as possible from the real conditions.

This 2-phases development completely confirms the approach of ESD modelling of the proposal for the Development of a Predictive Discharge Numerical Model on Solar Panels [PROP] in response to [ITT]. The following items are then recalled from the initial proposed approach of [ITT] with some new elements when necessary.

Remark: Phase 1 and Phase 2 shall not be necessarily performed in this order. On the contrary, it may be more efficient to perform code developments and experiments in a parallel iterative process.

○ *The triple point geometry.* First of all, the triple point must be carefully taken into account. Simulation at microscopic scale for which SPIS has already been used aimed at confirming the scenario of discharge triggering: enhanced field-effect emission leading to electron avalanche. However, since a lot of possible undetermined microscopic geometrical configurations exist (micro tips, dust, dielectric inclusion on metal, etc.), it is not realistic to generate micrometric geometries. As it is often done, we propose to introduce a local electric field amplification factor β , which takes account of microscopic geometries. This solution combines the simplicity of mesoscopic scale modelling of the triple point (co-planar or perpendicular dielectric metal junction) with the needed treatment of micro scale structures that induce discharge ignition. This later treatment is absolutely necessary since forgetting this microscopic effect simply leads to underestimation of the discharge risk. The value of the parameter β must be derived from experimental or physical data. For instance, the size of the micro tips must be capable of sustaining a sufficient electron avalanche current so as to induce a cathode spot, associated with its blow-off current. Indeed, the cathode heating results in melting and mass losses, and so on electric field decrease, which signifies that only sufficiently massive micro structures can sustain the heating and lead to the arc. In the case of micro tips, the minimum radius is 0.4 μm , following [34].

○ *IPG at triple point level.* IPG situations typically met in GEO can be modelled at spacecraft level or even from spacecraft to millimetre solar cells gap scale [15]. Here the triple point simulation at mesoscopic scale (typically microns to millimetres) shall be separated from the spacecraft level assessment. The heavy user shall supply the final code with the potential of the metal materials and with the potential of the boundary limits. This preliminary work is an input for the final ESD prediction tool, which do not aim at calculating the spacecraft response to the environment but rather at simulating the ESD hazard induced by given charging levels. During the validation and verification phase of the software development however (phase 2), the simulations shall be performed on configurations as close as possible from experiments. In order to obtain comparable and reliable results, simple mesoscopic geometries of the triple points shall be tested. It will be discussed in close cooperation with ESA TO. At a first approach we can consider the two configurations of Figure 18, in agreement with [ITT] and [PROP]. The experimental IPG situation will be obtained with electrons in order to reflect the real gradient of potential obtained in flight. In order to simulate the gradient of potential in the vicinity of the triple point, the numerical model shall not impose a voltage on top of the dielectrics. That would overestimate the ESD risk by increasing badly the macroscopic field. It shall be calculated self-consistently by the equilibrium between collected and emitted particles coupled with Poisson equation and conduction.

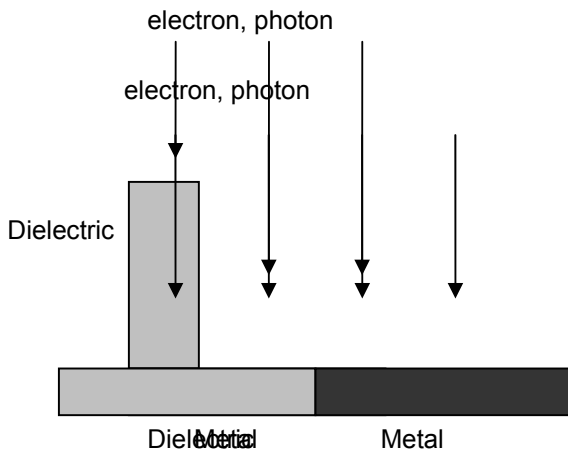


Figure 18 - The two proposed configurations of IPG at triple point: co-planar (left) and perpendicular (right); during phase 2

○ *Time scales.* Some of the simulations reported in [RD1] were performed with constant time step at charging time scale (seconds to minutes), but with the code diverging in case of ESD triggering due to the too large time step. We simply used this diverging as the diagnostic of the occurrence of an ESD. We are rather confident that it really proved physical divergence. However a significant improvement would be to really model further the ESD start, and not simply have the code diverge. Other simulations were made by accelerating charging (by enhancing the photoemission by ten orders of magnitude) to have all phenomena at the same time scale. This way we really modelled the ESD start over a significant duration (electron avalanche amplification). We found however that this second method introduced non-physical distortions. The reason is that three main phenomena with their own time scales are involved in the process: charging (through particle collection and emission), conductivity and eventually ESD development (field emission and field enhancement by secondary emission on the nearby dielectrics). Conductivity enters into play both to limit charging and ESD. Hence accelerating charging without accelerating conductivity spoils charging modelling, of which two major contributions are not modified on the same footing. But accelerating also conductivity (by increasing conductance), while it restores a correct modelling of charging, spoils ESD development because the increased conductivity unphysically limits the avalanche process. This approach had to be discarded. We are thus left with the only solution of a multi time scale modelling without artificially accelerating any of the processes.

○ *Dielectrics properties.* As discussed above, the dielectric property of materials completely influence the onset of the *discharge*. It will be then necessary to test different materials. During IPG experiments with the electron setup, the bulk conductivity can modify the charging state at triple point level. It can also mitigate the enhanced field emission during the electron avalanche. The complex interaction between charge, conductivity and field emission must be studied in the simplest case, *i.e.* without radiation induced conductivity, in order to understand clearly the precedence of the various parameters.

- *Dielectrics thickness.* The *capacitive* coupling of a thin dielectric surface top with the underlying ground can be modelled by a plane capacitor, as *e.g.* in SPIS modelling. Here close to a triple point, at a space scale close to or smaller than capacitors thickness, capacitive coupling also exists between neighbouring dielectric surfaces (a charge deposited on top of a dielectric surface modifies the potential not only at the same location but also on the nearby dielectrics, by influence). This shall be taken into consideration.
- *Secondary emission.* The *enhanced* field emission process is possible if field electrons obtain a suitable energy when colliding with the dielectric surface. This energy depends on the electric field map. The minimal and maximal energies E_1 and E_2 for secondary emission depend on the material used.
- *Metal type and field-effect.* Field-effect emission is the basic phenomenon in the modelling of ESDs. The dependence of the emitted current on the surface electric field and on the metal work function (through Fowler-Nordheim equation) is steep. It seems interesting to determine if that really influences the ESD development.
- *Particle trajectories.* The enhanced field emission theory of electron avalanche highlights the importance of field emission and secondary electron trajectories, which depend on the electric field map. If the field emission electrons do not collide with the dielectric surface, secondary emission is not possible. In the opposite case, the secondary electrons could be prevented from escaping the region they come from, as *e.g.* if there are local barriers of potential.
- *Dimension of the model.* The *geometry* of triple points is 2D, but once an ESD starts a singular point is generated and the problem becomes 3D. We think that performing a 2D modelling would introduce many large errors. Whether an ESD starts or not depends of a competition between charging, conductivity, field emission and field enhancement by secondary emission when field emission has started. Simulating all of these processes in a 2D code is equivalent to assuming that this ESD ignition does not have a point-like but a line-like geometry. Although the initial field can be correct (real 2D geometry), as soon as the ESD starts the very localised potential change makes the field map 3D and the 2D field computation wrong. Moreover the conductivity and the electron expansion are very different in 2D and 3D (very different electron and conductivity paths). All of that makes us believe that a 3D simulation is really unavoidable for realistic results.
- *Accuracy criterion.* During phase 2, the success of simulation *vs.* experiment results shall be assessed for each set of parameters by the comparison between the differential voltages that lead to the discharge, *i.e.* to an electron avalanche on a microstructure that can sustain Joule effect till cathode spot. Experimentally it will be obtained by measuring the surface potential profiles regularly (and so on just before discharge occurrence).

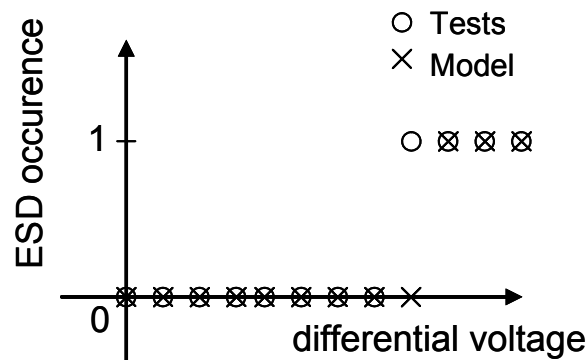


Figure 19 - Accuracy criterion for tests and simulations

- *Ease of use, portability and maintainability of the code.* The code shall take account of the necessity to provide users with an easily usable tool. The major parameters shall also be accessible in order that the ESD risk might be confidently assessed on various configurations.

2.4. Conclusion

The literature study performed in this Technical Note has highlighted the major parameters that influence the onset of ESDs on solar panels:

- The macroscopic electric field at triple points is generally too low to trigger an ESD, but local amplifications by microscopic irregularities always exist and constitute an actual risk for ESD onset. Nevertheless, only the biggest of these irregularities can sustain the electron avalanche till cathode spot initiation.
- The electric field lines may prevent the field emission electrons from colliding with the dielectric surface. As a result, the geometry of the triple points may have a crucial importance.
- When colliding with the dielectric, the field emission electrons may not have the suitable energy so as to produce secondary electrons with a yield greater than one. There is a dependence on electric field lines once more but also on dielectrics properties.
- The secondary electrons may be prevented from escaping the place where they are created. The recollection due to local barrier of potentials is a possible way of ESD risk mitigation.
- The dielectric conductivity may be sufficiently high so as to carry the charge from the top dielectric to the grounded metal, which would decrease the IPG level at triple point.

The experiments and the corresponding simulations that can be used to validate a numerical tool aiming at assessing the ESD hazard on solar panels have also been investigated in this report. The IPG situation in ground vacuum chamber shall be obtained with the electron setup. For each set of parameters (triple point geometry, metal type, dielectric conductivity and secondary emission), the accuracy of the code shall be assessed by the differential voltages leading to ESDs during experiments, and to electron avalanche during simulations.

3. USER REQUIREMENTS

The context of this software development and the situations that the code should be able to model are described in section 3.1. They naturally lead to requirements, presented in section 3.2.

User Requirements Referencing

User requirements were numbered to allow a proper tracking throughout the project.

URx refers to high level requirements.

URx.y refers to detailed level requirements of URx.

3.1. The Context

The context in which the present software shall be developed is described in section 2. The physics to model is the ESD triggering at triple points on solar panels. More precisely, the objective is to provide a code predicting discharge occurrence on typical configurations.

SPIS, the Spacecraft Plasma Interaction Software [RD9], has proven its capability in simulating plasma dynamics and spacecraft charging in a wide range of configurations. The present study aims at providing ameliorations of this code in the domain of ESD prediction.

SPIS has been designed in a modular fashion, allowing the interfacing with external tools and the integration of new routines or modules. The co-development in the frame of the SPINE community has shown the possibility to extend its capabilities to a wide range of configurations. In particular, the Time Dependent version of SPIS permits to simulate multi-physics multi-scale problems. This version is appropriate to innovative research and technology area such as the development of a code aiming at predicting ESDs on solar panels because it involves physical phenomena with different space and time scales.

Although the requirements and the structure of the software are still to be defined, the general structure of the modelling process is known. A simulation is based on data which must be prepared and provided to the code through a pre-processing task. It mostly consists in defining the triple point geometry and properties, and the environment it interact with (UR1, UR2 and UR3). It may also involve simulation control command, *e.g.* the IPG level. The simulation is the next step. Plasma dynamics is already managed by SPIS. Electron avalanche is the criteria for ESD hazard assessment. The code must handle their creation, transport and interaction with materials (UR4). The plasma /spacecraft coupling necessitates simulating the physics at two time scales: triple point charging and ESD ignition, which range from minutes to fractions of nanosecond (UR5). The correct way of handling this huge range of time scales is to have a variable time step with an implicit solver for the spacecraft equivalent circuit (to ensure stability). The implicit solver has been developed ("SPIS time-dependent" ESA contract, in progress at ONERA) and applied to common situations like charging in GEO. However this type of solver, using Newton-type methods, requires specific information on the variation of the emitted or collected currents with local potentials (to implement Newton-type implicit prediction). This information indeed based on physical assumptions is different for each type of interaction or population. This specific work has not yet been done for the very special interaction which is field emission. The major development to be done is thus the writing, coding, tuning and testing of the assumptions for the behaviour of field emission in case of small potential changes on the surrounding surface elements. The same is true for the re-collection of these electrons emitted by field emission. The

tuning of these data needed by the implicit solver might be delicate because of the number of orders of magnitude between the timescales of IPG creation and ESD triggering (at least 10). It might for example necessitate new work on the same mechanism for secondary electrons which also undergo a very fast time-evolution since they are generated from electrons stemming from field emission. The post-processing of simulation results is subdivided in the post-treatment of data and their representation, most of the time graphical (UR6).

3.2. User Requirements Formulation

3.2.1. UR1: IPG Situation

Electron avalanche due to IPG at Triple Point depends on: the macroscopic spacecraft charging, the mesoscopic geometry of triple points and the microscopic structures. It is necessary to take account of all these scales, but not to simulate all of them. It has been chosen to simulate the mesoscopic scale and to model the macroscopic and microscopic scales (as e.g. input parameters for the simulation).

UR1.1 Triple point geometry

Co-planar and perpendicular triple point geometries shall be delivered at mesoscopic scale, *i.e.* at triple point length scale. We must keep to a limited number of cases (possibly with parameters). These cases must probably not be limited to perpendicular or coplanar.

UR1.2 Boundary conditions

Means to take account of the macroscopic barrier of potential due to the solar panel rear side shall be delivered. An adequate set of boundary conditions shall be delivered to users.

UR1.3 Microscopic structures

The treatment of microscopic structures at the origin of field emission shall be performed by introducing a local electric field amplification factor β .

UR1.4 Interaction with the environment

The IPG shall be obtained by interaction of materials with photons or low energy electrons.

UR1.5 Dimension of the problem

The IPG at triple points shall be modelled in 3 dimensions.

3.2.2. UR2: Metals

UR2.1 Work function

Different metals with different work functions (for FEE of electrons) shall be accessible to users.

3.2.3. UR3: Dielectrics

UR3.1 Dielectric properties

Different dielectrics with different conductivities and secondary emission coefficient shall be accessible to users.

UR3.2 Dielectric thickness

The thickness of dielectrics shall be taken into account in term of capacitive and conductive coupling between surface charges and underlying conductors.

3.2.4. UR4: Electron Avalanche**UR4.1 Electron creation**

Seeding electron production shall be simulated by field-effect emission.

UR4.2 Electron trajectories

The 3D electron trajectory shall be calculated in order to assess the interaction with materials.

UR4.3 Electron interaction with materials

The secondary emission of electron by electron impact shall be simulated. The trajectory of these electrons shall be simulated.

3.2.5. UR5: Time scales

The two phases of ESD ignition (Charging and Electron avalanche) must be correctly handled, which implies the use of a multi time scale method. The Time Dependent version of SPIS must be used and ameliorated in the particular case of the physics of ESDs (field effect and secondary emission).

UR5.1 IPG phase

The behaviour of electrons emitted from the dielectrics in case of small potential changes on the surrounding surface elements must be implemented. This phase has already been performed during SPIS TD development.

UR5.2 Electron avalanche

The behaviour of field emission, re-collection of the so-created electrons and secondary emission due to these same electrons in case of small potential changes on the surrounding surface elements must be implemented.

3.2.6. UR6: Post Processing

SPIS capabilities in term of post processing shall be enhanced by the following possibilities.

UR6.1 ESD Hazard

The user shall be given the possibility to monitor the ESD risk, as *e.g.* a function of the IPG level.

UR6.2 Electron trajectory

The electron trajectories shall be possible to monitor in order to understand their possible interaction with materials.

UR6.3 Electric field

Electric field in volume and normal electric field on top of surfaces shall be possible to visualize.

3.2.7. UR7: Interface and Control

UR7.1 Ease of use

The code shall be easy for parameterization of pre-defined models, running and post processing.

3.2.8. UR8: Requirements Originating from Software Development Process

UR8.1 Computing structure and code development

The code shall consist in the amelioration of the existing SPIS code. It shall follow the same architecture and rules for code development.

UR8.2 Platform operational requirements

The code shall be portable to Linux and Windows and delivered both in source code and executable.

UR8.3 Documentation

Following [RD10], [ITT] and [PROP] specifications, the documentation shall include the following documents.

UR8.3.1 A user manual shall be delivered through "How To" pages for a quick start of software usage.

UR8.3.2 An advanced user and developer documentation shall be delivered through Javadoc updating.

UR8.4 Data hosting

The existing SPINE platform shall host developed documents and codes sources, on regular LS server with a different synchronizer.

4. SOFTWARE REQUIREMENTS

The software requirements (SR) were derived from the user requirements (UR) listed in section 3. For the reader to easily follow this derivation we use the same numbering of SR here that we used for UR. The SR are described concisely, and the most complex methods are postponed to last subsections (starting from 4.9).

4.1. SR1: IPG Situation

4.1.1. SR1.1 Triple Point Geometry

Co-planar and perpendicular triple point geometries shall be delivered at mesoscopic scale, *i.e.* at triple point length scale. We must keep to a limited number of cases (possibly with parameters).

If the physics of ESDs is a three dimensional problem, the parameterization of the triple points will however be performed in two dimensions (as *e.g.* the dielectric thickness). We will consider the problem as pseudo 2D because the parameterization will be 2D but the electron avalanche phase (starting from a localized emission zone) will be computed in 3D. A pre-defined CAD model of the triple point will be developed (with GMSH), with the possibility for the user to modify some of the geometrical parameters, *cf.* Figure 20:

- the global geometry (co-planar or perpendicular and possibly with an angle),
- the length and width of the materials,
- the thickness of the dielectrics

These parameters will stay within limits for code robustness.

The pre-defined models are limited to the following ones:

- Model 1: coplanar case possibly with a metal thickness (1b)
- Model 2: perpendicular case possibly with an angle (2b)

The exact relevant geometries of Model 1b and 2b will be determined later from testing them with the operational code.

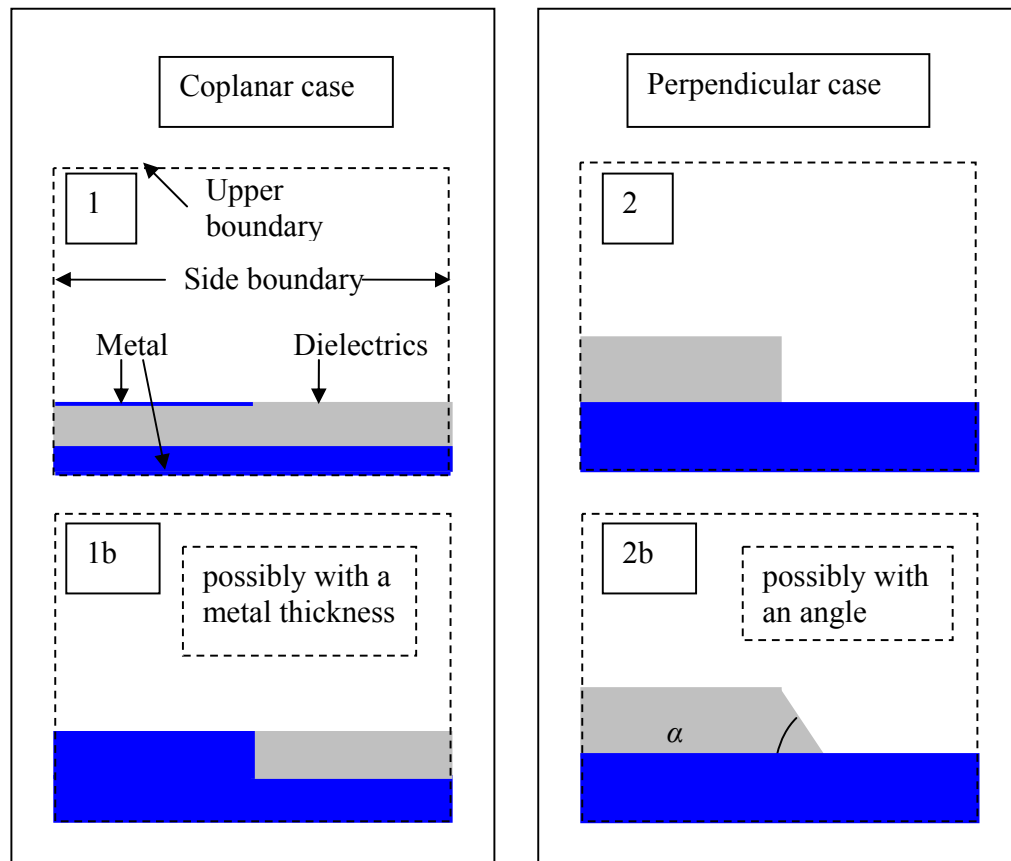


Figure 20 - Pre-defined CAD models, given as a first approach; the exact relevant geometries should rather be determined later from testing them with the operational code.

4.1.2. SR1.2 Boundary Conditions

The barrier of potential shall be simulated using a Dirichlet condition for the potential on the upper environment boundary. The differential voltage will then result from the metal voltage and from the barrier of potential. An extra boundary condition concerning the symmetry of particle fluxes shall be implemented. This later boundary condition is necessary to avoid the extraction of electrons from the dielectric surface once its surface has reached the voltage of the barrier of potential.

4.1.3. SR1.3 Microscopic Structures

The enhancement of the electric field by microscopic structures on the metallic surface shall be performed by using the SPIS capability to increase locally the electric field used in the Fowler-Nordheim emission by using an amplification factor β . The electric field itself is not changed. Possible ways to determine this coefficient are described in Section 4.9 "Electric Field Enhancement by Microscopic Structures".

4.1.4. SR1.4 Interaction with the Environment

The software shall support the possibility to perform the IPG situation with photon or with electrons. The SPIS TD evolution has already shown its capability for that kind of simulation.

The photo emission model is not a critical aspect for the ESD risk. In SPIS, they are described by a Maxwellian distribution whose energy is chosen by the users in the global parameters. Indeed, electrons are emitted with an energy approximately equal to the energy of the incoming photons minus the material work function. The emitted electrons have an energy kT_e of 1 to 20 eV. Once emitted, the electrons can escape to the environment or can be recollected on the surface. They can escape only if their energy is greater than potential barriers. So when the dielectric top surface reaches the value of the potential barrier (plus some kT_e), the electrons can not escape and are recollected. An increase of 20 eV only makes the differential charging decrease of 20 V, which is very weak in comparison to typical differential voltages of several hundreds or thousands of volts.

In GEO, the secondary emission by proton impact is orders of magnitude lower than the photo electron emission and secondary emission by electron impact. Moreover the ion current density is also orders of magnitude lower than ambient electron and photo electron current density, see for example [TN2]. It is then not necessary to take account of the protons for charging.

4.1.5. SR1.5 Dimension of the Problem

The IPG at triple point shall be performed in three dimensions, which is already a capability of SPIS.

4.2. SR2: Metals

4.2.1. SR2.1 Work Function

The metals already supported by SPIS are: gold, silver, oxidized aluminium and steel. By now, the value of the work function parameter is the same for all the metals (4.5 eV) in SPIS. The work function of the metals supported by SPIS shall be adjusted to their real values. The correct way to perform that is to add a parameter in the list of the material parameters supported by SPIS.

4.3. SR3: Dielectrics

4.3.1. SR3.1 Dielectric Properties

The dielectric materials supported by SPIS already cover the materials used on spacecraft surfaces: solar cell cover glass material (Cerium doped silicon with MgF_2 coating), Kapton®, optical solar reflector without MgF_2 coating, epoxy, Teflon® and non conductive paints. The possibility to extend the material list with new dielectrics shall be implemented. The user shall be granted the possibility to select the dielectric material from this list or more generally from an extended material list.

4.3.2. SR3.2 Dielectric Thickness

In the vicinity of the triple point, the thickness of the dielectric material shall be taken into account in term of capacitive and conductive coupling between surface charges and the underlying conductor. As the code was initially designed for macroscopic modelling, dielectrics are assumed to be thin. A first approach of what could be done to take account of their thickness is proposed in Section 4.10 "Capacitive and Conductive Coupling of Thick Dielectrics".

4.4. SR4: Electron Avalanche

4.4.1. SR4.1 Electron Creation

The production of seeding electrons shall be simulated by field effect emission. This requirement is already accomplished by the code.

4.4.2. SR4.2 Electron Trajectory

The 3D electron trajectory shall be calculated in three dimensions in order to assess the interaction with materials. This requirement is also already accomplished by the code.

4.4.3. SR4.3 Electron Interaction with Materials

The secondary emission of electron by electron impact shall be simulated and the trajectory of these electrons shall be simulated. This requirement is also already accomplished by the code.

4.5. SR5 Time Scales

The circuit solver shall be robust to integrate potential evolution even in the presence of the very variable time scales appearing in charging and discharges.

The SPIS evolution in this topic will consist in implementing the current scalers (see section 4.11 "Equivalent Circuit" for more details) for:

- the Fowler-Nordheim (FN) electron emission
- the collection of FN electrons
- the secondary emission of electrons due to FN electrons
- the recollection of these secondary electrons

4.6. SR6: Post Processing

4.6.1. SR6.1 ESD Hazard

The user shall be given the possibility to monitor the ESD risk, as a function of the IPG level. The ESD risk shall be detected as soon as the electron avalanche is triggered. The FN current shall be possible to monitor as a function of time.

4.6.2. SR6.2 Electron Trajectories

The electron trajectories shall be possible to monitor in order to understand their possible interaction with materials. In the present status of the code, the particle trajectories can be viewed in SPIS-UI but they are not generated in SPIS-Num. The code enhancement shall consist in generating these particle trajectories in SPIS-Num by tracking the wanted particles from their generation (field emission, secondary emission...). The visualization will be performed into Cassandra or Paraview using glyph (vectors) in a classic manner.

4.6.3. SR6.3 Electric Field

The electric field in volume and the normal electric field on top of surfaces shall be possible to visualize. The SPIS-Num code enhancement shall consist in generating these data. The SPIS-UI code enhancement

shall consist in producing vtk files permitting the visualization of these data, i.e. vtkDataSet with tuples of three data. The visualization will be performed into Cassandra or Paraview using glyph (vectors) in a classic manner.

4.7. SR7: Interface and Control

4.7.1. SR7.1 Ease of Use

The code shall be easy for the parameterization of a pre-defined model, running and post processing.

The system will be based on the parameterization of a pre-defined model, which will permit to simplify the work of spacecraft charging engineers by providing them the main characteristics of the triple point to model. A selected set of parameters will be left to the users in order they might model their particular configurations.

The pre-defined model will include:

- the triple-point geometry
- the materials
- the choice of the environment
- the computational box size
- the values of the potential barrier sweep

Each of these parameters will stay within limits to ensure the code robustness.

All other parameters will not be accessible from the wizard (as *e.g.* the choice of the solvers, the type of condition on the side boundaries). In any case and for more specific use, these parameters will be still accessible from the generic SPIS.

Some more details are given in Section 4.12 "Pre-Defined Models".

4.8. SR8: Requirements Originating from Software Development Process

4.8.1. SR8.1 Computing Structure and Code Development

The code shall consist in the amelioration of the existing SPIS code. It shall follow the same architecture and rules for code development. The amelioration will be coded in Java language.

4.8.2. SR8.2 Platform Operational Requirements

The code shall be portable to Linux and Windows and delivered both in source code and executable.

4.8.3. SR8.3 Documentation

SR8.3.1 A user manual shall be delivered through "How To" pages for a quick start of software usage including:

- How to install the software
- How to run the simulation
- How to change the parameters
- How to monitor the results

SR8.3.2 An advanced user and developer documentation shall be delivered through Javadoc updating.

4.8.4. SR8.4 Data Hosting

The existing SPINE platform shall host the developed documents and codes sources. The regular LibreSource server with the same synchronizer as the current development version (SPISNum4 and SPIS UI high Performance) will be used to avoid fusion problems. Eventually a synchronizer dedicated to the developers' team will be created in order to commit on the current development version synchronizer after verification steps.

4.9. Electric Field Enhancement by Microscopic Structures

While triple points increase the electric field at mesoscopic scale, microscopic structures can increase it further at microscopic scale. As it is often done we will introduce a local electric field amplification factor β , which takes into account microscopic effects. This solution will combine the simplicity of mesoscopic triple point geometries (co-planar or perpendicular dielectric metal junction), with the needed treatment of micro scale geometries that induce discharge ignition (simply forgetting this extra microscopic effect leads to completely unrealistic results, underestimating badly the ESD triggering risk). The possible value of this β factor will not be left open but will be derived from experimental or physical data, as *e.g.* the size of micro-tips having the capability to sustain a sufficient discharge current (thinner tips induce a larger amplification factor β but cannot sustain the needed current to reach arc regime), or the size of the thin dielectric layer in the case of electric field amplification due to a thin dielectric imperfection.

4.10. Capacitive and Conductive Coupling of Thick Dielectrics

The capacitive coupling of a thin dielectric surface top only exists with the underlying ground, the value of the capacitances being based on a plane capacitor assumption. Here close to a triple point, at a space scale close to or smaller than capacitors thickness, capacitive coupling indeed also exists between neighboring dielectric surfaces (a charge deposited on top of a dielectric surface modifies the potential not only at the same location but also on the nearby dielectrics, by influence).

To implement that, a first method consists in computing this improved capacitance matrix from Green functions (the potential generated by a single local charge deposit). This indeed supplies the inverse of the capacitance matrix (potential versus charge, not charge versus potential). Inverting this matrix to get the capacitance matrix might however lead to a rather heavy capacitance matrix describing the coupling between all surface elements of the model, whereas in the usual thin capacitor approximation we have light matrices (very sparse) allowing much more efficient computations. We shall first try to use this inverted matrix and check whether CPU cost remains acceptable, and try simplifying if not (*e.g.* only keeping largest local couplings). It would already be a large improvement with respect to the current situation. An alternative would be to handle the capacitive coupling of these thick dielectrics with a different method (for example directly deducing the potentials induced nearby from Green functions), with the difficulty to couple that consistently with the implicit solver elsewhere.

The bulk conductivity of a thin dielectric surface top only exists with the underlying ground too, the value of the conductance being also based on a plane conductor assumption. For the same reasons as for the capacitive coupling, it might be more realistic to perform a conductive coupling with the neighboring elements. The correct way to perform that is to calculate the conductance on each elements of the dielectric surface by taking account of the distance to the metallic parts.

4.11. Equivalent Circuit

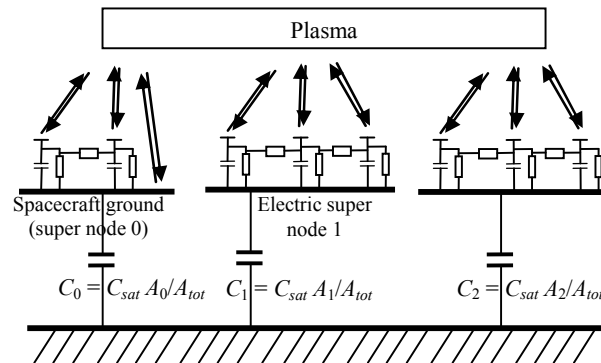


Figure 21 - Simple version of a spacecraft equivalent circuit, with continuous components (all small capacitors and resistors spread on top of each super node, one per surface element) and absolute capacitance C_{sat} . Here C_{sat} is distributed over all super nodes and results in three capacitors C_i , $i = 0, 1, 2$, relating them to the plasma ground at the bottom, with capacitances proportional to their areas A_i , of sum A_{tot} . Other discrete components can be plugged by the user between super nodes (resistors, capacitors, inductances and bias).

For the *circuit solver*, the huge range of time scales in the system requires using an implicit method with automatically variable time steps. Some of these time scales come from the electric circuit itself, which is linear (capacitances, inductances, resistors) but others come from non linear sources for the circuit due to the interactions between the linear circuit and the plasma (the arrows in Figure 21). This plasma interaction is denoted $\underline{I}(\underline{U}, t)$ in the global circuit equation

$$-\underline{C}\dot{\underline{U}} + \underline{G}\underline{U} + \underline{P}\underline{J} + \underline{I}(\underline{U}, t) = 0, \quad \underline{J} = \underline{H}\underline{U} \quad (1)$$

where \underline{U} is the vector of potentials on circuit nodes, \underline{C} and \underline{G} the capacitance and conductance matrices, \underline{J} the vector of currents through the inductances (hence not living in the same space as \underline{U}), \underline{P} a kind of projector relating the currents through the inductances to the currents on the nodes, and \underline{H} the inductance matrix. The unknowns are the vectors \underline{U} and \underline{J} . All matrices are constants, which makes most of the system linear. However the source term \underline{I} , the net plasma current collected/emitted from/to the plasma, is of a very different type. It depends non-linearly on the surface potentials \underline{U} , but also on the plasma state in unsteady situation, which was summarized in a time dependence in (1).

The principle of an implicit solver, based on a Newton-type method, is to take advantage of the knowledge on how currents change with potentials to anticipate their evolution and not overshoot the solution, which would result in instabilities. This knowledge, typically expressed to a first order as a dI_i/dU_j matrix (i and j are element indices), is contained in the linear part of (1) (conductivity currents and inductance currents). However the plasma term $\underline{I}(\underline{U}, t)$, while obtained from the plasma dynamics integration for given conditions (\underline{U}, t) , has *a priori* unknown (and of course non-linear) dependence on potentials, when they vary. The general idea implemented, to still be able to use an implicit hence stable solver, involves supplying the solver with an approximate dI_i/dU_j matrix, so-called *current scalars* in SPIS, based on physical assumptions. The uncertainty introduced by this approximation can be controlled by supplying a validity range (in term of voltage variation) for this linear interpolation of $\underline{I}(\underline{U}, t)$ for varying \underline{U} , and a maximum time step in case of explicit time dependence. Assumptions for dI_i/dU_j can typically be based on approximate analytical laws (Boltzmann distribution, Langmuir-Blodgett, Mott-Smith Langmuir ...). Even though usually only

approximate for realistic conditions, the combination of an exact computation for $I(\underline{U}, t)$ (e.g. through PIC method), and an approximate interpolation over a controlled validity range is thought to give good results.

Such simple methods have given good first results in basic situations (ambient plasma collection). For the present study, the definition of a correct dI_i/dU_j is a little trickier in more complex cases, such as the recollection of photoelectrons when blocked by a potential barrier in typical GEO conditions, the Fowler-Nordheim (FN) emission, the collection of FN electrons, the secondary emission of electrons due to FN electrons and the recollection of these secondary electrons.

4.12. Pre-Defined Models Wizards

A wizard based approach will be developed. The process is decomposed into several steps. When the user clicks the "Next" button, all data provided during the step have to be validated. In the same step, the user can modify the various parameters as he wants (no order). When the user clicks on the "Next" button, an 'internal machinery' checks if the modified data are valid. If invalid data are detected, a dialogue box of warning / error is displayed together with the list of parameters that should be corrected. When the data model is valid, the relevant actions are performed in order to pass to the next step (as e.g. CAD loading, meshing, groups deployment, field mapping, UI to Num conversion...).

5. SOFTWARE VERIFICATION AND VALIDATION PLAN

5.1. Verification Plan

The testing of each code routine will be done at functional level. The physical validation will be performed by comparison to experimental results, as described in the next chapter. It can only be done at higher level, by modelling a given situation.

Here, at routine level, the testing will be simpler. We list below the functional or coherence test proposed for each new routine or module, here is a one to one correspondence with Software Requirements:

- SR1.1 - Triple point geometry: check that the mesh is not deteriorated when the geometrical parameters change. It is understood here by “geometrical parameters”, the position of the points being modified through the ESD-wizard based GUI only (e.g x-y position of the triple point) and the local resolution. This excludes all other or external modification of the geometry. It is understood by “no deterioration of the mesh” that the standard deviation between two meshing of the distributions mesh quality factors as defined in Gmsh (γ, η et ρ) is lower than 20%. It is also understood that the variation of the “geometrical parameters” should not induce a modification of the smallest characteristic length of the geometry to the largest one higher than 50%.
- SR1.2 - Boundary conditions: check that the Dirichlet condition is correctly applied on the barrier potential limit. The verification of the symmetry condition will consist in checking the number of particles coming in and out of the boundary.
- SR1.3 - Microscopic structures: reproduces known FN currents corresponding to given field enhancement factors.
- SR1.4 - Interaction with the environment: SPIS has already shown its capability to simulate the IPG situation with photon or with electrons. Simply check the surface potentials and the currents are coherent with boundary potentials.
- SR1.5 - Dimension of the problem: meshes correctly the triple point in 3D.
- SR2.1 - Metals work function: check the influence of the metal in the FN current.
- SR3.1 - Dielectric material list extension: Check the change of materials is correctly handled
- SR3.2 - Improved capacitive and conductive coupling for thick dielectrics: check coupling values and the effect of charge collection on potential (potential value consistent with capacitance and conductance and influences neighbour dielectrics) with two test cases consisting in a dielectric surface parallel and perpendicular to the conductor respectively.
- SR4.1 - Electron creation: already accomplished during SPIS development, simply check the current emitted by the metal during FN emission.
- SR4.2 - Electron trajectory: already accomplished during SPIS development.
- SR4.3 - Electron interaction with materials: already accomplished during SPIS development, simply check the creation of secondary electrons from FN electrons and from secondary electrons.
- SR5 - Multi time scale: reproduces known time scales for differential charging and discharges, not generating instabilities.

- SR6.1 - ESD hazard monitoring: check the code can monitor the correct differential voltage that leads to the electron avalanche.
- SR6.2 - Electron trajectory monitoring: check the possibility to display the trajectories of a statistical number (but lower than $1e6$) of particles into Cassandra or Paraview, in particular FN electrons and secondary electrons in relation with the local electric fields.
- SR6.3 - Electric field: check the possibility to visualize correctly the electric field into Cassandra or Paraview under the form of vectors of symbolic glyphs.
- SR7.1 - Ease of use: In the wizard based UI, check the presence of a validation capability by software to the validity of set parameters in current page before pass to the next one.

Some other tests shall certainly be run at lower level routines, but cannot be defined now, since the code structure at this lower level is not yet known.

5.2. Validation Plan

According to SR, the code shall be able to predict the onset of ESDs in typical IPG configurations and shall be validated by dedicated experiments. The proposed experiments are described in this chapter.

The purpose of these experiments is to trigger an ESD in IPG on dummy samples. Two sets of samples will be studied with co-planar and perpendicular geometries. These experiments will be conducted in CEDRE chamber using photons or electrons to build the differential voltage on the samples, cf. Figure 22.

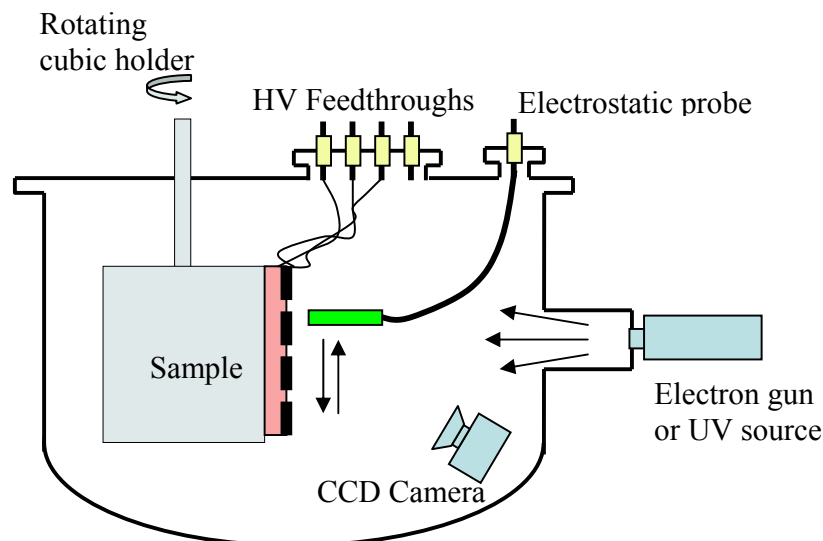


Figure 22 - Schematics of CEDRE chamber

The metallic part of the samples will be biased to negative potentials and connected to a capacitor for the Blow-Off. The profile of the differential voltage will be measured by using a surface potential probe. The main objective is to quantify the differential voltage that leads to the ESD initiation. Two means can be used to obtain the IPG situation:

- In the case we use an electron gun, the bias voltage will be approximately -5 kV so as to produce a secondary electron yield greater than unity.
- In the case we use photons (UV source), the bias voltage will be increased progressively from 0V. The advantage of this setup is that the barrier of potential is more realistic of flight configurations, cf. Figure 25.

The photon setup being more realistic this solution is our first choice. Moreover, the capability of the photon setup to perform the IPG situation is shown in Figure 24 in which the potential profiles were obtained in CEDRE chamber on the sample depicted in Figure 23 using a UV source for the IPG building. The dielectric surface rapidly tends to a near 0 V potential, which is the potential of the tank walls. A differential voltage of approximately +2000 V is then created. In comparison to the electron setup, the advantage is that we can control the evolution of the IPG by imposing its maximal value, the value of the bias voltage indeed.

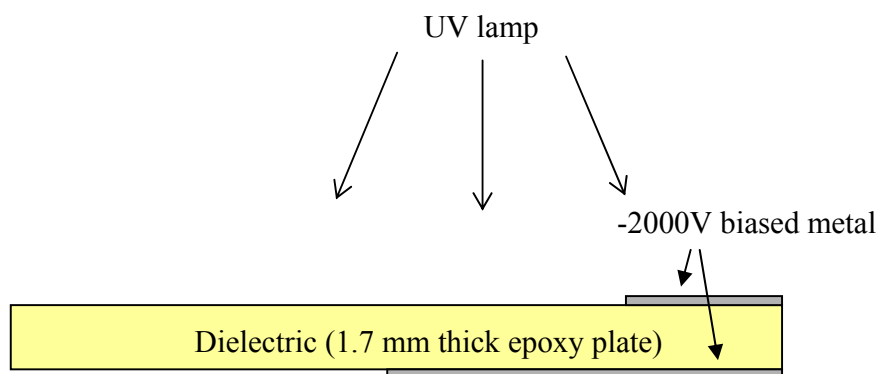


Figure 23 - Schematic of the sample used to demonstrate the photon setup capability

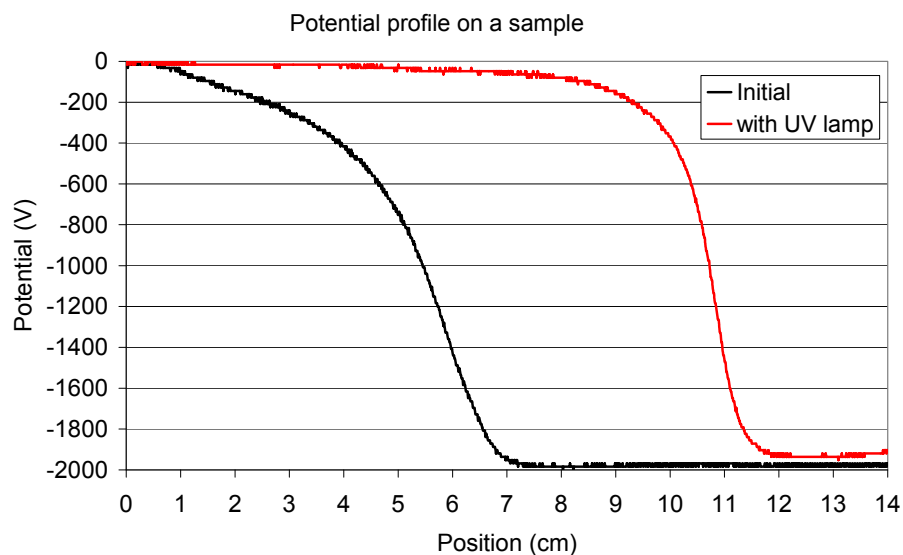


Figure 24 - Evolution of the surface potential on the sample of Figure 23 when using the photon setup for the IPG building

Samples will be designed and produced so as to cover the full list of parameters highlighted in the literature study:

- Triple point geometry at mesoscopic scale, *i.e.* at the triple point length scale: co-planar and perpendicular metal-dielectric junctions, *cf.* Figure 26. The co-planar geometry will be obtained by evaporating the metal on the dielectric material. The perpendicular geometry will be obtained by placing a dielectric sheet on a metal.
- Metals. Different metals can be used in the experimental facility: silver, aluminium, gold, copper. We will select two of them to compare the effect of the work function.
- Dielectrics. We will use Epoxy or Teflon, or possibly cover glasses. Kapton® can not be used in the photon setup since it is photo conductive.

For each of these 3 parameters, two configurations will be experimented. That leads to design 8 samples. For each of these samples, the threshold for the ESD ignition will be determined following the procedures:

- If we use a UV source, we will perform bias voltage steps δV of -200 V, beginning at 0 V. For each step, the differential voltage will be measured periodically till an ESD occurs. The periodicity (as for *e.g.* 10 min in Figure 27) may vary depending on the dynamics of the differential charging process. Once the steady state is obtained without any ESD occurrence, the bias voltage is increased. In the case the differential voltage has not changed from the previous step, it may signify that no ESD is possible in this configuration. We propose to wait for 4 hours of charging at this step before stopping the experiments and assess that there is no ESD risk.
- If we use an electron gun, the differential voltage between the metal and the dielectric top surface will be measured periodically so as to obtain the threshold for ESD ignition. The periodicity (as for *e.g.* 10 min in Figure 28) may vary depending on the dynamics of the differential charging process. The electron gun will be stopped during the potential measurements. If no ESD is obtained after 8 hours of electron irradiation, then the ESD risk is null.

Only one of these two procedures will be performed (preferentially the photon setup strategy).

For each of the configurations tested the observables will be:

- Irradiation time, potential profiles
- Blow-off signal, monitored by a current probe connected to an oscilloscope
- ESD light emission recorded with a video camera

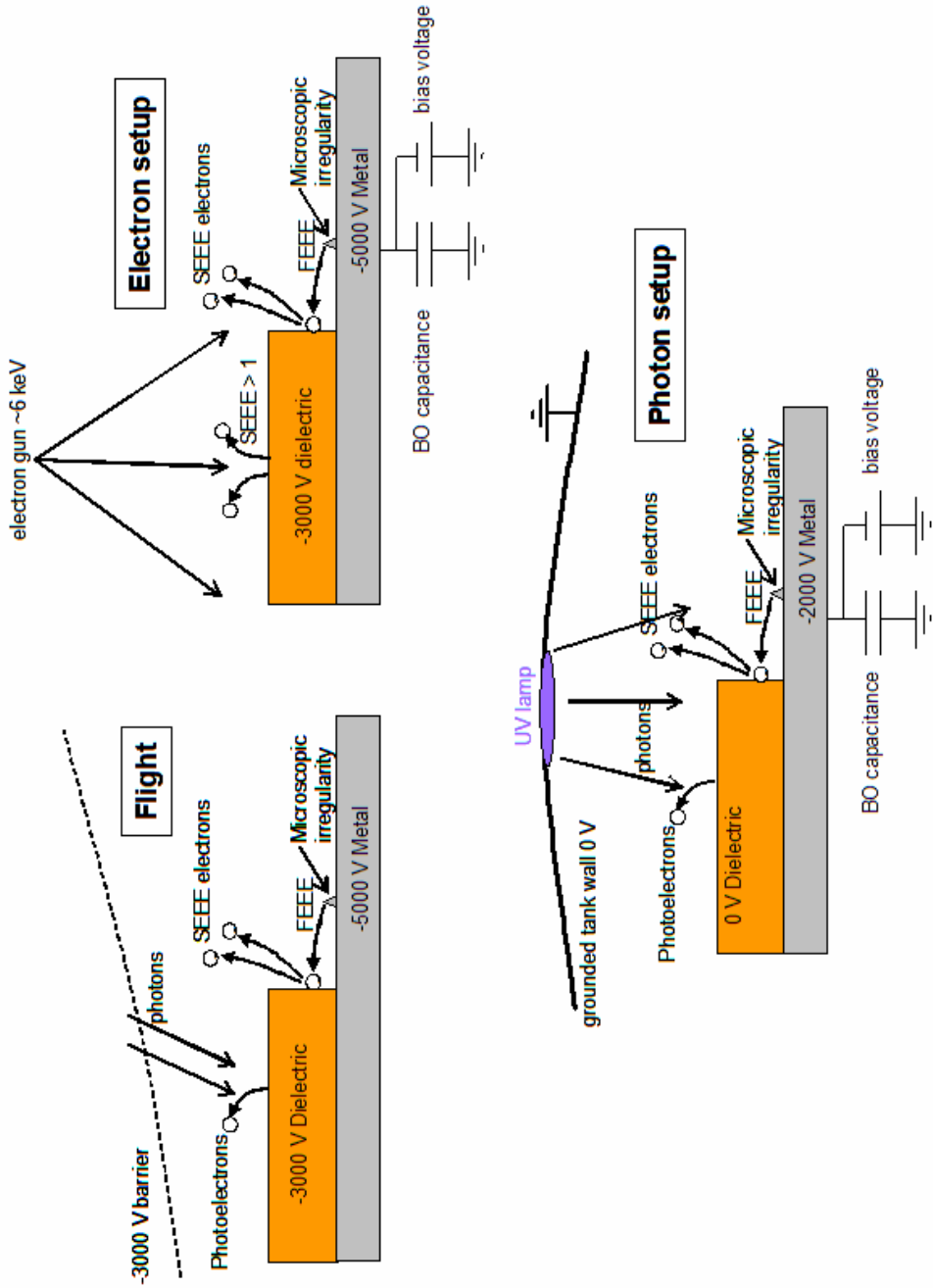


Figure 25 - IPG in flight and means to obtain it in ground tanks

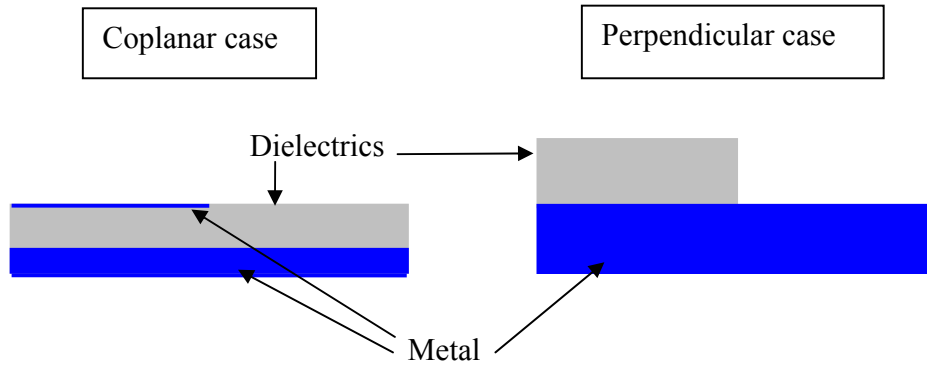


Figure 26 - Schematics of the two geometrical configurations of triple points foreseen for the experiments

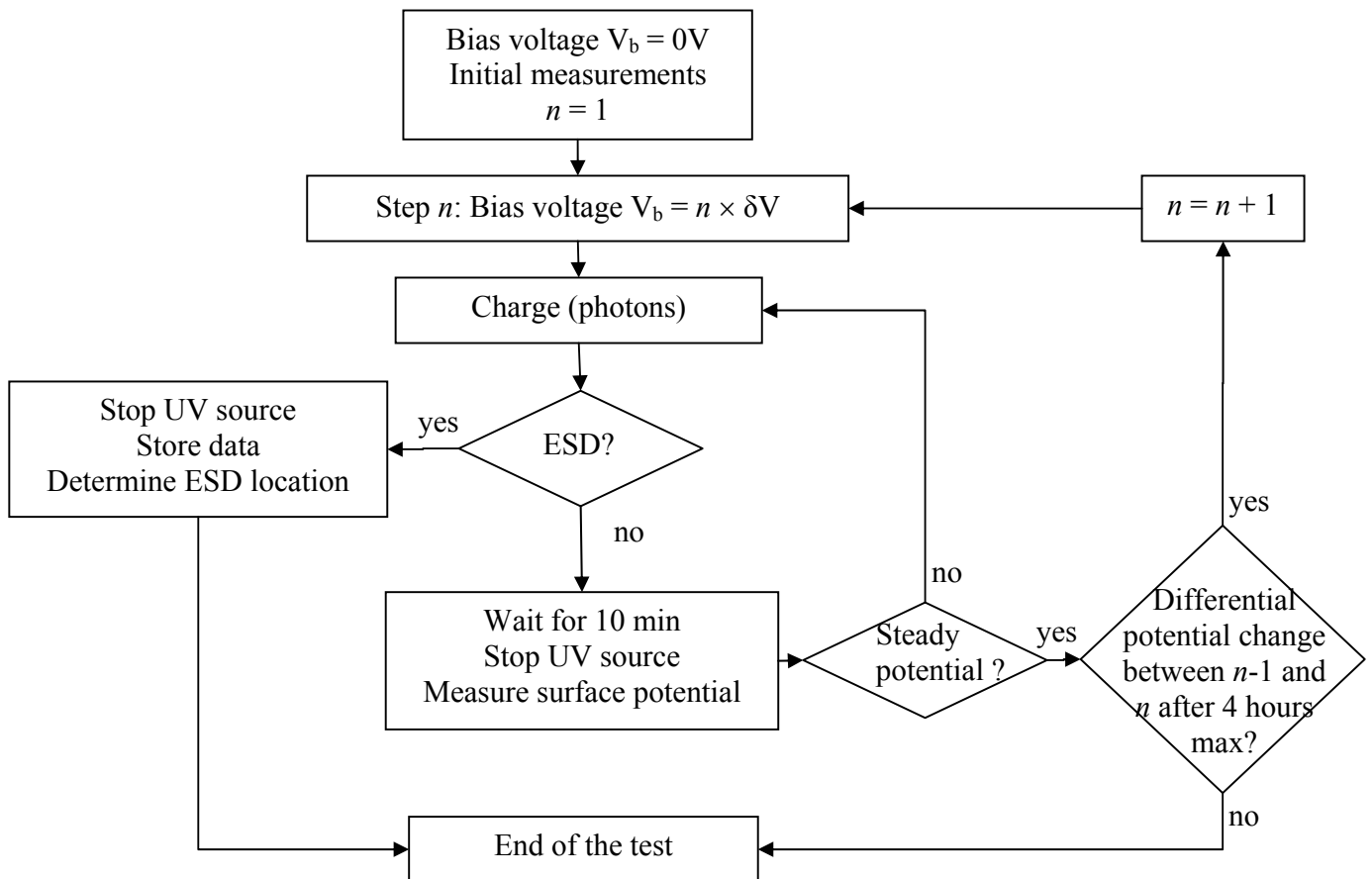


Figure 27 - Campaign with the photon setup

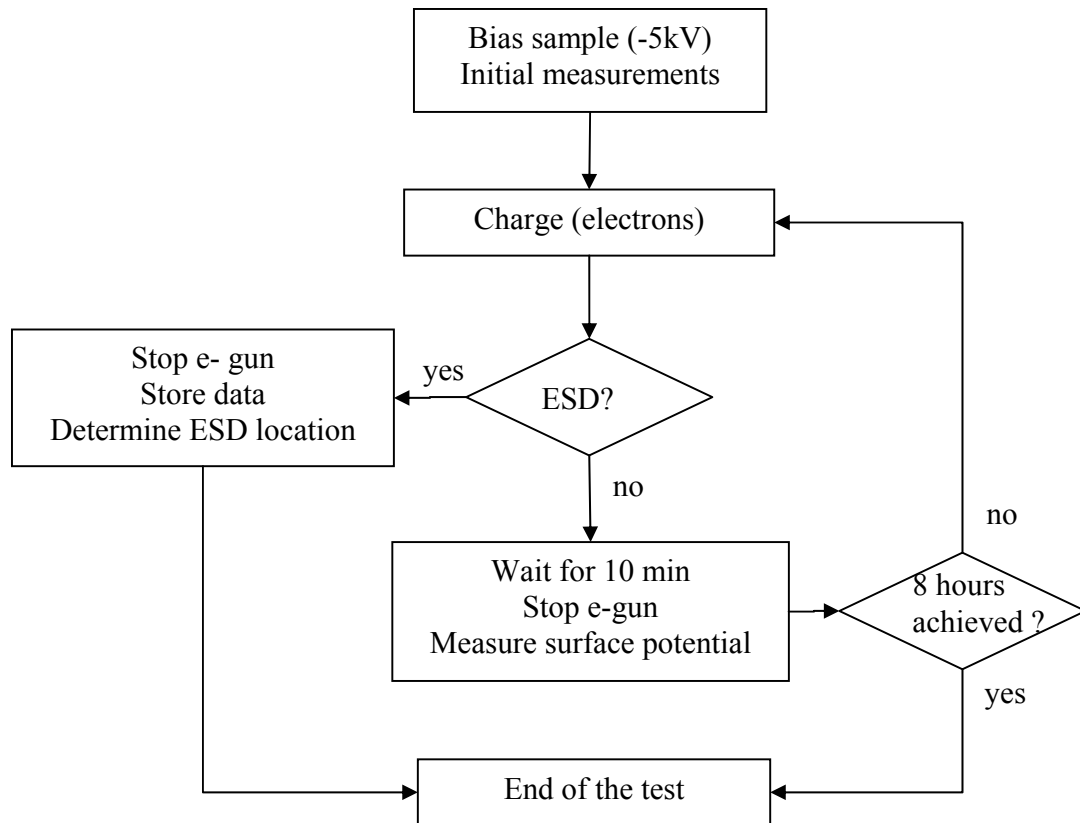


Figure 28 - Campaign with the electron setup

6. ARCHITECTURE DESIGN

This section deals with the general overview of the improvements done in SPIS NUM and UI to achieve the ESD prediction tool in IPG situation. The architecture design (AD) is derived from the software requirements (SR). The AD presentation is organized in three parts. The first part describes the IPG situation modeling and the inputs of the tool. The second part deals with the creation of the ESD prediction scenario and the SPIS/NUM developments. Finally, the third part concerns the SPIS project configuration and the wizard.

6.1. General Overview of the Model

A model overview is schematically represented in Figure 29. The macroscopic scale is taken into account through the boundary conditions imposed on the simulation box and representing the barrier of potential obtained in GEO under sunlight. The microscopic scale is modeled with a model of microscopic irregularities. The electric field and the particle dynamics is calculated on the mesoscopic scale of the triple point: geometry of the materials, height of the potential barrier. In the present situations, the main difficulties are:

- The generation and the recollection of particles (field-effect or secondaries) and the coupling with the circuit solver. Indeed, the time scales of the charging and discharge phase are very different (10 to 12 orders of magnitude)
- The calculation of the potential on thick dielectric (instead of using the initial thin dielectric hypothesis)
- The modeling of the microscopic structure evolution during the electron avalanche, including a thermal model of the tip
- The generation of an automatic scenario to command and monitor simply the simulation

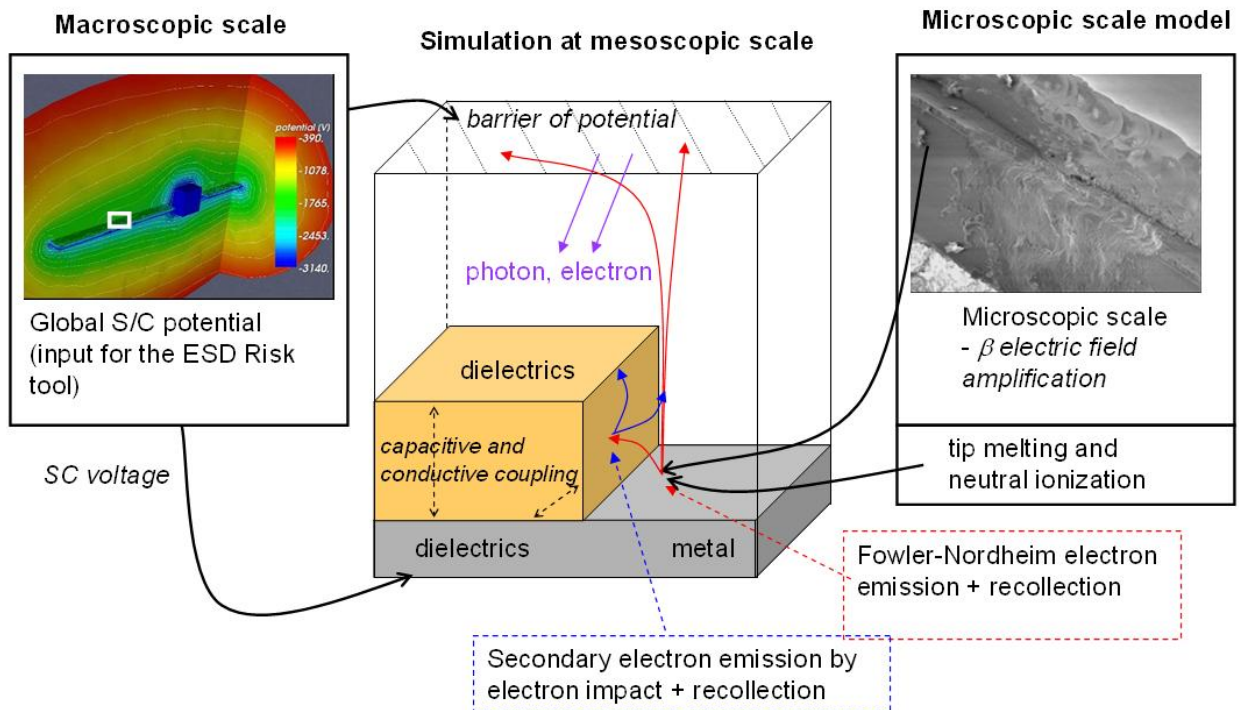


Figure 29 – Overview of the model of the IPG situation at triple point in GEO.

6.2. IPG Situation and Inputs for the Tool

The IPG situation of the ESD prediction tool is defined in three successive steps concerning: the geometry, the material used and the environment situation. These three steps are described in the following sections. As required in the SRD, the input parameters can be defined directly in the standard SPIS-UI or using the wizard developed for the ESD prediction tool.

6.2.1. Geometrical Mockup

The geometrical mockup for the ESD prediction tool consists on a pre-defined CAD model of the triple point. This model has been designed with GMSH with the possibility for the users to modify some of the geometrical parameters. The triple point geometry is declined into two different configurations at the mesoscopic scale (SR1.1):

- the coplanar case
- the perpendicular or with an angle case

These geometries are parameterized to represent a part of the solar cell cover glass, i.e. the dielectric, and the conductive part, i.e. the metal in three dimensions (SR1.5).

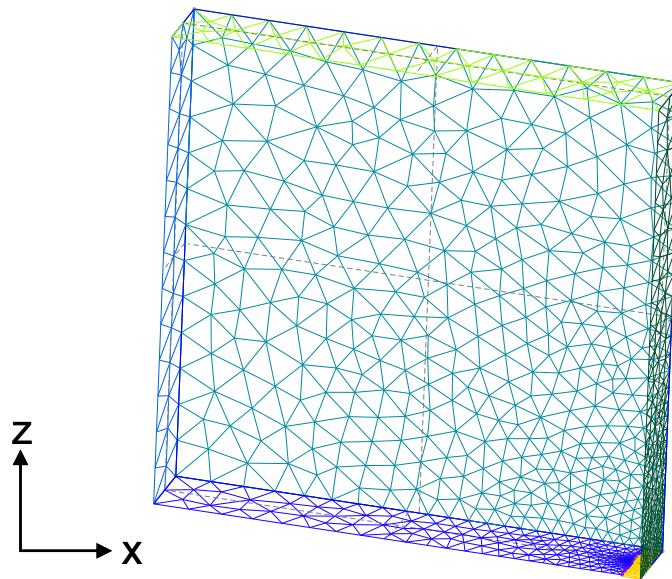


Figure 30 - CAD model visualization from GMSH of the geometrical mockup for the ESD prediction tool

Figure 30 represents the geometrical mockup used with the standard values (used for the validation, i.e. for the comparison with experimental part of the study) defined in Table 3. Four distinct boundaries can be seen for the external box:

- the dielectric is on the bottom in bleu,
- the metallic part in yellow,
- the external environment and the barrier potential is applied at the upper boundary in green,
- and symmetric boundary conditions for the four other sides.

At this scale length, the differences between the triple point geometries can not be seen.

Table 3 - User modifiable parameters in the geometrical mockup file

	Value of the mockup file parameters		
	Standard	Min	Max
Dielectric thickness (SR3.2) – LdielZ (m)	10^{-4}	5×10^{-5}	5×10^{-3}
Dielectric length – LdielX (m)	3.85×10^{-2}	$10 \times \text{LdielZ}$	5×10^{-2}
Dielectric angle – alpha (rad)	$\pi/2$	0	$\pi/2$
External box X dimension – LboxX (m)	4×10^{-2}	$\text{LdielX} + \text{LdielZ}$	6×10^{-2}
External box Y dimension – LboxY (m)	0.6×10^{-2}	0.5×10^{-2}	10^{-2}
External box Z dimension – LboxZ (m)	4×10^{-2}	LboxX	6×10^{-2}

Figure 31 shows a GMSH zoom at the TP scale length of the geometry for three dielectric angles. In these figures, we can see the refinement box around the electric field emission zone. This Fowler Nordheim emission site can also be seen at a smaller scale in Figure 32 (orange square).

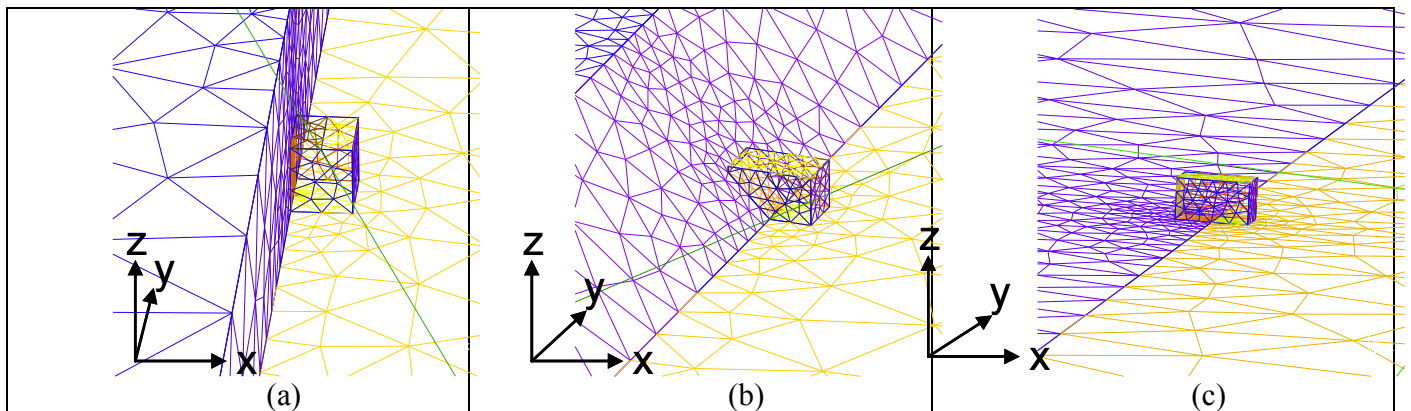


Figure 31- Zoom X 50 of the figure 2 – Schema of the dielectric trench as a function of angle α : (a) $\alpha = \pi/2$ – perpendicular case, (b) $\alpha = \pi/4$ and (c) $\alpha = 0$ – planar case.

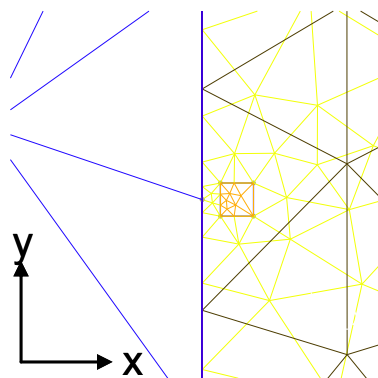


Figure 32 - Zoom X 20 of Figure 31. Schema of the Fowler-Nordheim emission site

It is considered in the ESD prediction model that ESDs occur from a single site where a micron tip locally enhanced the electric field (see tip model 6.3.3). This surface has a primordial importance because it represents the primary source that produced the electron avalanche (SR4.1).

The refinement box is designed to represent the zone where the trajectories of the primary electrons interact with the dielectric (SR4.2). At this distance from the emission site, recollected electrons and secondary electrons from recollected (SR4.3) are able to influence the electric field on the emission zone. Thus, in this box, there is a strong coupling between electron emission and dielectric local potentials which possibly leads to an electron avalanche.

Consequently, contrarily to the parameters of Table 3 which are based on the mesoscopic geometry, the refinement box and the TP dimensions are based on physical assumption. These parameters are grouped in

Table 4 and are fixed in the CAD file (no margins let to the users). Changes of these parameters can be only done by expert users verifying the mesh quality and adapting the project configuration (times steps, particle densification, etc ...) to the new dimensions and the physics modeled.

Table 4 - Fixed parameters in the geometrical mockup file

	Value of the mockup file parameters
Refinement box X dimension – LrefboxX (m)	7×10^{-5}
Refinement box Y dimension – LrefboxY (m)	4×10^{-5}
Refinement box Z dimension – LrefboxZ (m)	4×10^{-5}
Emission site dimension – PointR (m)	2×10^{-6}

As an output of the mockup geometry file, the following physical surfaces and the physical volume are meshed:

- Dielectric Up: Physical Surface(69)
- Dielectric Front: Physical Surface(70)
- Metal: Physical Surface(71)
- Emission site (i.e. Tip modeling): Physical Surface(72)
- Boundary lateral: Physical Surface(73)
- Boundary Up: Physical Surface(74)
- Plasma: Physical Volume(75)

6.2.2. Boundary Conditions

Following the SR1.2, the IPG situation is simulated by fixing the potential difference between the barrier potential boundary (Boundary Up) and the metallic parts (Metal + Emission site) of the geometry. Consequently, the boundary conditions for these physical surfaces are Dirichlet conditions for the potential. The dielectric surfaces (Dielectric Up and Dielectric Front) have also Dirichlet conditions for the potential. At the beginning of the simulation, the potential on this surface is set equal to the metal potential, i.e. no differential potential. Then, during the charging phase and the ESD triggering phase, the local potential evolution on these surfaces is solved by the SPIS circuit solver. The potential on the dielectrics evolves while the local net current on the dielectric is non null, i.e. the difference between current emission (photoelectrons and secondary emission), collection (from environment and recollection) and conduction (at the surfaces or in the volume of the dielectric).

The last boundary condition concerns the four lateral boundaries. For this boundary, a condition of symmetry is assumed. It means that the flux of particle is forced to zero (by reflecting the particles) and the electric field is set to zero in the normal direction. In particular, this boundary condition also permits to get a stationary situation during the charging phase when the dielectric potential reaches the barrier of potential fixed by users (i.e. equality between the electron emission and recollection when differential voltage equal barrier potential).

Concerning the particles (SR1.4), the environment incoming fluxes are imposed at the Boundary Up. Secondary emission and photoemission are activated for all the dielectric and metal surfaces. The Fowler Nordheim emission of electrons is also activated on a small surface called the "Emission site". It is assumed that FN emission is enhanced due to the presence of microscopic structures on the surfaces. A model of microscopic structures (SR1.3) has been developed for this project. This model is based on a single tip triggering the discharge (see detailed presentation in section 2.2.3.).

6.2.3. Material Inputs

The ESD prediction tool permits to define at least two materials: one for the metal and one for the dielectric. The possibility is also let to the used to define a different material:

- for the dielectric up surface and the trench (dielectric front)
- for the metal surface and the tip (emission site)

There is thus a maximum of four materials to define. The dielectric up and front and the metal surface consist on standard materials defined by the 19 NASCAP properties but the tip material need additional properties to compute the FN emission and the thermal model associated to the tip.

Consequently, the ESD tool is base on the latest version of SPIS (version 4.3). In this version two major enhancements have been released concerning the material input. The possibilities:

- To add new materials defined by user (without recompilation of SPIS/NUM). In SPIS/NUM, it is now possible to "import NASCAP material" using external file in an XML format. In this file, you can create one or several NASCAP materials also defining the 19 NASCAP properties called "nascapProperty" (see SPIS 4.3 user manual). One more advantage of this new format is to change the value of the nascapProperties easily without recompiling the NUM core.
- To add new properties called "extendedProperty". These properties permit to define new materials properties not comprised in the NASCAP ones and also for the relevant materials. For example, in your case, it concerns the metal work function needed to calculate the Fowler Nordheim emission. This property is not needed for a standard calculation of SPIS but it is needed when the FN sources are created.

While the use of the new properties is required only for the material of Emission site, SPIS does not permit to mixed new material and the old standard material (in NUM core) thus new format of materials is used for all the materials properties in the ESD tool. However, a list a 9 NASCAP materials is released in the version 4.3 and 5 NASCAP materials (gold, aluminium, CMX with MgF₂ coating and without and Teflon®) used for the ESD tool validation (SR3.1) are also distributed into the ESD tool with the additional properties need by the ESD triggering model.

We can notice that, for the two metals used in the ESD tool, 10 extended properties have been included (extract from the XML file for gold):

```
<MaterialProperties Name="GoldForESD" Color="65535" xmlns="material_schema">
  <Property Index="0" Value="1.0" />
  <Property Index="1" Value="0.0010" />
  <Property Index="2" Value="-1.0" />
  <Property Index="3" Value="79.0" />
  <Property Index="4" Value="0.88" />
  <Property Index="5" Value="0.8" />
  <Property Index="6" Value="88.8" />
  <Property Index="7" Value="0.92" />
  <Property Index="8" Value="53.5" />
  <Property Index="9" Value="1.73" />
  <Property Index="10" Value="0.413" />
  <Property Index="11" Value="135.0" />
  <Property Index="12" Value="2.9E-5" />
  <Property Index="13" Value="-1.0" />
  <Property Index="14" Value="197.0" />
  <Property Index="15" Value="19320.0" />
  <Property Index="16" Value="17.0" />
  <Property Index="17" Value="18.0" />
</MaterialProperties>
```



```

<Property Index="18" Value="19.0" />
<Property Index="19" Value="20.0" />
<ExtendedSpisProperty Name="WORK" Value="5.1" Type="float" Unit="[eV]" Description="Work function"/>
<ExtendedSpisProperty Name="THCO" Value="317.0" Type="float" Unit="[W/K/m]" Description="Thermal conductivity"/>
<ExtendedSpisProperty Name="HEAT" Value="128.0" Type="float" Unit="[J/K/kg]" Description="Specific heat "/>
<ExtendedSpisProperty Name="ATOM" Value="3.15E-25" Type="float" Unit="[kg]" Description="Atomic mass"/>
<ExtendedSpisProperty Name="ELRE" Value="0.2212E-7" Type="float" Unit="[Pa]" Description="Electric resistivity of metal"/>
<ExtendedSpisProperty Name="PREF" Value="2.37E-4" Type="float" Unit="[Pa]" Description="Reference pressure for
evaporation"/>
<ExtendedSpisProperty Name="TREF" Value="1337.73" Type="float" Unit="[K]" Description="Reference temperature for
evaporation"/>
<ExtendedSpisProperty Name="VAPE" Value="3.344E+5" Type="float" Unit="[J]" Description="Vaporization energy per mole"/>
<ExtendedSpisProperty Name="FUSE" Value="1.255E+4" Type="float" Unit="[J]" Description="Fusion energy per mole"/>
<ExtendedSpisProperty Name="VMAS" Value="19320.0" Type="float" Unit="[kg/m3]" Description="Volumic mass "/>
<ExtendedSpisProperty Name="MELT" Value="1337.73" Type="float" Unit="[K]" Description="Melting temperature"/>
<ExtendedSpisProperty Name="CION" Value="1E-19" Type="float" Unit="[m2]" Description="Ionization cross section"/>
</MaterialProperties>

```

We can notice that a new parameter is created for work function (in red in the list) as required in the SRD (SR2.1). It permits to precise this value whenever the FN source is selected for a material (not limited to the ESD tool).

6.2.4. Environment Inputs

The software supports the possibility to perform the IPG situation with photon or with electrons (SR1.4). Thus, the environment inputs of the ESD tool permit to users to define two populations of incoming electrons (*PICVolDistrib*), the sun direction and the interactions between environment and the spacecraft.

A warning message is implemented in the ESD prediction tool to inform the users of non IPG situation during the charging phase of the dielectric resulting from the environment definition.

The environment type is a *BiMaxwellianEnvironment*. It permits to define two Maxwellian populations of electrons at the environment boundary (potential barrier boundary). For each population, the reference density (at the infinity) and the temperature are defined by users. To compute the electron distribution at the potential barrier boundary (variable in the ESD tool scenario), the absolute spacecraft potential shall be defined by users (see scenario parameters).

The photo emission model is described by a Maxwellian distribution whose energy is chosen by the users in the global parameters of SPIS. As argued in the SRD, the temperature of emitted electrons is weak compare to the barrier potential thus this temperature as a second order influence for the ESD prediction. This temperature of emitted electrons is fixed to 2 eV for the photoemission and all the secondary emission processes.

All the particle sources from the environment of from the material surfaces are simulated by Particle In Cell methods using the standard *PICVolDistrib* of SPIS.

6.3. ESD Prediction Scenario and NUM Development

The ESD prediction tool is based on an ESD prediction scenario simulating the charging phase from zero differential potential to the IPG stationary situation, the electron avalanche and the ESD triggering.

6.3.1. SPIS-NUM Development Overview

The ESD prediction tool is completely integrated in the standard structure of SPIS 4.3. In Figure 33, a general overview of SPIS-NUM functioning is presented. The ESD prediction tool keeps the same the same

structure but several modules of this structure have been completed or adapted for the ESD tool (SR8.1). The concerned parts of the structure are in red. The modifications of these modules are achieved by extended class without modifying the existing ones to preserve the structure of the standard SPIS version.

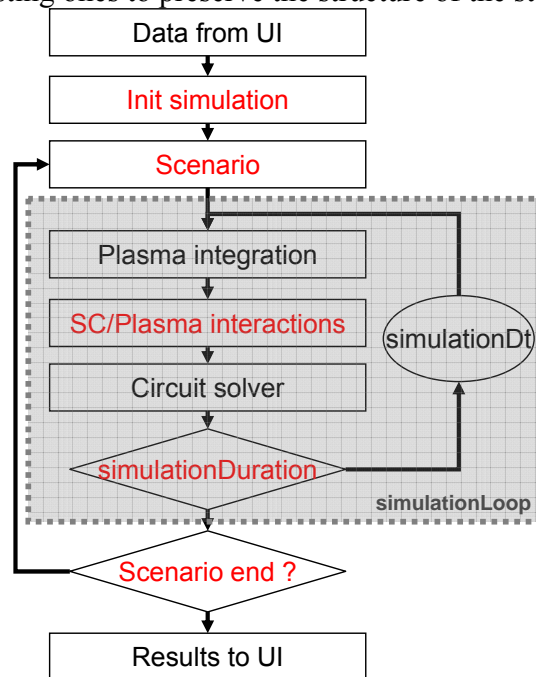


Figure 33 - Schema of the general overview of SPIS-NUM

6.3.2. ESD Prediction Scenario

For defined materials, mesoscopic geometry and environment conditions, the ESD triggering probability depends on the barrier potential applied and the surface states of the emissive zone (i.e. the tip geometry on the emission site). Consequently, the ESD prediction scenario is organized in two imbricate loops concerning the barrier potential value and the beta value (field enhancement factor due to the tip geometry). This scenario is schematically represented in Figure 34 where we can see the two loops controlling standard simulation loops.

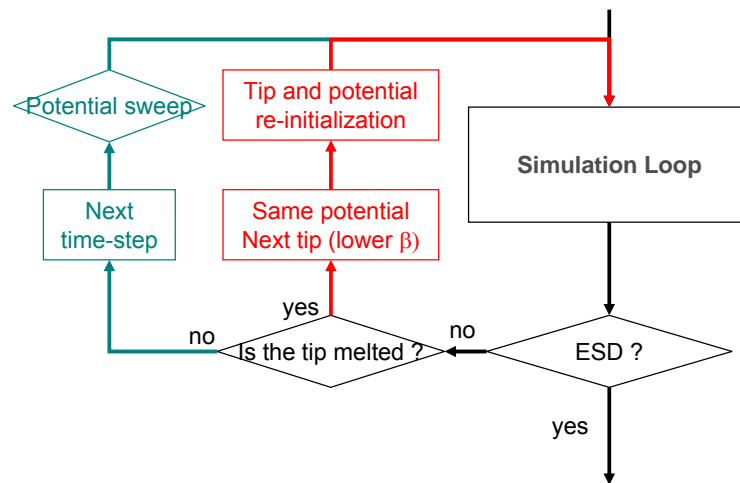


Figure 34 - Schema of the ESD risk scenario

The end of each loops are based on two condition implemented for the ESD prediction tool. The detections of:

- The tip fusion
- The ESD triggering

The both conditions depend on the assumption done for the tip model discussed in the next section. At the end of one simulation loop, the scenario can produce different actions following the tip model outputs (detection if the tip is melted and if the ESD is triggered):

- the tip is not melted and no ESD \Rightarrow barrier potential is increased – next step in potential
- the tip is melted but no ESD \Rightarrow the tip radius is increased – next step in beta
- an ESD is triggered \Rightarrow end of the scenario (depends on scenario configuration – see section 7.1.1)

As an output of the scenario (i.e. the ESD tool) two parameters have been evaluated during ESD prediction simulation: what tip geometry permit to trigger an ESD and for which barrier potential.

A detailed description of the *ESDPredictionScenario* class is provided in the section 7.1.1.

6.3.3. Tip Model and ESD Triggering Condition

The bibliography study on the tip geometry shows that zero or one dimensional models have been developed to model the tip: the field enhancement calculation [40] and the thermal behaviour [41]. In the ESD prediction tool, we choose to represent the tip by a cylinder.

For a cylinder, the field enhancement factor is defined by the ratio of the tip length on the tip radius. As it was shown in [40], it can be considered that the tip length is practically the same for two different tips on the surface. The tips length is approximately one micron. But the tip radius could be very different from one to another tip on the surface. Nevertheless, the tip radius distribution on the surface is a priori unknown but field enhancement factor have been measured for different material surface states. It has been shown that this factor can vary from 100 for very well conditioned surfaces (special treatment to erode the thinner tips) to 1000 for standard surfaces. Higher field enhancement factor corresponds to the smaller radius, i.e. to the thinner tip. From these data, we can define tip radius from 1 nm to 10 nm .

In another hand, the Rossetti model [41] is simplified in a zero-dimensional calculation (integration on 10% of the tip length shows very good agreement with the 1D results of Rossetti, cf. paragraph 7.2.2) and used to estimate the temperature of the tip as a function of the current of electrons emitted by the FN process. In this model, the following processes are taken into account in the energy balance of the tip:

- Joule heating of the FN current
- Conduction
- Electron extraction (loss or gain depending on electric field)
- Atom evaporation

This model permits to calculate the temperature of the tip at each time step. Knowing the temperature, it is possible to determine the evaporation flux from the tip and thus: the neutral density in volume and the mass loss of the tip. It permits to evaluate:

- If the tip is melted: the fusion temperature is reached and the tip has lost ½ of his mass. We can notice that the mass loss leads to tip length decreases. When the tip has lost ½ of its mass, the enhancement factor is decreased by a factor of 2. Thus we conclude in this case the tip melt before the ESD is triggered and the ESD tool test geometry with much more mass to evaporate (lower beta and larger radius).
- If an ESD is triggered: when the neutral density increases in volume, the probability of ionizing collisions between electrons and neutrals increases. Consequently, it is assumed the ESD is triggered when this probability reach 1, i.e. each electrons emitted produces at least one more electron.

Hence, there is a balance in evaporation between the mass loss that decreases the field enhancement factor (and so on the ESD probability) and the neutral density increases that is needed to produce ionization. Tips with a very small radius are rapidly evaporated and probably not sustains sufficiently the electron emission to leads to an ESD. Tips with larger radius not permit to emit sufficient FN current to melt the tip thus no ESDs are triggered.

A detailed description of the *TipRecession* interactor class is provided in section 7.2.2.

6.3.4. *Spacecraft Circuit Solver*

The standard circuit solver uses the equivalent circuit represented in Figure 35. The resolution is achieved by a implicit method with automatically variable time steps. Some of these time scales come from the electric circuit itself, which is linear (capacitances, inductances, resistors) but others come from non linear sources for the circuit due to the interactions between the linear circuit and the plasma (the arrows in Figure 35). This plasma interaction is denoted $\underline{I}(\underline{U}, t)$ in the global circuit equation:

$$-\underline{C}\dot{\underline{U}} + \underline{G}\underline{U} + \underline{P}\underline{J} + \underline{I}(\underline{U}, t) = 0, \quad \underline{J} = \underline{H}\underline{U} \quad (17)$$

where \underline{U} is the vector of potentials on circuit nodes, \underline{C} and \underline{G} the capacitance and conductance matrices, \underline{J} the vector of currents through the inductances (hence not living in the same space as \underline{U}), \underline{P} a kind of projector relating the currents through the inductances to the currents on the nodes, and \underline{H} the inductance matrix. The unknowns are the vectors \underline{U} and \underline{J} . All matrices are constants, which makes most of the system linear. However the source term \underline{I} , the net plasma current collected/emitted from/to the plasma, is of a very

different type. It depends non-linearly on the surface potentials \underline{U} , but also on the plasma state in unsteady situation, which was summarized in a time dependence in (1).

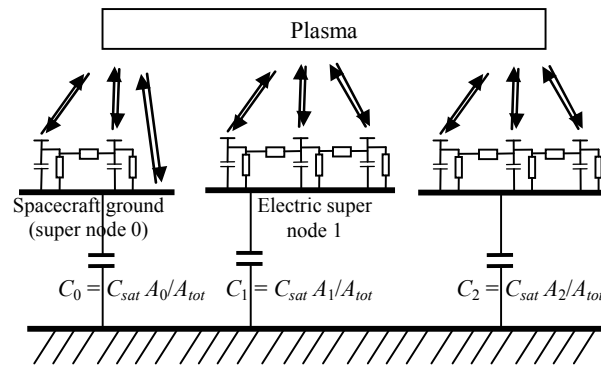


Figure 35 - Simple version of a spacecraft equivalent circuit, with continuous components (all small capacitors and resistors spread on top of each super node, one per surface element) and absolute capacitance C_{sat} . Here C_{sat} is distributed over all super nodes and results in three capacitors C_i , $i = 0, 1, 2$, relating them to the plasma ground at the bottom, with capacitances proportional to their areas A_i , of sum A_{tot} . Other discrete components can be plugged by the user between super nodes (resistors, capacitors, inductances and bias).

The principle of an implicit solver, based on a Newton-type method, is to take advantage of the knowledge on how currents change with potentials to anticipate their evolution and not overshoot the solution, which would result in instabilities. This knowledge, typically expressed to a first order as a dI_i/dU_j matrix (i and j are element indices), is contained in the linear part of (1) (conductivity currents and inductance currents). However the plasma term $\underline{I}(\underline{U}, t)$, while obtained from the plasma dynamics integration for given conditions (\underline{U}, t) , has *a priori* unknown (and of course non-linear) dependence on potentials, when they vary. The general idea implemented, to still be able to use an implicit hence stable solver, involves supplying the solver with an approximate dI_i/dU_j matrix, so-called *current scalars* in SPIS, based on physical assumptions. The uncertainty introduced by this approximation can be controlled by supplying a validity range (in term of voltage variation) for this linear interpolation of $\underline{I}(\underline{U}, t)$ for varying \underline{U} , and a maximum time step in case of explicit time dependence. Assumptions for dI_i/dU_j can typically be based on approximate analytical laws (Boltzmann distribution, Langmuir-Blodgett, Mott-Smith Langmuir ...). Even though usually only approximate for realistic conditions, the combination of an exact computation for $\underline{I}(\underline{U}, t)$ (e.g. through PIC method), and an approximate interpolation over a controlled validity range is thought to give good results. For the ESD prediction tool, significant improvements have been implemented to calculate the *current scalars*, the equivalent conductance and capacitance of the dielectric surfaces.

6.3.4.1. Current Scalars

For the ESD prediction tool, 4 current scalars have been developed to extend the current prediction to the electron avalanche during the ESD. It concerns the prediction of:

- the Fowler-Nordheim emission (general class): *FNCCurrentScaler* (see section 7.3.3.)
- the Fowler-Nordheim emission considering a tip (more precise than the previous): *FNWithTipCurrentScaler* (see section 7.3.4).

- the FN or secondary electron recollection: *CurrentScalerFromCurrentVariation* (see section 7.3.1)
- the secondary emission from recollected FN or secondary electrons (hoping effect): *CurrentScalerFromLocalCurrentVariation* (see section 7.3.2).

6.3.4.2. *Capacitive and Conductive Coupling*

The capacitive coupling of a thin dielectric surface top only exists with the underlying ground, the value of the capacitances being based on a plane capacitor assumption. Here close to a triple point, at a space scale close to or smaller than capacitors thickness, capacitive coupling indeed also exists between neighboring dielectric surfaces (a charge deposited on top of a dielectric surface modifies the potential not only at the same location but also on the nearby dielectrics, by influence).

The bulk conductivity of a thin dielectric surface top only exists with the underlying ground too, the value of the conductance being also based on a plane conductor assumption. For the same reasons as for the capacitive coupling, it might be more realistic to perform a conductive coupling with the neighboring elements. The correct way to perform that is to calculate the conductance on each elements of the dielectric surface by taking account of the distance to the metallic parts.

The capacitive and conductive coupling with neighboring surfaces is implemented in an extension of the standard equivalent circuit (*RLCSCcirc* class) called *RLCSCforESD* (see section 7.2.3 for the details of the implementation).

6.4. Wizard Creation and Project Configuration

6.4.1. *Standard Project Configuration in SPIS-UI*

A standard project preconfigured is released with the ESD prediction. In this project, all the components are predefined to run an ESD prediction test with the standard values for the geometry, materials, environment and effects. It includes the configuration of:

- The scenario parameters
- TipRecession interactor
- Photo emission source
- Fowler Nordheim with tip source
- Bi-Maxwellian source of electrons
- Secondary emission from environment, Fowler-Nordheim and secondary electrons
- Time steps: from physical assumption. We use the new possibility of SPIS to define integration duration and the time steps for all the processes.

6.4.2. *Pre-Defined Models Wizards*

A wizard based approach permit to modify the entry of the standard project for the ESD prediction tools. The process is decomposed into several steps. When the user clicks the "Next" button, all data provided during the step have to be validated. In the same step, the user can modify the various parameters as he wants (no order). The different steps of the ESD tool wizard are:

- Geometry definition
- Materials characteristics settings
- Space environment settings

- Simulation settings
- Post-processing and results

When the user clicks on the "Next" button, an 'internal machinery' checks if the modified data are valid. If invalid data are detected, a dialogue box of warning / error is displayed together with the list of parameters that should be corrected. When the data model is valid, the relevant actions are performed in order to pass to the next step (as *e.g.* CAD loading, meshing, groups deployment, field mapping, UI to Num conversion...).

7. DETAILED DESIGN

7.1. Simulation

7.1.1. *ESDRiskScenario*

The *ESDRiskScenario* is the core class of the ESD prediction tool. This class extends the *Scenario* class of SPIS. The *ESDRiskScenario* is based on the *LocalParameters* and the *GlobalParameters* defined in the standard SPIS-UI. It permits to configure the ESD prediction scenario and to define two external loops on the tip geometry and on the barrier potential. During each step, the simulation is integrated with a fixed barrier potential and tip geometry.

The barrier potential loop is always activated. At each step, the potential of the barrier potential material is changed following the scenario parameters. The densities of the environment boundary are adapted to this new potential using a Maxwell-Boltzmann law. This loop is configured by three parameters:

- *scenarioParameter1*: number of steps
- *scenarioParameter2*: the initial potential (>0)
- *scenarioParameter3*: the final potential (>0)

The second loop is on the tip geometry. At each step, the field enhancement factor evolves from higher to smaller. This corresponds to tips with larger and larger radius. This loop is also activated when a *FowlerNordheimWithTipAreaSurfDistrib* is defined in the simulation. This loop is controlled by three global parameters:

- *scenarioParameter4*: number of steps
- *scenarioParameter5*: the initial FN enhancement factor (higher)
- *scenarioParameter6*: the final FN enhancement factor (smaller)

In the *FowlerNordheimWithTipAreaSurfDistrib*, the tip height is fixed to 1 micron (not accessible in the global parameters in UI). The *scenarioParameter7* permits to fix this parameter to another value by the way of this global parameter.

The next two parameters permit to define the duration of the steps:

- *scenarioParameter8*: first step duration
- *scenarioParameter9*: other steps duration

The *scenarioParameter10* permit to choose between two conditions for the scenario end when there is a loop on the tip geometry:

- if set to 1, the scenario is stopped when the first ESD is triggered
- if set to 0, the scenario continue after triggering the ESD. After an ESD is triggered, the scenario continue with a smaller tip to compute the triggering potential for the new geometry. In this, it is possible to have several points of ESD triggering for different tip geometry.

At the end of one step, the scenario can produce different actions following the *tipRecession* outputs (detection if the tip is melted and if the ESD is triggered):

- the tip is not melted and no ESD \Rightarrow barrier potential is increased – next step in potential
- the tip is melted but no ESD \Rightarrow the tip radius is increased – next step in beta
- an ESD is triggered and *scenarioParameter10* is set to 1 \Rightarrow end of the scenario – outputs and reports are generated

- an ESD is triggered and *scenarioParameter10* is set to 0 \Rightarrow a report is generated for this ESD condition and the tip radius is increased – next step in beta

At the end of the scenario, specific outputs are generated for the ESD prediction tool:

- ESD report: condition of the tip at the end of each steps (for each potential and each tip geometry)
- Barrier potential applied as a function of time

7.1.2. *SimulationFromUIParamsESD*

The *SimulationFromUIParamsESD* class extends the *SimulationFromUIParams* class to adapt the initialization of the spacecraft circuit and the condition of the end of a simulation for the ESD prediction tool. This class is only used when the *ESDPredictionScenario* is used.

7.2. SC/Plasma Interactions

7.2.1. *FowlerNordheimWithTipAreaSurfDistrib*

This class also extends the *FowlerNordheimSurfDistrib* to take into account the tip effect on the emitted flux. In fact, *FowlerNordheimSurfDistrib* already assumes a field enhancement factor (Beta) which can come not only from a tip but also from dielectric layers or other phenomena. The *FowlerNordheimWithTipSurfDistrib* extends (more precise) this class by defining a field enhancement factor that comes from the tip geometry. Consequently, the real emission surface is not the surface element of the source but the tip emission surface.

For a cylindrical tip, the emitting surface is assumed to be the surface of the up disk: $S_{real} = 2\pi r^2$ with r the tip radius. Thus the emitted current density of the source is corrected by a factor taking into account this effect:

$$factor = S_{real} / S_{source} \quad (18)$$

with S_{source} the area of the surface where the source is defined.

7.2.2. *TipRecession*

The tip recession class aims to compute the interaction between the FN current and the tip behavior. It includes:

- Thermal model of the tip
- Tip geometry evolution calculation as a function of temperature: mass loss is responsible of a decrease of the tip length
- Neutral density evolution in volume and ESD triggering probability calculation

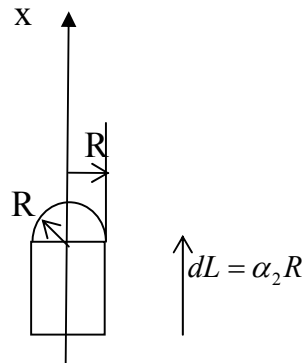


Figure 36 - Tip geometry

7.2.2.1. Thermal Model

The thermal model needs to resolve the equation:

$$\rho C_p \frac{\partial T}{\partial t} (\alpha_3 R^3) = P - \alpha_4 \kappa \frac{T - T_0}{R} R^2 - \frac{dm}{dt} \frac{L_{vap}}{N_{avogadro} M_a} - \alpha_9 \frac{I}{e} \varepsilon^*$$

$$P = \alpha_1 U_0 I + \alpha_2 (j_{total})^2 \frac{\pi R^3}{\sigma}$$

$$\alpha_1 = 0$$

$$\alpha_3 \approx \pi \times \alpha_2 \approx \pi \times 10$$

$$\alpha_4 \approx \pi / \alpha_2 \approx \pi / 10$$

$$\alpha_9 = 0$$
(19)

where the α_i parameters come from the cylindrical geometry of the tip. In this model, the following processes are taken into account:

- Joule heating of the FN current
- Conduction
- Electron extraction (loss or gain depending on electric field)
- Atom evaporation

The majority of extended materials properties presented in the first section are needed for the resolution of this equation.

7.2.2.2. Tip length evolution

The tip length variation comes from the mass loss due to evaporation of the tip extremity. The tip volume variation can be written:

$$\rho \frac{dV}{dt} = \frac{p M_a}{\sqrt{2\pi M_a k_b T}} A_{evap}$$

$$A_{evap} = A_{tip} + A_{latéral} = 2\pi R^2 + \alpha_6 R^2$$

$$\alpha_6 \in [0; 2\pi\alpha_2]$$
(20)

Thus we can deduce the tip length variations. Finally these variations as a function of the tip temperature lead to a decrease of the electric field enhancement factor:

$$\beta = \frac{L}{r} \quad (21)$$

7.2.2.3. Comparison to a 1D Model

This 0D model has been compared to Rossetti results [41] in the case of a tungsten tip 10 μm long with a radius of 0.1 μm . The time necessary to reach the fusion temperature on the micro tip are presented in the next tables, for initial temperature of 300K and 2000K. The electric field necessary to obtain the fusion of the tip with our 0D model is very close to the 1D-model, with an error of 10-15 %.

Tungstene Tinit = 300 K		
Electric field (1e10 V/m)	fusion time (ns)	
	0D - Model	1D model [ROSS]
1.2	0.25	0.04
1.1	0.85	0.5
1.08	1.1	1.26
1.07	1.25	2.35
1.06	1.45	10
1.05	1.7	no fusion
1.04	2	
1	3.8	
0.99	4.55	
0.985	5.1	
0.95	10.6	
0.92	32	
0.91	no fusion	

Tungstene Tinit = 2000 K		
Electric field (1e10 V/m)	fusion time (ns)	
	0D - Model	1D model [ROSS]
1.2	0.12	
1.1	0.4	0.08
1.08	0.52	
1.07	0.6	
1.06	0.7	0.3
1.05	0.8	
1.04	0.95	
1	1.8	5.3
0.99	2.15	24.8
0.985	2.3	53.4
0.95	4.3	no fusion
0.92	8.5	
0.91	11.15	
0.9	14.9	
0.89	21.4	
0.88	40.7	
0.87	no fusion	

7.2.2.4. ESD Triggering Probability

The ESD triggering probability is deduced from the quantity of evaporated neutrals from equation (4). From this quantity, we deduce the profile of neutral density as a function of the distance from the tip r . We assume that the profile form as an $1/r^2$ variation (flux conservation and isotropic in three dimensions).

Then, the ionization probability is estimated using the relation:

$$\text{Proba} = \int_0^R n(r) \sigma_{\text{eff.ion}} dr$$

with $\sigma_{\text{eff ion}}$ the effective cross section of ionization defined in the extended material properties. When this probability is higher than one, the ESD prediction tool consider an ESD is triggered.

7.2.3. RLCSCforESD

To implement that, a first method consists in computing this improved capacitance matrix from Green functions (the potential generated by a single local charge deposit). The potential image theory leads to the relation for a particle of charge q at a distance a from the conductor:

$$V(r, y) = \frac{1}{4\pi\epsilon_0} \left(\frac{q}{\sqrt{r^2 + (y - a)^2}} + \frac{-q}{\sqrt{r^2 + (y + a)^2}} \right) \tag{22}$$

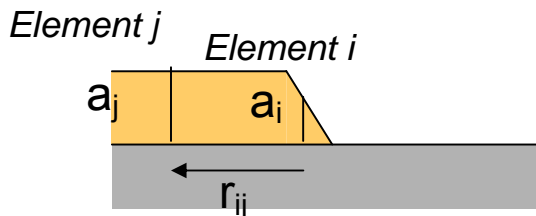


Figure 37 - Capacitive coupling

From this relation we deduce the inverse capacitance matrix which components are:

$$(C^{-1})_{ij} = \frac{1}{4\pi\epsilon_0} \left(\frac{1}{\sqrt{r_{ij}^2 + (y_i - a)^2}} + \frac{-1}{\sqrt{r_{ij}^2 + (y_i + a)^2}} \right) \tag{23}$$

$$(C^{-1})_{ii} = \frac{1}{2\pi\epsilon_0} \frac{1}{dr_i} \left(1 - \sqrt{1 + \frac{4a_i^2}{dr_i^2} + \frac{2a_i^2}{dr_i^2}} \right) \tag{24}$$

This indeed supplies the inverse of the capacitance matrix (potential versus charge, not charge versus potential). Inverting this matrix to get the capacitance matrix might however lead to a rather heavy capacitance matrix describing the coupling between all surface elements of the model, whereas in the usual thin capacitor approximation we have light matrices (very sparse) allowing much more efficient computations. We shall first try to use this inverted matrix and check whether CPU cost remains acceptable, and try simplifying if not (e.g. only keeping largest local couplings).

For the conductive coupling, the real distance from the surface cell to the ground a is take into account instead of the dielectric thickness d defined in the local properties of the material:

$$G_i = \frac{\sigma \times S_i}{a} \tag{25}$$

where σ is the conductivity of the material.

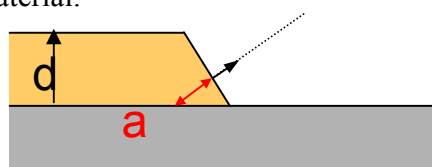


Figure 38 - Conductive coupling

7.3. Current Scalers for the Implicit Circuit Solver

7.3.1. CurrentScalerFromCurrentVariation

This current scaler assumes the current variations come from the global variation of a unique source. This is the case for the recollection of Fowler-Nordheim electrons. One can assume that the local recollected current is proportional to the global current emission from the source.

$$dI = I \times d|I_{source}| / |I_{source}| \quad (26)$$

with I the local current associated to the current scaler, dI the current variation calculated by the current scaler, $|I_{source}|$ the global current emitted by the source (sum of the global currents of each cells) and $d|I_{source}|$ the global variation of the source current.

7.3.2. CurrentScalerFromLocalCurrentVariation

This current scaler assumes the current variations come from the local variations of a unique source. This is the case for the secondary emission from recollected electrons. One can assume that the local emitted current is proportional to the local current collection.

$$dI = I \times dI_{coll} / I_{coll} \quad (27)$$

with I the local current associated to the current scaler, dI the current variation calculated by the current scaler, I_{coll} the local currents recollected and dI_{coll} the local variations of the collected current.

7.3.3. FNCurrentScaler

The current scaler for the Fowler-Nordheim emission is more complex than the previous cases because the FN emission does not only depend on the local potential of the source but also on the local potential on the dielectric. Consequently, the current scaler is presented in a matrix form:

$$\underline{\delta I}_{FN} = \underline{M}_{FN} \cdot \underline{\delta V} \quad (28)$$

with $\underline{\delta I}_{FN}$ the local current variation of FN emission as a function of the local potentials on the spacecraft $\underline{\delta V}$. At a first approximation, it can be assumed:

$$\delta J_{FN,i} = \left(\frac{dJ_{FN}}{dE} \right)_i \delta E_i \quad (29)$$

with E_i the electric field at the surface cell i and $J_{FN,i}$ the local FN current from the Fowler-Nordheim relation:

$$J_{FN,i} = \frac{e^3 E_i^2}{8\pi\hbar\phi_w t^2(y)} K_F \exp\left(-\frac{8\pi\sqrt{2m_e\phi_w^3}v(y)}{3\hbar e E_i}\right) \text{ A/m}^2, \quad (30)$$

with ϕ_w (eV) the work function of the material and $y = (e^3 E_i(s)/4\pi\epsilon)^{1/2} / \phi_w$. It is also assumed $t(y) \approx 1$, $K_F \approx 1$ and $v(y) \approx 1 + p \times E_i$, with $p = -7 \times 10^{-11}$ m/V. Thus, relation (7) can be rewritten to:

$$J_{FN,i} = A E_i^2 \exp\left(-\frac{B}{E_i}\right) \quad (31)$$

$$\text{with } A = \frac{e^3}{8\pi h \phi_w t^2(y)} K_F \exp(-B \times p) A/V^2 \text{ and } B = \frac{8\pi \sqrt{2m_e \phi_w^3}}{3he} \text{ V/m}$$

As a result, we obtain which is local for the moment:

$$\left(\frac{dJ_{FN}}{dE} \right)_i = A(2E_i + B) \exp\left(-\frac{B}{E_i}\right) = \gamma_i \quad (32)$$

The next step consists to write the relation between the variations of the local electric field δE_i and the neighboring potentials δV_j . In a first assumption, we can state the local electric E_i is proportional to the difference between the local potential V_i and a weighted average of the local potential on the dielectric:

$$E_i = \alpha(\langle V \rangle - V_i) \quad (33)$$

$$\text{with } \langle V \rangle = \sum_{j \neq i} p_{i,j} V_j \text{ and } \forall i, \sum_{j \neq i} p_{i,j} = 1.$$

To determine these weights, we propose a proportional dependence with the distances of the surfaces to the emission node and the potential difference:

$$\forall j \neq i, p_{i,j} = \frac{V_j}{d_j} \frac{1}{\sum_{k \neq i} \frac{V_k}{d_k}} \quad (34)$$

Finally, we obtain the relation:

$$\delta E_i = \alpha \left(\sum_{j \neq i} p_{i,j} \delta V_j - \delta V_i \right) \quad (35)$$

with α calculated from relation (10).

The current scaler matrix thus can be written in the form:

$$\underline{\underline{M}} = \alpha \begin{pmatrix} -\gamma_1 S_1 & \cdot & \gamma_1 p_{1,j} S_1 & \cdot & \cdot & \cdot \\ \cdot & \cdot & \cdot & \cdot & \cdot & \cdot \\ 0 & \cdot & 0 & \cdot & 0 & \cdot \\ \cdot & \cdot & \cdot & \cdot & \cdot & \cdot \\ \gamma_i p_{i,1} S_i & \cdot & \gamma_i p_{i,j} S_i & \cdot & -\gamma_i S_i & \cdot \\ \cdot & \cdot & \cdot & \cdot & \cdot & \cdot \end{pmatrix} \quad (36)$$

with S_i the area of the surface element i .

7.3.4. FNWithTipAreaCurrentScaler

This class is the current scaler for a *FowlerNordheimWithTipSurfDistrib*. It extends the *FNCurrentScaler* taking into account the tip geometry. For a cylindrical tip, the emitting surface is assumed to be the surface of the up disk: $S_{real} = 2\pi r^2$ with r the tip radius. Thus the emitted current density of the source is corrected by a factor taking into account this effect:

$$factor = S_{real} / S_{source} \quad (37)$$

with S_{source} the area of the surface where the source is defined.

7.4. SPIS-ESD User Interface / User Manual

Details are given in APPENDIX 2, section 0.

8. TEST REPORT

This document presents the tests performed in the frame of the activity: Development of a predictive discharge numerical model on solar panels. The objective is to perform calibrated experiments permitting to provide reliable results for the software validation phase on the basis of section 5 "Software Verification and Validation plan".

8.1. Triple Point Configurations

Dedicated samples have been manufactured. These triple point (TP) configurations aim at determining the influence of a set of three parameters: geometry, metal and dielectric material, see Section 8.1.1. The resulting sample design and manufacturing are presented in Section 8.1.2. During the experiments, the influence of two other parameters has been studied. These extra parameters are presented in Section 8.1.3. It aims at providing a more exhaustive data list. Finally, the complete list of configuration tested is summarized in Section 8.1.4.

8.1.1. Configurations Originating from SVVP

8.1.1.1. Geometry

The sample geometries are:

- perpendicular configuration
- coplanar configuration

In both cases, it is worth noting the coupon faces the tank walls as described in Figure 39. The important dimensions are depicted in Figure 39 and in Figure 40:

- the dielectric length l_{diel} ,
- the metal length l_{metal} ,
- the sample length $l_{sample} = l_{metal} + l_{metal}$,
- the dielectric thickness e_{diel} ,
- the triple point width w_{diel} ,

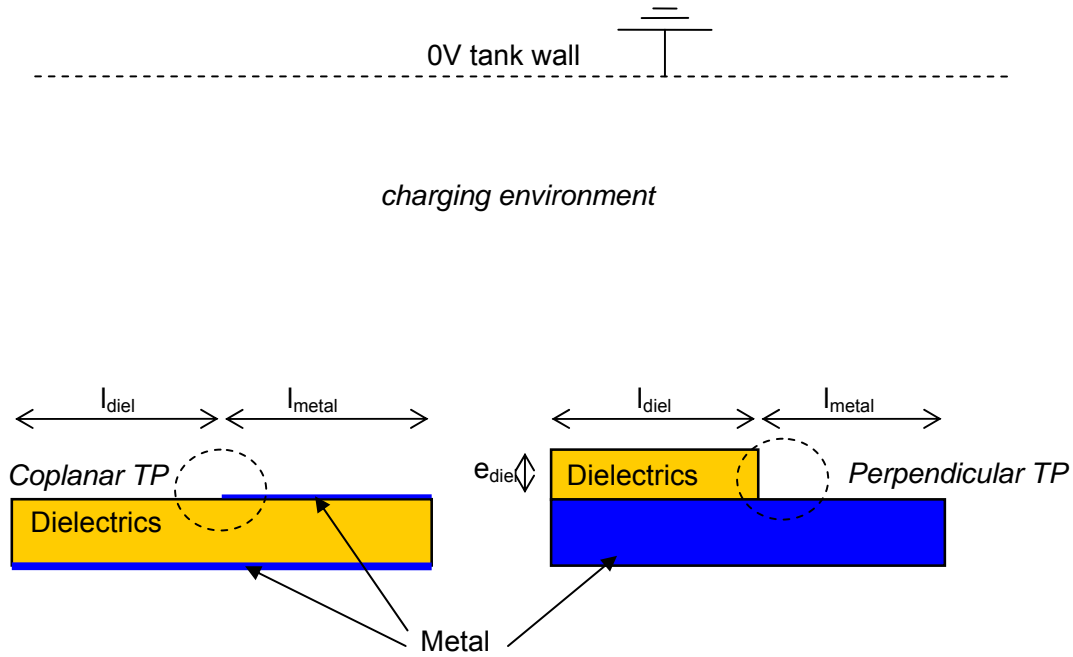


Figure 39 - Side view of the two triple point configurations used during the experiments

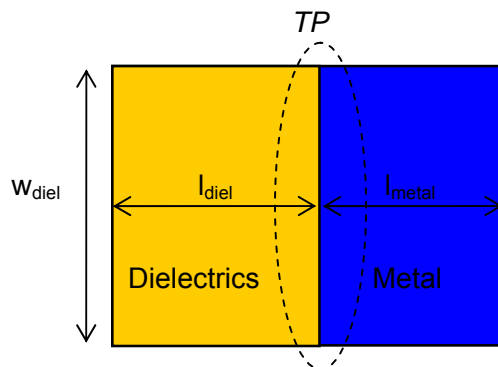


Figure 40 - Top view of the two triple point configurations used during the experiments

8.1.1.2. Metal

The main metal properties are work function and thermal properties. Two metals have been used: aluminium and gold. They have been chosen because their work functions are quite different: from 4.06 to 4.41 for aluminium and 4.83 to 5.47 for gold [37].

Remark: work functions are reported for pure material. The aluminium surface sheet is generally oxidized, which diminishes its work function. There is no consolidated data on the final value, which may range from 3.7 to 4.0.

8.1.1.3. Dielectric Material

The main dielectric material properties concerning the ESD phenomenon are: conductivity (bulk and surface), secondary electron emission yield by electron impact and dielectric constant. The value of these parameters must be precisely known or measured. It has been chosen to use materials previously studied in the frame of an ESA/ONERA previous activity: Material Characterization for Plasma Interaction Analysis [38]:

- The Teflon tape used is Sheldhal 127 μ m sheet, aluminized on the rear side. New samples have been used, which is referred as Beginning of Life (BOL) in [38].
- The solar cell coverglass used is a 100 μ m thick CMX with MgF₂ anti reflecting coating, referred as CMX-AR in this report. The sample measured and referred as Middle of Life (MOL) during [3] has been used in the present study,

The property data are presented in Table 5. The surface resistivity of Teflon has not been measured during the material characterization campaign [38]. The manufacturer data (GoodFellow) have then been considered in this study. Anyway, Teflon is known to be highly resistive and the surface conductivity may be considered as negligible. As secondary emission is very important for ESD triggering, the dielectric materials SEY have been measured at ONERA/DESP in the frame of this activity. The recently developed and so-called Kelvin Probe method has been used [36]. The measured secondary emission yield (SEY) curves are represented in Figure 41 and Figure 42 for Teflon and CMX-AR respectively. In Table 5, we give the maximal SEY and the incident electron energy that produces that maximum.

Table 5 - Dielectric properties measured during the MCPIA campaign⁽¹⁾ [1], in the frame of these study⁽²⁾, or given by the material manufacturer⁽³⁾

	Teflon FEP (BOL)	CMX-AR (MOL)
N° in MCPIA study	8	955
Bulk conductivity [$\Omega^{-1} \cdot m^{-1}$]	⁽¹⁾ 1.0×10^{-20}	⁽¹⁾ 5.0×10^{-14}
surface resistivity [Ω/\square]	⁽³⁾ 1.0×10^{16}	⁽¹⁾ 2.6×10^{16}
maximum SEY	⁽²⁾ 2.3	⁽²⁾ 3.2
Energy of the maximum SEY [eV]	⁽²⁾ 400	⁽²⁾ 400

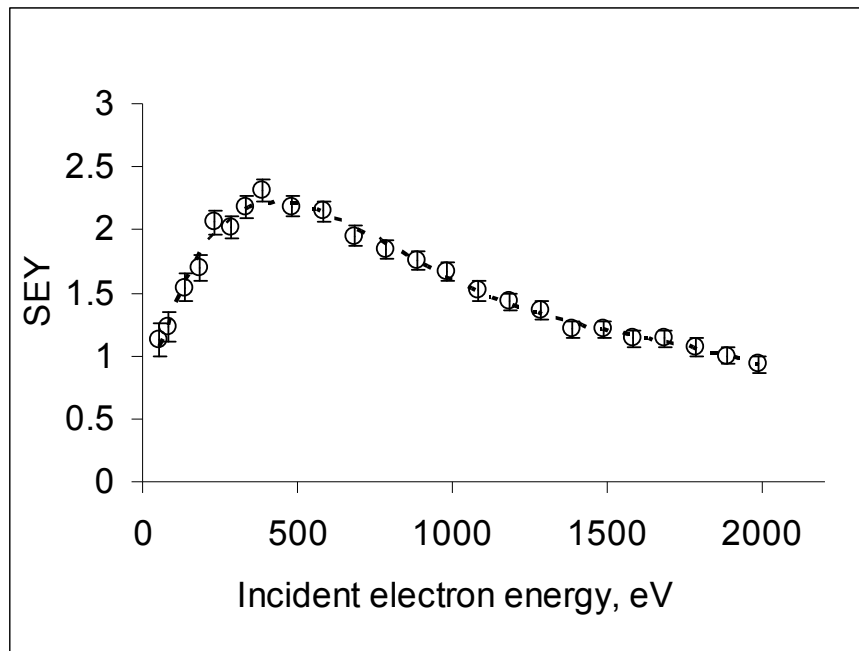


Figure 41 - SEY of Teflon

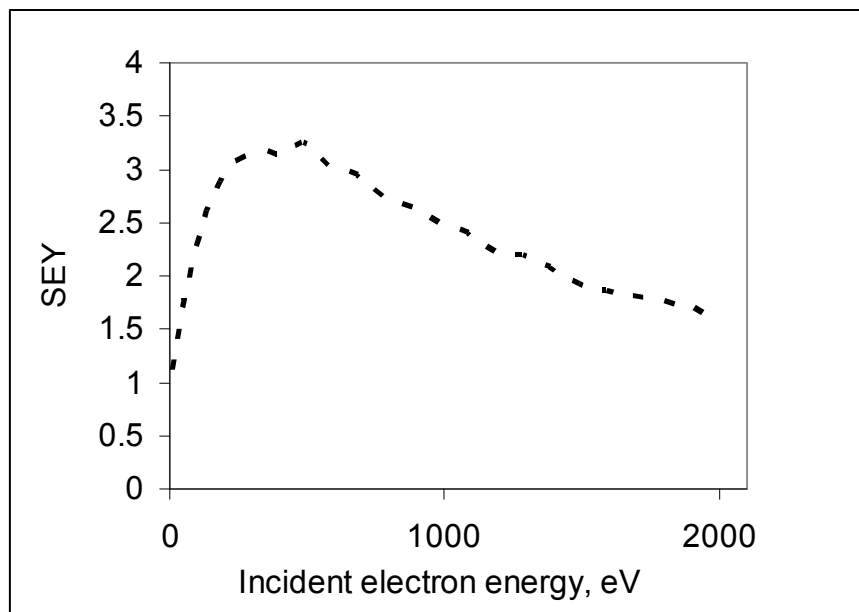


Figure 42 - SEY of CMX-AR coverglass

8.1.2. Sample Manufacturing

The samples have been in order to fit the [SVVP], in particular in term of geometrical configurations. Efforts have been made to create configurations as close as possible from the theoretical perpendicular and co-planar situations.

The co-planar situation is particularly difficult to obtain mechanically since it is only a theoretical situation. Experimentally, it was of course not possible to have a perfect smoothness of the triple point. The method adopted is **metallization** of a dielectric substrate. The ONERA vaporizing device has been used to deposit a precise sheet of metal on a dielectric substrate. The metal thickness could be adjusted from 10 nm to 1 μm in the case of aluminium, and from 10nm to 100nm in the case of gold. The perpendicular configurations have been manufactured using 0.7 μm thick aluminium and 58 nm thick gold sheets. The co-planar configuration has been manufactured using a 50 nm thick aluminium sheet.

The difference between theoretical and experimental achievement of the co-planar situation relies on the thickness of the metallization. The thinner it is, the closer to the theoretical situation. The irregularities at the origin of the electric field amplification (and so on generate ESDs) are typically sub micrometric in order to increase sufficiently the mesoscopic electric field (see for example: M. Cho et al., "Computer particle simulation of high voltage solar array arcing onset", Journal of Spacecraft and Rockets, Vol. 30, No 2, pp. 189-201, 1993; D. Payan et al., "Electrostatic Discharges on Solar arrays. Physical Model of Inverted Potential Gradient Electrostatic Discharge," 7th SCTC, Noordwijk, the Netherlands, 2001; B. Jüttner, V. F. Puchkarev, E. Hantzsche, I. Beilis, "Cathode spots," in Handbook of vacuum arc science and technology, *Fundamentals and applications*, R. L. Boxman, P. J. Martin, D. M. Sanders, Ed. New Jersey: Noyes Publications, 1995, pp. 73-281). As a result, submicrometric tips may exist on the edge of the metal vaporization close to the dielectric and produce ESDs in a triple point configuration which is not perfectly co-planar, see Figure 43. This is why we choose to vaporize only 50 nm for the coplanar configuration.

The **co-planar** configuration is obtained by vaporizing the metal on a Teflon tape, *cf.* Figure 43.

The **perpendicular** configuration is obtained by vaporizing the metal on a Teflon tape, which is used as a substrate in this case. The perpendicular triple point is then obtained by applying a dielectric layer (Teflon or CMX-AR) on the metallization, *cf.* Figure 44.

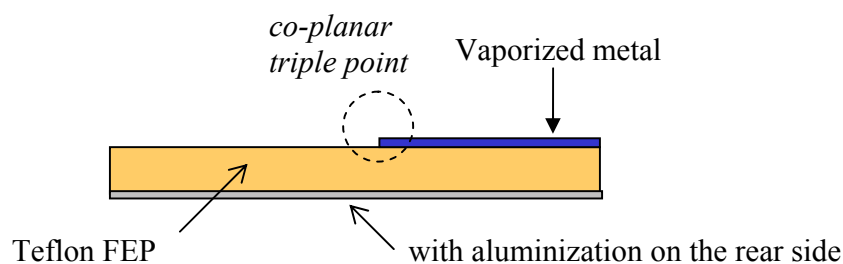


Figure 43 – Design of the samples used for the co-planar configuration

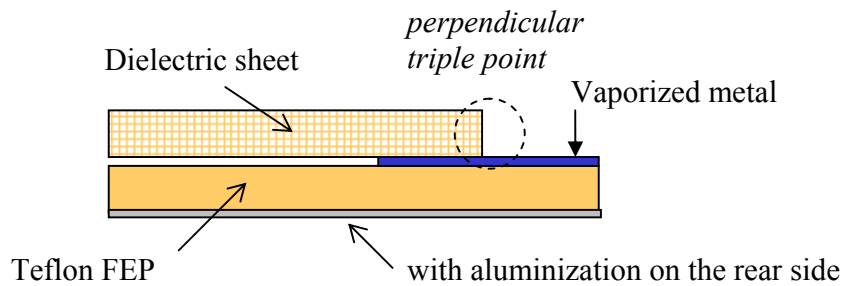


Figure 44 – Design of the samples used for the perpendicular configurations

The sample dimensions are described in Table 6:

Table 6 - Sample dimensions

l_{sample}	40 mm
l_{metal}	[variable, see 8.1.3.2]
e_{diel}	127 μm with Teflon
	100 μm with CMX-AR
	N/A in co-planar
w_{diel}	40 mm

8.1.3. Extra Configurations

8.1.3.1. Photon incidence angle

In this study it has been chosen to use the UV photon method to obtain the Inverted Potential Gradient (IPG) situation, see Section 8.2. In that case, the photon incidence angle might be important **in the angular case** since it can change significantly the potential profile at the triple point. In CEDRE chamber, the fixed UV source incidence angle with the holder is $\alpha = 15^\circ$. By turning the samples, two configurations are obtained:

- incidence angle of 15° ,
- incidence angle of -15° in which the dielectric edge is not irradiated.

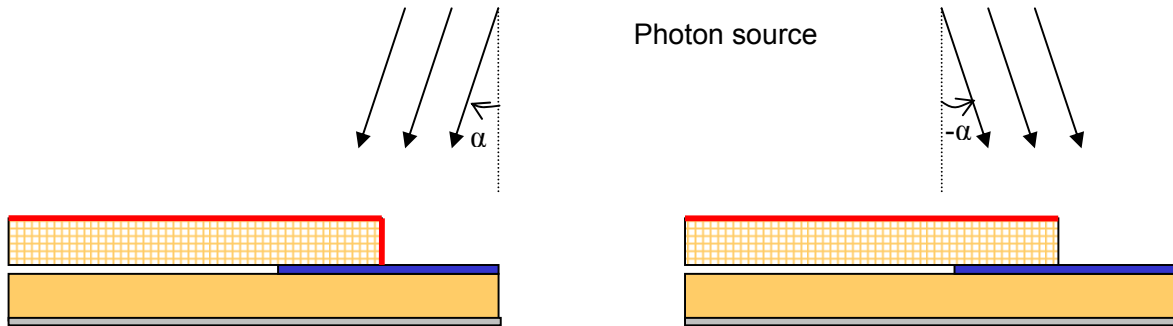


Figure 45 - Influence of the photon incidence angle. On the left side, the dielectric edge is fully irradiated ($\alpha=15^\circ$). On the right side, the dielectric edge is not irradiated ($\alpha=-15^\circ$).

8.1.3.2. Metal vs. Dielectric length

The effect of the metallic element size is also studied experimentally by setting 2 different metal vs. dielectric lengths.

- metal length $l_{metal} = 3 \text{ mm}$
- metal length $l_{metal} = 15 \text{ mm}$

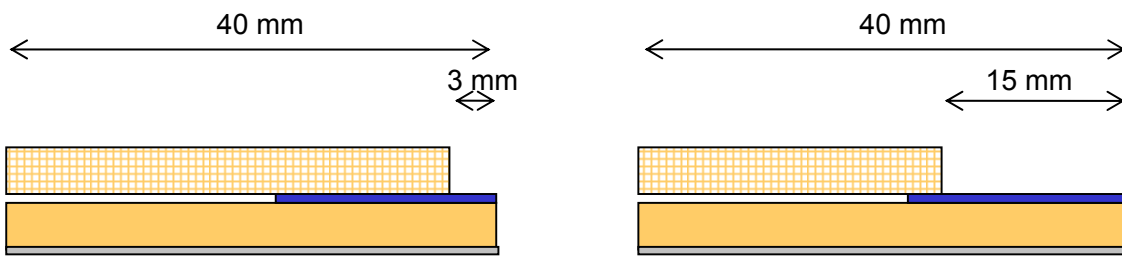


Figure 46 - The two configurations used to study the influence of the metal length

8.1.4. Configurations to be Tested

The strategy followed consists first in defining a nominal case. Around this nominal case, we investigated in the three initial directions: change of dielectric, change of metal, change of geometry. We also investigated in the two extra directions: metal length l_{metal} , photon incidence angle. These six configurations are summarized in Table 7.

Table 7 - TP configurations to be tested

Configuration	Geometry	Metal	Dielectric	Metal length	Photon incidence angle
1- Nominal	Perpendicular	Aluminum	Teflon	3 mm	+15°
2- UV incidence angle	Perpendicular	Aluminum	Teflon	3 mm	-15°
3- Metal length	Perpendicular	Aluminum	Teflon	15 mm	+15°
4- Dielectric	Perpendicular	Aluminum	CMX-AR	3 mm	+15°
5- Metal	Perpendicular	Gold	Teflon	3 mm	+15°
6- Geometry	Co-planar	Aluminum	Teflon	3 mm	+15°

8.2. Experimental Setup

In this section, the experimental setup used to perform the ESD tests on the defined configurations is presented. Section 8.2.1 presents the experimental facility. Section 8.2.2 details the new method used to obtain the IPG situation. The ESD test procedure is finally presented in Section 8.2.3.

8.2.1. Experimental Facility

The ONERA/DESP CEDRE chamber schematically represented in Figure 47 is a 1m diameter and 1m long cylinder equipped with a diffusion pump permitting to reach 3×10^{-6} mbar during the experiments. A cubic rotating holder supports the sample which is placed in front of the charging environment.

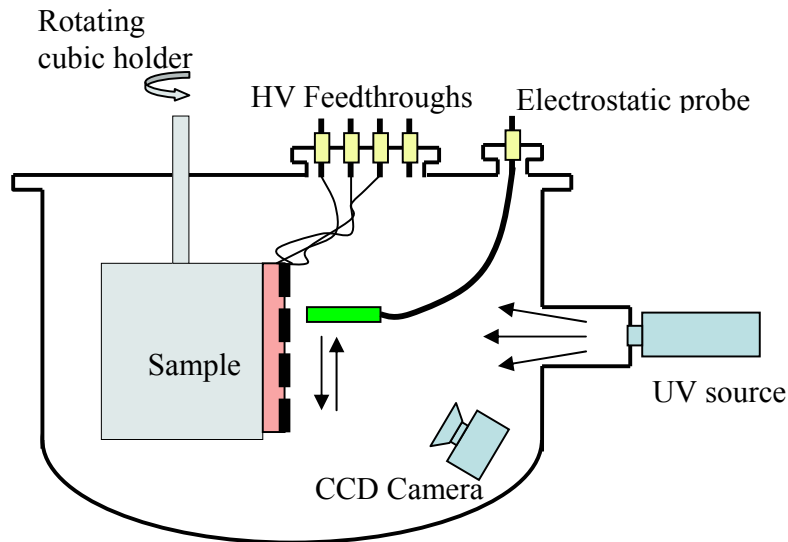


Figure 47 - Schematic view of CEDRE chamber

An electrostatic probe is used to measure the surface potential profile on the samples and to assess the IPG situation level. A CCD camera records the light emitted by the discharge events, which gives the capability to determine the precise location of the ESD.

Remark: This kind of image recorder is absolutely obligatory since ESDs may possibly ignite elsewhere than on the triple point, as *e.g.* at an undesired and poorly insulated element of the coupon. ESDs can also trigger successively at the same location on the triple point. In that case, it is not possible to ascertain that the ESDs following the first one are independent. In that case, it is not possible to rely on the obtained results.

The electrical circuit used to bias the samples is described in Figure 48. It is composed of a capacitor C_{sat} charged under the negative voltage V_{bias} . The voltage supply is decoupled from the coupon by a high resistance. As a result, only the capacitor discharges during the blow-off. The blow-off current is measured with a Pearson current probe and with a TCP 202 Tektronix current probe. The bias voltage applied to the sample metallic part is measured with a 5 kV HV probe. The measurements are recorded by a Tektronix TDS 3014B oscilloscope.

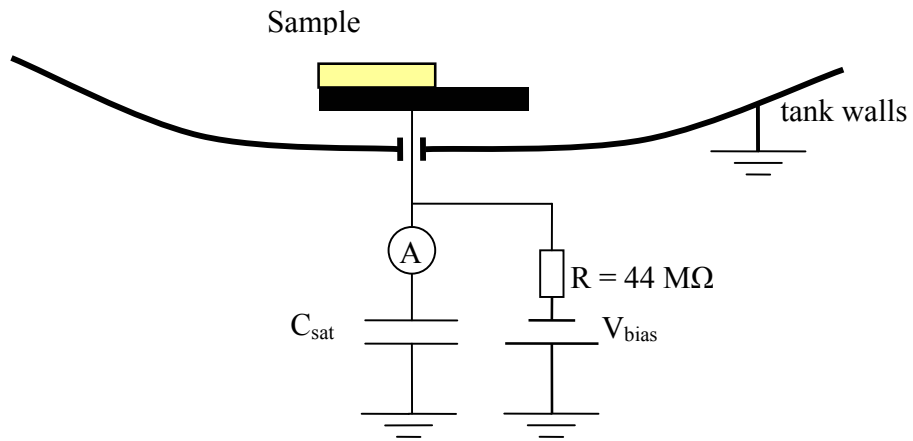


Figure 48 - Bias voltage circuit

8.2.2. Inverted Potential Gradient using V-UV photons

The charging environment is produced using a L2D2-L7293 Deuterium lamp from Hamamatsu. The light spectrum ranges from 115 to 400 nm with two peaks at 125 nm and 160 nm respectively, see Figure 49 and Figure 50.

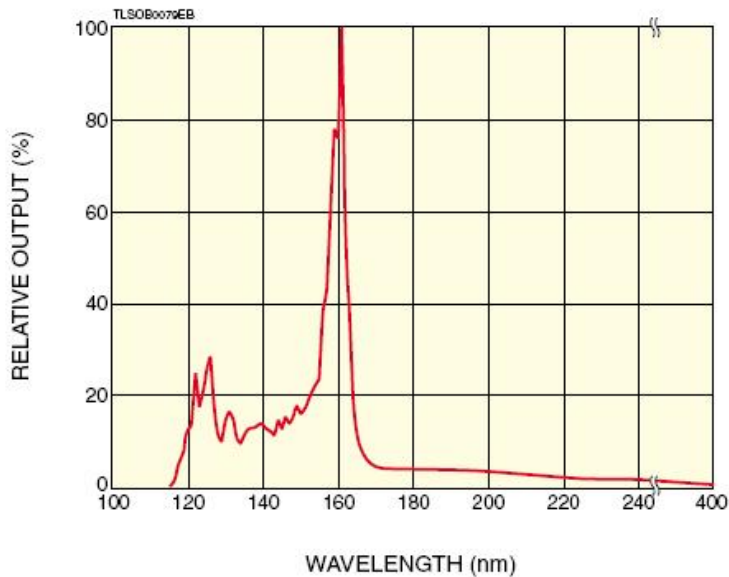


Figure 49 - Relative intensity of L7293 lamp, from Hamamatsu data sheet

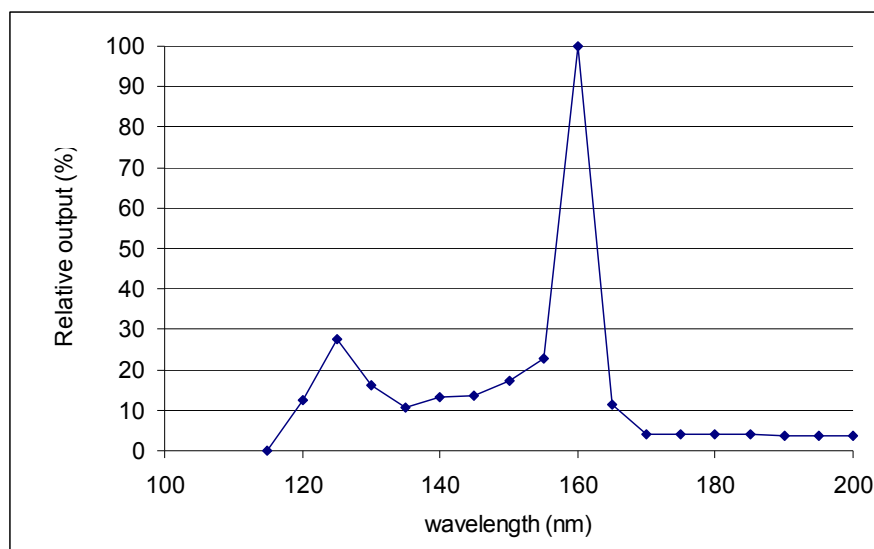


Figure 50 - Relative intensity of L7293 lamp, from ONERA measurements

In this wavelength range, the photo emission process is very efficient. In CEDRE, the photon incidence angle with the sample holder is $\alpha=15^\circ$. At the sample holder location, *i.e.* 50 cm from the UV source, the beam diameter is approximately 10 cm, see Figure 51. The photo current measured on copper ranges between 15 and 25 nA/cm². Of course, this current depends on the material used. Nevertheless, it confirms that 40 mm dimension samples are appropriate for the used charging environment.

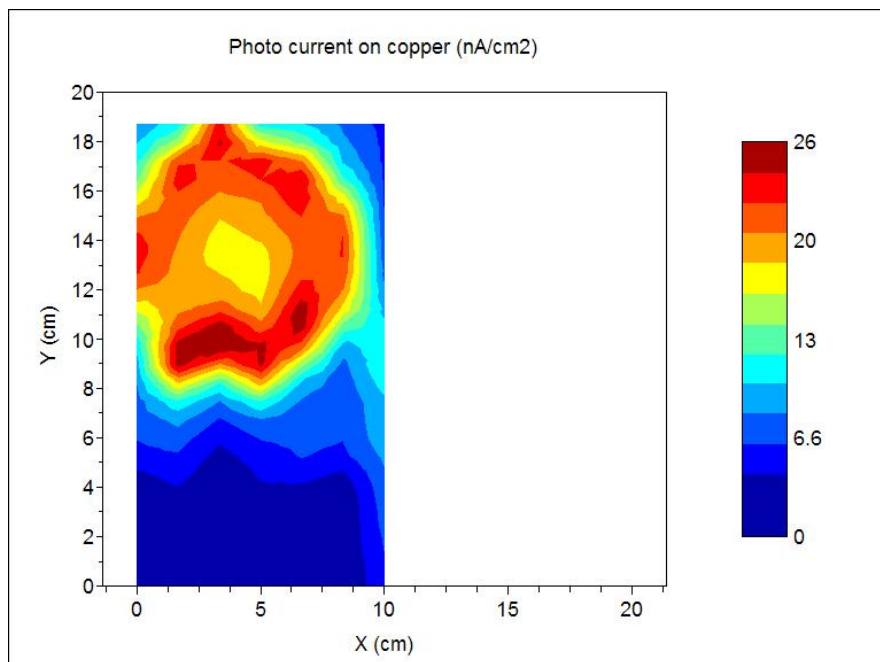


Figure 51 - Photo current density measured on copper, at the sample holder location

The next figures present the picture of a sample in CEDRE chamber. The sample is insulated from the grounded holder by a 1 cm thick Teflon plate and placed in the middle of the lightened zone. A mask is used to prevent the IPG situation occurring elsewhere than in the selected triple point vicinity.

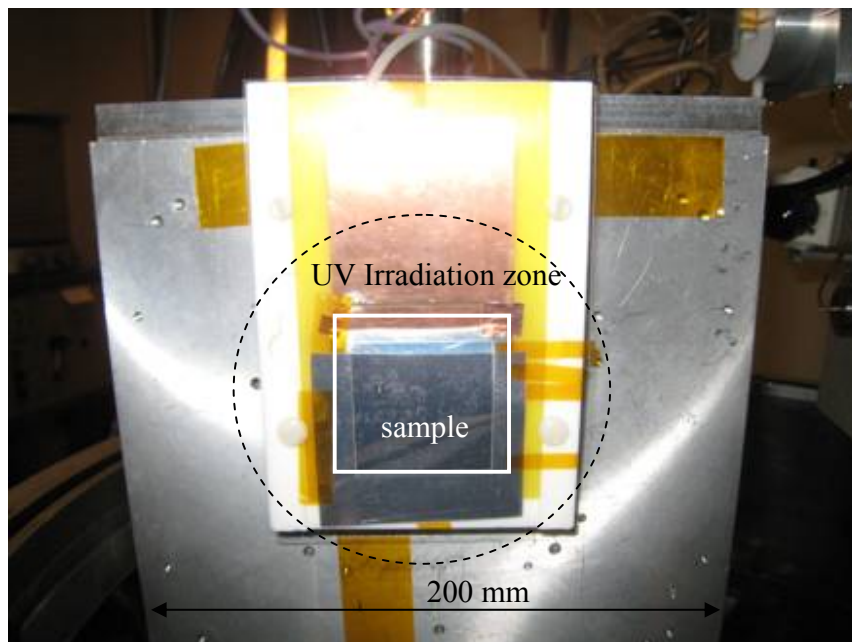


Figure 52 - Picture of the nominal configuration sample

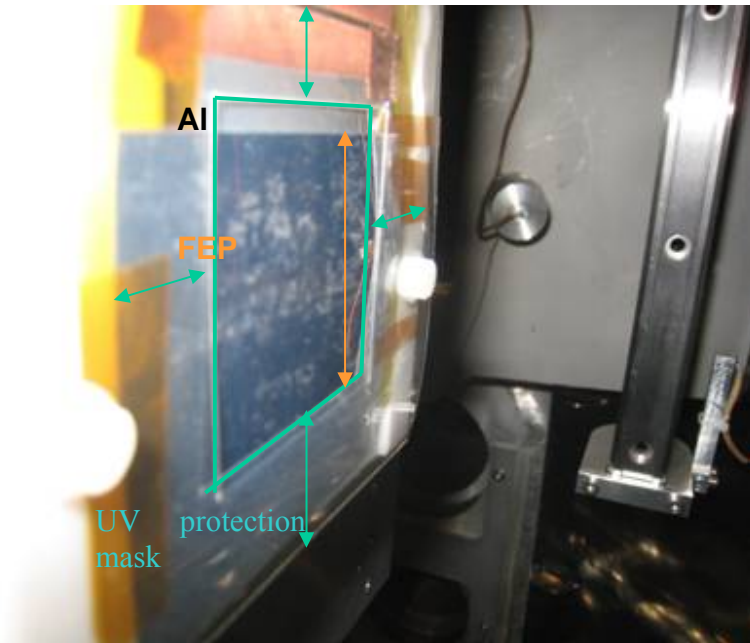


Figure 53 - Detailed view of the nominal configuration

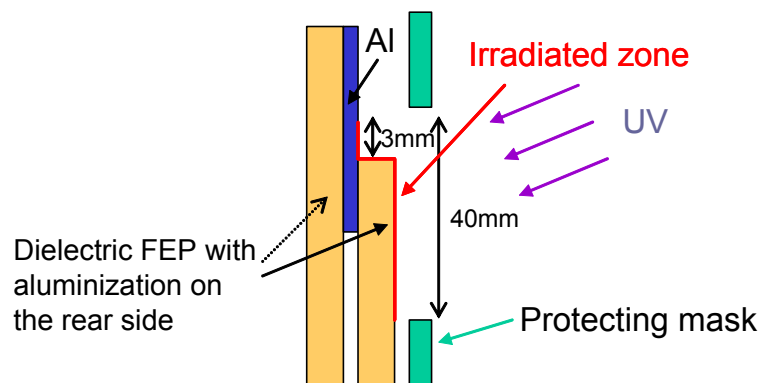


Figure 54 - Schematic view of the nominal triple point with the UV protection mask permitting to select the region irradiated by the UV source

Under UV irradiation, the initially negatively floating surfaces tend to get more positive. This phenomenon is used to make the dielectric material float to a positive voltage in comparison to the negative voltage V_{bias} applied to the metallic part. That leads to the expected IPG situation. The maximum differential voltage is obtained once the dielectric surface floats approximately to the tank walls potential, *i.e.* zero volts. Indeed, the photo electrons are emitted with a typical energy of 2 eV. Once the dielectric surface potential is greater than a few volts positive, photo electrons are recollcted and the net current becomes null. This method is summarized in Figure 55. This signifies that the differential voltage can be precisely known if the photo emission current is greater than the conductive current flowing through the dielectric material. In that case, the differential voltage can be sequentially increased simply by increasing the bias voltage and waiting the time necessary to attain the equilibrium.

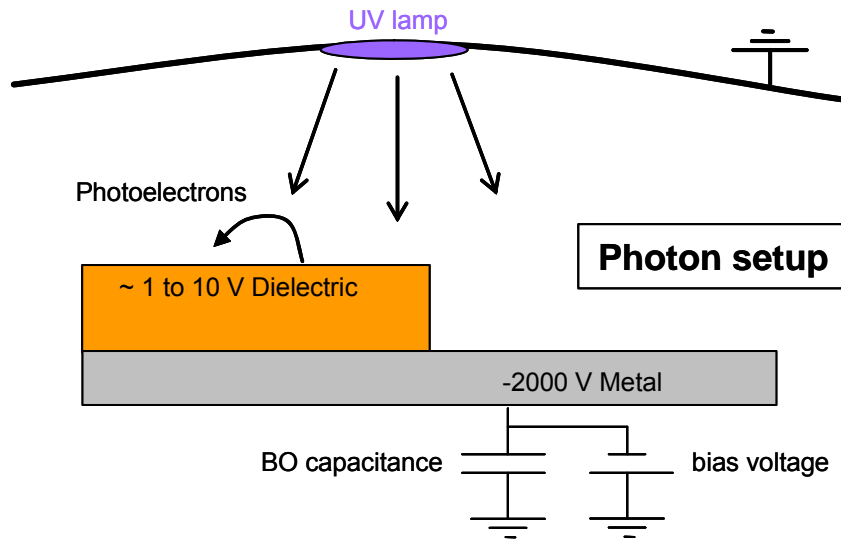


Figure 55 - Principle of the IPG obtained with UV photons

A typical IPG situation is represented in Figure 56, in which the potential profile of a sample has been measured before and after UV irradiation of some tens of seconds. The effect of the photo emission is clearly visible. The dielectric floats to a potential close to zero volts, building an IPG situation of 2000V!

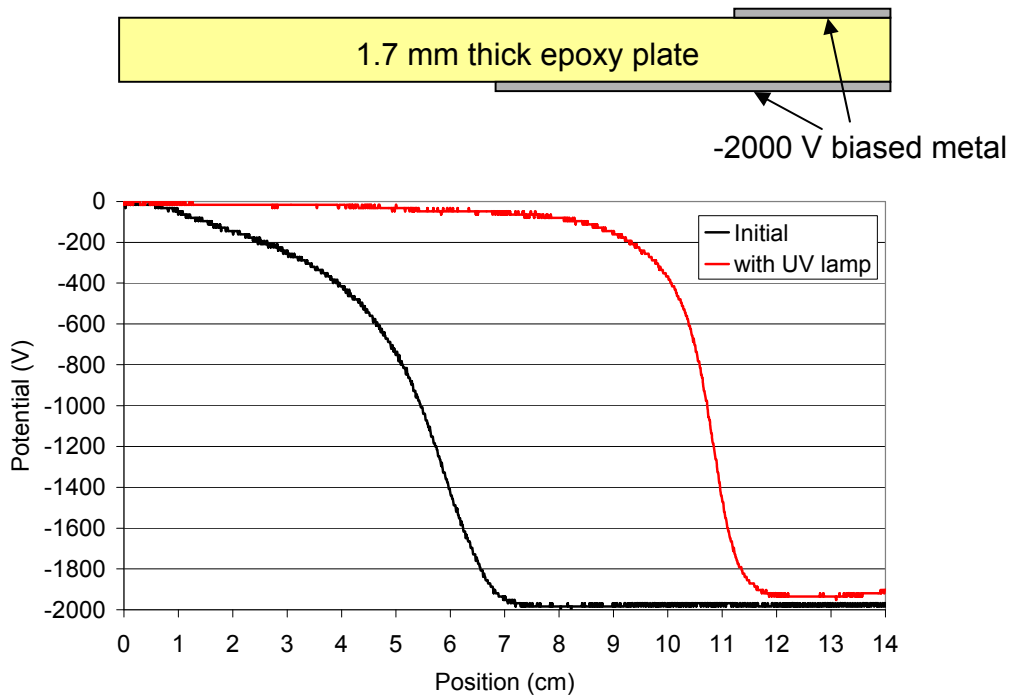


Figure 56 - Typical IPG situation obtained with the UV method

8.2.3. ESD Test Procedure

The ESD test procedure consists in increasing the bias voltage V_{bias} till an ESD occurs. That will directly give access to the voltage threshold. If no ESD occurs and if the measured potential profile remains constant and near to zero volts, then the negative bias voltage is increased by 100 volts negative. This procedure is repeated a certain number of times in order to obtain sufficient results on each configuration. For each ESD, the video camera picture is analysed in order to determine if this is a correct ESD, *i.e.* produced on the triple point and at a different location from the previous ones.

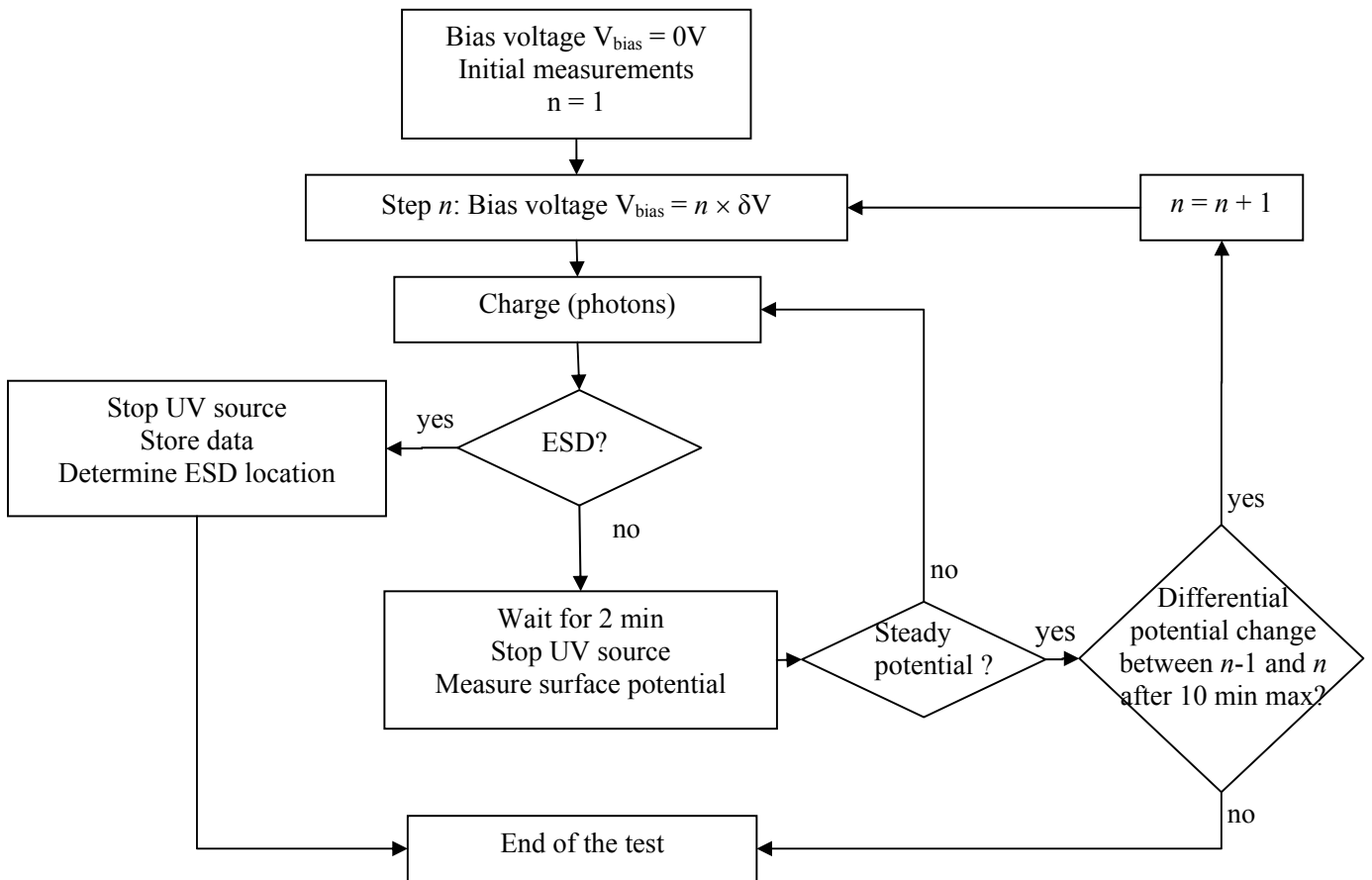


Figure 57 – ESD test procedure diagram

Remark: the loop "Differential potential change between $n-1$ and n after 10 min max?" aimed at stopping the experiments in case of a relatively conductive dielectric, in which case the differential potential could possibly reach a maximum before any ESD occurred. However, during the present experiments, this was never the case and this question was always answered by *yes*.

8.3. ESD Tests Results

The results obtained with the six configurations are presented in this paragraph.

8.3.1. Nominal Case

8.3.1.1. Results

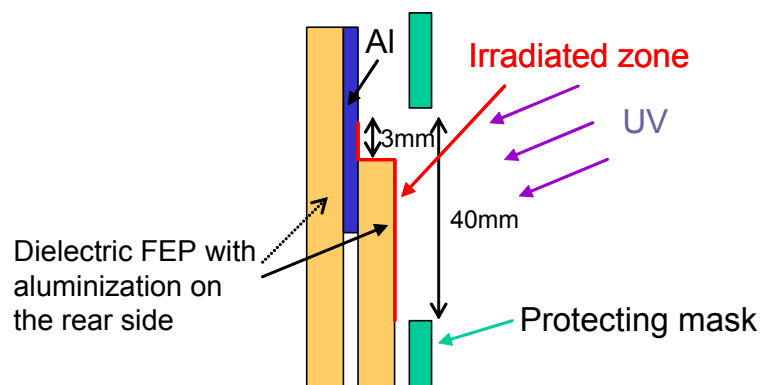


Figure 58 - Design principle of the nominal configuration TP

Remark: at the time of the experiments performed with Teflon, the technique used to measure the photo emission current density was not yet available. Anyway, Teflon is so resistive that the photo charging current is orders of magnitude greater than the conductivity current. Experiments of Teflon relaxation highlighted characteristic relaxation time of hours while charging characteristic time is about seconds or maximum tens of seconds. The Teflon is generally considered as perfect insulator. In other words, the triple point potential map is only influenced by the barriers of potential (globally due to the tank walls, locally due to the biased metal of the TP).

Eight ESDs have been obtained in the nominal configuration. They were obtained on different locations at the triple point edge. An example of the ESD light emission is represented in Figure 59. The ESD threshold is between 700 to 900 volts negative, *cf.* Figure 60.

The Blow-off peak current is about 1 to 2.5 A and its duration is 10 to 15 μ s, see Figure 61 and Figure 62.

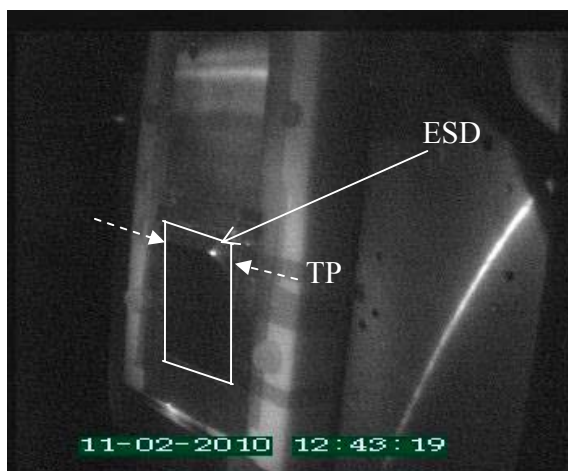


Figure 59 - Picture of an ESD in the nominal configuration. The white lines represent the irradiated zone of the sample; the dashed arrows represent the triple point location

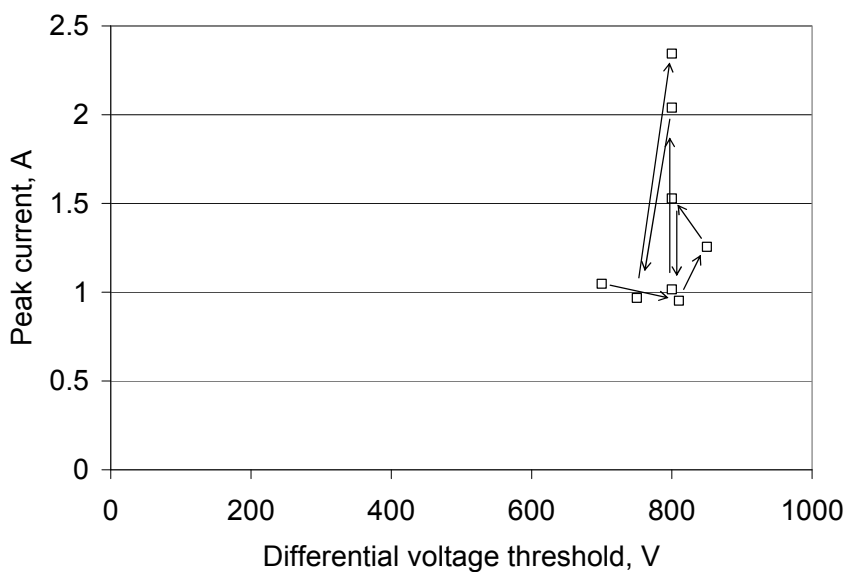


Figure 60 - Peak current vs. ESD voltage threshold in the nominal configuration. The arrows refer to the order of appearance of ESDs

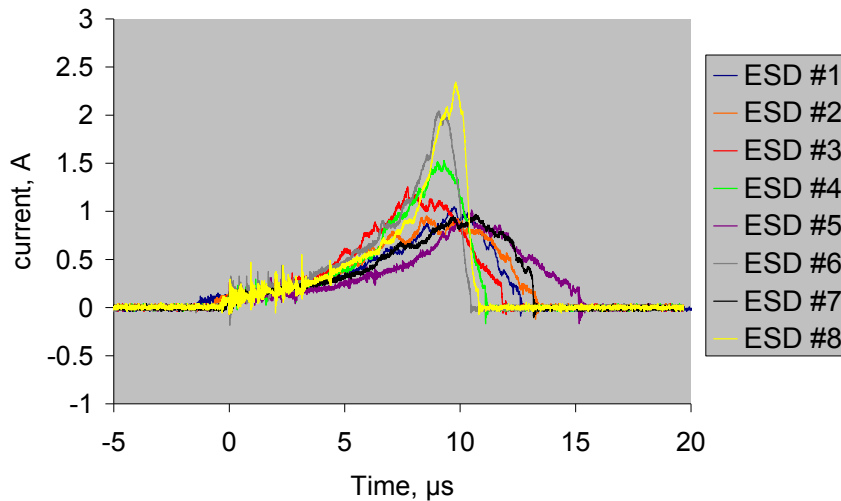


Figure 61 - Blow-off current of the ESDs obtained in the nominal configuration

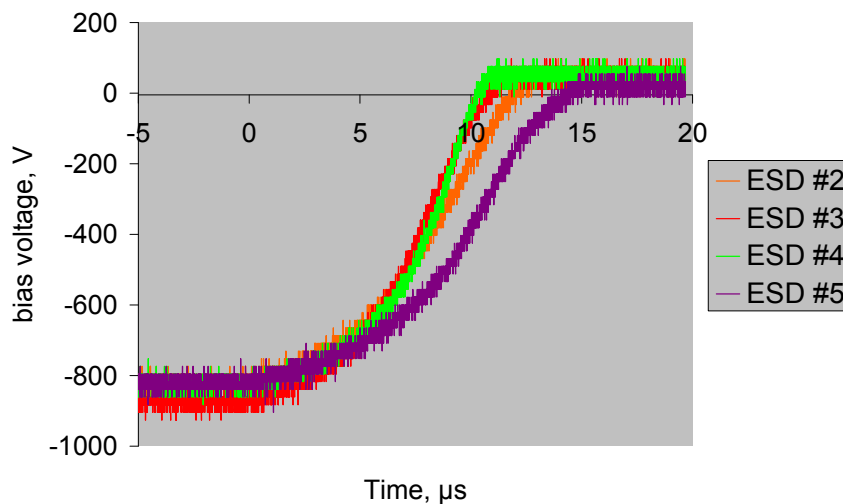


Figure 62 - Bias voltage of the ESDs obtained in the nominal configuration (some ESD bias voltage measurements are missing)

8.3.1.2. Lessons to be learned

The ESD threshold obtained here is representative of the differential charging that can occur on GEO spacecraft. By the past, we have exhaustively tested the electron and plasma method to create the IPG. The ESD threshold on solar cell assemblies is known to be approximately 1000 V with the electron and plasma setup (a bit more for the electron setup). It may of course depend on the solar cell used (and here the sample

is not a solar cell assembly!) but the order of magnitude is good. The experiments performed in this activity are satisfactory in term of ESD triggering and ESD threshold compared to the past experience in the domain. Moreover, it is more realistic of flight conditions (at least in comparison to the plasma setup). Finally, it is easier to determine the ESD threshold than with the electron setup. The only drawback is that it can only be used by now in CEDRE with small samples (no more than 10 cm in diameter).

8.3.2. Photon Incidence Angle

8.3.2.1. Results

Qualitatively, the ESD currents have the same shape as the ESDs obtained in the 1st configuration. The peak current and the duration are about 2.5 amps and 10 μ s respectively. In this configuration however, the ESD threshold is about -1300V, which is significantly higher than the nominal configuration with a photon incidence angle α of +15°.

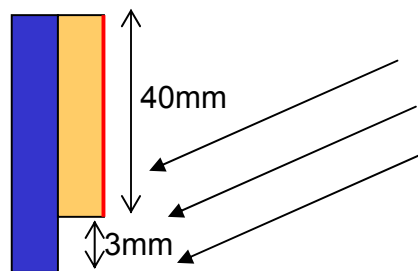


Figure 63 - Design principle of the photon incidence angle configuration

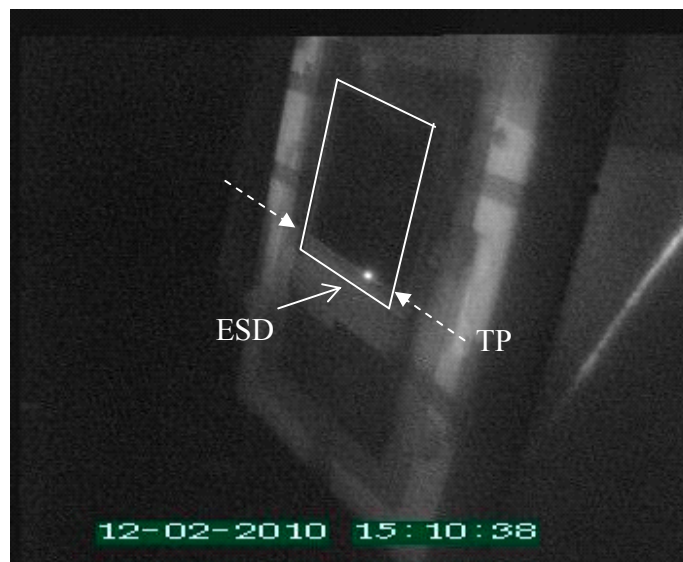


Figure 64 - Picture of an ESD in the photon incidence angle configuration

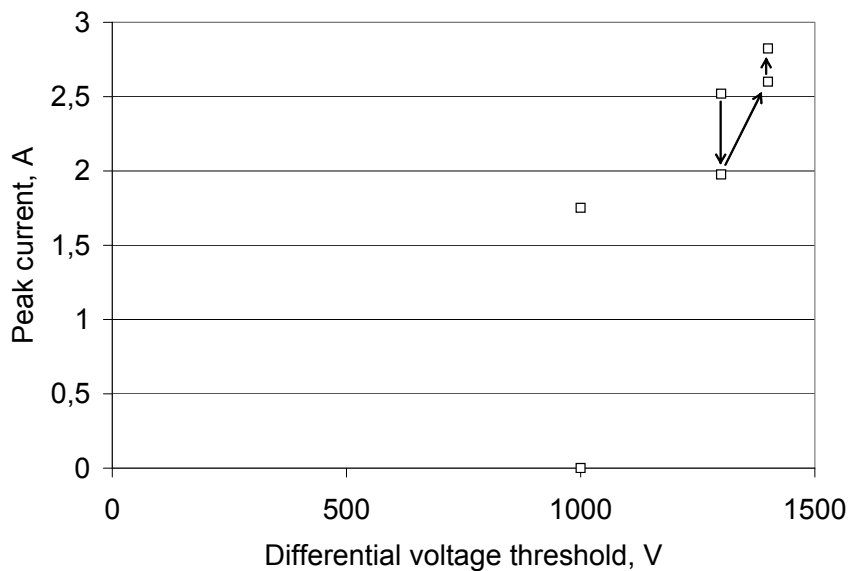


Figure 65 - Peak current vs. ESD voltage threshold in the photon incidence angle configuration. The two events at 1000 V could not be detected by the video camera. As a result, we do not consider them as ESD events.

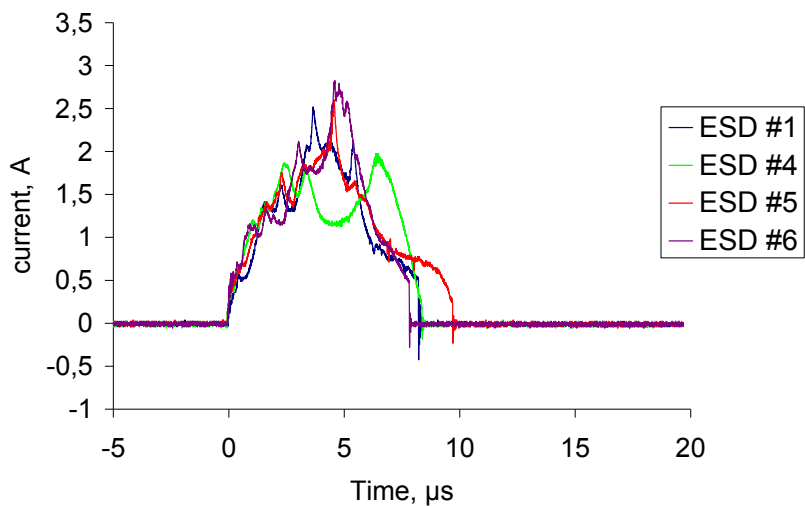


Figure 66 - Blow-off current of the ESDs obtained in the photon incidence angle configuration

8.3.2.2. *Lessons to be learned*

The results clearly show that the triple point charging configuration is very important at the length scale of the dielectric thickness (100 μm). It is demonstrated that the way the charging occurs on the perpendicular configuration is fundamental. When photons do not collide with the dielectric edge, it is much more difficult to build the differential voltage close to the metal. At a fixed bias voltage, the resulting electric field is then lower than in the nominal configuration. **It leads to a lower ESD risk.** In flight, some ESDs may possibly occur or not due to the inclination of the dielectric material edges with respect to the sun direction.

Remark: It was unfortunately not possible to measure the surface potential at the dielectric edge scale, the potential probe being located approximately 6 mm from the surface (it was not possible to do better because the probe shall stay at floating potential and so on it shall never touch the sample). The resulting potential probe is a mean value of the surrounding potentials...

8.3.3. *Metal vs. Dielectric Length*

8.3.3.1. *Results*

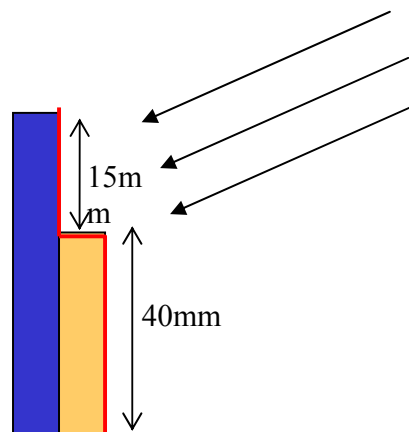


Figure 67 - Design principle of the Metal vs. Dielectric length configuration

In this configuration, the first two ESD have been obtained for a differential voltage of 1600 V and the third one for 1900 V. It was not possible to increase the bias voltage anymore because arcing occurred in undesired locations of the setup!

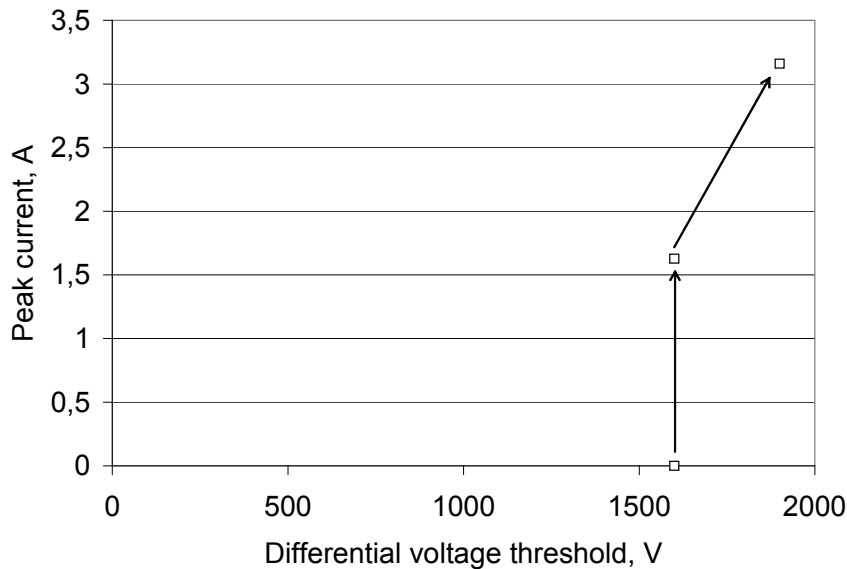


Figure 68 - Peak current vs. ESD voltage threshold in the Metal vs. Dielectric length configuration. The first event was detected by the video camera but not by the oscilloscope.

8.3.3.2. Lessons to be learned

The results clearly show that it is much more difficult to trigger an ESD with a long biased metal. This is due to the local barrier of potential produced by the metallic material, see Figure 69. When the metallic gap gets larger, it influences the potential map on larger length scale. The iso potential lines tend to extend far from the triple point itself, leading to a lower electric field and so on to a higher value of the global barrier of potential (equivalent to a higher bias voltage in our setup) necessary to initiate ESDs. In the extreme case of a small dielectric surrounded by a large negatively biased metallic plate, ESDs could eventually be impossible because the local barrier of potential may prevent photo electrons to escape from the dielectric surface. The net current would be null and the dielectric would stay at the same potential as the metal.

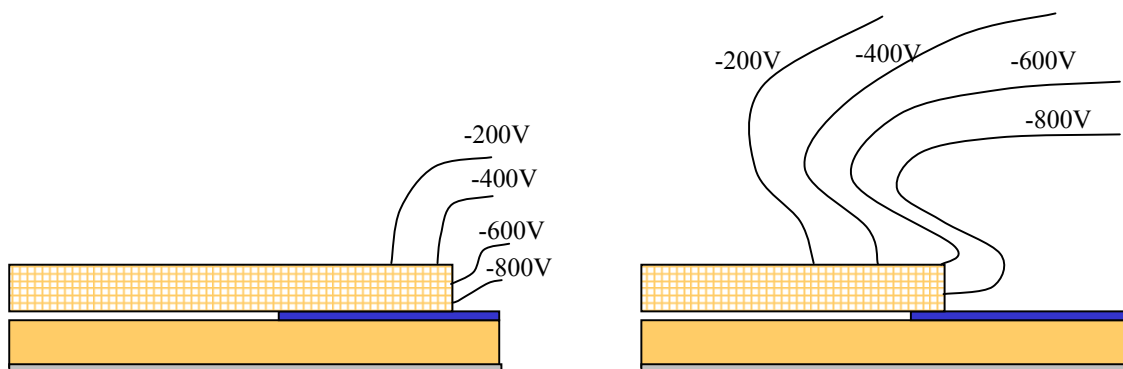


Figure 69 – Schematics of typical iso potential lines in two configurations of metal length. On the right side, the local barrier of potential due to the long metallic gap provokes a high local recollection of the photo electrons. The potential gradient at the vicinity of the triple point is lower than on the left side.

8.3.4. Dielectric Material

In this configuration, the CMX-AR cover glass is used instead of Teflon tape. In this case, the photo emission current has been measured to 2 to 4 nA/cm² on the cover glass.

8.3.4.1. Results

The ESD threshold is between 1800 V and 2100 V. The peak current is about 3 to 5 A and the duration about 7 μs. The peak current is higher because the energy dissipated ($1/2 \cdot C_{sat} V_{bias}^2$) is higher.

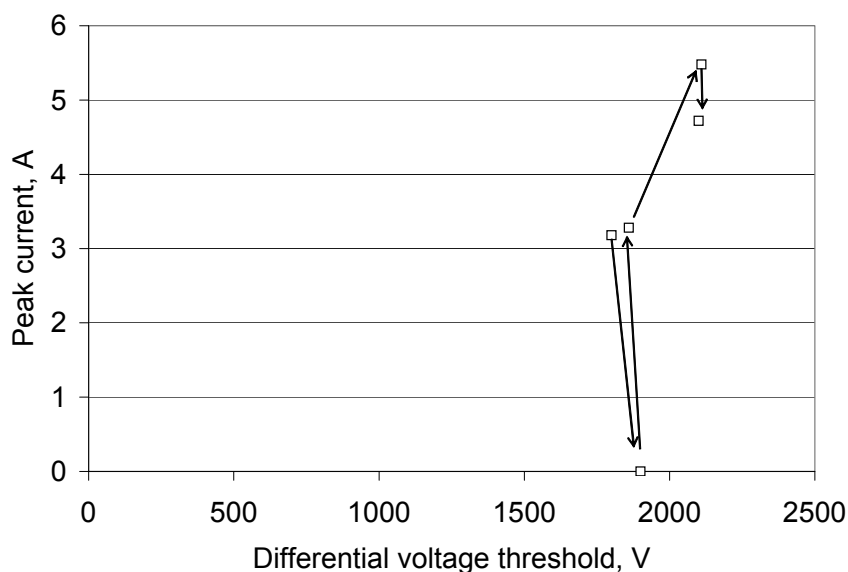


Figure 70 - Peak current vs. ESD voltage threshold in CMX-AR configuration. The 2nd ESD has been localized with the video camera but the current measurement is missing.

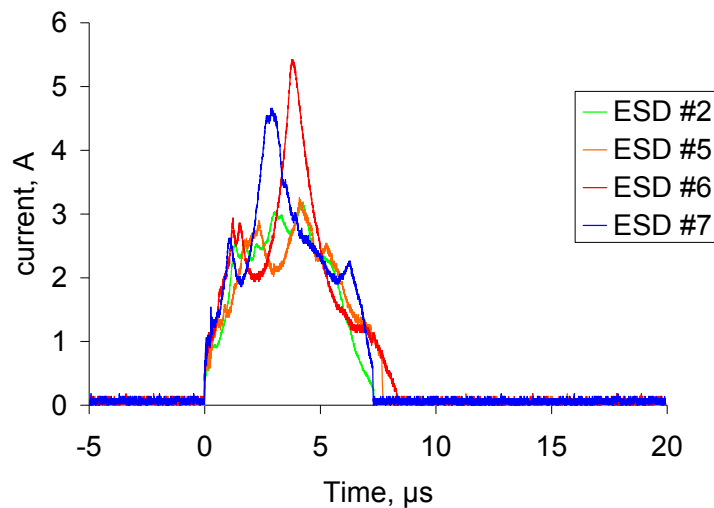


Figure 71 - Blow-off current of the ESDs obtained in the CMX-AR configuration

8.3.4.2. Lessons to be learned

The bulk and surface conductivity of materials are known to limit the differential voltage at macroscopic scale, as *e.g.* at solar panel level. It does of course influence also the charging at triple point. The competition between conductivity and charging is ruled by the conductive and capacitive coupling. The important parameters are: dielectric thickness, shape and conductivity. In this paragraph, it is shown that a 127 μm dielectric CMX-AR with a conductivity of about $10^{-14} \Omega^{-1}\text{m}^{-1}$ still present a risk in term of electrostatic discharge under a photo current of 2 nA/cm^2 approximately. It may of course also depend on the other parameters.

8.3.5. Metal

Sample with gold instead of aluminium is used.

8.3.5.1. Results

The ESD threshold observed here varies significantly from the first to the fifth ESD, passing from 650 V to 1000 V. Then, the following ESD threshold stays relatively constant, around 1100V.

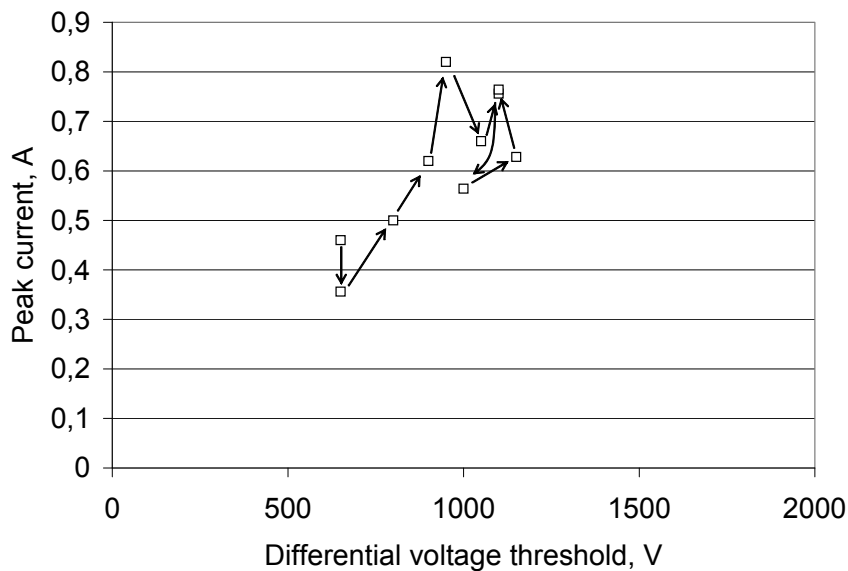


Figure 72 - Peak current vs. ESD voltage threshold in the gold configuration

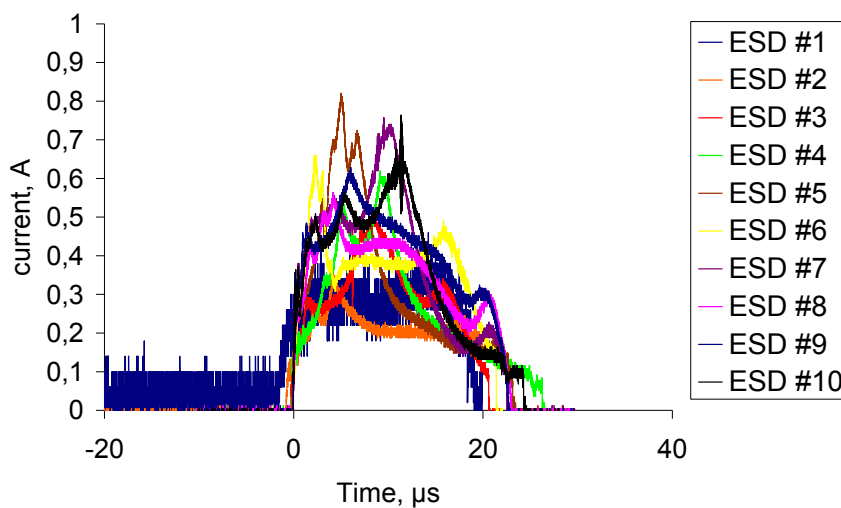


Figure 73 - Blow-off current of the ESDs obtained in the gold configuration

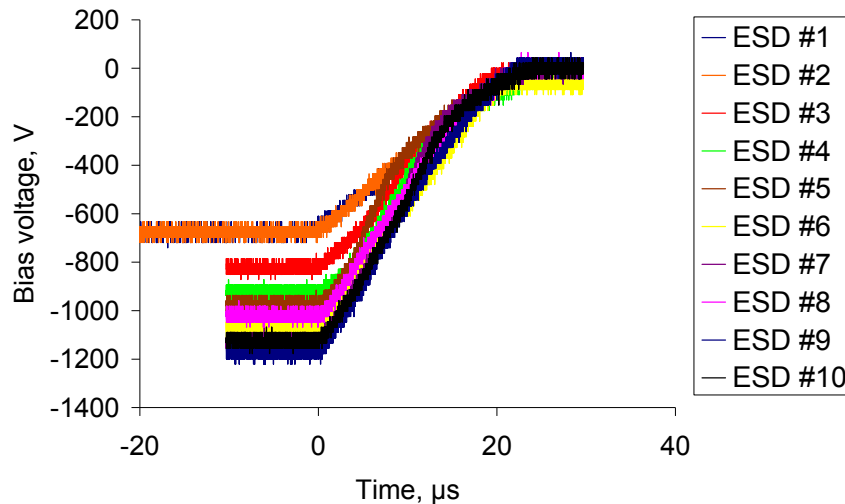


Figure 74 - Bias voltage during ESDs obtained in the gold configuration

8.3.5.2. Lessons to be learned

This case shows that ESD triggering at triple points is a phenomenon not completely understood yet. The fact that the threshold varies that much may be due to different microscopic structures. Once the smallest microscopic irregularities capable to sustain an ESD have burnt, only bigger ones can trig ESDs. As a result, the degree of uncertainty in the threshold determination is not negligible. The error bar is about ± 300 V. Anyway, the metals used here did not seem to lead to very different ESD thresholds.

8.3.6. Co-planar Triple Point

8.3.6.1. Results

In the co-planar configuration, the charging capacitor was 5 nF instead of 10 nF. In this configuration, the first ESD occurred for differential voltages of 1300 V, 1700 V and 1800 V successively. The fourth one, which occurred at 2000V, produced a coupling with the ground. This kind of vacuum arc is known to occur when the applied voltage is high (which is the case here!!). It consists in the creation of an anode spot on a grounded metallic element, in addition to the cathode spot on the triple point. For more details, see [4]. The next 9 ESDs occurred systematically at the same place and with a decreasing differential voltage. These discharges can not be taken into account for the determination of the ESD threshold, which is here between 1300 and 2000 V.

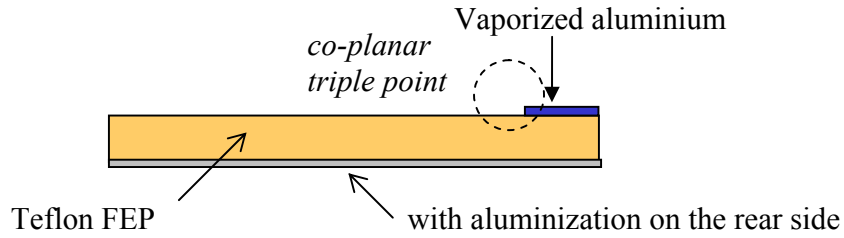


Figure 75 - Design principle of the co-planar configuration

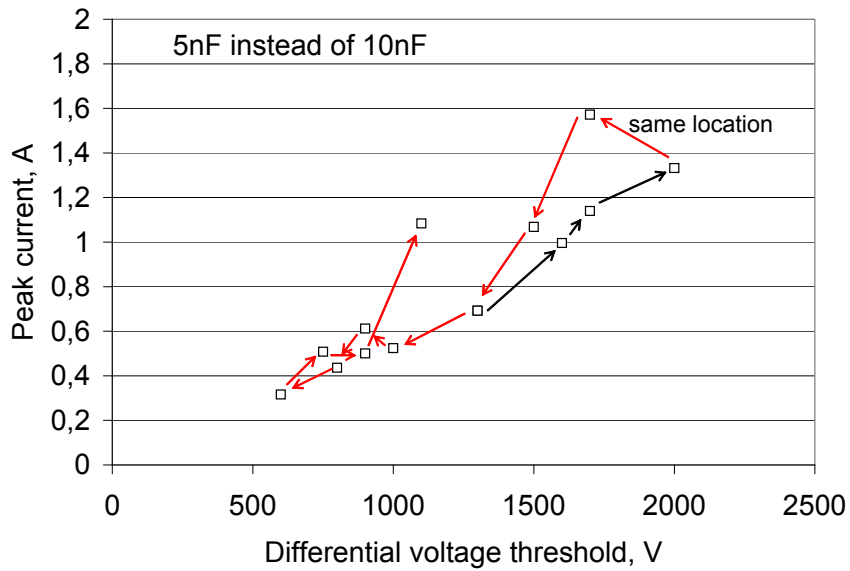


Figure 76 - Peak current vs. ESD voltage threshold in the co-planar configuration

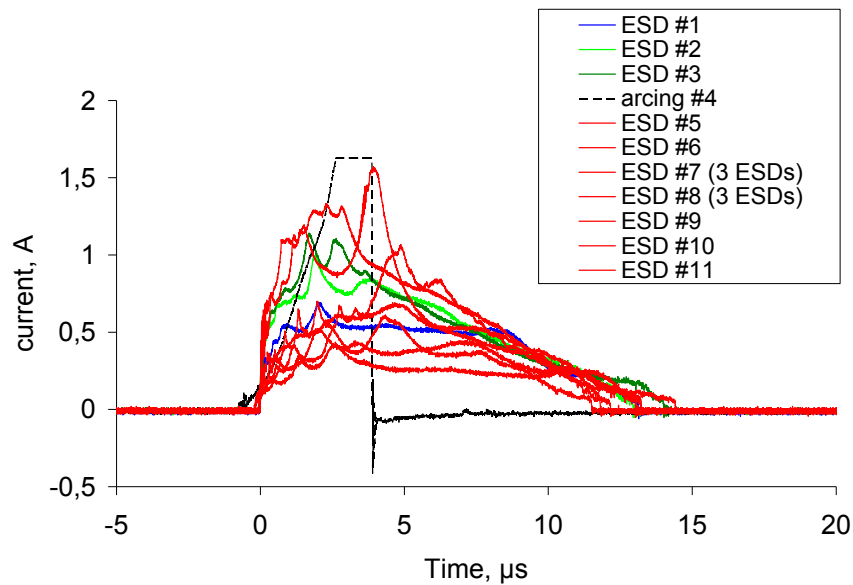


Figure 77 - Blow-off current of the ESDs obtained in the co-planar configuration

8.3.6.2. Lessons to be learnt

The ESD threshold appears to be hardly repetitive, even in the same configuration. There is a relatively high dispersion of the results. From the experience acquired in the "co-planar" configuration, it seems that ESDs are very difficult to trig in this configuration. It is then quite safe with regard to ESD risk.

Remark: During the preliminary tests performed on other co-planar samples (and not reported here in detail for clarity), we saw that the discharges could occur all at the same place. Of course, no reliable results could be extracted from these discharges.

8.4. Test Report Conclusion

The experiments reported in this Test Report constitute a large basis for the validation of the numerical tool. The UV method permits to determine the ESD threshold of each ESD.

A summary of the experimental results is represented in Figure 78.

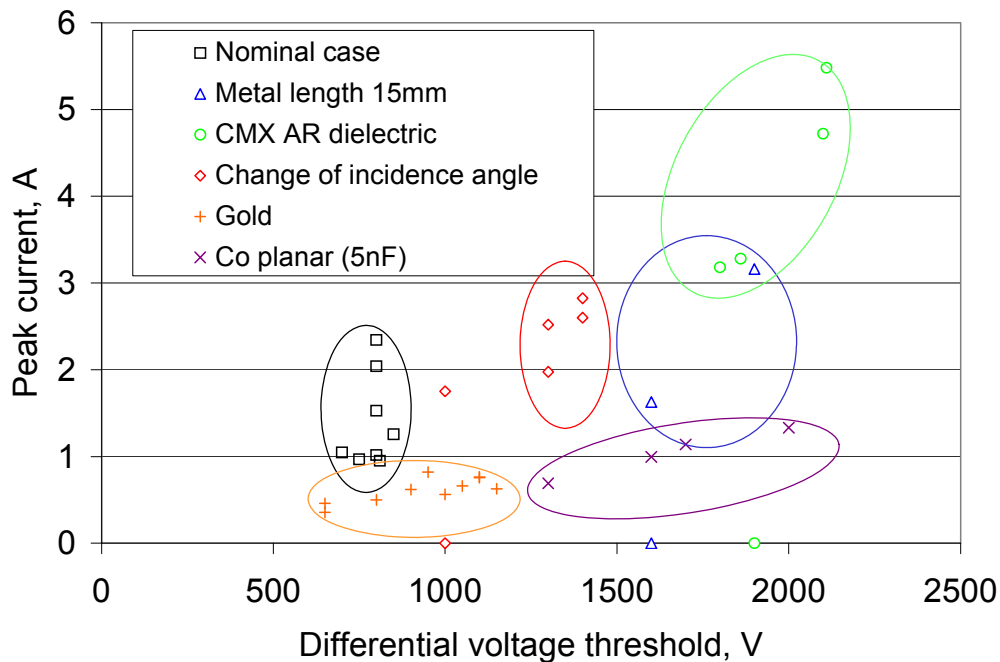


Figure 78 – Summary of the ESD thresholds

Qualitatively, interesting lessons can be learnt. It is definitively more difficult to trig ESDs in the following configurations:

- More conductive dielectric
- Low photon incidence angle (or even more for "negative" incidence angle in the perpendicular case depicted here)
- Longer metallic plate
- Co-planar geometry

Quantitatively, it seems hardly feasible to assess the ESD threshold with a precision better than ± 200 V or 300 V. This is due to the statistical characteristics of ESDs. No ESD is fully reproducible in triple point configurations. The physics of ESDs remain complex and the microscopic scale has a predominant impact (as *e.g.* the amplification factor on each configuration, the possible existence of uncontrollable dielectric thin sheets, neutral desorption ...).

9. SOFTWARE VERIFICATION AND VALIDATION

Sections 9.1 and 9.2 present the main assumptions and algorithms used to verify SPIS-ESD capabilities and to compare with experiments presented in section 8. The detailed architecture was first provided in section 6 and 7. That section aims at presenting the numerical parameters settings adjusted during the testing and verification phase of the code. They reflect the best tuning of the code.

The verification of the software performance is presented in Section 9.3. It consists in verifying the behaviour of the software in term of modelling the multi physics and the multi time and length scale of the ESD onset at triple points on solar arrays. Section 9.4 describes the software validation phase, in which the numerical results are compared to the parametric experimental study [TR].

Finally, a detailed analysis of the results and possible code improvements are proposed in Section 9.5.

9.1. ESD Prediction Tool

This section presents the main assumptions and algorithms used to compare with experiments performed at ONERA in the frame of this study [TR]. A detailed description of the numerical tool was given in [ADD]. Here we focus on presenting the parameter settings adjusted during the verification phase (Section 9.3) and used during the validation phase (Section 9.4). These parameters represent the best tuning of the code and are set as default parameters in the template project provided to users. Paragraph 9.1.1 details the default parameters used at simulation top level, *i.e.* the ESD scenario. Paragraphs 9.1.2 and 9.1.3 present the reference modelling of the inverted potential gradient situation and the so-called nominal geometry extracted from [TR] respectively. Paragraph 9.1.4 is a description of the ESD onset model and of the corresponding parameters used.

9.1.1. SPIS ESD Tool Overview

The SPIS ESD tool aims to assess the ESD threshold as a function of the IPG level. The tool permits to simulate the charging phase from zero differential potential to the IPG stationary situation, the electron avalanche and the ESD triggering. The configuration simulated by SPIS-ESD is represented in Figure 79. The SPIS ESD tool is completely integrated in the standard structure of SPIS. In Figure 80, a general overview of SPIS numerical core is presented. SPIS-ESD keeps the same structure as the standard SPIS version but several modules have been completed or adapted. The concerned parts of the structure are in red in Figure 80.

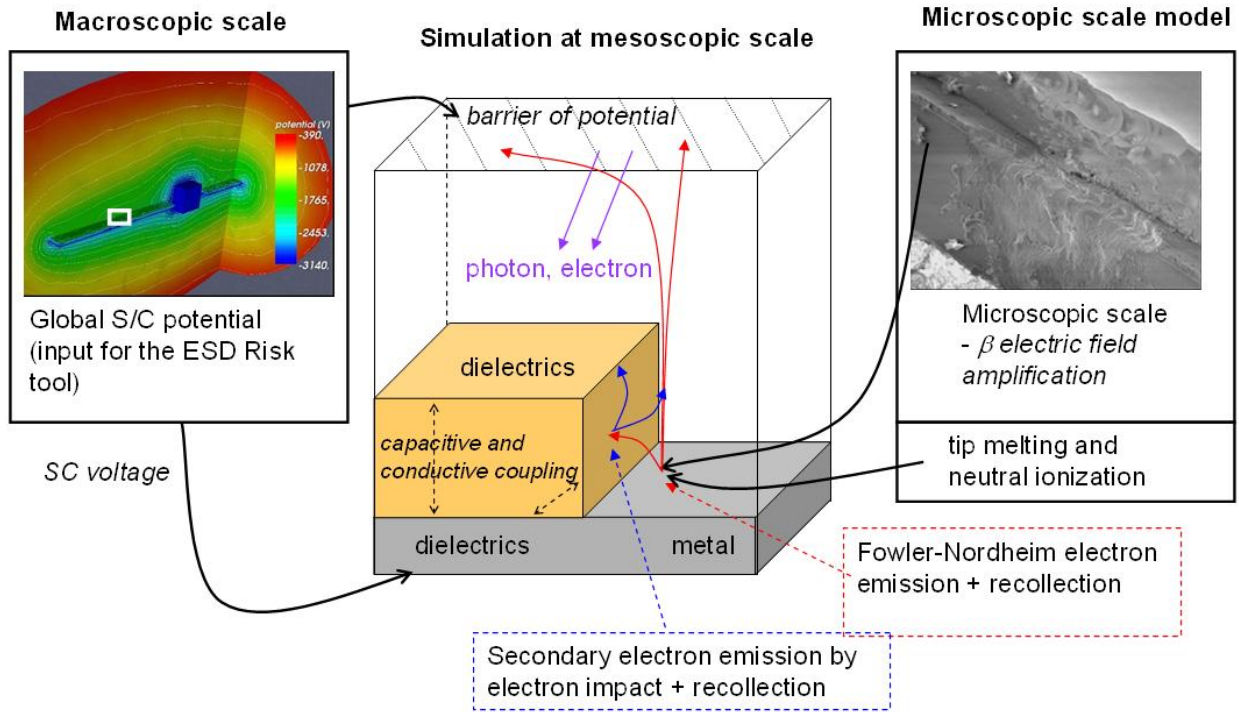


Figure 79 - SPIS-ESD model of the IPG situation at triple point in GEO. The triple point can be perpendicular, angular or co-planar

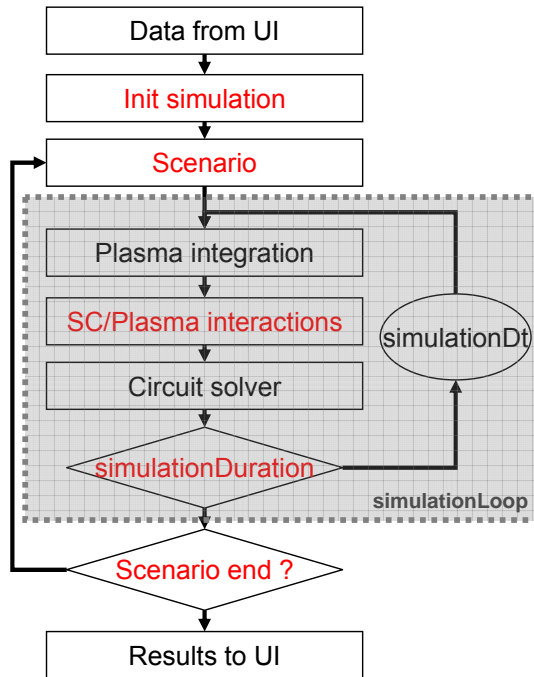


Figure 80 - General overview of SPIS-NUM

For defined materials, mesoscopic geometry and environment conditions, the ESD triggering probability depends on the potential barrier applied and on the surface state of the emissive zone (i.e. the tip geometry on the emission site). Consequently, the ESD tool scenario is organized in two imbricate loops concerning the potential barrier value and the beta value (field enhancement factor due to the tip geometry). This scenario is schematically represented in the Figure 81 in which the two loops controlling the standard simulation loops are represented.

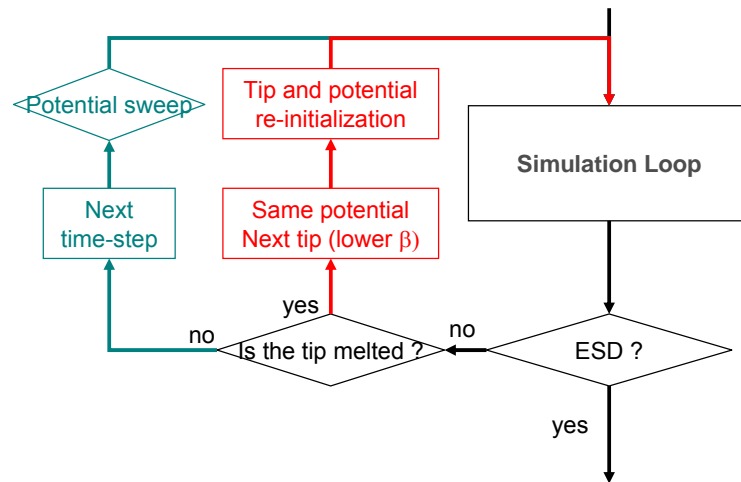


Figure 81 – Schema of the ESD risk scenario

The end of each loop is based on the detection of the tip fusion or ESD triggering. Both conditions depend on the assumption done for the tip model discussed in the next section.

The results presented in this report are done with the following configuration of the ESD prediction scenario:

Table 8 - Global parameters configuration concerning the SPIS-ESD scenario

Global parameter	Comment	Type	Unit	Value
scenario	Scenario class name	string	None	ESDRiskScenario
scenarioParameter1	Number of barrier potential steps	int	[-]	10
scenarioParameter2	Initial barrier potential	float	[V]	500
scenarioParameter3	Final barrier potential	float	[V]	2000
scenarioParameter4	Number of steps in beta (field enhancement factor)	int	[-]	10
scenarioParameter5	Initial beta (max field enhancement factor)	float	[-]	800
scenarioParameter6	Final beta (min field enhancement factor)	float	[-]	300
scenarioParameter7	Tip length	float	[m]	1.0E-6
scenarioParameter8	First step maximum duration	float	[s]	60
scenarioParameter9	Following step maximum duration	float	[s]	40
scenarioParameter10	Scenario end switch: - if 0, scenario continue after the first ESD - if 1, scenario end at the first ESD	int	[-]	1

9.1.2. IPG Situation

The IPG situation is simulated by fixing the potential difference between the potential barrier boundary (Boundary Up) and the metallic parts (Metal + Emission site) of the geometry (see Figure 82). Consequently, the boundary conditions for these physical surfaces are Dirichlet conditions for the potential. The metallic parts are set to a constant zero volts potential while the potential barrier is set by the ESD scenario.

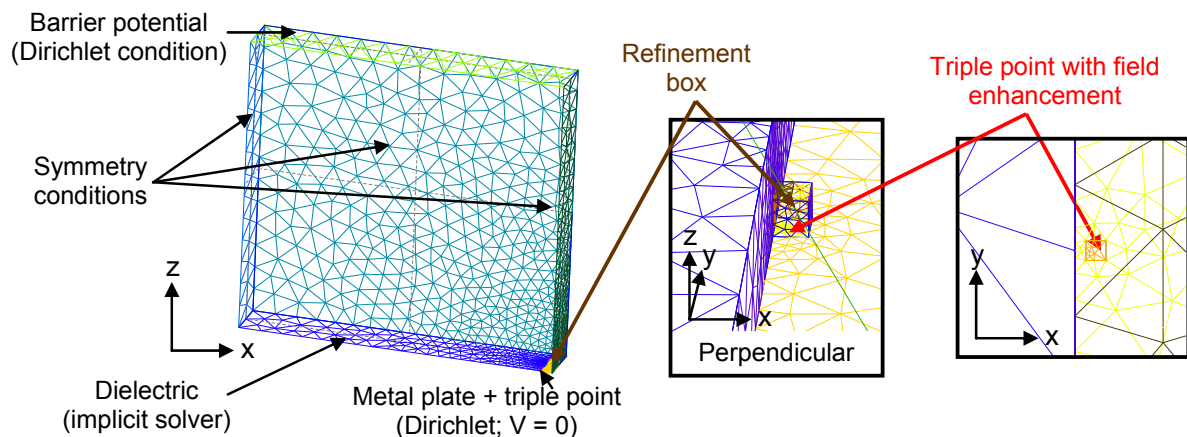


Figure 82 – Geometrical mock-up of the IPG situation

The dielectric surfaces (Dielectric Up and Dielectric Front) have also Dirichlet conditions for the potential. At the beginning of the simulation, the potential on this surface is set equal to the metal potential, i.e. no differential potential. Then, during the charging phase and the ESD triggering phase, the SPIS circuit solver solves the local potential evolution on these surfaces. The potential on the dielectrics evolves while the local net current on the dielectric, i.e. the difference between current emission (photoelectrons and secondary emission), collection (from environment and recollection) and conduction (at the surfaces or in the volume of the dielectric), is non null.

The last boundary condition concerns the four lateral boundaries. For these boundaries, a condition of symmetry is assumed: the flux of particles is forced to zero (by reflecting the particles) and the electric field is set to zero in the normal direction. In particular, this boundary condition permits to get a stationary situation during the charging phase when the dielectric potential reaches the barrier of potential fixed by users (i.e. equality between the electron emission and recollection when differential voltage equal barrier potential).

Table 9 summarizes the configuration of the SPIS-UI group editor.

Table 9 - Group editor configuration

Physical Surf. or vol.	Name	Material	ElecNode	Plasma
69	DielectricUP	Teflon FEP (BOL)	2	Spacecraft, Default
70	DielectricFront	Teflon FEP (BOL)	2	Spacecraft, Default
71	MetalSurface	AluminiumForESD	0	Spacecraft, Default
72	Tip	AluminiumForESD	1	Spacecraft, source 1 on

Physical Surf. or vol.	Name	Material	ElecNode	Plasma
73	Lateral	None	None	Boundary, symmetry
74	Up	None	None	Boundary, DiriPot = 0 V
75	Plasma (Volume)	None	None	Plasma Model In Volume, Default

For the results presented in this report, the differential potential reached during the charging phase is obtained by photoemission only. Photoemission is activated for all dielectric and metal surfaces. The corresponding parameters used for the simulation are represented in Table 10.

Table 10 - Global parameters configuration for the photoemission

Global parameter	Comment	Type	Unit	Value
photoEmission	If 3: turn on with photoelectron dynamic modelling	int	[-]	3
photoElectronDensification	Densification coefficient	float	[-]	5.0
photoElectronTemperature	Photoelectrons temperature	float	[eV]	1.0
photoElectronTrajFlag	Photoelectron trajectories?	int	[-]	1

The Fowler Nordheim emission of electrons is also activated on a small surface called the "Emission site" (see Figure 82). Secondary emission from the Fowler-Nordheim is activated for all the dielectric and metal surfaces for the ESD triggering model (see section 9.1.4).

9.1.3. Nominal Case

The strategy of the experimental and numerical studies consisted in defining a nominal case. Around this nominal case, we investigated in five directions by changing the following parameters: metal length, photon incidence angle, dielectric type, metal type and geometry.

The nominal geometry used during experiments was a perpendicular triple point obtained by vaporizing aluminium on a Teflon tape, which was used as a substrate. The perpendicular triple point was then obtained by applying a dielectric layer (Teflon in the nominal case but CMX-AR is also used in this study) on the metallization (see Figure 83). More details were given in [TR].

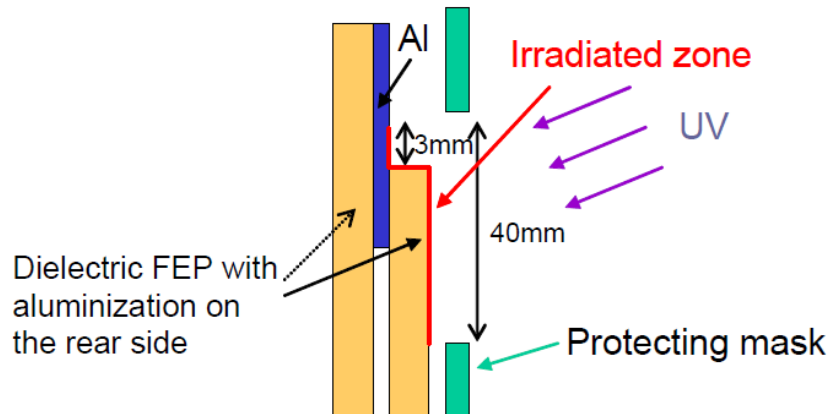


Figure 83 - IPG design principle of the nominal triple point configuration used during experiments

As can be seen in Figure 83, the part of the sample submitted to the charging environment, i.e. UV photons, was 40 mm long. The metallization and dielectrics were 3 mm and 37 mm long respectively. The dielectric was irradiated by the UV lamp with an incidence angle of 15° compared to the dielectric normal. As a consequence the dielectric edge close to the metal was irradiated with an incidence angle of 75° with respect to the local dielectric normal.

Following this geometry, the modifiable parameters in the mockup file of the ESD prediction tool are set as follow in Table 11 and in Table 12.

Table 11 - Modifiable global parameters configuration for UV incidence angle

Global parameter	Comment	Type	Unit	Value
sunX	X – component of the sun direction	float	[-]	0.21
sunY	Y – component of the sun direction	float	[-]	0.0
sunZ	Z – component of the sun direction	float	[-]	0.98

Table 12 - User modifiable parameters in the geometrical mockup file

Full name	Variable name	Unit	Value
Dielectric thickness	LdielZ	m	10^{-4}
Dielectric length	LdielX	m	3.85×10^{-2}
Dielectric angle	alpha	rad	$\pi/2$
External box X dimension	LboxX	m	4×10^{-2}
External box Y dimension	LboxY	m	0.6×10^{-2}
External box Z dimension	LboxZ	m	4×10^{-2}

9.1.4. ESD Triggering Model

This paragraph summarizes the ESD onset model, which was detailed in [ADD]. It also presents the relevant corresponding parameters.

9.1.4.1. Electron avalanche

The very beginning of the discharge, i.e. the initial electron avalanche that produces cathode heating, melting and vaporization, is of great interest in the present study. Since carrier generation is a key factor in discharges, the important phenomena are emission mechanisms near the triple point. The mechanism of emission from this area consists on field effect emission (FEE). The electric field can then extract electrons (by tunnel effect) from the conductor with a current density JFN given by the Fowler-Nordheim equation:

$$J_{FN} \sim E^2 \exp\left(-B \phi_w^{3/2} / E\right) \quad (38)$$

where E is the electric field normal to the surface, ϕ_w the metal work function and B a constant.

At the triple point vicinity, the macroscopic electric field is typically 10^6 to 10^7 V/m, which is not sufficient to produce electron extraction by tunneling effect. However, at microscopic scales, geometrical irregularities significantly increase the electric field strength. Two types of field enhancement mechanisms can be found in the literature. The first one comes from the roughness of the conductor on which surface microstructures such as a micro tips [RD1] or whiskers can affect the electric field. The second one is field enhancement due to a micro dielectric material inclusion on the conductor [30], as e.g. dust. In this study, only the field enhancement due to the tip geometry mechanism is investigated. Contrarily to Girard [RD1] who modelled the tip scale, in the present study the tip is modelled by a field enhancement factor applied on a small area (micrometer scale) near the triple point zone.

Williams et al. [40] investigated the effect of the surface irregularities (roughness) on the breakdown threshold in vacuum between two planar electrodes. Like in ESDs triggering, these discharges were initiated by Fowler-Nordheim emission enhanced by the tip geometry. These experiments permitted to extract two characteristics of tip geometries on cathode surface: field enhancement factor β and emitter surface. They also showed the conditioning process that leads to the destruction of the thinner tip (with higher β) as a function of the number of discharges in the same surfaces. From these data, we deduce the range of possible tip enhancement factor from 800 to 300 and the corresponding surfaces area of emission.

The so-emitted electrons are emitted with energy close to the material work function, which is close to 4.5 eV for the majority of conductors. Their trajectories are then influenced by local potentials. They are accelerated towards the positive dielectric elements to an energy of several hundreds of volts, which is in the typical range for efficient secondary electron emission, i.e. with a yield greater than one. The produced electrons are evacuated to the dielectric-vacuum frontier while keeping a positive charge on the dielectric surface. That immediately amplifies the electric field and so on the field effect emission. The loop is closed and an electron avalanche is triggered.

Hastings et al. also demonstrated that the combination of field emission and secondary emission at triple point geometry can provide electron avalanche at the earlier stages of the discharge process [29]. The time scale for the development of the electron avalanche is typically some nanoseconds.

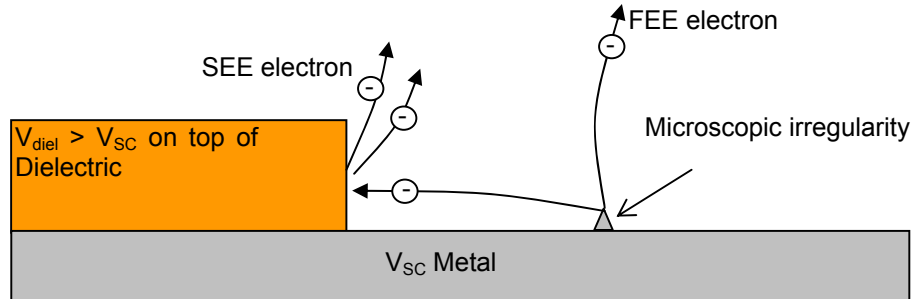


Figure 84 - Mechanisms of electron avalanche from surface micro irregularities

The parameters used during this study are presented in Table 13, Table 14 and Table 15.

Table 13 - Global parameters configuration for the Fowler-Nordheim emission

Global parameter	Comment	Type	Unit	Value
sourceFlag1	Define activation and densification factor of the artificial source1	float	[-]	0.05
sourceType1	Class name of the source1	string	[-]	FowlerNordheimWithTipAreaSurfDistrib
sourceParticleType1	Name of the particle emitted	string	[-]	electron
sourceTrajFlag1	FN electrons trajectories?	int	[-]	1
sourceDt1	Maximum integration time step for the FN electrons	float	[s]	2.5E-11
sourceDuration1	Maximum integration duration for the FN electrons	float	[s]	1.0E-10
sourceSpeedUp1	Not used	float	[-]	1.0

Table 14 - Global parameters configuration for the secondary emission by electrons

Global parameter	Comment	Type	Unit	Value
electronSecondaryEmission	448 if secondaries from source1 (FN) only 455 if source 1 +elecPop1 511 if source 1 +elecPop1 + elecPop2	int	[-]	448
electronSecondaryDensification	Densification coefficient	float	[-]	0.05
secondaryTemperature	Electron secondary temperature	float	[eV]	2.0
electronSecondaryTrajFlag	Photoelectron trajectories?	int	[-]	1

Table 15 - Time integration configuration for all the secondary electrons

Global parameter	Comment	Type	Unit	Value
secondaryDt	Maximum integration time step for all the secondary electrons	float	[s]	2.5E-10
secondaryDuration	Maximum integration duration for all the secondary electrons	float	[s]	1.0E-9
secondarySpeedUp	For ESD, Duration are used instead of speedUp	float	[-]	1.0

9.1.4.2. Tip model

The tip model aims to compute the interaction between the Fowler-Nordheim current and the tip evolution. It includes a thermal model of the tip, the tip geometry evolution as a function of temperature (mass loss is responsible of a decrease in the tip length) and the neutral density evolution in volume that produces ESD triggering through ionization process.

As in Rossetti model [41], the tip is represented by a cylinder (see Figure 85). The dimension of this cylinder is deduced from the experimental data of Williams [40]. The range considered for the field enhancement factor β correspond to a 1 μm long tip with a radius ranging from 1 to 10 nm. Zero or one dimensional models of tip geometry evolution during field-effect emission were proposed in the literature: field enhancement calculation [40] and the thermal behaviour [41]. In the ESD prediction tool, we choose to represent the tip by a cylinder.

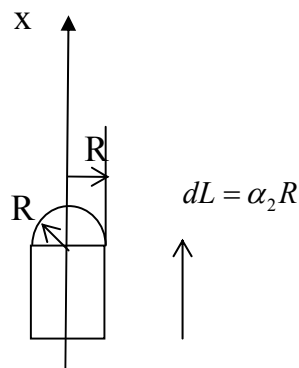


Figure 85 - tip geometry

For a cylinder, the field enhancement factor is defined by the ratio of the tip length on the tip radius. As it was shown in [40], it can be considered that the tip length is practically the same for two different tips on the surface but the tip radius could be very different from one to another tip on the surface. Nevertheless, the tip radius distribution on the surface is *a priori* unknown. It can however be deduced from the enhancement factor and the surface area of emitters measured for different material surface states.

In this model, the Rossetti model is simplified in a zero-dimensional calculation (integration over 10% of the tip length shows very good agreement with 1D results, see [ADD]). This model is used to estimate the temperature of the tip as a function of the current of electrons emitted by the FN process. The model is based on a power balance equation (39) on a part of the tip. It takes into account the joule heating of the FN

current, the conduction in volume, the electron extraction (loss or gain depending on electric field) and the atom evaporation.

$$\rho C_p \frac{\partial T}{\partial t} (\alpha_3 R^3) = P - \alpha_4 \kappa \frac{T - T_0}{R} R^2 - \frac{dm}{dt} \frac{L_{vap}}{N_{avogadro} M_a} - \alpha_9 \frac{I}{e} \varepsilon^*$$

$$\alpha_3 \approx \pi \times \alpha_2 \approx \pi \times 10 \quad (39)$$

$$\alpha_4 \approx \pi / \alpha_2 \approx \pi / 10$$

$$\alpha_9 = 0$$

where the α_i parameters come from the cylindrical geometry of the tip, ρ is the tip mass density, C_p the specific heat, P the joule heating power, κ the thermal conductivity, T_0 the metal temperature, dm/dt the mass loss rate, L_{vap} the vaporization energy, $N_{avogadro}$ the Avogadro number, M_a the mass of the metal atoms, I the FN current and ε^* the energy loss or gain by extracted FN electrons.

This model permits to calculate the tip temperature at each time step and so on to calculate the evaporation flux from the tip, the neutral density in volume and the mass lost by the tip. Because of its vaporization, the tip length decreases. The tip volume variation can be written as:

$$\rho \frac{dV}{dt} = \frac{\rho M_a}{\sqrt{2\pi M_a k_b T}} A_{evap} \quad (40)$$

From equation (40), the tip length L variation can be deduced by considering a conservation of the tip radius R . Finally, the electric field enhancement factor decreases as L :

$$\beta = \frac{L}{R} \quad (41)$$

Finally, the ESD triggering probability is deduced from the quantity of evaporated neutrals from equation (40). The neutral density profile is computed as a function of the distance r from the tip. A $1/r^2$ profile is assumed for the neutral density (flux conservation and isotropic in three dimensions). The ionization probability is estimated using the relation:

$$Proba = \int_0^R n(r) \sigma_{eff.ion} dr \quad (42)$$

with $\sigma_{eff.ion}$ the effective cross section of ionization.

When this probability is higher than one, volume ionization starts which in turn provides the medium with new charge carriers that heat the cathode. In the case of *Proba* greater than one, the SPIS ESD tool considers then that an ESD is triggered.

Table 16 - Tip recession configuration in SPIS UI

Global parameter	Comment	Type	Unit	Value
interactorFlag1	Interactor1 on	float	[-]	1.0
interactorType1	Interactor1 class name	string	[-]	TipRecession
interactorPopSource1	Name of the source that interactor affect	string	[-]	Source1

The thermal properties used by the tip recession interactor are defined in section 9.2 in addition to the standard SPIS material properties.

9.2. ESD Materials Database (xml SPIS format)

The material properties used in this Verification and Validation section are listed and described in this paragraph.

9.2.1. Index Names in the xml File

The values designed by <Property> are the basic 19th NASCAP properties. These properties are identified by an index number (see Table 17).

Table 17 - 19 NASCAP properties in the xml SPIS file

Index	Name	Comment	type	Unit
0	RDC	Relative dielectric constant	float	[-]
1	DTM	Dielectric material thickness	float	[m]
2	BUC	Bulk conductivity, must be set negative if a conductor (in place of infinite for a perfect conductor)	float	[ohm-1.m-1]
3	ATN	Atomic number	float	[-]
4	MSEY	Maximum secondary electron emission (SEE) yield for electron impact	float	[-]
5	PEE	Primary electron energy that produces maximum SEE yield	float	[keV]
6	RPN1	Range parameter r1 in the range expression $r1 (E/E0)^{n1} + r2 (E/E0)^{n2}$, with $E0 = 1$ keV (or equivalently with no $E0$ coefficient and E expressed in keV)	float	[Angstroms]
7	RPR1	Range parameter n1	float	[-]
8	RPN2	Range parameter r2	float	[Angstroms]
9	RPR2	Range parameter n2	float	[-]
10	SEY	Secondary electron yield due to impact of 1 keV protons	float	[-]
11	IPE	Incident proton energy that produces maximum secondary electron yield	float	[keV]
12	PEY	Photoelectron current for normally incident sunlight	float	[A/m2 at 1 AU]
13	SRE	Surface resistivity	float	[ohms]
14	MAP	Maximum (absolute) potential attainable before a discharge	float	[V]

		occurs		
15	MPD	Maximum potential difference between surface and underlying conductor before a discharge occurs	float	[V]
16	RCC	Radiation induced conductivity coefficient K in the law $K \cdot (\text{rate}/\text{rate0})^D$, with $\text{rate0} = 1$ Rad/s (TBC), (or equivalently with no rate0 coefficient and rate expressed in Rad/s)	float	[ohm-1.m-1]
17	RCP	Radiation induced conductivity power (D)	float	[-]
18	MAD	Material density	float	[kg/m3]

Additional properties are also needed for the metal material of the tip. These properties are not from the NASCAP standard. There are designed by <ExtendedSpisProperty>. These properties are designed by key word (names). The new properties used in the ESD tool are presented in Table 18.

Table 18 - SPIS extended properties in the xml SPIS file

Name	Comment	type	Unit
WORK	Work function	float	[eV]
THCO	Thermal conductivity	float	[W/K/m]
HEAT	Specific heat	float	[J/K/kg]
ATOM	Atomic mass	float	[kg]
ELRE	Electric resistivity of metal	float	[ohm.m]
PREF	Reference pressure for evaporation	float	[Pa]
TREF	Reference temperature for evaporation	float	[K]
VAPE	Vaporization energy per mole	float	[J]
FUSE	Fusion energy per mole	float	[J]
VMAS	Volumic mass	float	[kg/m3]
MELT	Melting temperature	float	[K]
CION	Ionization cross section	float	[m2]

9.2.2. AluminumForESD

```
- <Assembly>
- <MaterialProperties Name="AluminumForESD" Color="16776960"
xmlns="material_schema">
  <Property Index="0" Value="1.0" />
  <Property Index="1" Value="0.0010" />
  <Property Index="2" Value="-1.0" />
  <Property Index="3" Value="13.0" />
  <Property Index="4" Value="0.97" />
  <Property Index="5" Value="0.3" />
  <Property Index="6" Value="154.0" />
  <Property Index="7" Value="0.8" />
  <Property Index="8" Value="220.0" />
```

```

<Property Index="9" Value="1.76" />
<Property Index="10" Value="0.244" />
<Property Index="11" Value="230.0" />
<Property Index="12" Value="4.0E-5" />
<Property Index="13" Value="-1.0" />
<Property Index="14" Value="26.98" />
<Property Index="15" Value="2699.0" />
<Property Index="16" Value="17.0" />
<Property Index="17" Value="18.0" />
<Property Index="18" Value="1.0E-16" />
<Property Index="19" Value="20.0" />
<ExtendedSpisProperty Name="WORK" Value="4.27" Type="float" Unit="[eV]"
Description="Work function" />
<ExtendedSpisProperty Name="THCO" Value="237.0" Type="float" Unit="[W/K/m]"
Description="Thermal conductivity" />
<ExtendedSpisProperty Name="HEAT" Value="900.0" Type="float" Unit="[J/K/kg]"
Description="Specific heat" />
<ExtendedSpisProperty Name="ATOM" Value="0.86E-25" Type="float" Unit="[kg]"
Description="Atomic mass" />
<ExtendedSpisProperty Name="ELRE" Value="0.2653E-7" Type="float" Unit="[ohm.m]"
Description="Electric resistivity of metal" />
<ExtendedSpisProperty Name="PREF" Value="2.42E-6" Type="float" Unit="[Pa]"
Description="Reference pressure for evaporation" />
<ExtendedSpisProperty Name="TREF" Value="933.4" Type="float" Unit="[K]"
Description="Reference temperature for evaporation" />
<ExtendedSpisProperty Name="VAPE" Value="2.93E+5" Type="float" Unit="[J]"
Description="Vaporization energy per mole" />
<ExtendedSpisProperty Name="FUSE" Value="1.08E+4" Type="float" Unit="[J]"
Description="Fusion energy per mole" />
<ExtendedSpisProperty Name="VMAS" Value="2702.0" Type="float" Unit="[kg/m3]"
Description="Volumic mass" />
<ExtendedSpisProperty Name="MELT" Value="933.4" Type="float" Unit="[K]"
Description="Melting temperature" />
<ExtendedSpisProperty Name="CION" Value="1E-19" Type="float" Unit="[m2]"
Description="Ionization cross section" />

```

9.2.3. GoldForESD

```

</MaterialProperties>
- <MaterialProperties Name="GoldForESD" Color="65535" xmlns="material_schema">
  <Property Index="0" Value="1.0" />
  <Property Index="1" Value="0.0010" />
  <Property Index="2" Value="-1.0" />
  <Property Index="3" Value="79.0" />
  <Property Index="4" Value="0.88" />
  <Property Index="5" Value="0.8" />
  <Property Index="6" Value="88.8" />

```



```

<Property Index="7" Value="0.92" />
<Property Index="8" Value="53.5" />
<Property Index="9" Value="1.73" />
<Property Index="10" Value="0.413" />
<Property Index="11" Value="135.0" />
<Property Index="12" Value="2.9E-5" />
<Property Index="13" Value="-1.0" />
<Property Index="14" Value="197.0" />
<Property Index="15" Value="19320.0" />
<Property Index="16" Value="17.0" />
<Property Index="17" Value="18.0" />
<Property Index="18" Value="19.0" />
<Property Index="19" Value="20.0" />
<ExtendedSpisProperty Name="WORK" Value="5.1" Type="float" Unit="[eV]"
Description="Work function" />
<ExtendedSpisProperty Name="THCO" Value="317.0" Type="float" Unit="[W/K/m]"
Description="Thermal conductivity" />
<ExtendedSpisProperty Name="HEAT" Value="128.0" Type="float" Unit="[J/K/kg]"
Description="Specific heat" />
<ExtendedSpisProperty Name="ATOM" Value="3.15E-25" Type="float" Unit="[kg]"
Description="Atomic mass" />
<ExtendedSpisProperty Name="ELRE" Value="0.2212E-7" Type="float" Unit="[ohm.m]"
Description="Electric resistivity of metal" />
<ExtendedSpisProperty Name="PREF" Value="2.37E-4" Type="float" Unit="[Pa]"
Description="Reference pressure for evaporation" />
<ExtendedSpisProperty Name="TREF" Value="1337.73" Type="float" Unit="[K]"
Description="Reference temperature for evaporation" />
<ExtendedSpisProperty Name="VAPE" Value="3.344E+5" Type="float" Unit="[J]"
Description="Vaporization energy per mole" />
<ExtendedSpisProperty Name="FUSE" Value="1.255E+4" Type="float" Unit="[J]"
Description="Fusion energy per mole" />
<ExtendedSpisProperty Name="VMAS" Value="19320.0" Type="float" Unit="[kg/m3]"
Description="Volumic mass" />
<ExtendedSpisProperty Name="MELT" Value="1337.73" Type="float" Unit="[K]"
Description="Melting temperature" />
<ExtendedSpisProperty Name="CION" Value="1E-19" Type="float" Unit="[m2]"
Description="Ionization cross section" />

```

9.2.4. Teflon FEP (BOL)

9.2.4.1. Teflon FEP (BOL)

```

</MaterialProperties>
- <MaterialProperties Name="Teflon FEP (BOL)" Color="255" xmlns="material_schema">
  <Property Index="0" Value="2.2" />
  <Property Index="1" Value="1.27E-4" />
  <Property Index="2" Value="1.0E-20" />
  <Property Index="3" Value="7.0" />

```

```

<Property Index="4" Value="2.3" />
<Property Index="5" Value="0.4" />
<Property Index="6" Value="45.4" />
<Property Index="7" Value="0.4" />
<Property Index="8" Value="218.0" />
<Property Index="9" Value="1.77" />
<Property Index="10" Value="0.455" />
<Property Index="11" Value="140.0" />
<Property Index="12" Value="2.0E-5" />
<Property Index="13" Value="1.0E16" />
<Property Index="14" Value="19.0" />
<Property Index="15" Value="2150.0" />
<Property Index="16" Value="17.0" />
<Property Index="17" Value="18.0" />
<Property Index="18" Value="1.0E-16" />
<Property Index="19" Value="20.0" />

```

9.2.4.2. Teflon FEP (BOL with Infinite SRE)

```

</MaterialProperties>
- <MaterialProperties Name="Teflon FEP (BOL with Infinite SRE)" Color="255"
xmlns="material_schema">
  <Property Index="0" Value="2.2" />
  <Property Index="1" Value="1.27E-4" />
  <Property Index="2" Value="1.0E-20" />
  <Property Index="3" Value="7.0" />
  <Property Index="4" Value="2.3" />
  <Property Index="5" Value="0.4" />
  <Property Index="6" Value="45.4" />
  <Property Index="7" Value="0.4" />
  <Property Index="8" Value="218.0" />
  <Property Index="9" Value="1.77" />
  <Property Index="10" Value="0.455" />
  <Property Index="11" Value="140.0" />
  <Property Index="12" Value="2.0E-5" />
  <Property Index="13" Value="1.0E20" />
  <Property Index="14" Value="19.0" />
  <Property Index="15" Value="2150.0" />
  <Property Index="16" Value="17.0" />
  <Property Index="17" Value="18.0" />
  <Property Index="18" Value="1.0E-16" />
  <Property Index="19" Value="20.0" />

```

9.2.5. CMX

9.2.5.1. CMX (MOL)

```

</MaterialProperties>
- <MaterialProperties Name="CMX (MOL)" Color="16776960" xmlns="material_schema">
  <Property Index="0" Value="3.80" />
  <Property Index="1" Value="100.E-6" />
  <Property Index="2" Value="5.0E-14" />
  <Property Index="3" Value="10.0" />
  <Property Index="4" Value="2.70" />
  <Property Index="5" Value="0.4" />
  <Property Index="6" Value="70.0" />
  <Property Index="7" Value="0.5" />
  <Property Index="8" Value="150.0" />
  <Property Index="9" Value="1.65" />
  <Property Index="10" Value="0.244" />
  <Property Index="11" Value="230.0" />
  <Property Index="12" Value="2.0E-5" />
  <Property Index="13" Value="2.6E16" />
  <Property Index="14" Value="10000.0" />
  <Property Index="15" Value="9000.0" />
  <Property Index="16" Value="1.E-13" />
  <Property Index="17" Value="1.0" />
  <Property Index="18" Value="1000.0" />
  <Property Index="19" Value="20.0" />

```

9.2.5.2. CMX-AR (MOL)

```

</MaterialProperties>
- <MaterialProperties Name="CMX-AR (MOL)" Color="16776960"
xmlns="material_schema">
  <Property Index="0" Value="3.80" />
  <Property Index="1" Value="100.E-6" />
  <Property Index="2" Value="5.0E-14" />
  <Property Index="3" Value="10.0" />
  <Property Index="4" Value="3.20" />
  <Property Index="5" Value="0.4" />
  <Property Index="6" Value="70.0" />
  <Property Index="7" Value="0.5" />
  <Property Index="8" Value="150.0" />
  <Property Index="9" Value="1.65" />
  <Property Index="10" Value="0.244" />
  <Property Index="11" Value="230.0" />
  <Property Index="12" Value="2.0E-5" />
  <Property Index="13" Value="2.6E16" />
  <Property Index="14" Value="10000.0" />
  <Property Index="15" Value="9000.0" />

```

```

<Property Index="16" Value="1.E-13" />
<Property Index="17" Value="1.0" />
<Property Index="18" Value="1000.0" />
<Property Index="19" Value="20.0" />

```

9.2.5.3. CMX (Low SRE)

```

</MaterialProperties>
- <MaterialProperties Name="CMX (Low SRE)" Color="16776960"
xmlns="material_schema">
  <Property Index="0" Value="3.80" />
  <Property Index="1" Value="100.E-6" />
  <Property Index="2" Value="5.0E-14" />
  <Property Index="3" Value="10.0" />
  <Property Index="4" Value="3.20" />
  <Property Index="5" Value="0.4" />
  <Property Index="6" Value="70.0" />
  <Property Index="7" Value="0.5" />
  <Property Index="8" Value="150.0" />
  <Property Index="9" Value="1.65" />
  <Property Index="10" Value="0.244" />
  <Property Index="11" Value="230.0" />
  <Property Index="12" Value="2.0E-5" />
  <Property Index="13" Value="5E15" />
  <Property Index="14" Value="10000.0" />
  <Property Index="15" Value="9000.0" />
  <Property Index="16" Value="1.E-13" />
  <Property Index="17" Value="1.0" />
  <Property Index="18" Value="1000.0" />
  <Property Index="19" Value="20.0" />
</MaterialProperties>
</Assembly>

```

9.3. Software Verification

The software performance is analyzed in the nominal configuration presented in paragraph 9.1.3. It aims at demonstrating the modelling relevance in term of multi physics, multi time and multi length scales capabilities.

9.3.1. Potential Evolution

At the beginning of the simulation, the metal plate and the dielectric are set to 0 V. Then, a barrier of potential is applied step by step. As observed in Figure 86, the first step is 500 V for a duration of 60 s. Then, the potential barrier is increased every 40 s by steps of 150 V.

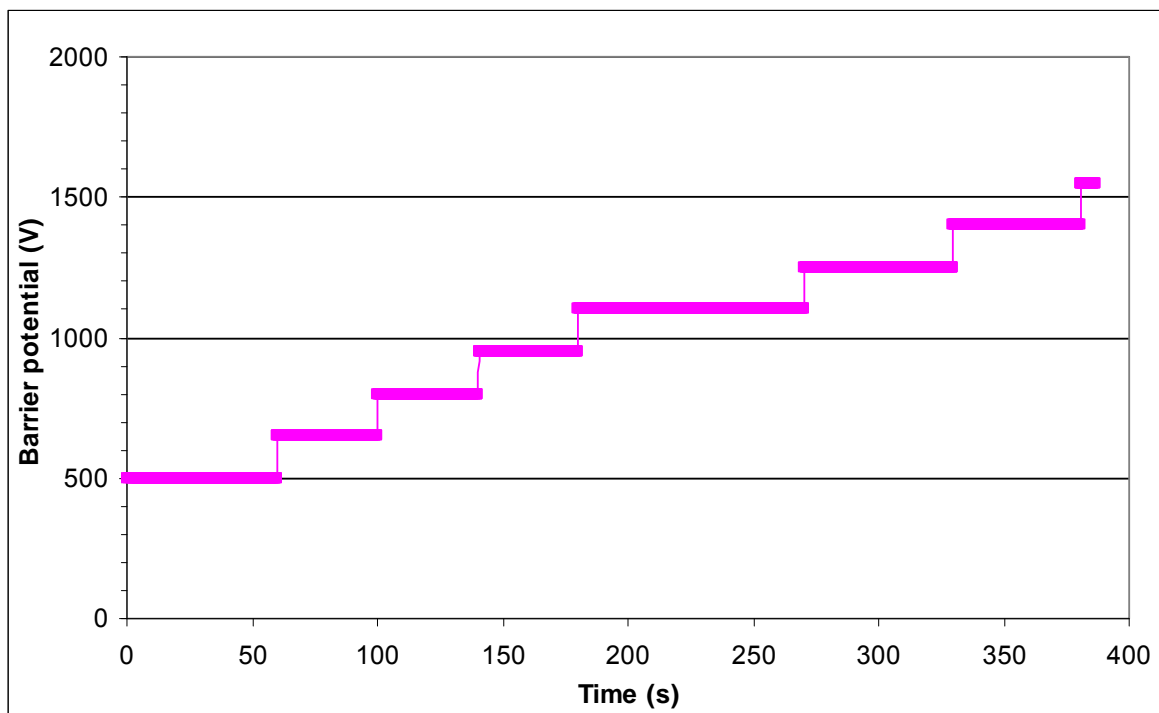


Figure 86 – Barrier of potential imposed by the SPIS ESD tool as a function of time

Due to photoemission, the initially zero floating surfaces tend to get more positive. That leads to the expected IPG situation. The maximum differential voltage is obtained once the dielectric surface reaches approximately the barrier of potential. Once the dielectric surface potential is greater than a few volts positive, the 1 eV photo electrons are recollected and the net current becomes null.

9.3.2. Emitted and Collected Currents

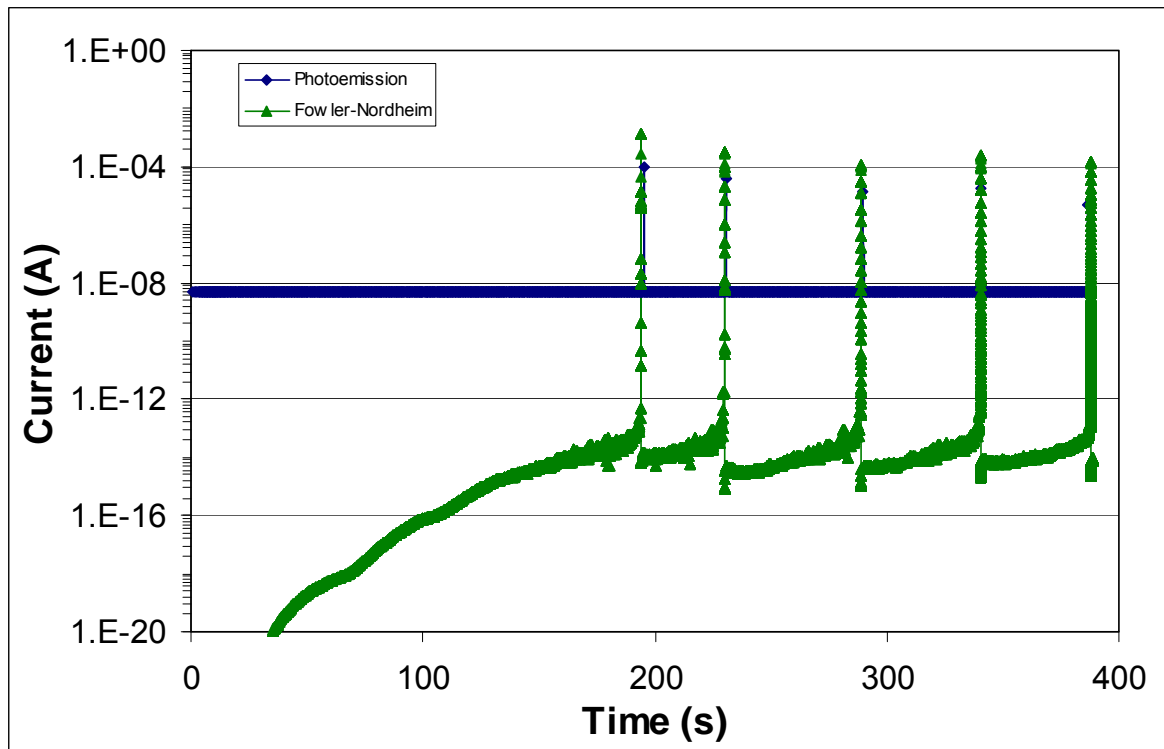


Figure 87 – Emitted photoemission and Fowler-Nordheim currents (in Log scale) as a function of time. For photoemission: emission from all surfaces. For Fowler-Nordheim emission: emission from the tip.

Figure 87 presents the time evolution of the photo emitted current from all the surfaces and the Fowler-Nordheim current coming from the tip. The progressive increase of the Fowler-Nordheim current is due to the progressive differential charging of the dielectric. As the dielectric potential becomes more and more positive, the differential voltage, the electric field on the triple point and the emitted current increase. At the end of the first four steps in potential, the dielectric reaches the barrier of potential on a large part of its surface. Thus, the differential potential cannot increase more and the FN current increases very slowly.

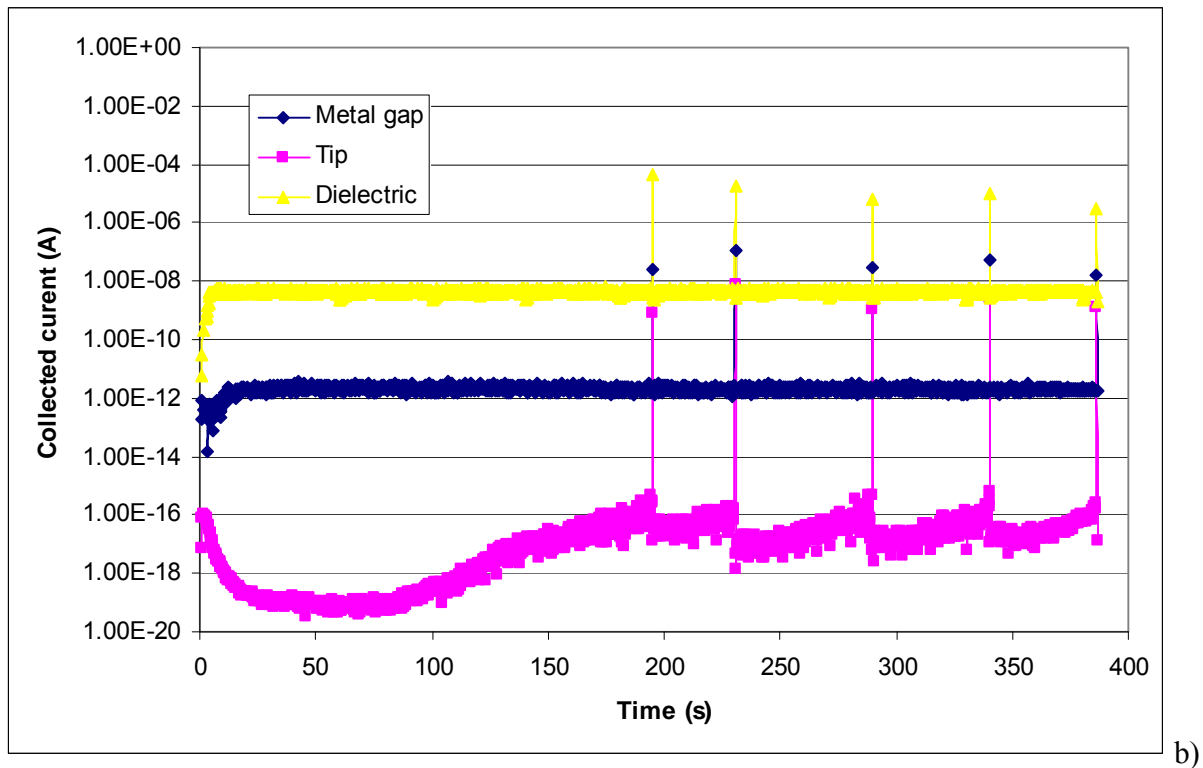


Figure 88 – Current collected on the metallic part, the emission zone and the dielectric (in Log scale) as a function of time.

During the fifth step in potential, corresponding to 1100 V, the FN current rapidly increases due to the electron avalanche initiation (represented in Figure 94). At that time ($t = 190 \mu\text{s}$), an ESD is triggered for a tip geometry corresponding to $\beta = 800$. Figure 87 and Figure 88 present four other ESD triggering at different potential barrier corresponding to β ranging from 750 to 600 for the last ESD. It can be noticed that the value of beta necessary to trigger an ESD decreases when the potential barrier increases.

9.3.3. Time Step Adaptation

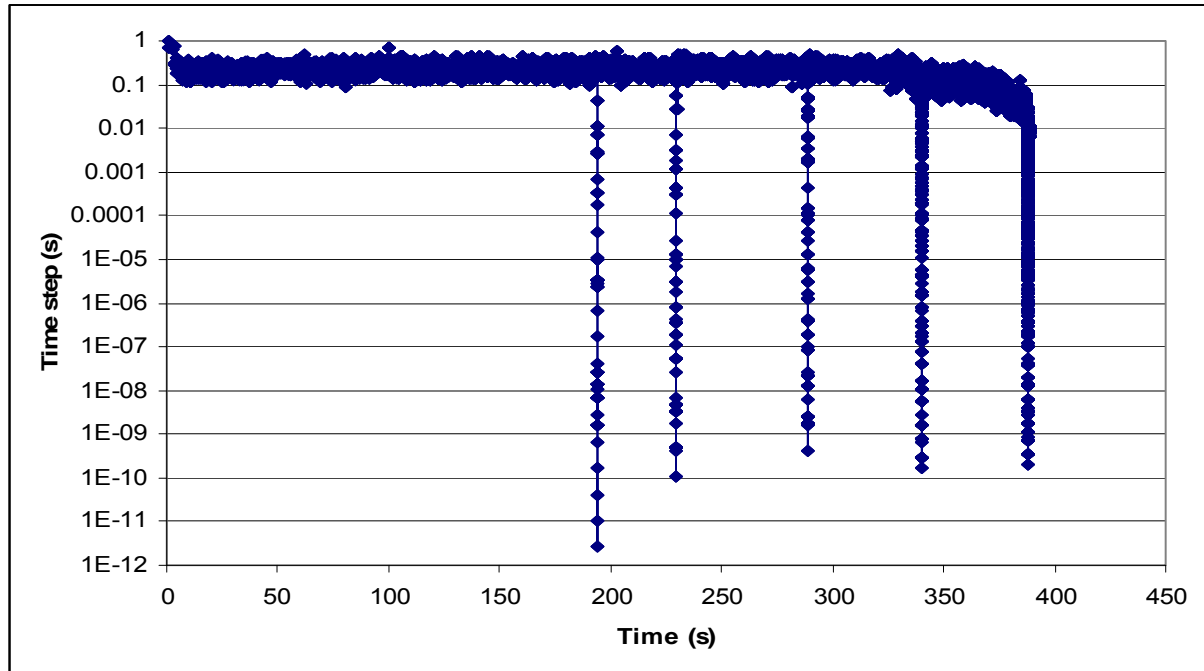


Figure 89 – Simulation time step as a function of time.

When the current increases, the time step is automatically adapted by the implicit solver of SPIS, cf. Figure 89. The time step is then gradually decreased from 1 s for the charging phase to 10^{-12} s at the maximum of the electron avalanche.

That clearly demonstrates the capability of the code to solve the multi-time scale of the problem.

9.3.4. Tip Evolution

The tip characteristics evolutions are represented in the next figures. The tip temperature during electron avalanche increases sharply to thousands of Kelvin. The melting and vaporization leads to neutral pressure of 10^{26} to 10^{27} particles per cubic meter (pressure of tens of bars). This corresponds to mass losses from the tip and so on to a decrease in tip length of 10 to 50 %. As a result, the amplification factor is also decreased. That can limit the ESD risk in the case of too small tips.

These results show that the model is capable to handle the multi physics of the ESD onset. As expected, the thermal behaviour of the tip depends on the emitted current together with its size.

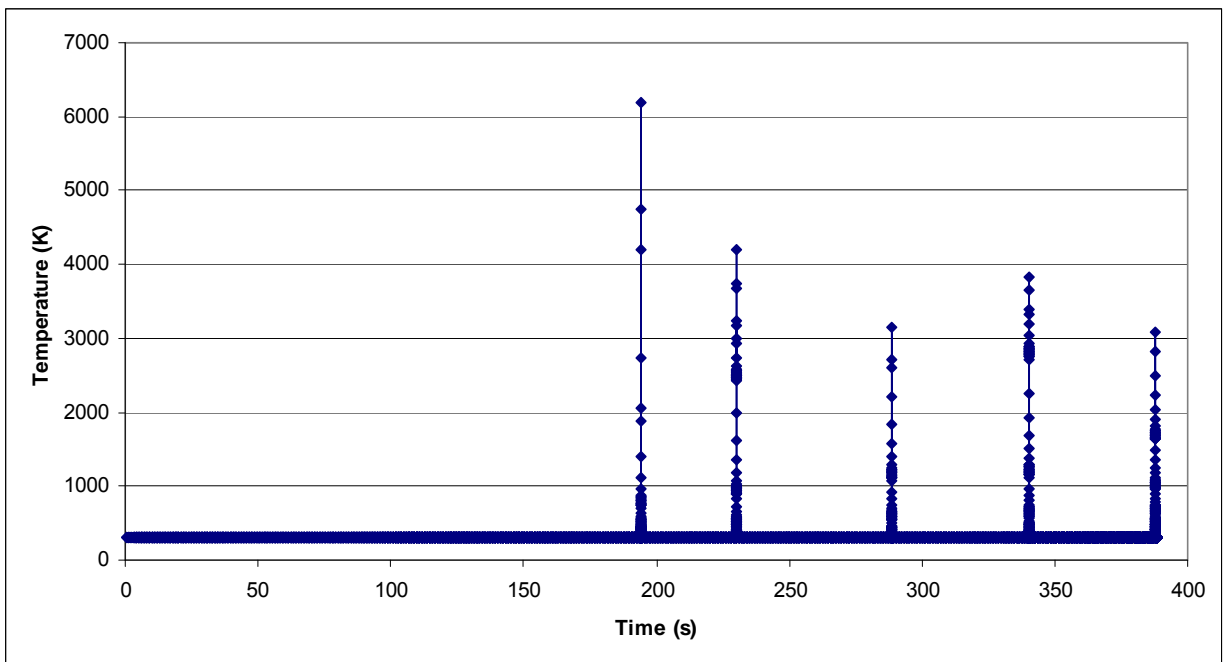


Figure 90 - Tip temperature evolution

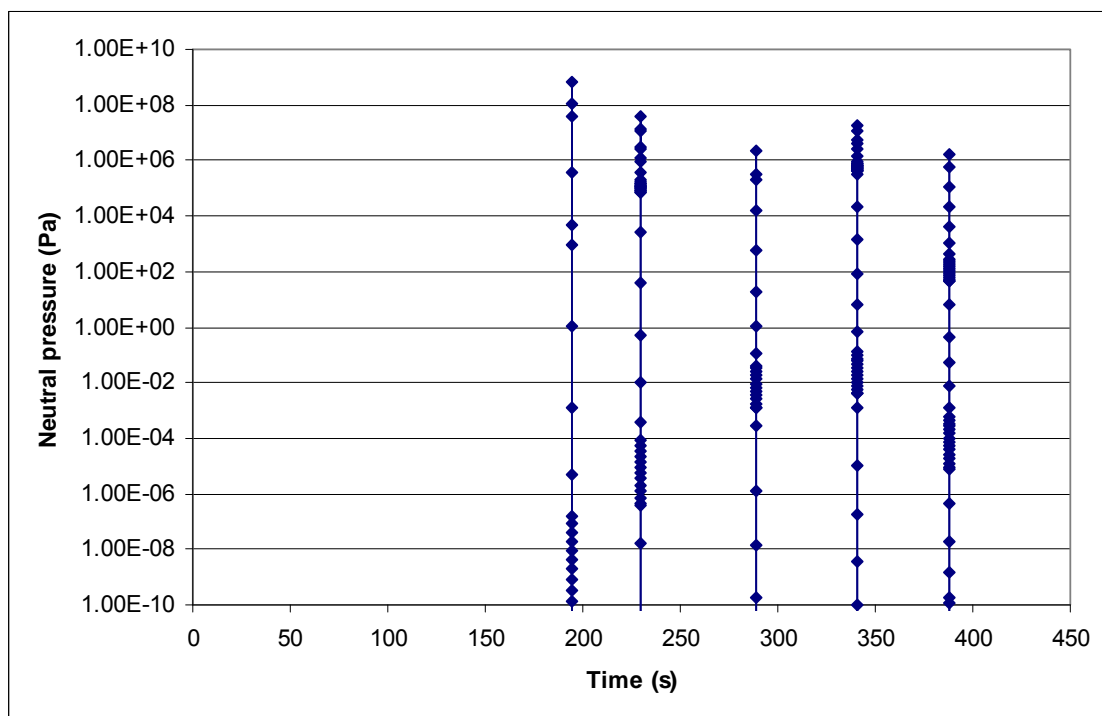


Figure 91 - Neutral pressure evolution

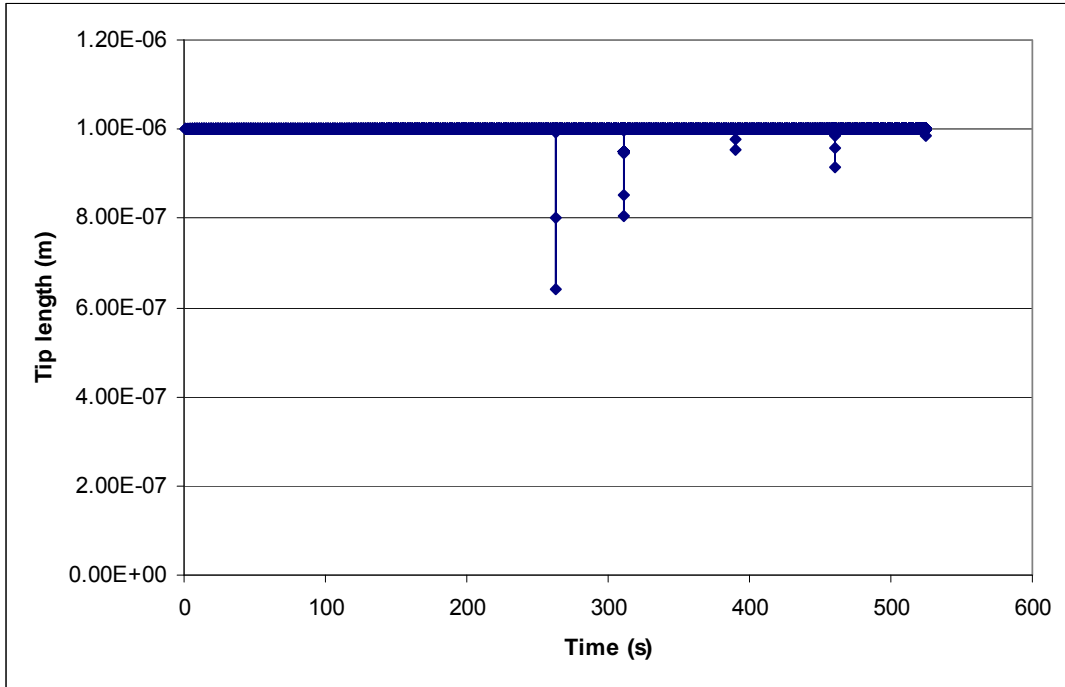


Figure 92 - Tip length evolution

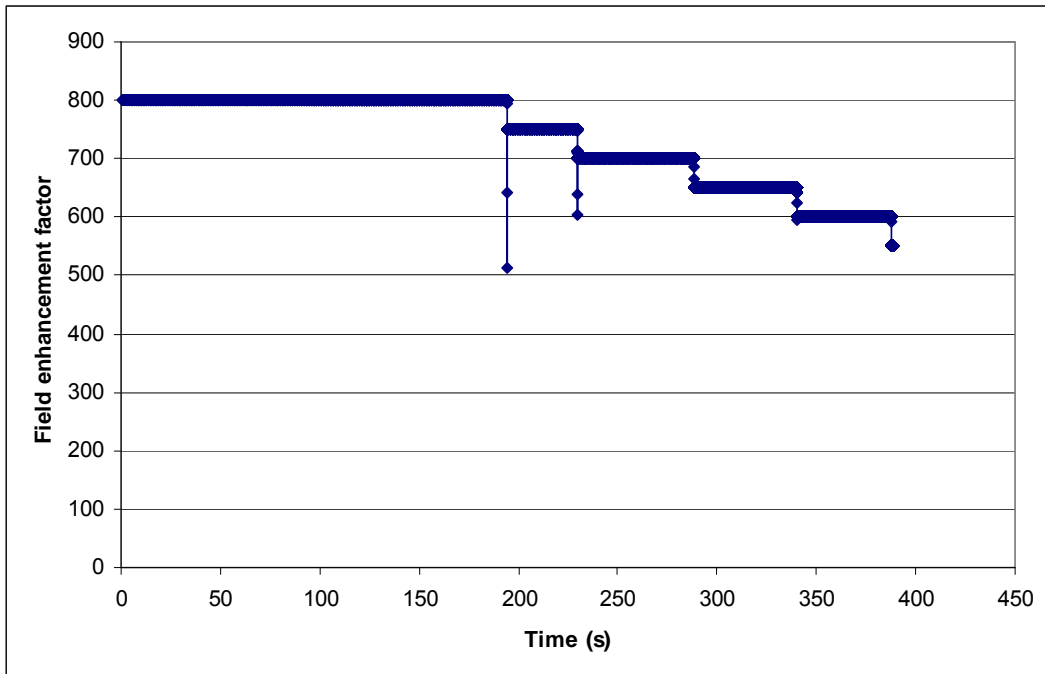


Figure 93 - Amplification factor evolution

9.3.5. Electrons Density in Volume: Space Charge Effect?

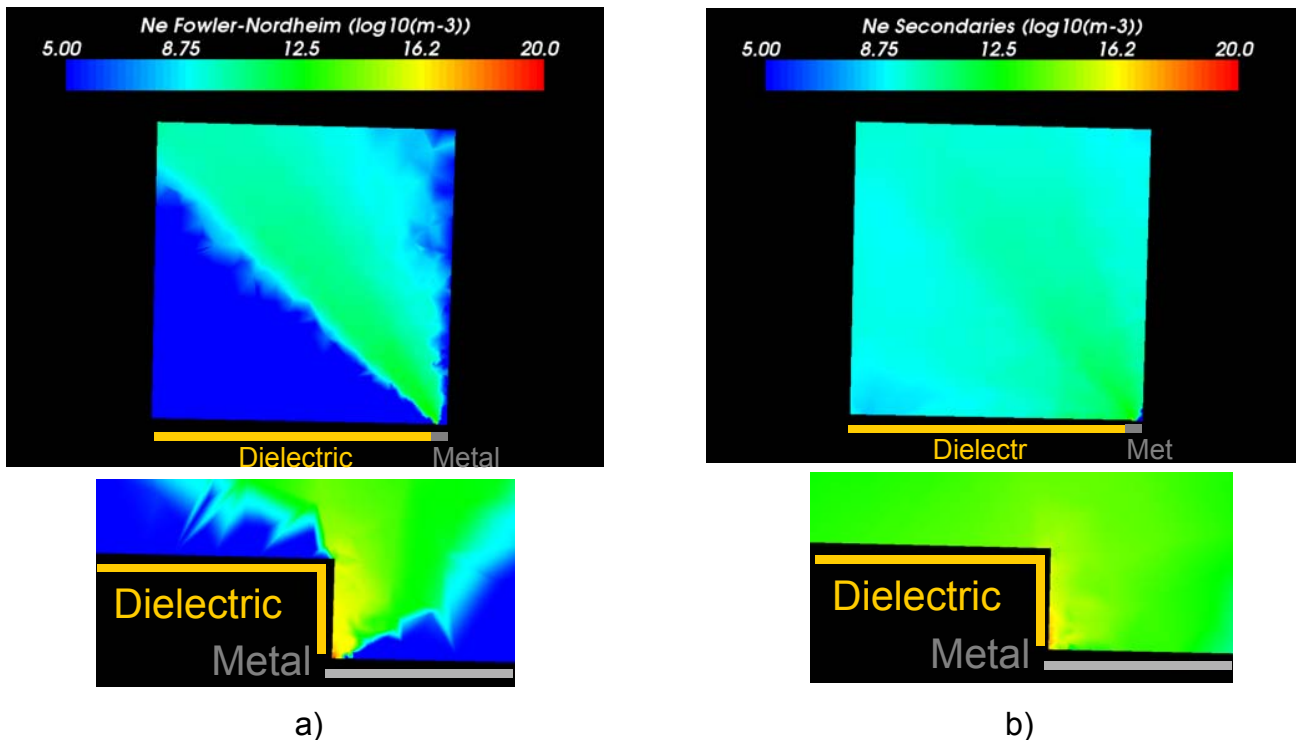


Figure 94 – Electron density during the first ESD: a) Fowler-Nordheim electron and b) secondary emission electron.

The Fowler-Nordheim electron and the secondary electron densities during the first electron avalanche of Figure 87 are represented in Figure 94. The FN density can reach 10^{20} m^{-3} near the triple point and the secondary electrons more than 10^{19} m^{-3} on a larger surface. For these densities, the space charge limitation exists can be seen on Figure 88 as the recollected current on the metal plate and on the tip rapidly increases at each ESD onset. Nevertheless, due to the three dimensional character of the electron avalanche, the FN is not completely limited by the space charge. Consequently, the current can reach values in order of milliamps that permit to melt the tip and trigger an ESD.

As a conclusion, the SPIS-ESD capability to model multi length scale of the ESD onset is clearly demonstrated.

9.3.6. Verification Phase Conclusion

The verification of the code is successful as SPIS-ESD is capable to model the multi physics domains of the problem, involving multi time and length scales. The tool is able to estimate the ESD risk in typical IPG situations and triple point configurations. The thermal model of the micro irregularities has a predictive capability since it permits to take account of tip size effect on the ESD onset. Small tips are necessary to trigger the electron avalanche but too small tips are melted before the neutral pressure is sufficient to sustain a real vacuum arc, i.e. a metal vapour arc.

9.4. Software Validation

The SPIS-ESD tool is compared with the experimental results presented in [TR] consisting in parametric studies during which five parameters were changed. The simulation of the nominal case is presented in paragraph 9.4.1. The effect of two geometrical parameters is presented in paragraph 9.4.2. The effect of dielectric and metallic material properties is shown in paragraphs 9.4.3 and 9.4.4 respectively. Finally, the geometry of the triple point is tested in paragraph 9.4.5.

9.4.1. Nominal Case

Figure 16 represents in the same plot the numerical and experimental results obtained in the nominal configuration. As a remark, the results are represented on the same plot for comparison convenience but the peak current is meaningless in the case of numerical results, as the peak current physically appears during the vacuum arc, not modelled here. The ESD thresholds presented in Figure 95 are comparable (800 V for experiments and 1100 to 1500 V for SPIS-ESD). The discrepancy between numerical and experimental results is about 300 V for very small tips ($\beta = 800$) and 700 V for larger ones. Tips smaller than tips with $\beta = 800$ melt before reaching the ionization probability greater than 1.

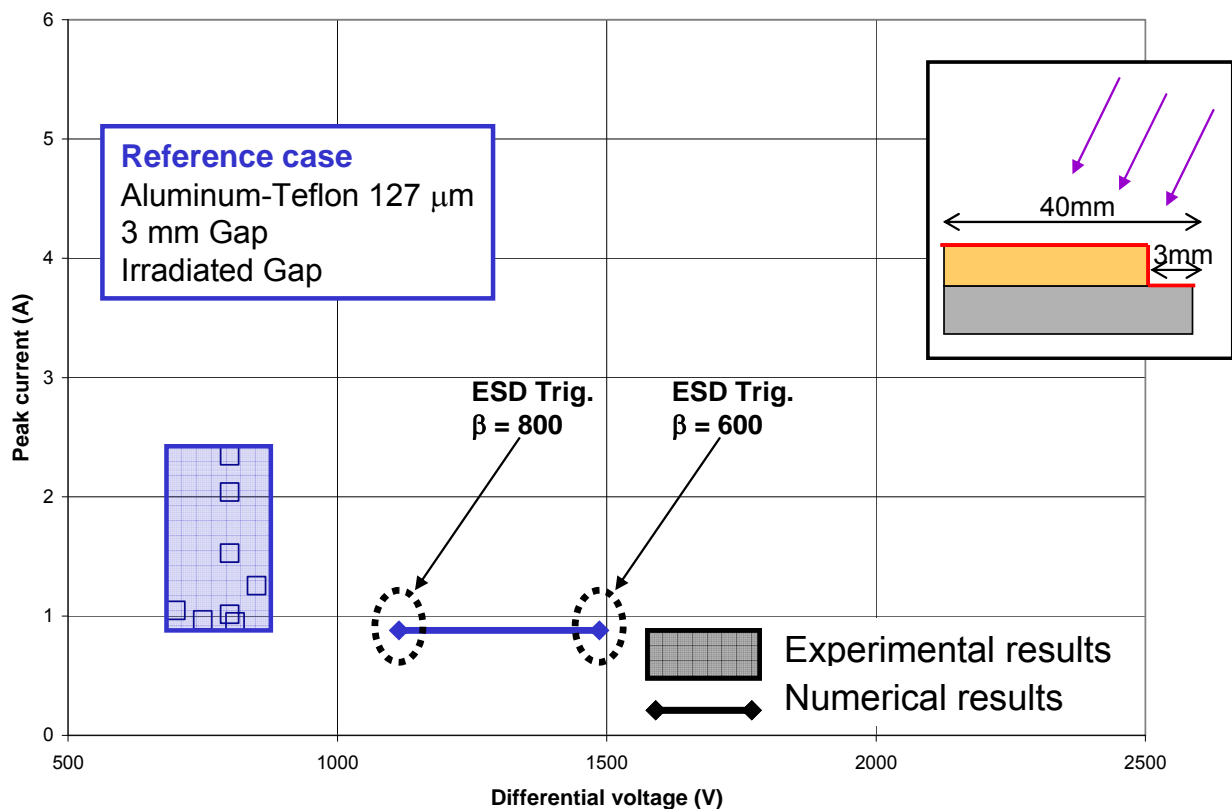


Figure 95 – Comparison of experimental and numerical results in the nominal configuration.

9.4.2. Geometry Effect

From the nominal case presented in the previous paragraph, we vary two parameters of the triple point geometry in order to assess the ESD threshold changes as a function of these parameters.

The results on Figure 96 are obtained with the same geometry as the nominal case but the angle of irradiation by the UV lamp is changed from +15° to -15°. As a consequence, the dielectric edge is not irradiated and it becomes more difficult to charge the dielectric on its edge. Numerical and experimental results qualitatively agree: when the dielectric edge is not irradiated by the UV source, it is much more difficult to trigger an ESD. The results on Figure 96 then clearly show that the triple point charging configuration is very important at the length scale of the dielectric thickness (100 μm). It is demonstrated that the way the charging occurs on the perpendicular configuration is fundamental as it may be difficult to build the differential voltage close to the metal. At a fixed bias voltage, the electric field resulting from the present case is lower than in the nominal configuration. Better than a qualitative agreement, the threshold variation of 400 V between the nominal case and the non-irradiated case quantitatively agrees between experiments and simulations.

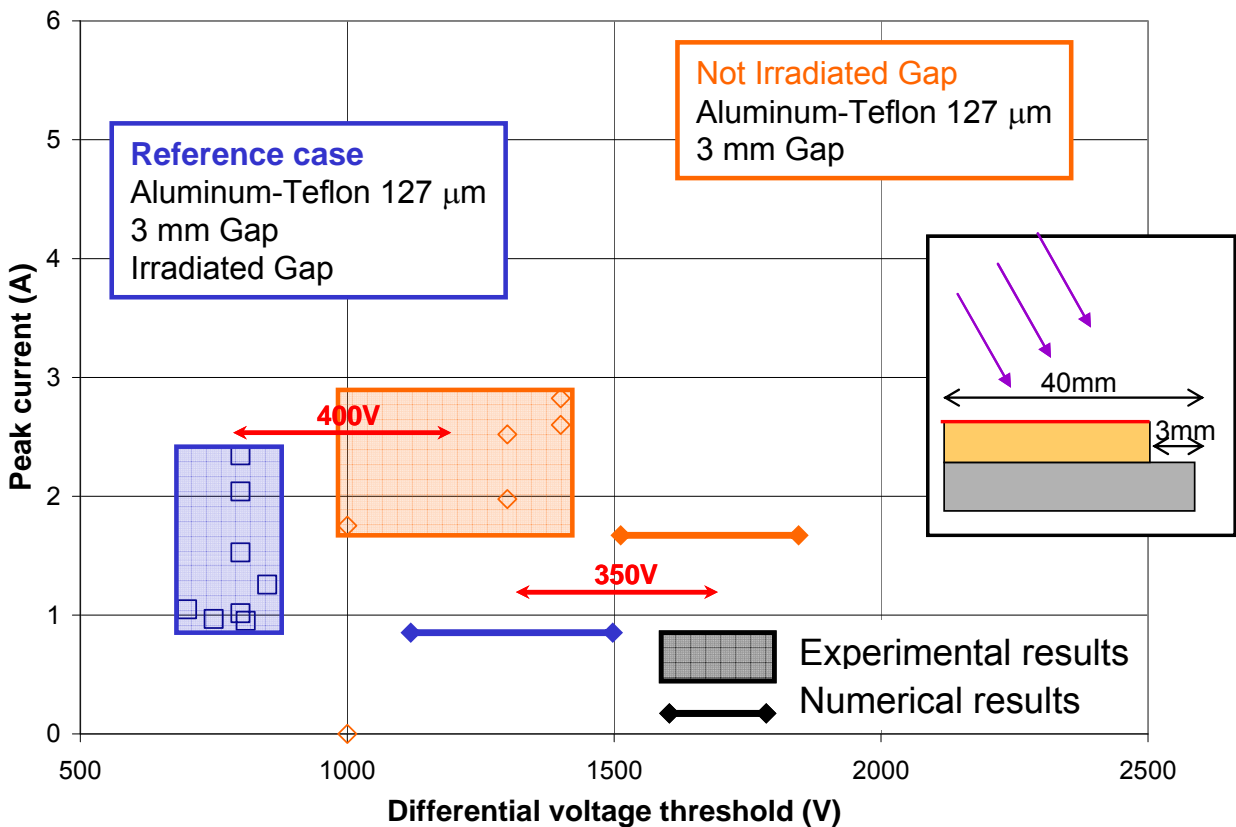


Figure 96 – Comparison of experimental and numerical results changing the incidence angle of UV to -15° (+15° in the nominal case).

The results on Figure 97 are obtained with the same geometry as the nominal case except the metal length is increased from 3 mm to 15 mm. In this case, the local barrier of potential coming from the metal gap is greater. For the same global barrier of potential, this leads to a lower potential gradient near the triple point thus to a lower electric field. As a consequence, we can see in Figure 97 that it is much more difficult to trigger an ESD. Like in the non-irradiated case, the results agree qualitatively but also quantitatively concerning the relative variation of the ESD threshold.

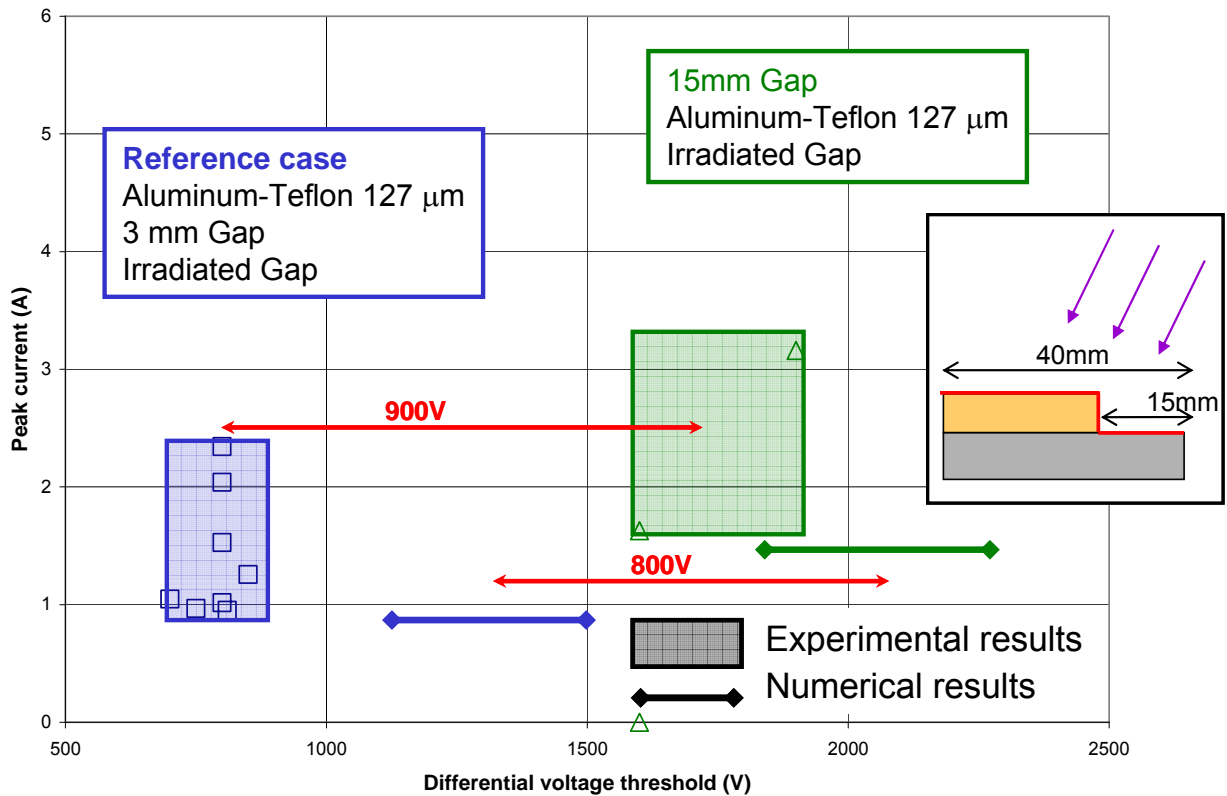


Figure 97 – Comparison of experimental and numerical results changing the metal length to 15mm compared to 3mm in the nominal case.

9.4.3. Surface Resistivity at the Dielectric Edge

The results presented in Figure 98 are obtained with the same geometry as the nominal case except the dielectric is changed from Teflon to CMX-AR. The bulk conductivity of Teflon and CMX are $1.0E-20 \Omega^{-1}.m^{-1}$ and $5.0E-14 \Omega^{-1}.m^{-1}$. As we can see in this figure, the experimental data show that it is much more difficult to trigger an ESD in the case of CMX-AR material. This was thought to be due to its highest conductivity. The difference between voltage thresholds is around 1100 V compared to the nominal case. Concerning the simulation results, three different threshold bars are shown in Figure 98. In these simulations, the top surface resistivity is fixed to $2.6 \times 10^{16} \Omega$ for the dielectric. This value comes from ONERA measurement of the CMX-AR sample used in experiment. But on the dielectric edge, this resistivity is unknown because we can reasonably think that there is no antireflective coating on the edges. Thus this

parameter is varied from $2.6 \times 10^{16} \Omega$ (more resistive than Teflon!) to $10^{15} \Omega$ (the results of this value are not shown in Figure 19 because the ESD threshold is greater than 3500 V). As seen in Figure 19, when the surface resistivity of the dielectric edge varies by a factor of two, the ESD threshold voltage varies of about 400 V.

That clearly shows that the surface resistivity is a key parameter which has a strong effect on ESD risk as it influences the potential map at triple point. We can also estimate that the surface resistivity used for Teflon $10^{16} \Omega$ (extracted from constructor data) is known with only a precision of 2 as this property measurement is difficult. The results obtained in the nominal configuration may be significantly changed using a surface resistivity two times the value initially used.

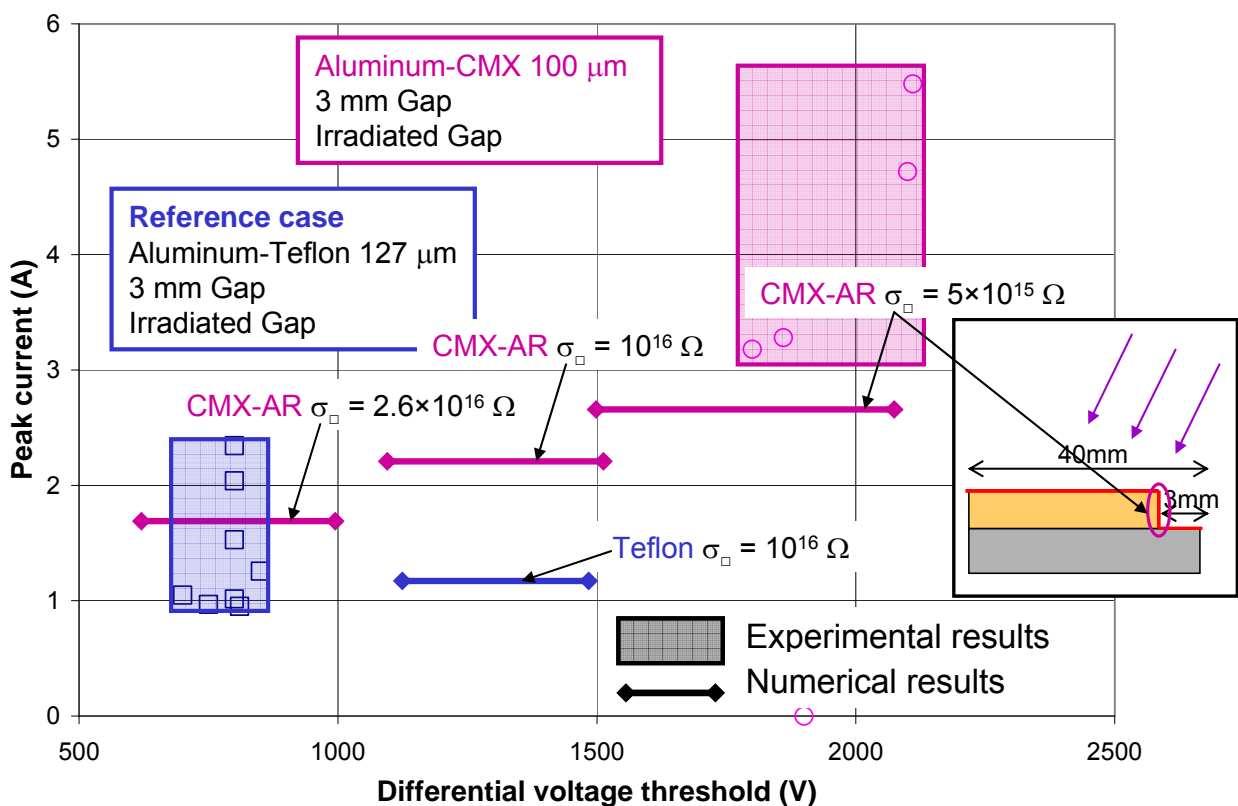


Figure 98 – Comparison of experimental and numerical results as a function of the surface resistivity at the dielectric edge.

9.4.4. Tip Material Effect

The results presented in Figure 99 are obtained with the same geometry as the nominal case except the metal is changed from Aluminum to Gold. The experimental data dispersion did not permit to definitively conclude on the material effect. The difference between voltage thresholds was around 100 V compared to the nominal case but with a 500 V dispersion for the gold results.

Concerning the simulation results, the effect of the metal material is due to the work function difference. But its effect on the voltage threshold is not very important in these conditions.

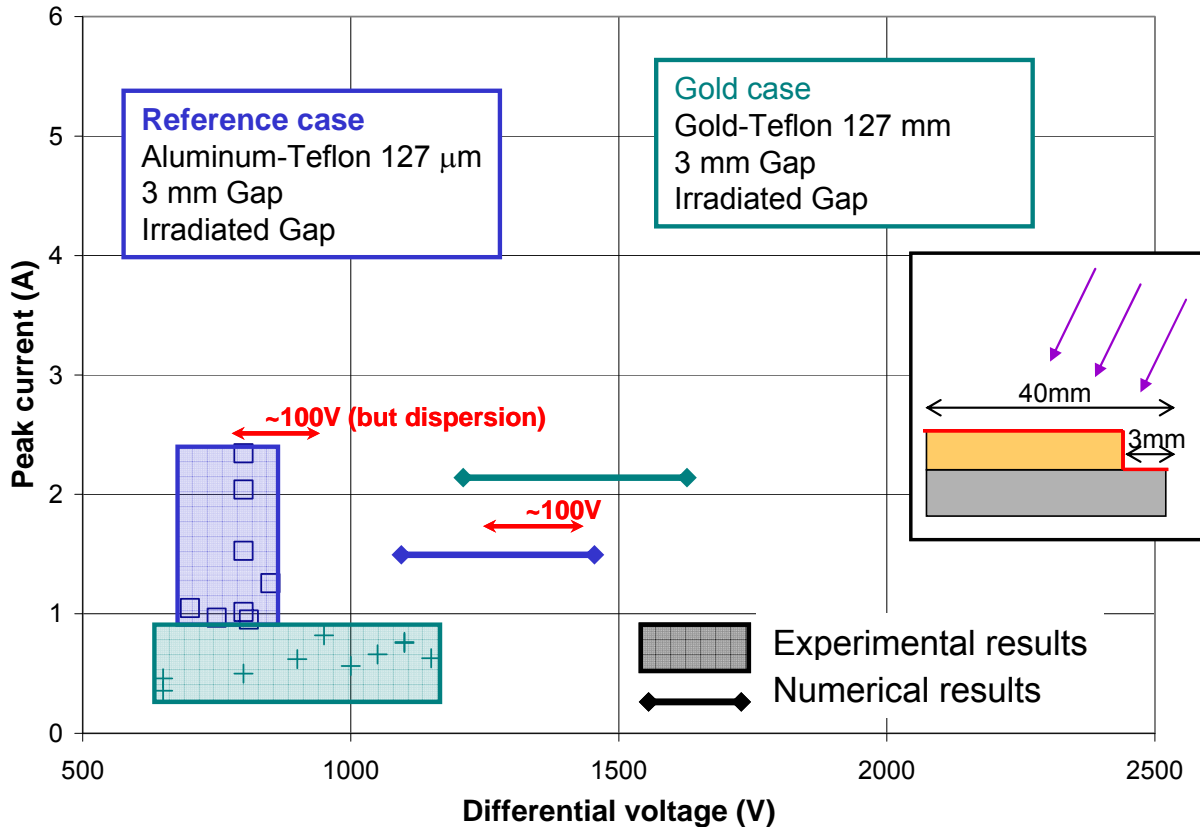


Figure 99 – Comparison of experimental and numerical results as a function of the metal material

9.4.5. Planar Configuration

The experimental results presented in Figure 100 clearly show that it is definitively more difficult to obtain a breakdown in the coplanar configuration.

The numerical simulation exhibits the same qualitative result. However, the ESD onset with the numerical simulation is possible only for a field enhancement factor of 800. Other cases with smaller or higher enhancement factors lead to numerical instabilities. These instabilities are due to the fact that it is almost not possible to trigger an ESD in such a co-planar configuration as FN electrons have to completely go back to from their initial trajectory (towards the upper limit) to be collected on the dielectrics. This is of course very difficult to model when electrons gain hundred of eV due to the potential difference between the dielectric and the tip. Only a very small amount of electrons is recollected (less than 1% of the FN current emitted to compare to > 10 % in the perpendicular case). Consequently the avalanche is much more difficult to trigger. In most cases, the ESD prediction tool does not permit to reach accuracy smaller than 1% for the recollection of FN electron on the dielectric. However, as during experiments, it is clearly shown that the co-planar situation is less dangerous than the perpendicular one.

On the other hand, a question rises from the previous observations: is the experimental coplanar situation really as coplanar as in the simulation? The answer is definitively not, there is always a step between the

dielectric and the metallic part. So the perpendicular or at least angular situation is more relevant for simulation than the coplanar one, the latest being only theoretical.

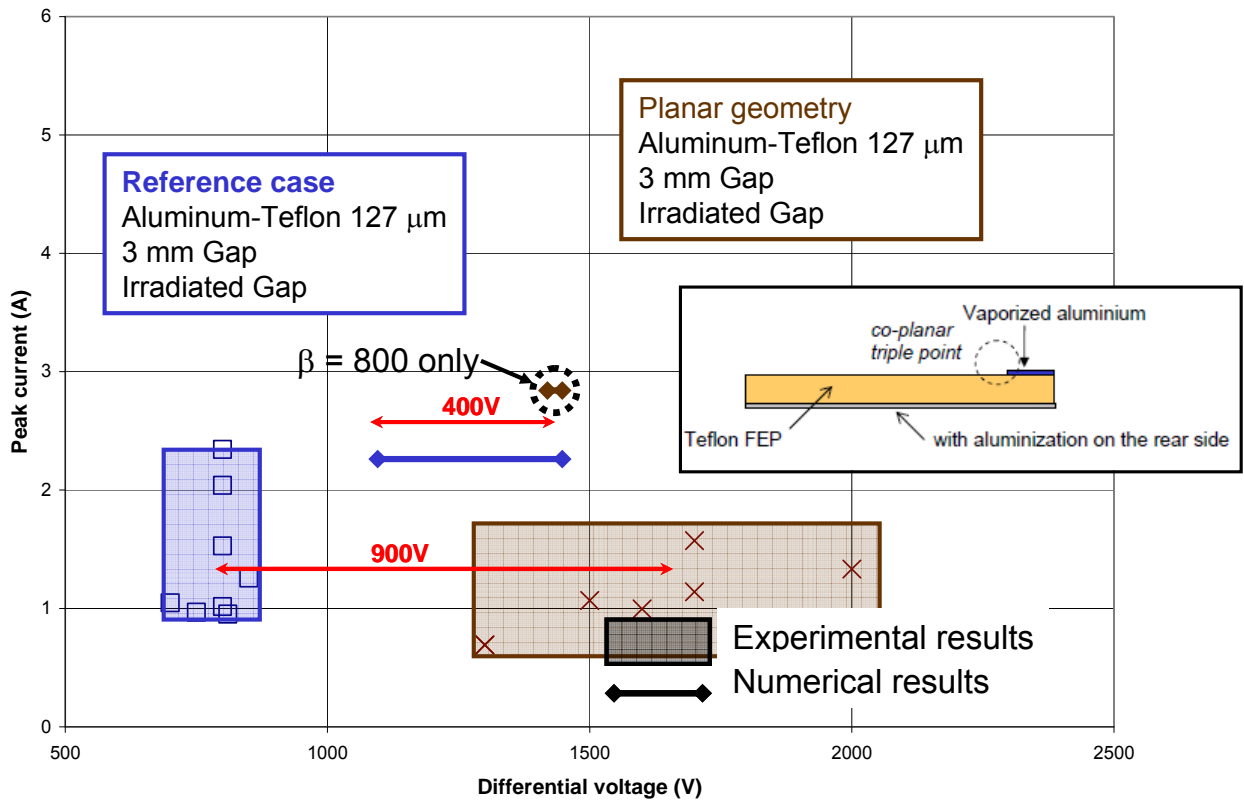


Figure 100 – Comparison of experimental and numerical results in the planar configuration.

9.5. Results Analysis and Possible Code Improvements

In conclusion, the very ambitious developments planned in this activity were largely successful. The simulations demonstrated the capability to model the multi physics and the multi time and length scales of the problem. The SPIS-ESD tool is able to determine the possibility to trigger an ESD on typical IPG situations on solar panels.

Comparing the experimental and numerical results, the relative variations of ESD thresholds have a good agreement. The results have shown that it is definitively more difficult to trigger an ESD in the following configurations: more conductive dielectric, low photon incidence angle (or even more for a shadowed triple point) or longer metallic plate. As a result, the SPIS-ESD tool may be possible to use by design engineers or scientists in order to compare different configurations of IPG on triple points.

Quantitatively, it seems however hardly feasible to assess the ESD threshold with a precision better than ± 200 V or 300 V with the SPIS-ESD tool. This is due first to the statistics of ESDs. No ESD is fully reproducible in any triple point configuration as it involves microscopic scales. On the numerical side, two uncertainty sources make it impossible to obtain predictive quantitative results. The first ones come from the micro scale geometry of the tips. For β varying from 800 to 600, the ESD threshold can be estimated with a precision of ± 200 V which is however quite acceptable compared to experiments. Secondly, the surface resistivity is not precisely known for a majority of materials. This parameter can lead to huge variations (greater than 2000 V) in ESD threshold just changing this parameter at the edge of the dielectric.

The observed imperfections and inaccuracies of the code were mainly linked to the difficulties to obtain consolidated and reliable values for material surface resistivity. The simulations showed a strong effect of this parameter. Future works would certainly necessitate performing dedicated material properties measurements.

An important improvement would consist in description of the microscopic scale. The chosen model of electric field amplification is valid for microscopic tips but not necessarily for microscopic thin dielectric layers. A possible improvement would be to have a model for such thin layers. That would lead to modify the interaction between the electric field amplification model and the thermal model. Thin layers are however more complex to model than metal tips and it is not guaranteed that would give better agreement with experiments. SPIS-ESD could also be improved by taking into account multiple microscopic irregularities at the metal surface or field emission from a semi-conductor.

Another possible improvement concerns the modeling of conductivity under photon illumination. Combined with the existing (electron) radiation induced conductivity, the charging phase would probably be more precisely described. That would require developing a new module in agreement with the state of the art of material photo conduction.

The SPIS perpendicular, angular or co-planar geometrical models developed in this activity is representative of solar cell interconnects. A possible amelioration could take account of more complex 3D geometries such as solar cell gaps. That would require defining different dielectric layers for the solar cell cover glass and the glue between the solar cell and the cover glass, possibly associated with partial sun shadowing. It would be also interesting to model the glue between the solar cell and the substrate in order to determine the possibility to trigger an ESD at this location. The circuit solver would have to be updated with new capacitive and conductive coupling of thick dielectrics.

10. ESD MONITOR CONCEPTUAL DESIGN AND ASSESSMENT

The purpose of this section is to propose a concept for the measurement of the ESD occurrence on solar panels in-flight and to assess it.

10.1. ESD Monitor Concept

A first iteration of the ESD monitor concept was proposed in [ITT] and in [PROP]. It consists in metallic plates located on the panel front side. A schematic view of this solution is presented in Figure 101. It is required that the metallic plates shall float at the same potential as the adjacent cover glasses so as to permit the detection of a surface discharge.

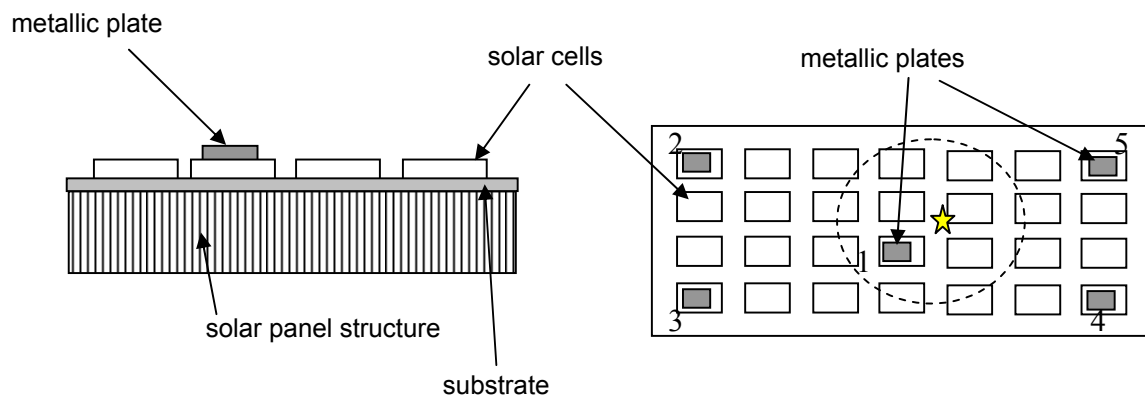


Figure 101 - Basic schematic of the ESD monitor concept; example with 5 metallic plates

The differential voltage between the structure and the solar array surface is obtained thanks to a resistive voltage divider, see Figure 102. The voltage V_S between the metallic plate and the spacecraft structure is written as: $V_S = \frac{R_1 + R_2}{R_2} V$. [ITT] required that the potential of the plates shall be transformed in the 0 to 5 V

range, suitable for input to housekeeping channel in a spacecraft data processing unit. Section 2 indicates that typical differential voltages of about 2 to 3 kV are obtained on solar panels. As a result, a ratio R_1/R_2 equal to 1000 should be sufficient to answer to this requirement. It might be pointed out that the resistor should be placed as close as possible from the metallic plates and all the cables perfectly insulated so as to avoid current leakage from the metallic plate to the structure. The entry impedance of the voltmeter should also be sufficient. If it is not possible to select a voltmeter with sufficient entry impedance, an alternative way could consist in measuring the current flowing through the resistors. The physical considerations used to determine the value of R_1 are estimated to 1 T Ω , see Section 10.2. The deduced value of R_2 is 1 G Ω .

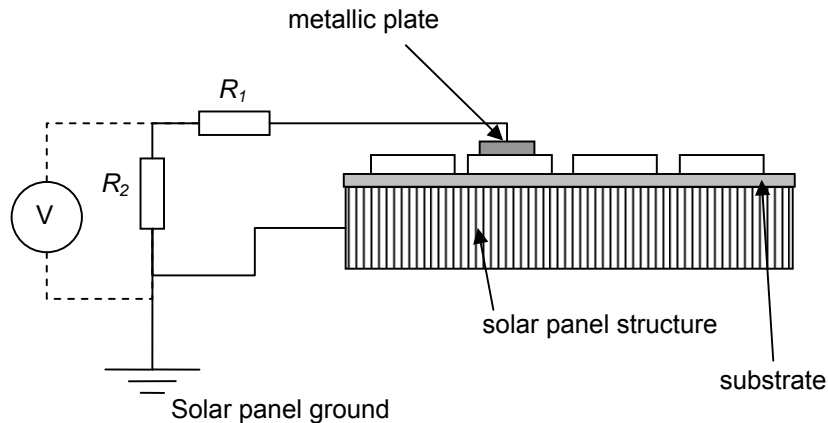


Figure 102 - Electrical connection of the ESD monitor

The sampling must be adapted to the time evolution of spacecraft potentials, in order to follow the charging up of the solar array with respect to the structure and to detect the decrease in the differential voltage (through the measured V) due to ESDs. As expressed in Section 2, the differential charging occurs at minute scale and discharges last tens or hundreds of microseconds. Let us consider a blow-off initiated in the vicinity of the metallic plate #1 in Figure 101, followed by a flash-over that discharges a surface including the patch #1. In Figure 103, the instant T_0 represents the initiation of the BO which lasts approximately ten microseconds. At that time, the differential voltages have not yet changed since only the spacecraft absolute capacitance has discharged. The instant T_1 represents the beginning of the flash-over, which is in fact the instant from which the ESD can be detected by the metallic plate #1. The differential voltage decreases from approximately +1000 V to 0 V in some tens of microseconds due to the neutralization of the dielectric surface. It is important to notice that the ESD risk appears again on the panel as soon as the spacecraft structure reaches a negative potential, which is rapidly obtained by the collection of environment electrons. Indeed, the dielectric surfaces that have not discharged yet still present a risk: negative potential of the structure and IPG situation. The instant T_2 represents the time when the patch has recovered the potential of the dielectrics. In order to be sure that a discharge has occurred, it is then necessary to have a sampling time step much lower than 1 minute, which is typically the duration between T_1 and T_2 . *We recommend a sampling with a period of 1 s or less* if the capability of data acquisition and storage on board are adequate, cf. the section on spacecraft integration issues.

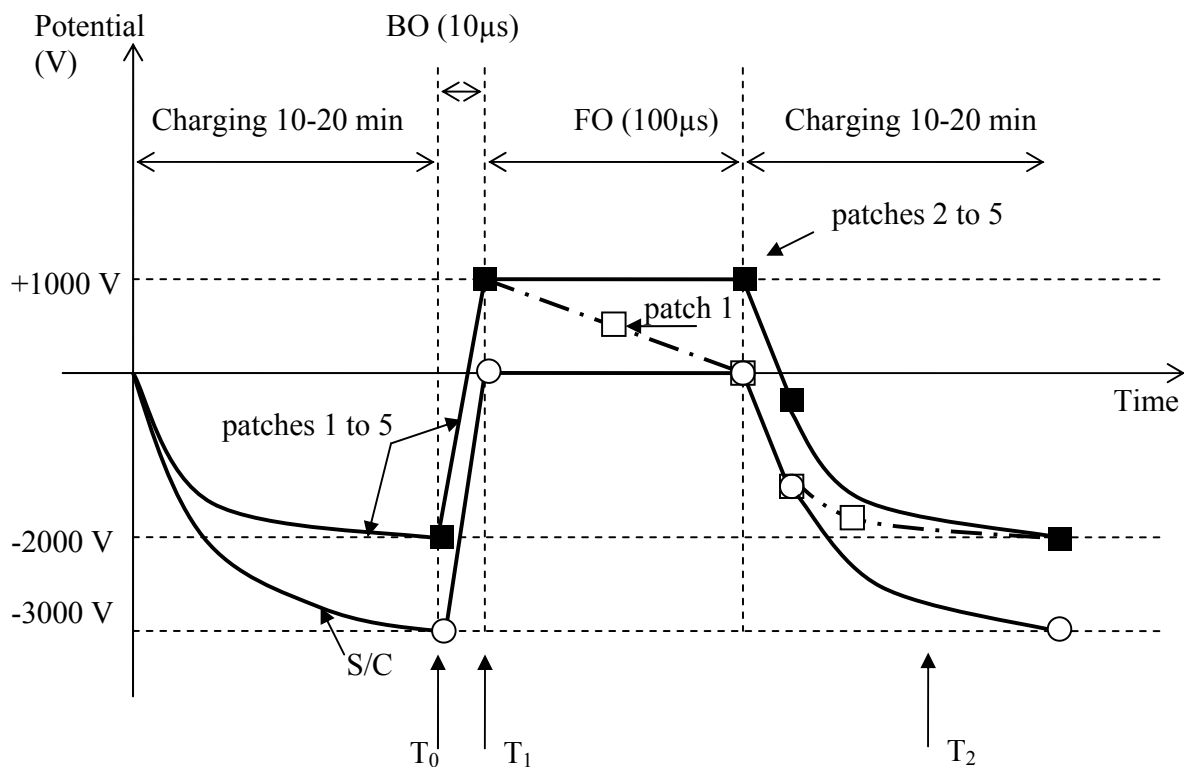


Figure 103 - Evolution of potential during charging and discharges; example of the flash-over represented in Figure 101; near the metallic plate #1

This device permits to detect if a flash over has occurred in the vicinity of the plates. Section 2 indicates that the flash over can discharge more than 1 m^2 of solar cell coupon. Experiments using a dielectric sheet instead of solar cell assemblies shows that a flash over of 10 m^2 is possible. Nevertheless, this kind of experiments should be confirmed by tests with real flight coupons so as to determine the area of the surfaces implicated during the flash over. This kind of experiments has not yet been carried out and we might need them to determine the necessary number of metallic plates. This could be achieved during the experimental campaigns foreseen in the ESA ITT aiming at determining the capability of the flashover to discharge large solar arrays [ITT-FO]. During the flash over, the capacitance between the top of the cover glasses and the underlying conductor discharges due to the neutralization of the positive charges on top of the glasses. That only concerns the cover glasses that are touched by the flash over, as represented schematically by the circle surface represented in Figure 101 around the ESD triggering location (represented by a star). As the plates are supposed to float at the same potential as the adjacent cells, only the plates that are concerned with the flash over will permit the monitoring of the ESD. If the space between the plates is too long, we might miss a certain number of ESDs. As the flash-over discharges of 1 m^2 have already obtained on solar panels in

vacuum chamber, we suggest a *minimum distance of 1 m between the plates*. Nevertheless, the question of the number of plates must also be answered considering spacecraft integration issues, cf. Appendix 1.

The SoW required that the device shall give access to the barrier of potential due to the front side of the solar panel. In Section 2, it was shown that the surface potential of the solar array adjusts itself locally so that the normal electric field is very close to zero. It signifies that the surface potential is close to the potential of the barrier. If we assume that the plates will float at the same potential as the adjacent cells, then the barrier of potential will be simply the differential voltage between the structure and the plates, and the measurement of V will be sufficient.

Finally, the monitor itself must limit unwanted effects, among which the ESD hazard is the more dangerous. The monitor can possibly create new triple points. Providing some attention is given to the design of the metallic plates system, the ESD risk should be easily avoided:

- Firstly, the plates will float at the potential of the surface dielectrics because of the homogenization of the surface potentials by the photo electrons, as it is explained in the following paragraph. Nevertheless, there could be a risk at eclipse
- Secondly, let us consider that an electron avalanche occurs due to the electric field emission enhancement by a microscopic irregularity on the triple point composed of the metallic plate, the cover glass and the vacuum. As the metallic plate is insulated from the spacecraft structure with a resistor of the order of the TeraOhms, there is no risk of cathode spot creation due to an inrush current flowing through the resistor.
- It could however be possible that the transient current passes through the dielectric material underlying the metallic patch if the capacitance C_d of this dielectric sheet is high enough, see Figure 104. As a result, we propose to follow the ECSS recommendations and to limit the surface of each patch to 1 cm^2 with a capacitance less than 10 pF with respect to the structure [RD4]. **In the case these requirements are not possible, ECSS requires that tests shall be performed to assess the ESD risk.**

Remark: for a solar cell cover glass, the capacitance per surface unit is typically 200 to 300 nF/m^2 . 10 pF corresponds then to a patch surface of 0.3 to 0.5 cm^2 .

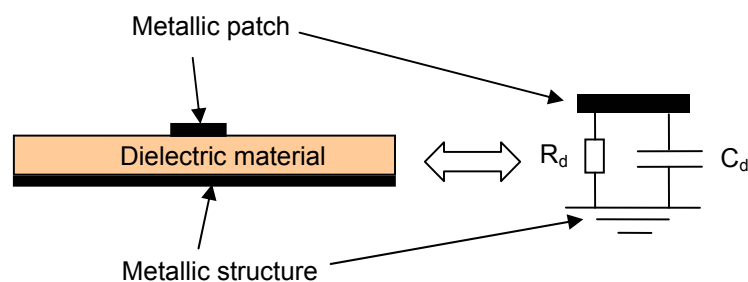


Figure 104 - Equivalent circuit of the dielectric sheet during transient currents

Moreover, the plates must be placed on the same material as the covering dielectrics, *i.e.* the cover glasses, in order to be representative of the surface potentials. We recommend however not to use full solar cell assemblies for supporting the plates because that could enhance locally the differential charging at the triple point between the solar cell and the dielectric. The solution would be to use only cover glasses without

underlying solar cells. Another solution would be to use glue as dielectric insulator between the plates and the structure. It would be also safer in term of wiring because we could make these wirings not interfere with the adjacent active gap. Such a solution is envisaged in Appendix 1.

10.2. ESD Monitor Assessment

10.2.1. Physical Considerations

The device proposed in the previous section mainly relies on the photoemission process. In GEO, the absolute and differential voltages are ruled by the collection of environment electrons in the range 1 to 10 keV and photoelectrons. Generally, spacecraft float at some kilovolts negative while the cover glasses are less negative; the differential voltage being 1 to 3 kV typically. On the front side, the barrier of potential due to the rear side prevents the photoelectrons to escape the array vicinity once its surface potential is slightly more positive than the local barrier of potential.

The same rationale is used to asses that the metallic plates in Figure 105 will float to the same potential as the adjacent dielectric surfaces.

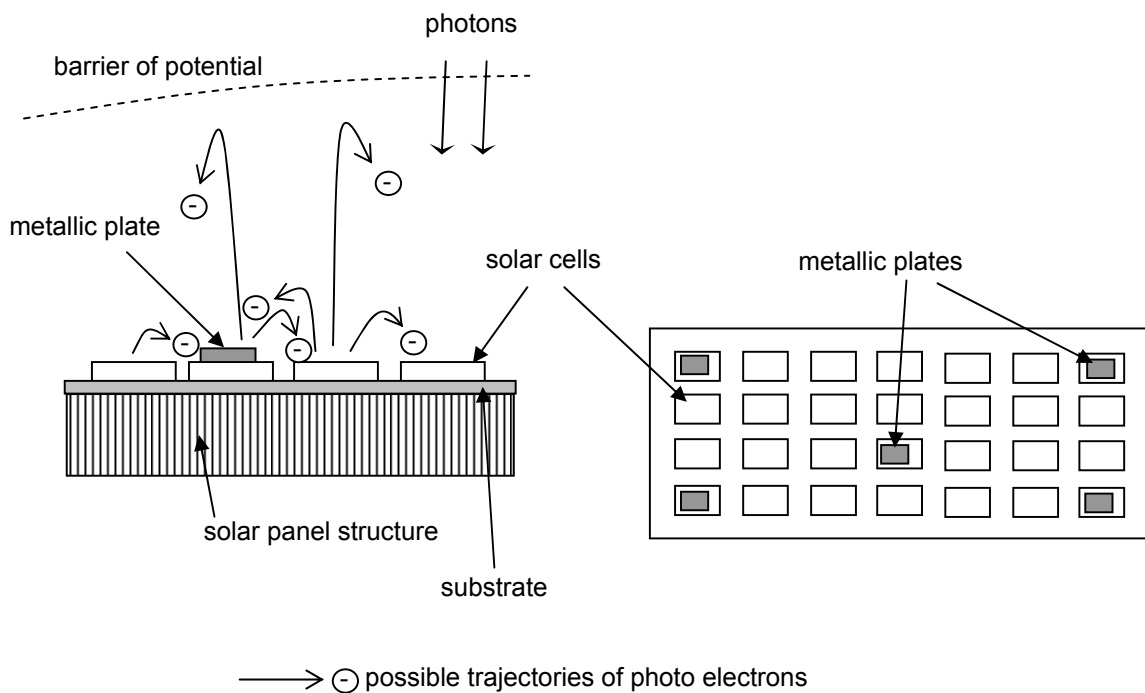


Figure 105 - Surface potential homogenization by recollection of photoelectrons

The photoemission process consists in the emission of electrons by solar UVs. Briefly, if the photon energy is higher than the material work function, then an electron can be emitted, its energy being the photon energy minus the material work function. The photoemission yield corresponds to the ratio between the emitted

electron flux and the photon flux. It depends on the material work function, but also on its smoothness together with the angle of incidence and the energy of the photons. In GEO at 1 AU, the photoemission current is estimated to 2 nA/cm^2 for dielectrics such as cover glasses, a little bit more for metals (3 nA/cm^2 for gold).

The photo electrons are emitted with an energy of typically 2 eV. These cold electrons are then submitted to the local potentials and follow the electric field lines. Let us first consider that the metallic plate potential is more positive than the surface potential of the cover glasses, whose potential is close to the barrier of potential. It may be due to the fact that the metallic patch is more sensitive to UVs and emits a higher current density. In that case, the electrons emitted by the plate and by the dielectric surrounding the plate are deflected from their original emission direction and are preferentially directed towards the metallic plate. Indeed, the barrier of potential induced by the large scale solar panel becomes highly repulsive for the electrons emitted in the positive region of the metallic patch vicinity. This plate tends then to become less positive since it collects more electrons than it emits. Finally, the system tends to reach the equilibrium state in which the plate has the same potential as the dielectric surface.

Let us now consider that the metallic plate is negative in comparison to the dielectric surfaces. The emitted electrons are then accelerated in the direction of the barrier of potential and only a few of them can be recaptured by the patch. As a result the patch simply gets more positive and the equilibrium state is the same as before.

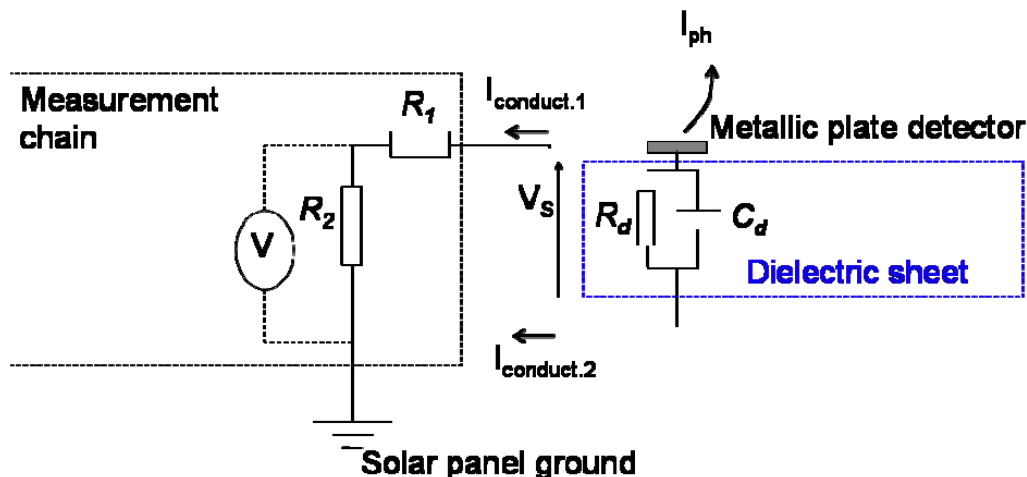


Figure 106 - Equivalent electric circuit of the ESD monitor

At this step it is important to notice that the scenario described above is valid only if the metallic plates are sufficiently isolated from the spacecraft structure. The current flowing through the resistor $R_M = R_1 + R_2$ is V_S / R_M with V_S the differential voltage between the patch and the solar panel structure. This current helps to replace the current emitted by the patch. The capability of the patch to float at the same potential as the dielectric surface depends then on the isolation resistor R_M . It is also necessary that the dielectric supporting the patch (which is possible to represent as a resistor R_d in parallel with a capacitance C_d) shall be sufficiently resistive. The equivalent electric circuit is represented in Figure 106, in which the dielectric support resistance is related to the dielectric resistivity ρ , to the thickness l and to A by $R_d = \rho \cdot l / A$.

Finally, the current balance writes:

$$C_d \frac{dV_s}{dt} = \sum I = I_{photo,emitted} - I_{photo,collected} - \frac{V_s}{R_M} - \frac{V_s}{R_d}$$

For a given voltage between the patch and the structure, if the conducted current is smaller than the net photoemitted current I_{ph} then the patch potential becomes more positive. The critical value of the isolation resistance R_c is defined by the area A of the patch, by the potential difference V_s between the dielectric coverings and the underlying structure, and by the photo electron current density j_{ph} and is written as:

$$R_c = \frac{V_s}{I_{ph}} = \frac{V_s}{Aj_{ph}}$$

Typically, for a photo current of 1 nA/cm², a difference of potential of 1000 V and a patch of 1 cm², the critical resistance is 1 TΩ.

Such kind of resistors have been found in the market, *cf.* Table 19. Extra exhaustive research could help find other resistors. Their value is 1 TΩ and they can be used with voltage of more than 6 kV.

Table 19 - High resistors supporting high voltage from SRT Resistor Technology

Type	Size	Value/Tolerance/TCR
HVR	30	1T 10% 10kV
GST	4020-NA	1T 10% 6kV

The isolation of the plate will be efficient only if the chain resistor is at least one order of magnitude greater than the critical resistor:

$$\frac{R_M R_d}{R_M + R_d} \gg R_c$$

10.2.2. Numerical Simulation

SPIS has been used to assess the capability of the monitor conceptual. The Time Dependent version has been used to take benefit of some of the last improvements of the code, *i.e.* the automatically variable time steps for the circuit solver and the particle backtracking for the calculation of the collected currents. The goal is to prove that the metallic plates will float to the neighbouring dielectrics floating potential if the resistors used to isolate the plates have a sufficiently high value.

10.2.3. Numerical Model

The geometrical model used is a spacecraft which is composed of a satellite whose dimension is 2 m × 2 m × 2 m and two solar panels whose dimensions are 10 m × 2 m × 0.2 m, *cf.* Figure 107. A metallic patch of 5 cm × 5 cm has been added in the middle of one solar panel front side.

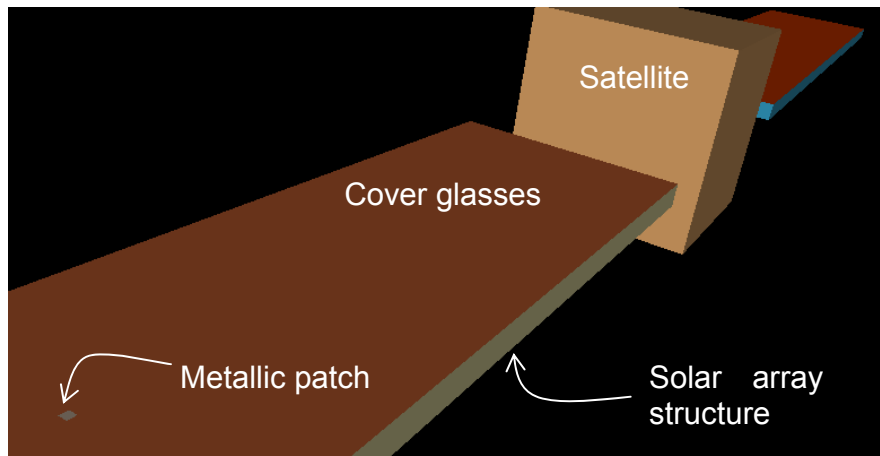


Figure 107 - CAD model of the patch of the spacecraft

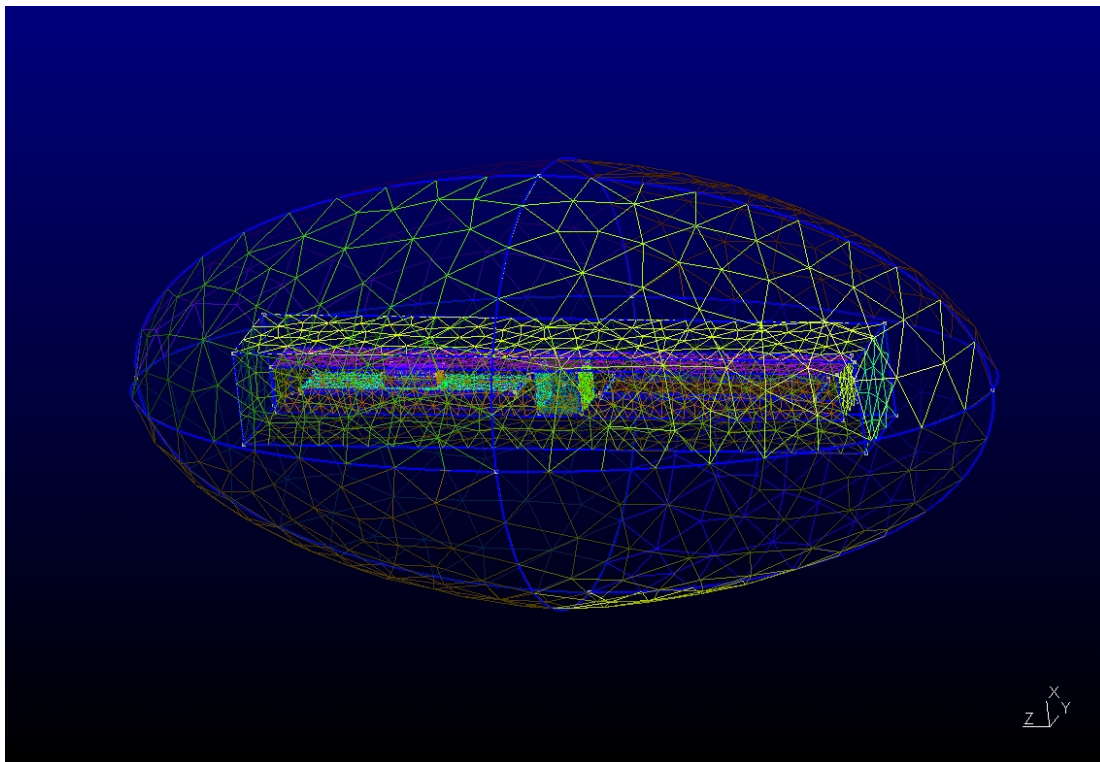


Figure 108 - Surface meshing at spacecraft length scale

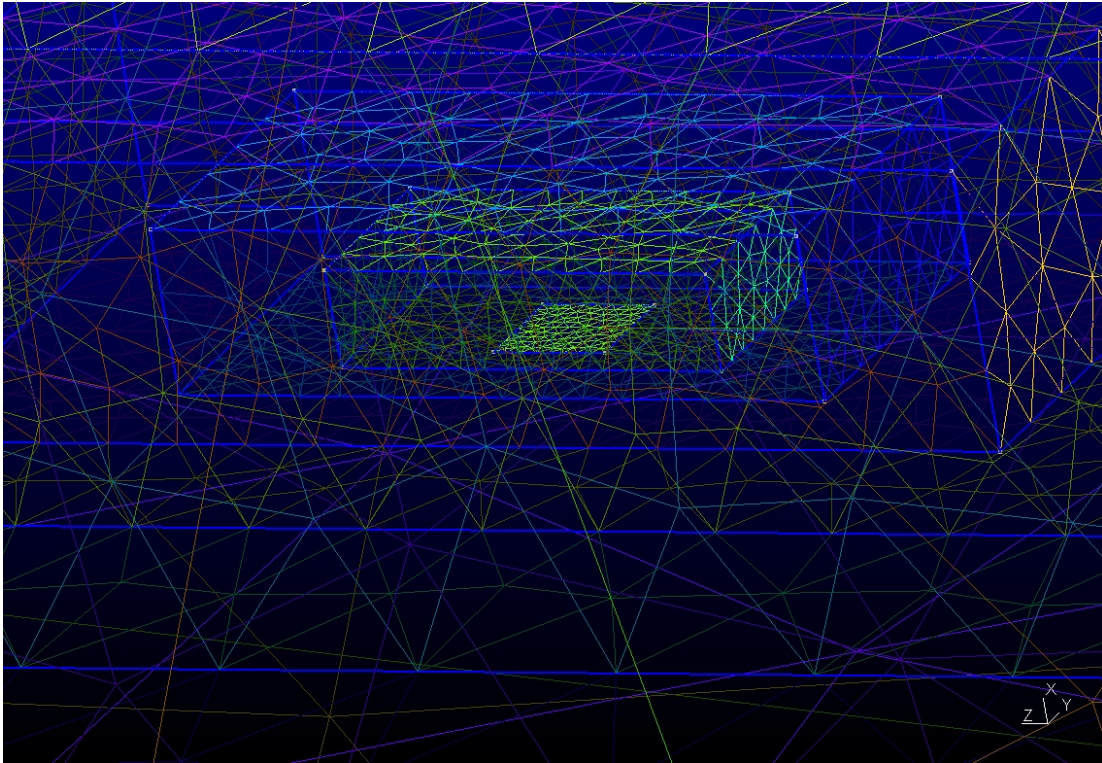


Figure 109 - Surface meshing at patch length scale

The meshing is depicted in Figure 108 and in Figure 109. In the vicinity of the patch, several nested boxes ensure the progressive refinement of the mesh grid. The mesh size is 6 mm on the patch and extends till 40 cm on the rest of the solar panel. The external boundary limit extends over 40 m and 20 m.

The spacecraft is immersed in a plasma composed of $3 \times 10^6 \text{ m}^{-3}$ of cold 1 eV electrons, $3 \times 10^6 \text{ m}^{-3}$ of warm 10 keV electrons and $6 \times 10^6 \text{ cm}^{-3}$ of 100 eV protons, *cf.* Table 20. Electrons follow a Boltzmann distribution, which is correct since all the potentials are negative in the present case. The ion dynamics is described by a Particle-In-Cell (PIC) method. The ion current collection on the surface elements is simulated by the backtracking method proposed by the code. For the circuit solver, the estimator of dI/dV relies on an OML assumption. The front side of the solar arrays are exposed to the sun and are covered with covering dielectrics (CERS, Cerium doped silicon with MgF2 coating). The photoemission current density is 2 nA/cm^2 on the solar array dielectric surface and 3.2 nA/cm^2 on the metallic plate. The photo electrons are followed by a PIC method and the dI/dV estimator for the circuit solver is based on the barrier model proposed by SPIS.

Table 20 - Environment for SPIS simulation of outer magnetosphere

	Electron density (cm ⁻³)	Electron temperature (eV)	Ion density (cm ⁻³)	Ion temperature (keV)
Population 1	3.0	1	6.0	100
Population 2	3.0	10 ⁴	-	-

The computation of the potential on a spacecraft immersed in the same environment has been performed previously [15]. The results showed that the spacecraft chassis floats at a potential of about -3000 V while the cover glasses float at -2000 V. In order to limit the CPU time, the simulation is started by initiating the potential to -2000 V on the cover glasses and to -3000 V on the spacecraft structure. For the circuit solver, a spacecraft capacitance of 10⁻⁶ F is taken into account and the patch is isolated from the structure by the resistor R_M . The system has been simulated with two different values of R_M . The goal of these simulations is to assess that the photoelectron current emission and recollection can be responsible of the homogenization of the surface voltages only if the isolation resistor exceeds the critical value R_C . In the present case, the voltage difference V_S between the dielectric coverings and the underlying structure is close to 1000 V, and the area of the patch is 25 cm². The equation (1) indicates that the critical value of the resistance $R_M (= R_1 + R_2)$ is then $R_M > R_C = 1.25 \times 10^{10} \Omega$.

The patch potential is initialized to a different potential from the dielectrics or structure potentials in order to assess its time evolution. In the first case, a resistor of 10¹² Ω is used. In that case it is expected that the floating potential of the final metallic patch would be close to the dielectric coverings potential, *i.e.* -2000 V. As a result we began the simulation with the patch potential of -2100 V. In the second case, the resistor is 10⁹ Ω in which case the isolation is thought to be no longer sufficient. We then initialized the potential of the patch to -2800 V. The reason why we choose to initialize the potentials to values not too far from the expected final potentials is to achieve reasonable CPU times. That does not change at all the physics of the problem.

10.2.4. Results

The results obtained with $R_M = 10^{12} \Omega$ are presented in the figures below. The potential evolution on the spacecraft is in agreement with the physical considerations introduced in paragraph 10.2.1. The potential on the spacecraft ground and on top of the cover glasses slightly evolves while the potential of the metallic patch rapidly tends towards the cover glasses potential, *i.e.* approximately -2000 V, *cf.* Figure 110.

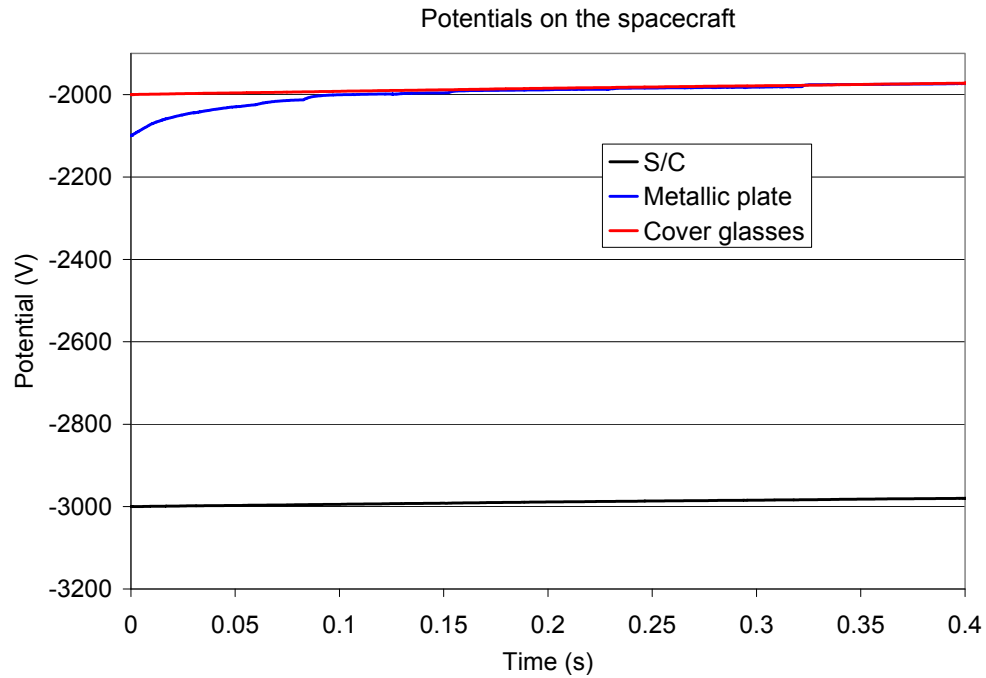


Figure 110 - Evolution of the potentials on the spacecraft in the case of $R_M = 10^{12} \Omega$

The plasma potential is represented in Figure 111. Even if the equilibrium state is not reached at satellite scale, the global barrier of potential is coherent with previous simulations [15]. The presence of the plate is not visible in Figure 112 (which represents the potential map in the cutting plane containing the patch) because the potential on the front side of the solar panel is quite homogenous.

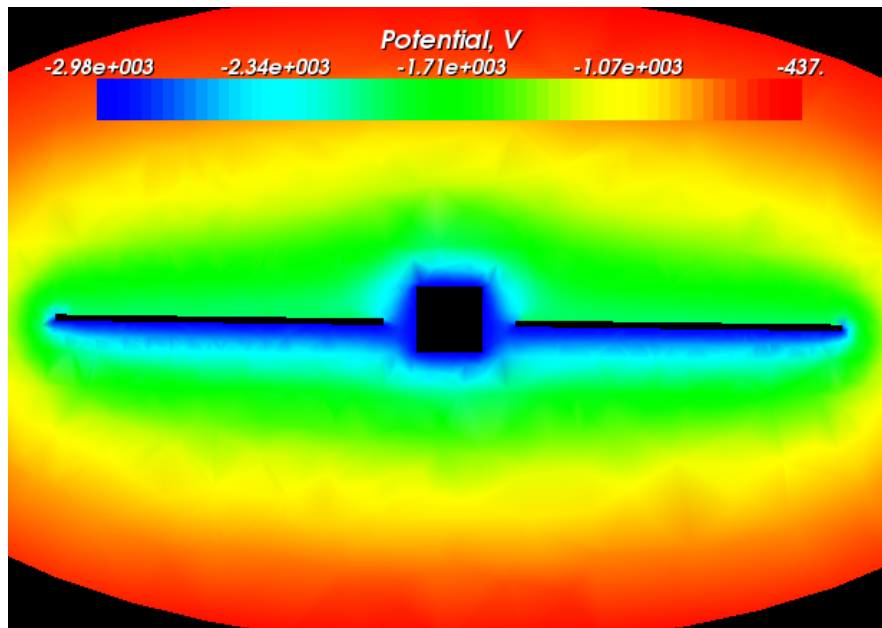


Figure 111 - Potential map around the spacecraft with $R_M = 10^{12} \Omega$

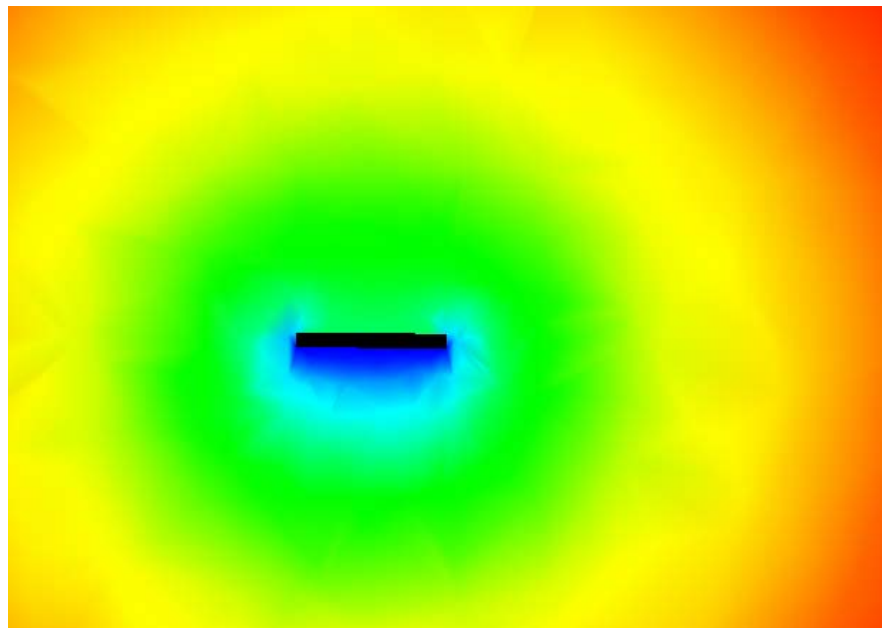


Figure 112 - Potentials in the cutting plane of the metallic plate with $R_M = 10^{12} \Omega$

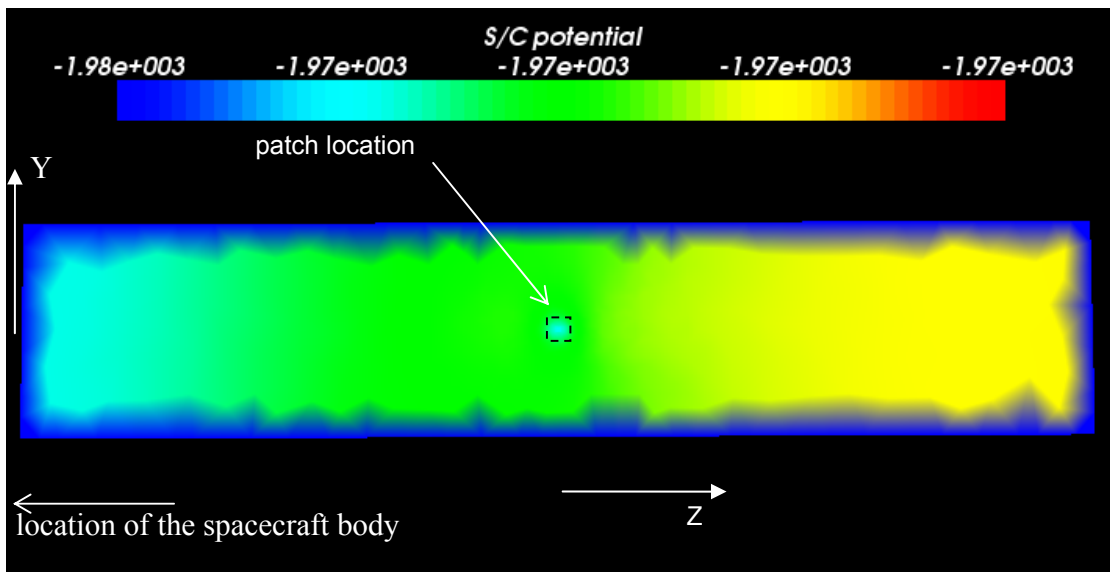


Figure 113 – Potential on the top surface of the solar array

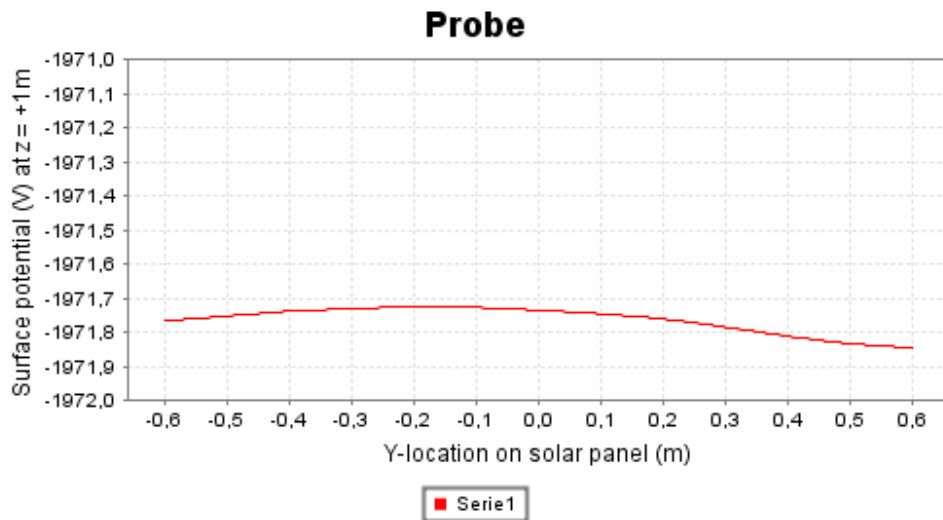


Figure 114 – Potential Y-profile on top of the solar array at location Z = 1 m from the patch

Figure 113 shows that the differential potential is higher at the end of the solar array than at the vicinity of the spacecraft, which is a classical result. Moreover, the differential potential is higher in the middle of the array width, where the barrier of potential is more positive than on the sides, see Figure 114. As a result, we can say that the ESD risk is higher and we recommend locating more patches there.

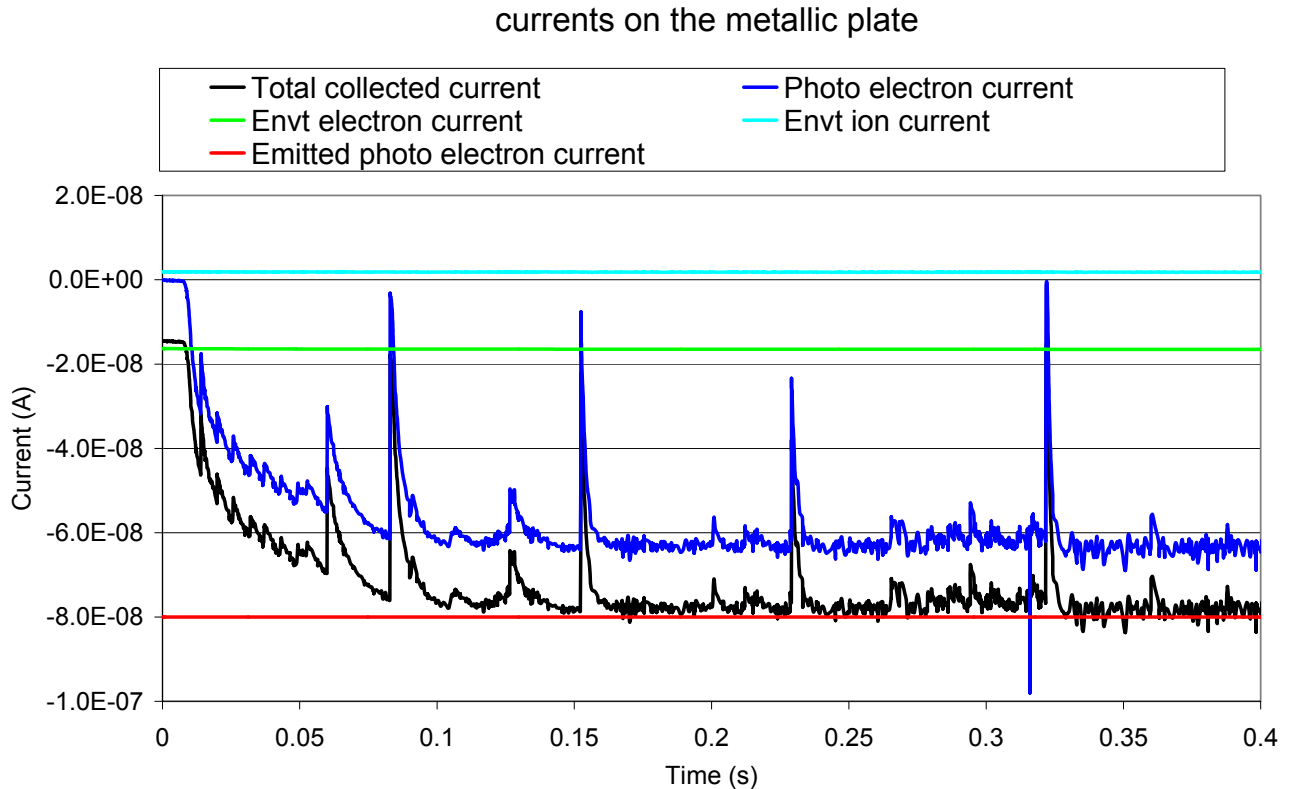


Figure 115 Evolution of the currents on the metallic plate in the case of $R_M = 10^{12} \Omega$

The currents emitted and collected by the patch are represented in Figure 115. The photo electron current emitted by the patch is $I_{ph} = 25 \text{ cm}^2 \times 3.2 \text{ nA/cm}^2 = -80 \text{ nA}$. The ambient electron and ion collected currents are -16 nA and $+2 \text{ nA}$ respectively. At the beginning, as the potential of the patch is negative w.r.t. the cover glasses, there is a very low recollection of photo electrons and the potential of the patch gets more positive, which in turn increases the recollection of photo electrons. At current balance, the potentials are uniform on the front side of the solar panel. The recollected photo electron current is about -65 nA , which signifies that 20% of the emitted electrons are extracted towards the limits of the domain. These electrons are replaced by 10 keV electrons collected from the environment. The equilibrium is reached when the total collected current is -80 nA (-65 nA from the photo electrons, -16 nA from the environment electrons, $+2 \text{ nA}$ from the environment electrons and $-1 \text{ nA} = -1000\text{V}/10^{12} \Omega$ from the electrical connection with the structure). Finally, there is no ESD risk since the differential voltage is less than 100 V , as required in ECSS [RD4].

In the case $R_M = 10^9 \Omega$, the initial current I_R is $-1 \mu\text{A}$, which is much higher than the photo current I_{ph} . The patch potential then rapidly decreases and converges to -2977 V , *cf.* Figure 116. At that time, the voltage difference between the patch and the structure is $+66 \text{ V}$ and the replacement current flowing through the resistor is $I_R = -66 \text{ nA}$. The ambient electron and ion currents are still -16 nA and $+2 \text{ nA}$ respectively. The equilibrium state of the patch is then reached ($-66 \text{ nA} - 16 \text{ nA} + 2 \text{ nA} = -80 \text{ nA}$). There is no recollection of photo electrons on the patch because of its highly negative potential w.r.t the cover glasses. In this case,

there could be an ESD risk since the differential voltage is much higher than 100 V and since the capacitance between the patch and the structure is greater than 10 pF.

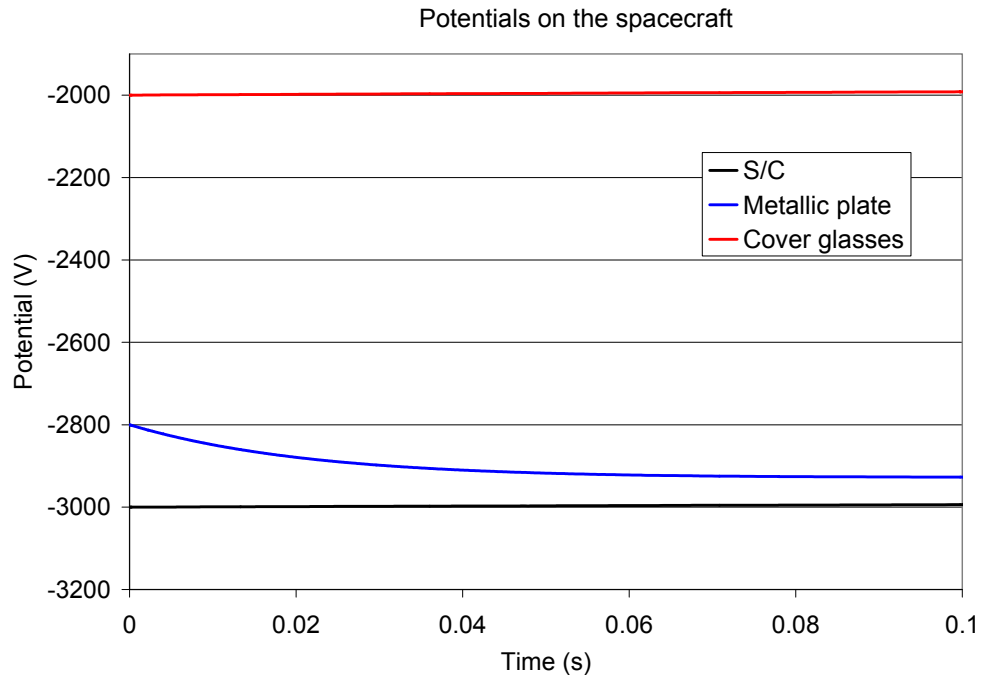


Figure 116 - Evolution of the potentials on the spacecraft in the case of $R_M = 10^9 \Omega$

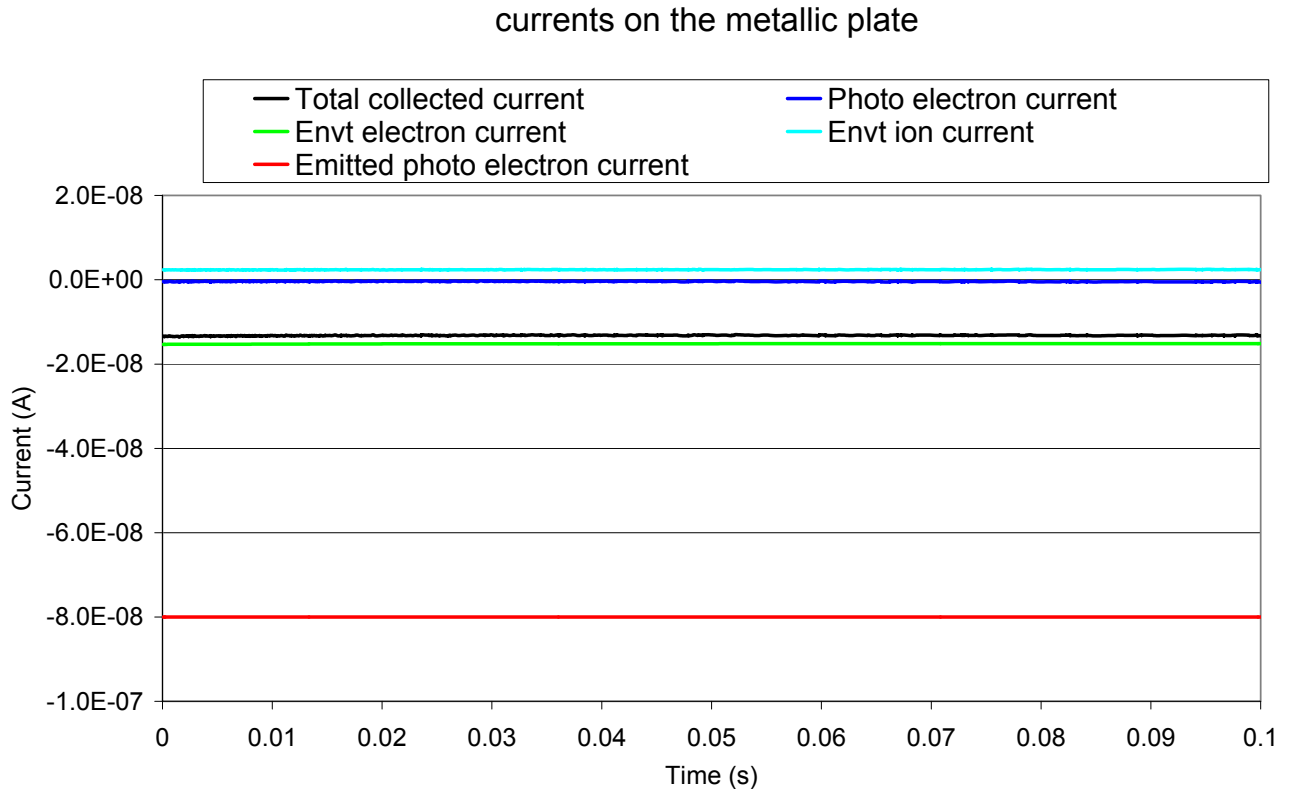


Figure 117 - Evolution of the currents on the metallic plate in the case of $R_M = 10^9 \Omega$

The simulated cases aimed at simulating a substorm environment in which energetic electrons are injected. In comparison to the ECSS worst case environment presented in section 2.2.1 and summarized in Table 21, we can notice that the present electron energy and density are respectively 0.36 and 2.5 of the ECSS worst case values. That leads roughly to the same thermal current density ($5 \mu\text{A}/\text{m}^2$ for the ECSS environment and $10 \mu\text{A}/\text{m}^2$ in the present simulations). In the two cases, the photo currents ($20 \mu\text{A}/\text{m}^2$ on the dielectrics and $32 \mu\text{A}/\text{m}^2$ on the metallic patch) are much higher than the environment currents. In conclusion, we can extrapolate the monitor assessment to the ECSS worst case environment (and to lower GEO charging environments too).

Table 21 - ECSS-E-10-04A Worst-case bi-Maxwellian environment for outer magnetosphere

	Electron density (cm^{-3})	Electron temperature (keV)	Ion density (cm^{-3})	Ion temperature (keV)
Population 1	0.2	0.4	0.6	0.2
Population 2	1.2	27.5	1.3	28.0

10.2.5. Experiments

10.2.5.1. Preliminary Experiments

Preliminary experiments have been performed in order to provide a first estimation of the behaviour of such an ESD monitor. The goal of these preliminary experiments is to show that an adequate isolation of the substrate on which the metallic plates are placed is necessary. It also aims at validating the fact that even if the metal and the dielectrics have not the same photo electron current (as *e.g.* 2 nA/cm² for epoxy and 4 nA/cm² for aluminium oxide, for normally incident sunlight at 1 AU), they can float at the same potential because of the photo electron recollection on the surface elements that tend to get more positive than the barrier of potential.

The sample consists of a thin aluminium patch of dimensions 20 mm × 20 mm simply placed on a 1.7 mm thick and 120 mm × 70 mm large epoxy plate, which is metallized on its rear side surface, *cf.* Figure 118. The resistance between the metallic patch and the metallization (which simulates the spacecraft structure) is very high (the resistance of the epoxy layer indeed). The resistivity of epoxy is $10^{-14} \Omega^{-1} \cdot \text{m}^{-1}$, which gives an approximate value of the resistance between the patch and the metallization of $4 \times 10^{14} \Omega$. According to equation (1), this value should be sufficient to ensure the isolation of the patch. The capacitance between the patch and the metallization is approximately 8 pF.

The sample is placed in the ONERA vacuum chamber CEDRE, *cf.* Figure 47. The vacuum is about 10^{-5} mbar. A UV source (Deuterium lamp) is used to simulate the photo emission. The tank walls are at ground potential. The metallization is set to a potential of -1000 V potential. We then simulate the photoemission process in the case of a barrier of potential of +1000 V. The surface potential profile is measured thanks to a potential probe at the initial time and after an irradiation of some minutes.

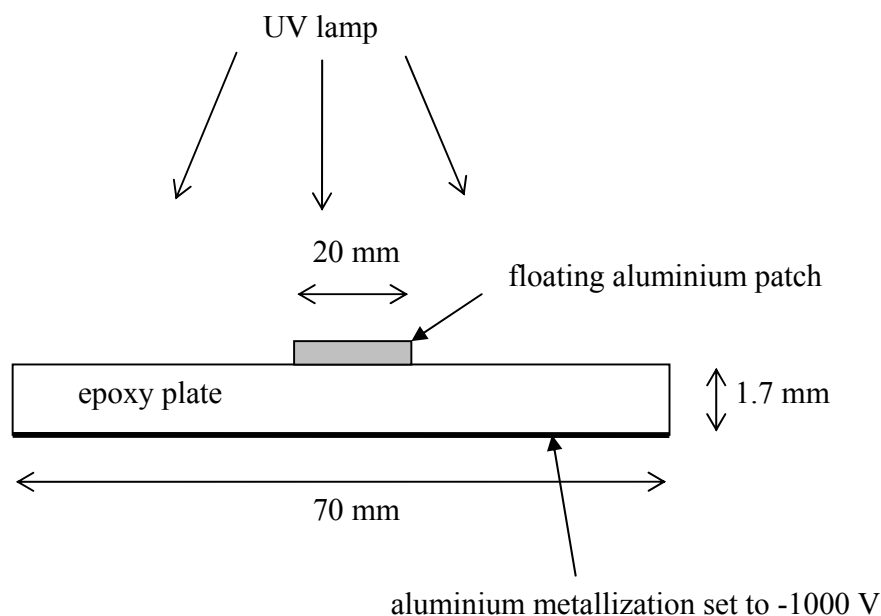


Figure 118 - Sample used during the experiments

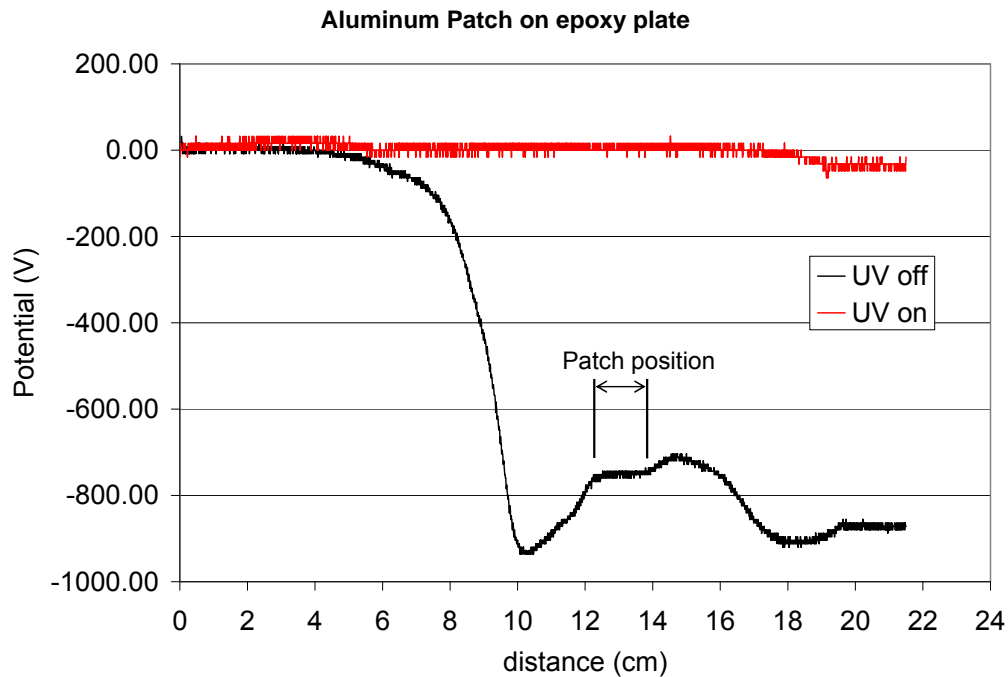


Figure 119 - Potential profile on top of the sample; bias voltage is -1000 V

It appears clearly in Figure 119 that the photoemission rapidly homogenizes the surface potential of the sample. The patch potential is the same as the epoxy surface potential, *i.e.* 0 V, the voltage of the tank walls. That confirms that the dielectrics potential reaches the value of the barrier and that the resistance between the patch and the structure is sufficient to ensure the isolation of the metallic plate. We can expect that a sufficiently high resistor component would also have the same capability. Moreover, no ESD has been observed. The evidence of the monitor behaviour with adequate resistors R_1 and R_2 could be performed during a devoted experimental campaign.

10.2.5.2. Experiments with High Resistors

The same setup as in paragraph 10.2.5.1 has been adding a resistor between the sample structure and a 1 cm² metallic patch. In a first time, the photoemission current was measured to 0.95 nA with the setup of Figure 121. As result, the critical resistor for a -1000 V bias potential was close to $10^{12} \Omega = 1 \text{ T}\Omega$. The setup used to validate the ESD monitor concept is represented in Figure 121. The bias potential is -1000 V and different values have been used for the resistor R_1 . The results of show clearly that the metallic patch floats to the near 0volt potential of the surrounding dielectrics if R_1 is greater than 1 T Ω . This result validated the capacity of the ESD monitor concept to give access to the surrounding dielectrics and so on to the barrier of potential (0V in the CEDRE tank).

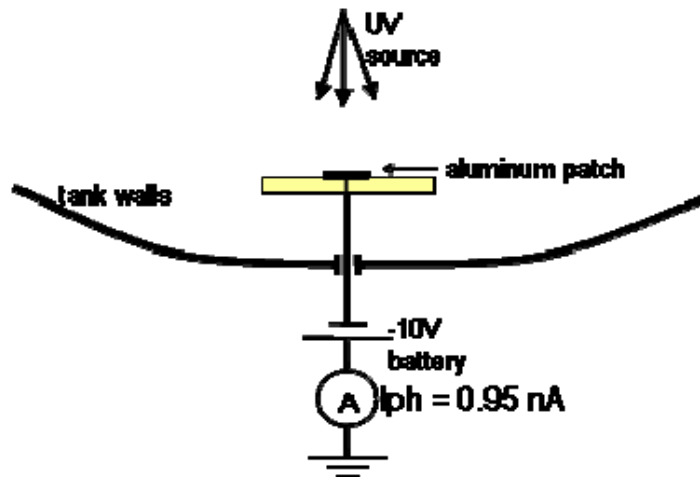


Figure 120 – Photoemission current setup

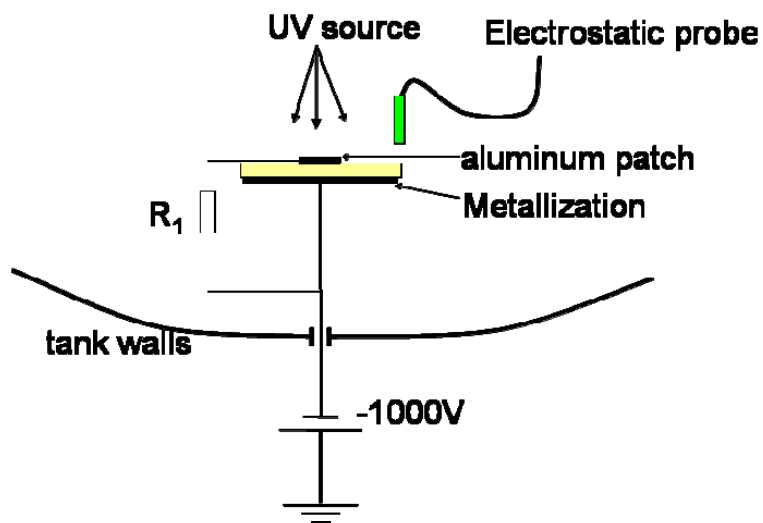


Figure 121 – Experimental setup for the validation of the ESD monitor concept

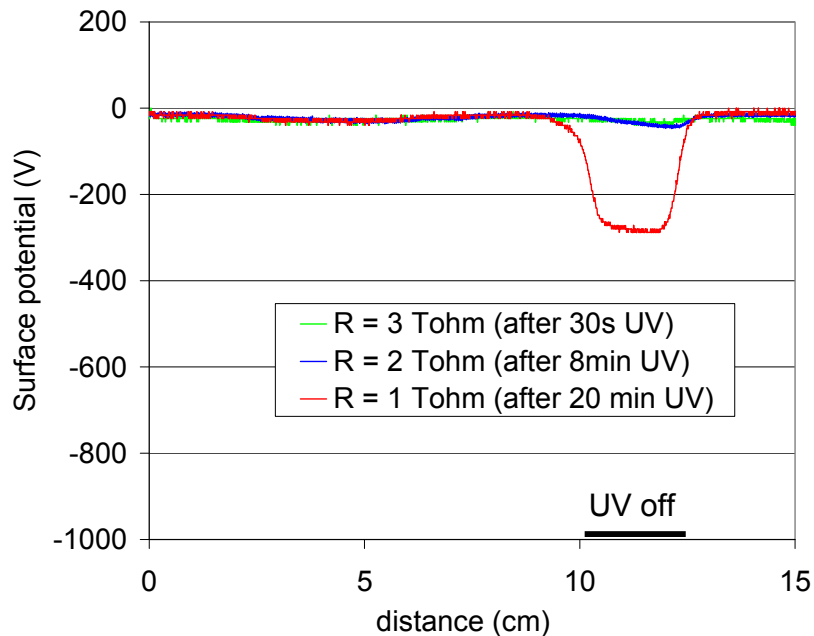


Figure 122 – Equilibrium potential profile upon the patch for different insulating resistors

10.2.6. Discussion

The theoretical considerations on the recollection of photo electrons on the solar panels have been confirmed by numerical simulations and by a test campaign. The photo emission tends to homogenize the surface potentials. With metallic plates sufficiently isolated from the spacecraft structure it seems possible to have a fairly good estimation of the dielectric potential at any stage of the charging and discharge processes if the measurement sampling is adapted.

10.3. Conclusion

Associated with the background knowledge of ESDs on solar cells coupons and solar panels, this study revealed the main topics to be addressed. It is recommended:

- to place the metallic plates on the front panel,
- to place them on cover glasses without underlying solar cell or on adequate dielectric such as glue with a sufficient resistivity,
- to make the wiring go through the cover glass (or the glue) without interfering with the adjacent solar cells,
- to have a maximal distance of 1 m between them,
- to preferentially locate them in the regions in which the differential voltages are the higher, *i.e.* at the end of the solar array,
- to perform a measurement with a period of 1 s (**to be adapted to environment conditions**)
- to isolate the plates with respect to the structure with a resistance one order of magnitude greater than the critical resistor (resistors of $1\text{T}\Omega$ exist on the market),

- to use metallic patches whose capacitance with respect to the structure is less than 10 pF,
- to use a voltmeter with an input impedance greater than R_2 (typically more than 1 Gohm) with no leakage to the structure,
- if it is not possible, then to use an adequate nano ammeter.

We also strongly recommend performing tests in vacuum chamber in order to:

- **consolidate the validation of the ESD monitor on more realistic solar panel configurations, associated with a patch potential measurement chain**
- **assess that there is no ESD risk associated with the presence of the metallic plates.**

The possibility to integrate of such an ESD monitor on telecom satellites solar panels is discussed in APPENDIX 1.

11. APPENDIX 1 - ESD MONITOR CONCEPTUAL DESIGN – SPACECRAFT INTEGRATION

See the document referred as: "Technical Note 2 - Part 2 – Spacecraft Integration" in annex.

12. APPENDIX 2 – SPIS-ESD USER MANUAL

See the document referred as: "User Manual (UM) of Wizard Based Modules" in annex.



**Contract No.
22048/09/NL/AT**

Ref : **2125.NT.MS.10.0288.ASTR**
Issue : 01 Rev. : 00
Date : 19-01-10
Page : i


Title

**Development of a Predictive Discharge Numerical Model on
Solar Panels**


TECHNICAL NOTE 2

Part 2 - SPACECRAFT INTEGRATION

ESTEC Contract No. 22048/09/NL/AT

	Name and Function	Date	Signature
Prepared by	Marc SEVOZ <i>Telecoms EMC-ESD Specialist</i>	<i>19.01.10</i>	

Document type	Nb WBS	Keywords
		ESD – Satellite - Integration

	Contract No. 22048/09/NL/AT	Ref : 2125.NT.MS.10.0288.ASTR Issue : 01 Rev. : 00 Date : 19-01-10 Page : ii
---	--	---

SUMMARY

Main requirements and constraints to implement the ESD monitor chain on a GEO Spacecraft, as proposed by ONERA in TN2 Part1 of WP200, have been identified and recalled in this document :

Isolation from Solar array ground > 1e+13 ohms : reuse of space qualified insulators and harness : **OK**; isolation inside **SADM** needs to be checked.

For dielectric items judged critical, isolation is recommended to be checked by vacuum ground tests, in space environment (SIRENE-like electron irradiation)

Numbers of Sensors (metal plates bonded on Solar array panel front side) : **location** on Solar array front side = **OK**, but numbers of channels limited by the number of spare slip rings allocated to signals at SADM level.

Absence of ESD risk due to highly isolated metal plates (triple points) to be demonstrated by ground tests.

Resistor bridge for potential conversion to be located on Solar array rear side (as per bleeding resistors or blocking diodes) : **OK**

DHS acquisition chain may need to integrate additional constraints for measurement **accuracy** purpose : current leakage from Operational amplifier limited to 500pAmps max (thermal control ?)

Wireless acquisition not mature for such embarked application.

Immunity to noise sources (**EMC**) needs to be assessed (Analysis and/or tests : expected **OK**)

Quality assurance aspects : intensive use of space qualified parts, materials and processes is recommended;

ESD monitor must be declared as **EEE part** (for a simplified documentation and qualification test campaign); **Open point : no found existence of (space) qualified 1TΩ resistor as a discrete component (delta or full qualification seems unavoidable)**

Validation plan needs to be raised at subsystem level.

Document controlled by MS



Contract No.
22048/09/NL/AT

Ref : **2125.NT.MS.10.0288.ASTR**
Issue : 01 Rev. : 00
Date : 19-01-10
Page : iii

DOCUMENT CHANGE LOG

Issue/ Revision	Date	Modification Nb	Modified pages	Observations
01/00	Nov09	-	All	Original

PAGE ISSUE RECORD

Issue of this document comprises the following pages at the issue shown

Page	Issue/ Rev.	Page	Issue/ Rev.	Page	Issue/ Rev.	Page	Issue/ Rev.	Page	Issue/ Rev.	Page	Issue/ Rev.

TABLE OF CONTENTS

1	INTRODUCTION	1
1.1	NOMENCLATURE.....	2
1.2	ACRONYMS.....	2
1.3	REFERENCE DOCUMENT	2
2	ESD MONITOR CONCEPTUAL DESIGN (WP210 MAIN OUTPUTS).....	3
3	REQUIREMENTS & CONSTRAINTS FOR IMPLEMENTATION ON SPACECRAFT	4
3.1	FUNCTIONAL & INTERFACE REQUIREMENTS.....	5
3.1.1	<i>Implementation constraints on Solar Array</i>	5
3.1.2	<i>Compatibility to Solar Array Drive Mechanism (SADM)</i>	9
3.1.3	<i>Compatibility to Data Handling Subsystem (DHS)</i>	10
3.2	DESIGN & MANUFACTURING REQUIREMENTS	12
3.2.1	<i>Parts Materials & Process</i>	12
3.3	QUALITY ASSURANCE REQUIREMENTS	15
3.3.1	<i>Classification & Documentation</i>	15
3.3.2	<i>Inspection & Tests</i>	15
4	CONCLUSIONS	16

	<p align="center">Contract No. 22048/09/NL/AT</p>	<p>Ref : 2125.NT.MS.10.0288.ASTR Issue : 01 Rev. : 00 Date : 19-01-10 Page : 1</p>
---	---	---

1 INTRODUCTION

"Development of a Predictive Discharge Numerical Model on Solar Panels" is a project (ESA Co-22048) whose purpose is both to :

- develop a numerical tool for the assessment of the electrostatic discharge (ESD) hazard on spacecraft solar arrays,
- propose a conceptual design for ESD monitoring on solar panels (Task2 – WP200 – ONERA responsibility)

In the frame of the ESD monitor conceptual design & physical assessment, the purpose of the WP220 Task is to identify all applicable requirements and constraints for a proper implementation of the potential sensor + acquisition chain on a Spacecraft in GEO orbit (Telecoms typical application).

WP 220 activity is attributed to EADS-Astrium-SAS EMC-ESD team for its wide knowledge of the System electrical architecture and ESD expertise on Telecoms Spacecraft & Solar Arrays.

This technical note, after a synthesis of the ESD Monitor conceptual design (= outputs from WP210, RD1) will identify the main constraints of implementation (layout, electrical requirements, parts and process) on a standard Solar Array, and will elaborate on the feasibility to validate & embark such ESD monitor on a Telecom Spacecraft.

1.1 NOMENCLATURE

Ibias	Input bias current of Operational Amplifier [pA]
ρ	Dielectric bulk resistivity [Ω .m]

1.2 ACRONYMS

CVG	Cover glasses
DHS	Data Handling Subsystem
ESD	Electrostatic Discharge
FMECA	Failure Mode Effects and Criticality Analysis
OA	Operational Amplifier
PMP	Parts Materials & Processes
RHA	Radiation Hardness Assurance
SA	Solar Array
SADM	Solar Array Drive Mechanism
SC	Spacecraft
SCA	Solar Cell Assembly
TBC	To Be Confirmed
TBD	To Be Defined
TC	Tele command
TM	Telemetry

1.3 REFERENCE DOCUMENT

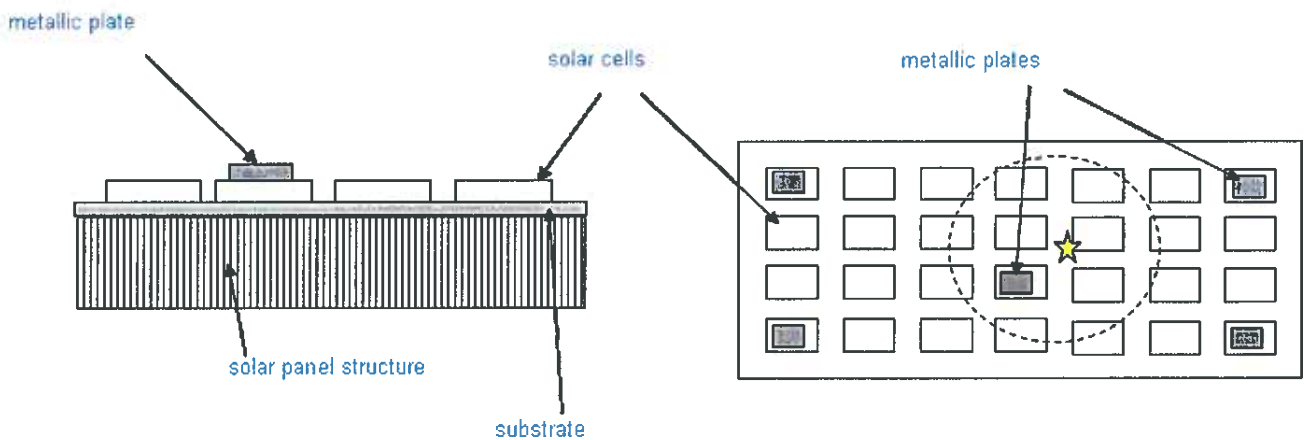
[PROP]	Proposal for the development of a predictive Discharge numerical model on Solar panels, in response to AO/1-5849/08/NL/AT, ONERA, ARTENUM, EADS-ASTRIUM
[RD1]	Technical Note 2, Part 1 ESD Monitor Conceptual Design & Assessment (WP 210- ONERA)
[RD2]	Generic Eurostar E3000 Solar Array Specification (EUR3-SP-07079-T-MMS, iss04) – (Restricted)

2 ESD MONITOR CONCEPTUAL DESIGN (WP210 MAIN OUTPUTS)

ESD Monitor concept is based on small metallic plates (few cm²) bonded on Solar array front side (on solar cells coverglasses), floating at the same potential than adjacent coverglasses, and disseminated on extended locations, for possible large surface discharge detection (Flashover-type).

Homogeneous potential between metallic plate & adjacent coverglasses is ensured if achieved isolation of the metallic plates versus Solar array panel ground is at least in the same magnitude of order than the series resistance of the measurement circuit (i.e 1TΩ); photo-emission mechanism trends then to homogenize the surface potentials, even if photoelectron currents of metals are different from dielectrics photoelectrons ones.

Barrier of Potential is expected close to the Differential potential between Front side metallic plate potential and Spacecraft structure potential (ground).



Repartition of the metallic plates on the front side of the Solar array panel shall be defined to allow large surface discharge detection : min 1 meter (ground test experience)

Integrity of the flight hardware (immunity to ESD & Secondary arcing) has to be guaranteed during lifetime, despite of unavoidable addition of Triple junction points (metal plate/coverglass/vacuum) : high series resistance is believed to play a mitigation role by limiting available current to few nano-Amps, such current value being not sufficient to obtain transition to cathodic spot then ESD (few milli-Amps are necessary as a minimum).

3 REQUIREMENTS & CONSTRAINTS FOR IMPLEMENTATION ON SPACECRAFT


For qualification purpose, ESD monitoring chain will be compliant to the whole requirements given in Generic Solar Array Specification (RD2) :

- **Functional & Interface Requirements**
 - Implementation constraints on Solar array
 - Compatibility to SADM Interface (Mechanical, Electrical)
 - Compatibility to Data Handling Subsystem

- **Design & Manufacturing Requirements**
 - Parts Materials and Process
 - Electrical /Mechanical /Thermal design /Safety

- **Quality Assurance Requirements**
 - Classification & Documentation
 - Inspection & Tests

The whole constraints listed here above will be discussed in details in the following sections.

	Contract No. 22048/09/NL/AT	Ref : 2125.NT.MS.10.0288.ASTR Issue : 01 Rev. : 00 Date : 19-01-10 Page : 5
---	--	--

3.1 FUNCTIONAL & INTERFACE REQUIREMENTS

3.1.1 Implementation constraints on Solar Array

3.1.1.1 Isolation from Solar Array structure

In order to achieve potential on the metallic plates identical to the Solar cells cover glasses potential, **high isolation between the plates and the Solar Array panel** must be ensured : the metallic plates on front side will be bonded by epoxy adhesive, space qualified in a wide operational temperature range (-180°C/+60°C) :

- either on Solar cell cover glasses (CMX), mounted without the cell substrate, and bonded on 50µm thickness Kapton film
- or directly on 50µm thickness Kapton film (preferred, except if isolation expected not sufficient)

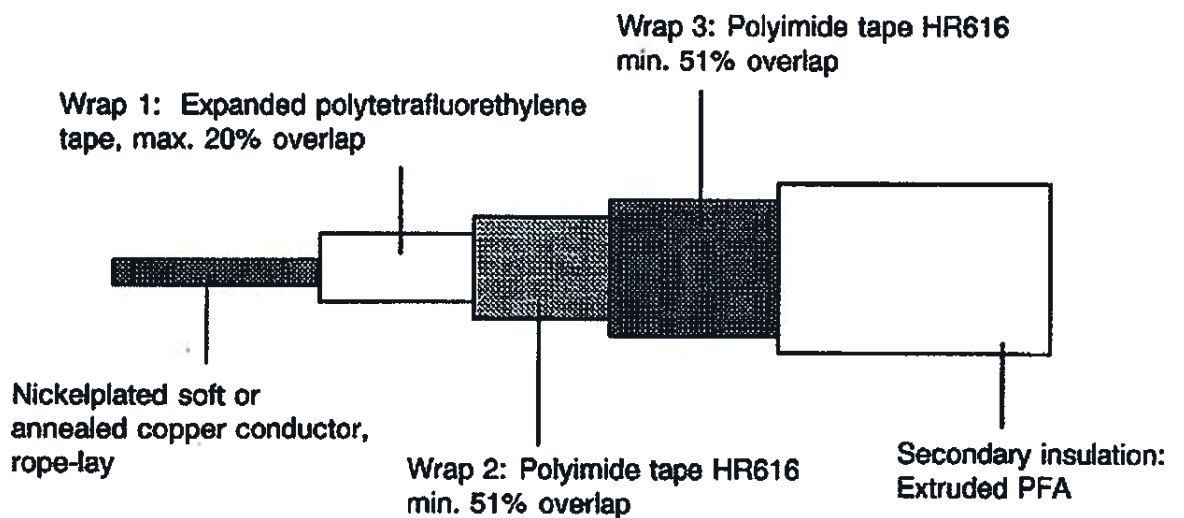
Plates are requested to be insulated from the solar array structure to avoid that high current leakages give inaccurate potential measurements. The measured resistance shall be greater than $R_{critical} = 1e+12 \text{ Ohm}$ (1TOhm) between metallic plates and the mounting panel. **A value of $R = 1e+13 \text{ Ohm}$ (10 TOhms) is targeted** (10 factor margin).

-> **RTV691S, DC93500 or Tactix (Epoxy) adhesive** can be proposed, as space qualified adhesive, already used in Solar Cell Assembly, so compatible of specified thermal and mechanical environments, and are presenting **Bulk resistivity higher than $1e+13 \text{ Ohm.m}$** (End of life, and Temperature): assuming metal patches of 1cm² bonded with minimum adhesive thickness of 100µm, equivalent isolation resistance is expected compatible to (i.e higher than) $R_{critical} = 1e+13 \text{ Ohm}$.

Requested isolation is recommended to be checked by vacuum ground tests, in space environment (SIRENE like electron irradiation)

Harness isolation is expected to be achieved through **triple layers** insulated space qualified wiring, as per ESA/SCC specification applicable to space applications harness, like,

ESA/SCC N°3901/017 specification :



Bare Kapton (Polyimide) insulative layers are proposed.

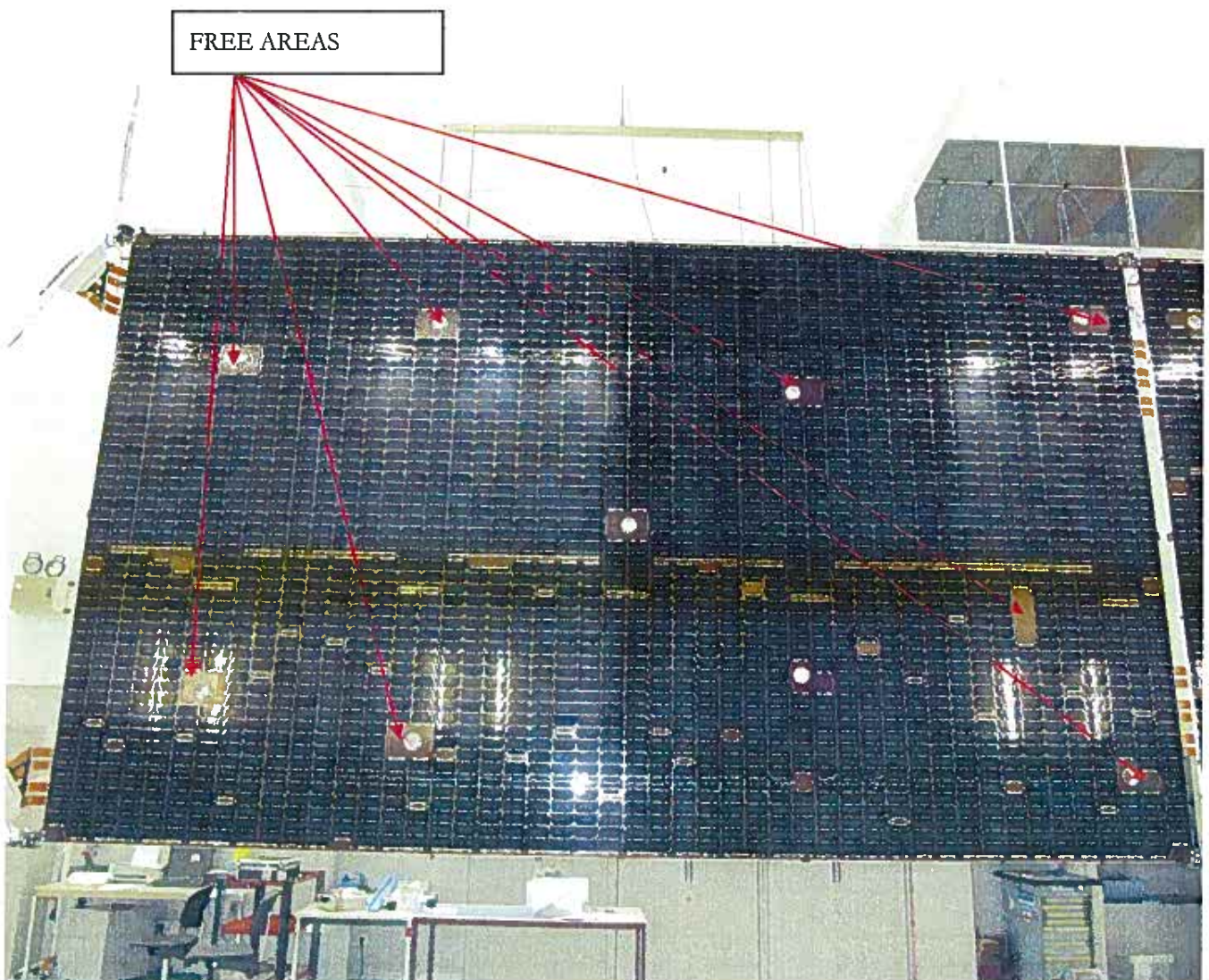
Remark : Anti-Static Wire (ASW) is not recommended, since slightly conductive, as well as Tefzel (PTFE) or Teflon derivative is prohibited by most of the commercial customers for ESD risk.

Solar array Harness being mainly routed on the **rear side** of the solar panel, shadowing will limit photoconductivity effect, and would keep acceptable isolation versus structure.

3.1.1.2 Solar Array free mounting areas

It can be envisaged to bond the metal plates on areas free of solar cells, on the front side of the solar array (Kapton baseplate). Minimum 9 locations around hold down points are available on each panel.

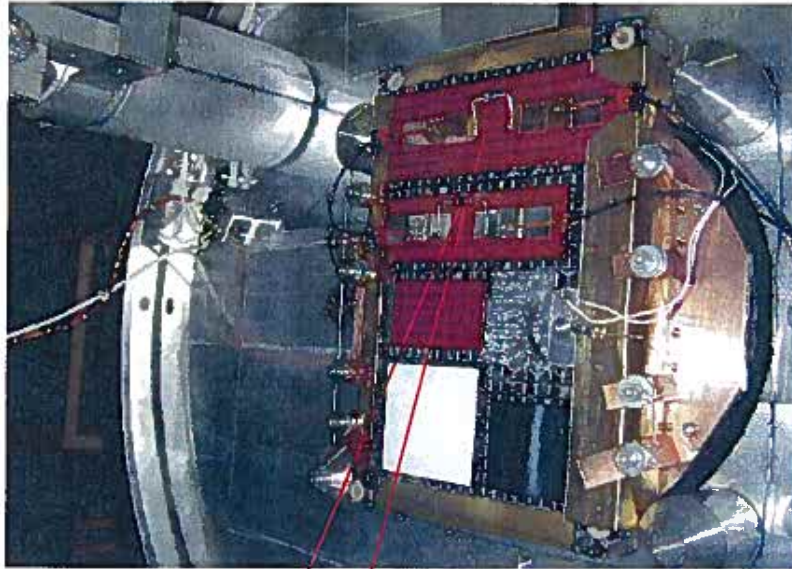
Inner panel is preferred to minimize harness length and then to comply with isolation requirements, but on another hand, max potentials (ESD risk situations) are expected to be found on outer panel of the solar wing. Compromise still to find.



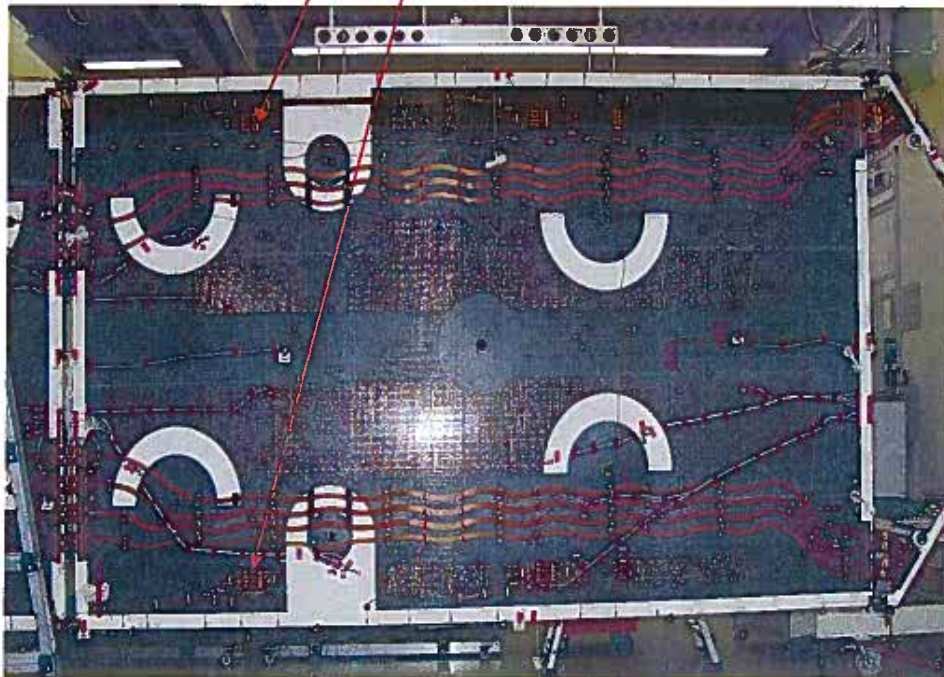
Exemples of free areas on Solar Array panel (front side)

Rear side : resistor boards location

Harness will connect metal plates to a resistor bridge externally mounted on the rear side of the Solar array (as per existing bleeding resistors or blocking diodes typically mounted on 50µm thickness Kapton boards, via qualified processes).



Diode and resistor boards ESD qualified in Sirene chamber (Onera)



Solar Array panel (rear side)

	<p align="center">Contract No. 22048/09/NL/AT</p>	<p>Ref : 2125.INT.MS.10.0288.ASTR Issue : 01 Rev. : 00 Date : 19-01-10 Page : 9</p>
---	---	--

3.1.1.3 Metallic triple junction points creation on ESD sensitive areas (Solar array front side)

Implementation of highly isolated metallic & uncoated patches, showing an absolute potential close to Coverglasses one, i.e in Inversed Potential Gradient situation (surface potential less negative than SC structure) may be seen as a Metallic discharge risk (ESD) in Blow off (discharge of the Satellite capacitance)

Such primary discharge close to solar cells, could ignite an electrical arc, responsible of potential damages on hardware (solar cells efficiency loss) : This is NOT ACCEPTABLE.

Nevertheless, it is stated by ONERA that transition to cathodic spot (electron avalanche and blow off), would not be possible, due to lack of current (some milliAmps minimum might be necessary, when available current will be limited to some nanoAmps max by 1e+13 series resistors.

THIS STATEMENT IMPERATIVELY NEEDS TO BE VALIDATED BY ESD TESTS IN ORDER TO CONFIRM ABSENCE OF ANY ESD RISK TRIGGERED BY THE ESD MONITOR DESIGN ITSELF !!

3.1.2 Compatibility to Solar Array Drive Mechanism (SADM)

Each metallic plate potential signal is routed from the Solar array to the acquisition boards through the **Solar Array Drive Mechanism (SADM) Interface**.

One specific connector and corresponding slip rings inside the SADM is dedicated to low levels signals; Solar Array sections are routed on dedicated power connectors and segregated slip rings inside the SADM.

ESD monitor signal is **compliant** to max voltage/current rating specified for SADM, in the case where the Voltage conversion (division) is performed on Solar array side.

For each metal plate, one 1 slip ring + dedicated wire will be allocated.

Remark : on typical Telecoms Spacecrafts, depending on the design capability, only few signal slip ring are left spare... (and very few spare power slip rings, but they are not recommended to be used for transferring SC external signals, which might be a high electrical arcing risk when routed close to power slip rings inside the SADM).

Isolation constraints will have to be characterized between ESD monitor signal on slip ring, and SADM structure (= SC structure)

Wireless solution ? it would allow to save SADM slip rings + cabling, but **not qualified**, and anyway needs implementation of transmitters on solar array and receivers on acquisition board (Delta qualification)

3.1.3 Compatibility to Data Handling Subsystem (DHS)

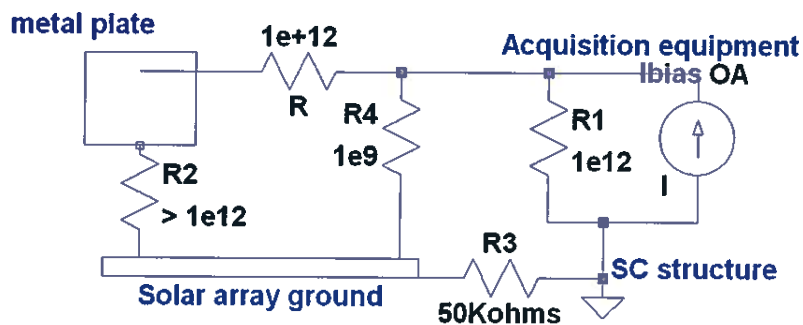
Measurements of potential will be achieved through voltage divider bridge, converting few Kilo Volts range in a **full scale 5V range**, with adequate sampling rate (better than 1second is easily achievable) for observability purpose.

Trade off :

- Resistors are externally mounted on the rear side of the Solar array (as per Solar array 100KOhms bleeding resistors or blocking diodes): **preferred solution**
- Voltage division performed by the DHS equipment : save additional components on Solar array, but :
 - Relatively high differential potentials are routed through power connectors/SADM slip rings (Arcing risk to manage)
 - Isolation loss + noisy signal situation is more risky (because of higher harness length for which isolation requirement apply)
 - DHS Interface to specify, develop and qualify


EMC : Sources of Noise as Solar array section toggling (few KHz) must be characterized in term of Crosstalk coupling toward ESD monitor harness (impact could be physical segregation or additional over-shielding requirements)

3.1.3.1 Electrical scheme (principle)



- Full scale 5V signal can be coded on 12bits with current design : accuracy of the measurement = $5V / 2048 \approx 2.5V / \text{LSB}$ (OK)
- Electrical constraints on Acquisition equipment side are the following :
 - Negative potentials reading capability must be ensured (limited number of inputs on existing DHS design)
 - Acquisition Operational Amplifiers with Low Input bias current, for accuracy purpose : must be much lower than full scale nominal current = $5\text{Volts} / 1\text{Gohms} = 5\text{nAmps}$
- Target : **max I_{bias} = 5nA / 10 = 500pAmps**
- **Standard OA** used in current DHS acquisition interfaces present typical input bias current of 10nAmps to 100nAmps : **NOT compliant.**
- **JFET based OA** (LF 155 Operational Amplifier) may be a solution : **30pAmps and $1e+12$ input impedance at ambient T°**(see further slide)

Remark : I_{bias} is exponentially increasing with T°!!! (50nAmps at +125°C) : Thermal control may be an additional constraint for measurement accuracy purpose.

 National Semiconductor	December 2001
LF155/LF156/LF256/LF257/LF355/LF356/LF357 JFET Input Operational Amplifiers	
General Description These are the first monolithic JFET input operational amplifiers to incorporate well matched, high voltage JFETs on the same chip with standard bipolar transistors (BI-FET™ Technology). These amplifiers feature low input bias and offset currents/low offset voltage and offset voltage drift, coupled with offset adjust which does not degrade drift or common-mode rejection. The devices are also designed for high slew rate, wide bandwidth, extremely fast settling time, low voltage and current noise and a low 1/f noise corner.	<ul style="list-style-type: none"> ▪ Logarithmic amplifiers ▪ Photocell amplifiers ▪ Sample and Hold circuits Common Features <ul style="list-style-type: none"> ▪ Low input bias current: 30pA ▪ Low Input Offset Current: 3pA ▪ High input impedance: $10^{12}\Omega$ ▪ Low input noise current: $0.01 \text{ pA}/\sqrt{\text{Hz}}$ ▪ High common-mode rejection ratio: 100 dB ▪ Large dc voltage gain: 106 dB

LF155/LF156/LF256/LF257/LF35

Datasheet of JFET input Operational Amplifier (Extract)

3.2 DESIGN & MANUFACTURING REQUIREMENTS

3.2.1 Parts Materials & Process

- Electrical **Parts** (*) of the ESD monitoring chain shall be compliant to **Product Assurance generic requirements**.

- All **materials** used shall be compliant to Product Assurance generic requirements, in particular :

a) *Toxicity, out-gassing and volatile condensable materials,*

b) *Degradation,*

c) *Corrosion,*

d) *Thermal Cycles,*

e) *Magnetic.*

- All **processes** used in manufacturing of the ESD monitor shall be compliant to Product Assurance generic requirements

Open point (*) : existence, qualification status and procurement of a 1TΩ discrete resistor for a GEO application (15years) is still To Be Confirmed with EEE parts procurement agencies.

At this stage, no space qualified 1TΩ resistor has been found on space industry side.

In ground/commercial market, **1T-10TΩ resistors** (SRT Resistor Technology, GST or HVR types, see next page) have been found (ref. to RD1), operating in a temperature range of -55°C - +125°C (lowest T° met on a solar array in Eclipse = -180°C; not compatible)

Further actions would consist to assess possibility to **Delta or even Full qualify** such parts in order to comply with GEO environmental (life duration, mechanical, thermal cycling ranges, radiations..) and operational constraints (Some few differential Kilovolts).

SRT Resistor Technology

High Value Resistors radial leaded
Type: GST
Size: 1210, 25, 2512, 4020

Technical data – depending on size:

Size	1210	25	2512	4020
Power Rating $P_{TC}(W)$ ($P_{125} = 0W$)	0.5	0.7	1.0	2.0
Working Voltage U_{-}, U_{eff} (V) trimmed untrimmed (Tol. $\geq 5\%$)	300 1000	300 500	1200 2500	4000 6000

Ranges / Tolerances / TCR ¹⁾ / VCR ²⁾				
1M – 100M	0.5/1/2/5/10% TC 25/50/100 50 ppm/V	2/5/10% TC 50/100 50 ppm/V	0.5/.../10% TC 25/50/100 10 ppm/V	0.25/.../10% TC 25/50/100 5 ppm/V
>100M – 500M	2/5/10/20% TC 50/100/250 100 ppm/V	5/10/20% TC 100/250 100 ppm/V	1/2/5/10/20% TC 25/50/100 25 ppm/V	0.5/1/2/5/10/20% TC 25/50/100 10 ppm/V
>500M – 1G	5/10/20% TC 100/250 100 ppm/V	5/10/20% TC 100/250 100 ppm/V	1/2/5/10/20% TC 100/250 25 ppm/V	1/2/5/10/20% TC 25/50/100 10 ppm/V
>1G – 10G	5/10/20/30% TC 250/500 500 ppm/V	10/20/30% TC 250/500 500 ppm/V	2/5/10/20% TC 100/250 100 ppm/V	2/5/10/20% TC 50/100 25 ppm/V
>10G – 100G	5/10/20/30% TC 500/1000 1000 ppm/V	10/20/30% TC 500/1000 1000 ppm/V	5/10/20/30% TC 250/500 250 ppm/V	5/10/20/30% TC 100/250 100 ppm/V
>100G – 1T	–	–	10/20/30/50 TC 1000 500 ppm/V	5/10/20/30% TC 500 250 ppm/V

¹⁾ TCR: in ppm/K; TC25/50: Temperature range +25°C...+85°C

²⁾ VCR: typical values

Closer values of tolerances, TCR and VCR or other dimensions: on request and agreement.

Technical data – general:

Temperature range	-55°C ... +125°C
Climatic category acc. to EN 60068-1	55/125/56
Humidity- / contact protection	Lacquer coating ³⁾

Long term stability	≤1G	≤10G	>10G
Storage 125°C/1000h	<1%	<2%	<5%
Max voltage/1000h	<0.5%	<1%	<2%

Datasheet of High voltage resistors-GST type (Extract)

SRT Resistor Technology

High Voltage Resistors

Type: HVR

Sizes: HVR 25, HVR 30, HVR 40, HVR 50

Technical data – depending on size:

Size	HVR 25	HVR 30	HVR 40	HVR 50
Power rating $P_{70}(W)$ ($P_{125} = 0W$)	1.0	1.0	1.2	3.0
Working voltage U_{max} , U_{eff} (V)	15 KV	10 KV	20 KV	30 KV
Ranges / Tolerances / TCR¹⁾ / VCR²⁾				
1M – 100M	0.25/.../10% TC 25/50/100 1 ppm/V	0.25/.../10% TC 25/50/100 2 ppm/V	0.25/.../10% TC 25/50/100 1 ppm/V	0.25/.../10% TC 25/50/100 1 ppm/V
>100M – 1G	1/2/5/10/20% TC 50/100/250 2 ppm/V	1/2/5/10/20% TC 50/100/250 5 ppm/V	1/2/5/10/20% TC 50/100/250 2 ppm/V	1/2/5/10/20% TC 25/50/100 1 ppm/V
>1G – 100G	5/10/20/30% TC 250/500 10 ppm/V	5/10/20/30% TC 250/500 20 ppm/V	5/10/20/30% TC 250/500 10 ppm/V	5/10/20/30% TC 100/250 5 ppm/V
>100G – 1T	5/10/20/30% TC 500/1000 50 ppm/V	5/10/20/30% TC 500/1000 100 ppm/V	5/10/20/30% TC 500/1000 50 ppm/V	5/10/20/30% TC 250/500 25 ppm/V
>1T – 10T	-	-	-	10/20/30% TC/VCR on request

¹⁾ TCR: in ppm/K; TC25/50: Temperature range +25°C...+85°C

²⁾ VCR: typical values

Closer values of tolerance, TCR and VCR, other dimensions or voltage dividers on request and agreement

General technical data:

Temperature range	-55°C ... +125°C
Climatic category to EN 60068-1	55/125/56
Humidity- / contact protection	Lacquer coating ³⁾

Long term stability	≤10G	>10G
Storage 125°C/1000h	<1%	<2%
Max. voltage/1000h	<1%	<2%

Datasheet of High voltage resistors-GST type (Extract)

	<p align="center">Contract No. 22048/09/NL/AT</p>	<p>Ref : 2125.NT.MS.10.0288.ASTR Issue : 01 Rev. : 00 Date : 19-01-10 Page : 15</p>
---	---	--

3.3 QUALITY ASSURANCE REQUIREMENTS

3.3.1 Classification & Documentation

Answer to the question : “which **category** belongs the ESD Monitor to ?” will determine the way to develop, qualify then procure the different parts/hardware of ESD monitor.

It will determine :

- the applicable **Specifications**
- the type of design /manufacturing/ delivery formal **Reviews** to carry out during development and qualification phases

Two ways :

- ESD monitor = **Mini-Equipment**
- ESD monitor = **Component** (EEE parts category)

As an example : thermal sensors & strain gauges are treated as EEE parts; in this case, the applicable specifications are = PMP specifications + RHA only

If integrated on the Solar array (preferred), ESD monitor implementation is seen as a SA design modification, and in this case, impacted **SA manufacturer documentation** = Design report, Interface Control Documentation, FMECA, Worst Case Analysis, Parts Stress analysis, Declared Materials List, Declared Processes List + TBD depending on impacts (Qualification, Validation?)

3.3.2 Inspection & Tests

Key points inspections will be planned during manufacturing / integrations / environmental test phases in order to validate ESD monitor proper integration and workmanship.

Proper **operation** (Correct acquisition of the signal by DHS subsystem) must be checked first on a breadboard to validate design/architecture, then on the flight hardware, with simulated potential on metal plates (feasibility to assess; hard point).

Such DHS functional checks during Thermal vacuum tests at SC level might be very difficult with managing high voltage in (potentially) residual pressure (Corona discharge risk!).

4 CONCLUSIONS

Main requirements and constraints to implement the ESD monitor chain on a Spacecraft have been identified:

Isolation from Solar array ground > 1e+13 ohms : reuse of space qualified insulators and harness : **OK**; isolation inside SADM needs to be checked

For dielectric items judged critical, isolation is recommended to be checked by vacuum ground tests, in space environment (SIRENE like electron irradiation)

Numbers of Sensors (meta plates) : **location** on Solar array front side = **OK**, but numbers of channels limited by the number of spare slip rings allocated to signals at SADM level.

Absence of ESD risk due to highly isolated metal plates (triple points) to be demonstrated by ground tests.

Resistor bridge for potential conversion to be located on Solar array rear side (as per bleeding resistors or blocking diodes) : **OK**

DHS acquisition chain may need to integrate additional constraints for measurement **accuracy** purpose : current leakage from Operational amplifier limited to 500pAmps max (thermal control ?)

Wireless acquisition not mature for such embarked application.

Immunity to noise sources (**EMC**) needs to be assessed : expected **OK**

Quality assurance aspects : intensive use of space qualified parts, materials and processes is recommended;

ESD monitor must be declared as **EEE part** (for a simplified documentation and qualification test campaign); **Open point : no found existence of (space) qualified 1TΩ resistor as a discrete component (delta or full qualification seems unavoidable)**

Validation plan needs to be raised at subsystem level

DISTRIBUTION LIST

	Overall document		Summary
	Action	Information	
JC Mateo Velez (ONERA)		X	
JF Roussel (ONERA)		X	
D. Rodgers (ESA)		X	
P. Pélissou (EADS-ASTRIUM)		X	

Technical Note (TN)

User Manual (UM) of Wizard Based Modules

TN 2010/11-001

	Name and Function	Date	Signature
Prepared by	Julien Forest	20/10/2010	
Verified by	Julien Forest	20/11/2010	
Approved by	Jean-Charles Mateo-Velez	14/12/2010	

Reference: SPIS-TN-2010-10-001	Version: 1	Revision: 2
Status: Approved	Date: 2010/10/30	

Executive summary

This Technical Note (TN) is a general User Manual (UM) for Wizard Based Modules of SPIS. It presents the key concepts, the general purpose of wizards and, as illustration, its specific use in the frame of modelling of ESD effects.

Wizards requires a version of SPIS equal or higher to 4.3 and their use may depend on the loaded scenarios.

The key concepts related to the Keridwen's Shaman Wizard Manager are presented as used in the frame of the SPIS context.

The specific settings and data related to the ESD wizard are presented in details.

NB: This documents should be read in complement of the general SPIS-UI User Manual [RD1] and the SPIS-NUM ESD user manuals [RD2] and [RD3].

The present document has been written in the frame of the SPIS-ESD project under ESA contract N°22048/09/NL/AT.

Diffusion

Nom	Organisation
Not classified	All

Modifications

Version	Révision	Date	Auteur / Observations
1	1	20/11/2010	Julien Forest
1	2	11/12/0210	Julien Forest

Reference: SPIS-TN-2010-10-001	Version: 1	Revision: 2
Status: Approved	Date: 2010/10/30	

Table of contents

1. Generalities	5
Reference and applicable documents	5
Glossary	5
2. Introduction	6
3. Key concepts and principle	7
Why a wizard based approach, which differences w.r.t the main SPIS-UI GUI and its Tasks Manager	7
Differences between Wizards, Template Projects and SPIS-Tracks	7
What is Shaman?	8
4. Step-by-step ESD modelling using the wizard	9
Initial status	9
Loading of the ESD wizard scenario	9
Generate a new project for the existing ESD template	10
Settings of the geometry configuration	12
Attribution of material properties	13
5. Interaction with the “normal” and main SPIS-UI interface	19
Parameters settings and data consistency	19
Project persistency: Can save the project? And how to do it?	19
Can I use additional post-processing tools like Cassandra?	19
Can I load and use the ESD template as usual for a classic SPIS project?	19
Can I reload and use the generated spis-project as usual for a deeper and more detailed study?	19
Is the current project still present in the SPIS-UI framework after I have closed the wizard?	19
6. Advanced uses and developments	20
For the developers: “Where the wizard is defined ? How to modify it ? ”	20
7. Conclusion	21
Annexe 1: XML ESD wizard scenario	22

Reference: SPIS-TN-2010-10-001	Version: 1	Revision: 2
Status: Approved	Date: 2010/10/30	

(This page is let voluntary blank)

Reference: SPIS-TN-2010-10-001	Version: 1	Revision: 2
Status: Approved	Date: 2010/10/30	

	SPIS User Manual - Wizards	
	TN 2010/11-001: Wizard Based Modules	PAGE 5 /22

1. Generalities

1.1. Reference and applicable documents

1.1.1. Reference documents

[RD1] TN 1.0 SPIS User Manual

[RD2] SPIS-ESD: Architecture Design Document (ADD), ONERA

[RD3] SPIS-ESD, Software Verification and Validation Docuent (SVVD), ONERA,

[RD4] Keridwen's Web page, www.keridwen.org

1.1.2. Applicable document

N/A

1.2. Glossary

• N/A

Reference: SPIS-TN-2010-10-001	Version: 1	Revision: 2
Status: Approved	Date: 2010/10/30	

This document is the property of Artenum SARL, France, and cannot be reproduced or diffused without a prior authorisation.

	SPIS User Manual - Wizards	
	TN 2010/11-001: Wizard Based Modules	PAGE 6 /22

2. Introduction

This Technical Note (TN) is a general User Manual (UM) for Wizard Based Modules of SPIS. It presents the key concepts, the general purpose of wizards and, as illustration, its specific use in the modelling of ESD effects.

The use of wizards requires a version of SPIS equal or higher to 4.3 and their use may depend on the loaded scenarios.

The key concepts related to the Keridwen's Shaman Wizard Manager are presented in the frame of the SPIS context.

The specific settings and data related to the ESD wizard are presented in details.

NB: This document should be read in complement of the general SPIS-UI User Manual [RD1] and the SPIS-NUM ESD user manuals [RD2] and [RD3].

Reference: SPIS-TN-2010-10-001	Version: 1	Revision: 2
Status: Approved	Date: 2010/10/30	

3. Key concepts and principle

3.1. Why a wizard based approach, which differences w.r.t the main SPIS-UI GUI and its Tasks Manager

SPIS-UI has been initially designed for expert users and to let open all possibilities of access and modification on the modelled system. Such approach allows a lot of possibilities but may appear as a complex tool for a non expert, especially for targeted purposes, like the modelling of a specific phenomenon as ESD effects.

In practice, the *SPIS Wizard* appears as a set of panels, between each one the user can navigate using Next/Previous buttons. Each panel presents a reduced and thematic set of parameters to set (e.g. space environment), in order to help the user to focus on the key elements only. The wizard offers also validation processes at each step.

The *SPIS Wizard* approach is not antagonist to the global and main GUI of SPIS. It should be understood as an integrated tool to help to user to run SPIS on specific configurations. More especially, the spis wizard is not incompatible with the *Spis Task Manager*. The first one tries to help to user to follow the downstream evolution of the modelling process. On the The aim of the *Task Manager* is to check at each step the upstream dependency and the consistency of the model.

The *SPIS Wizard* aims to be used for a large set of configurations in the near future. However, the present document focus on its use in the case of ESD modelling.

3.2. Differences between Wizards, Template Projects and SPIS-Tracks

SPIS gathers several concepts to help the user to follow a consistent modelling process and/or to perform automatically the largest set of actions possible. In the first reading these concepts may appear complex and redundant, but, in fact, their are deeply related to each other and designed to be complementary.

Wizards: As quickly described above, wizards are tools to help the user to follow, through a GUI, a pre-defined modelling process corresponding to a specific configuration and/or physical problem to study, like ESD modelling or propulsion system. This typically corresponds to the preprocessing phase, where the user should defined a specific set of parameters and properties on a predefined system. The modelling process is here defined though an XML based scenario for each specific configuration. These wizards scenarios are processed the Artenum's Shaman Wizard Manager, which also handles, in a transparent manner for the user, the link with the SPIS-UI Data Model and the Task Manager. The user access to the wizard through a set of serialised panels. The switch from one panel to the next one can be controlled by a set of conditions on the filled parameters of the current one. Typically a wizard is run in the frame of the main SPIS-UI and modelled systems remain fully compliant with the standard approach.

Wizards should be then seen as a guide or help for the user to perform, in the simplest way, a process in SPIS, for instance to set a simulation project.

Template Projects: In SPIS-UI, Templates Projects are predefined spis-projects that can be used as starting points to define in the simpler way new simulation projects, by changing only a few key parameters and using a same pre-defined geometry, for instant. Depending on the settings initially defined, they can be "ready to run a simulation", with all needed parameters preset to defaults values or be only partially set. But in any case, they will contain outputs data or results. Structurally, they are similar to standard spis-projects.

Reference: SPIS-TN-2010-10-001	Version: 1	Revision: 2
Status: Approved	Date: 2010/10/30	

Wizard and Template Projects are frequently intimately linked because most of wizards scenarios start their processes from data pre-defined in a template-project.

Spis Tracks: *Spis Tracks* are Jython based scripts that can directly be processed by the kernel of SPIS-UI. *Spis Tracks* are typically used to perform automatically fully preset processes or actions, where the intervention of the user is not needed in interactive mode, like pre-processing for fully defined templates, systematic simulation runs for parametric studies, automatic post-processing and data conversion. *Spis Tracks* can be performed as well as in inside the main GUI, for a specific action like data export for instance, or in batch mode, to perform simulations on a remote computer without graphic export for instance.

Spis Tracks are generally predefined (so their is also spis-tracks templates) and/or can be generated through a wizard for instance.

This leads to the typical logical scheme illustrated in figure 1.

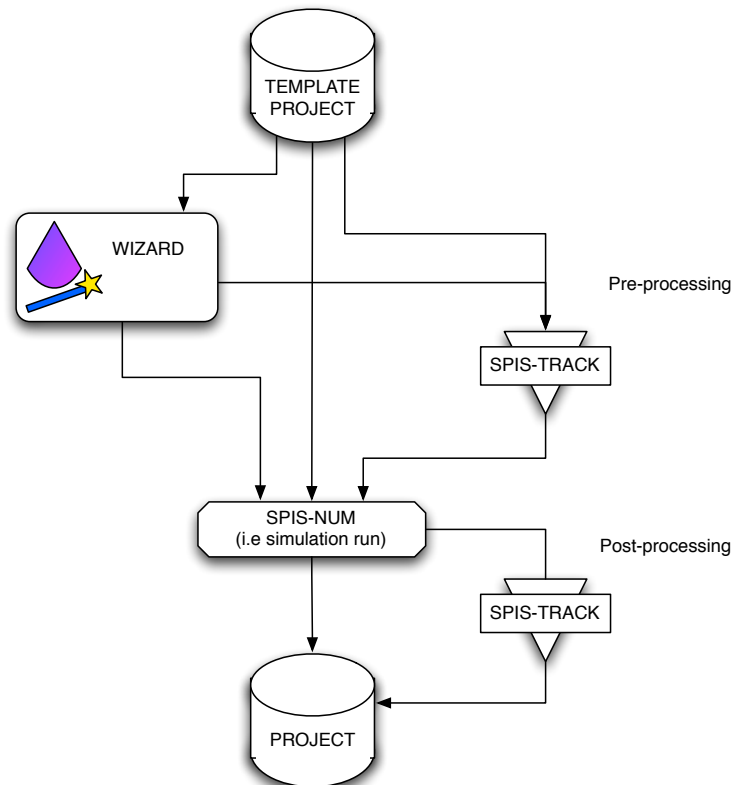


Figure 1: Illustration of the purpose of each type of tool (i.e wizards, templates, tracks)

3.3. What is Shaman?

Shaman is the generic wizard manager initially developed in the frame of the Artenum's Kerdiwen project [RD4] and is freely available as standalone application in this frame. The purpose of Shaman is to play, according an XML based scenario, a sequence of GUI panels through a generic contained called *shamaneable*, offers a central controller to control the progression of panel and allow a link between the views (i.e. the panels) and the model (e.g. the SPIS-UI Data Bus).

If Shaman is generic and parametrisable, the design of each panel and the link with the underlined model should be defined specific to each software, like SPIS-UI, for instance.

Reference: SPIS-TN-2010-10-001	Version: 1	Revision: 2
Status: Approved	Date: 2010/10/30	

4. Step-by-step ESD modelling using the wizard

4.1. Initial status

First run you SPIS system as usual, calling the relevant launching script as explained in [RD1]. Please notice that ESD models require a specific version of SPIS-NUM and a specific launching script is generally defined (e.g. runSpisESD.sh under Apple Mac OSX and/or Linux systems). The main GUI should appear as usual and illustrated in figure 2.

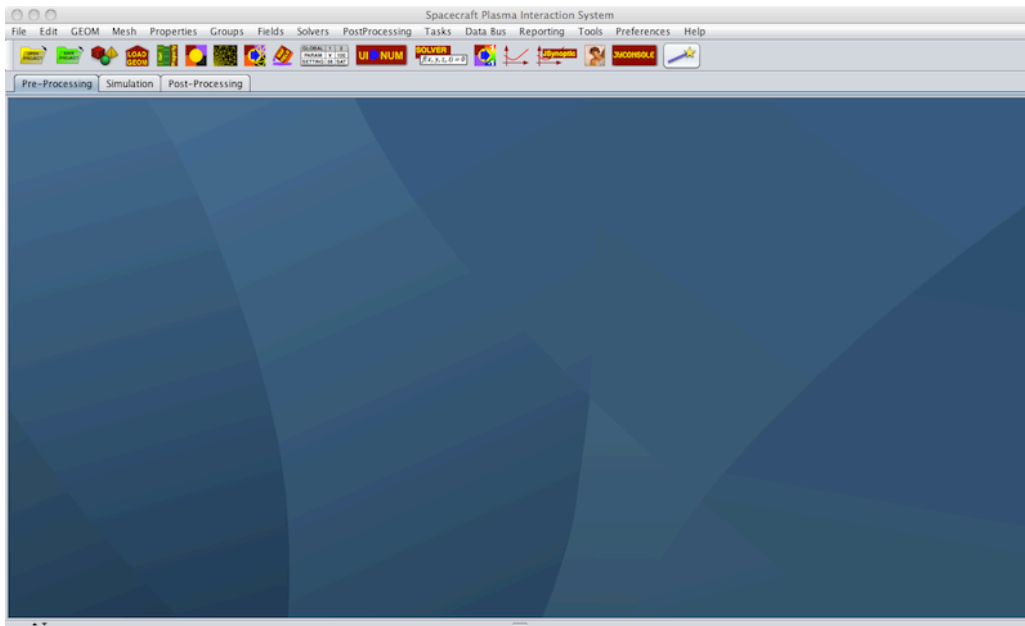



Figure 2: View of the SPIS-UI main GUI in the initial status.

4.2. Loading of the ESD wizard scenario

Wizards can be called just by clicking on the icon with a magic-stick on ( surrounded by an orange ring in the next figure) , in the tool bar. A file chooser should appear and propose the access to several wizards scenarios, as illustrated in figure 3.

For the ESD modelling, please select the `ESDscenario1.xml` file.

This should lead to the apparition of an internal frame corresponding to the wizard in the main GUI, as illustrated in figure 4.

Reference: SPIS-TN-2010-10-001	Version: 1	Revision: 2
Status: Approved	Date: 2010/10/30	

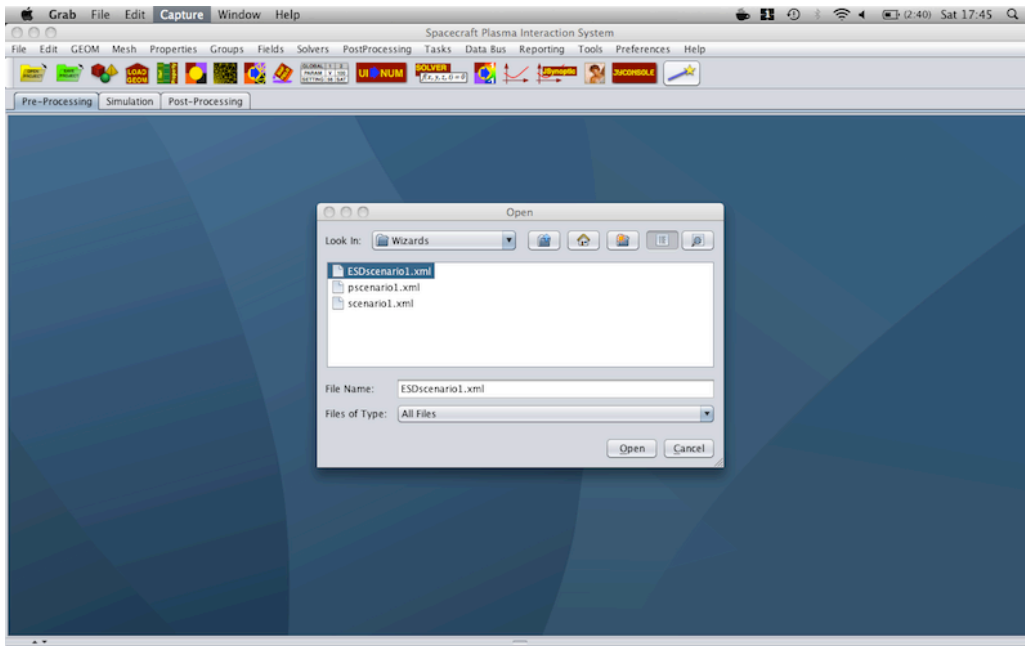


Figure 3: Selection of the relevant wizard scenario. For ESD modelling please select the *ESDscenario1.xml* file.

4.3. Generate a new project for the existing ESD template

To be processed, the ESD wizard scenario needs a existing project with a specific pre-built geometry. If you do not start from an existing project, this one can automatically generated from a pre-existing template, just by checking the “Generate from template” check box. It is then necessary to create a new project, by clicking on the Select button of the project path. When both are properly set, you can click on the Next button to pass to the next step. This will call the project manager and generate the new project from the template at the selected target path.

NB: If you wish reload a pre-existing project without generating it from the template (e.g. to keep specific settings previously set), just select the relevant project with the project file choose without selecting the “Generate from template” check box.

Reference: SPIS-TN-2010-10-001	Version: 1	Revision: 2
Status: Approved	Date: 2010/10/30	

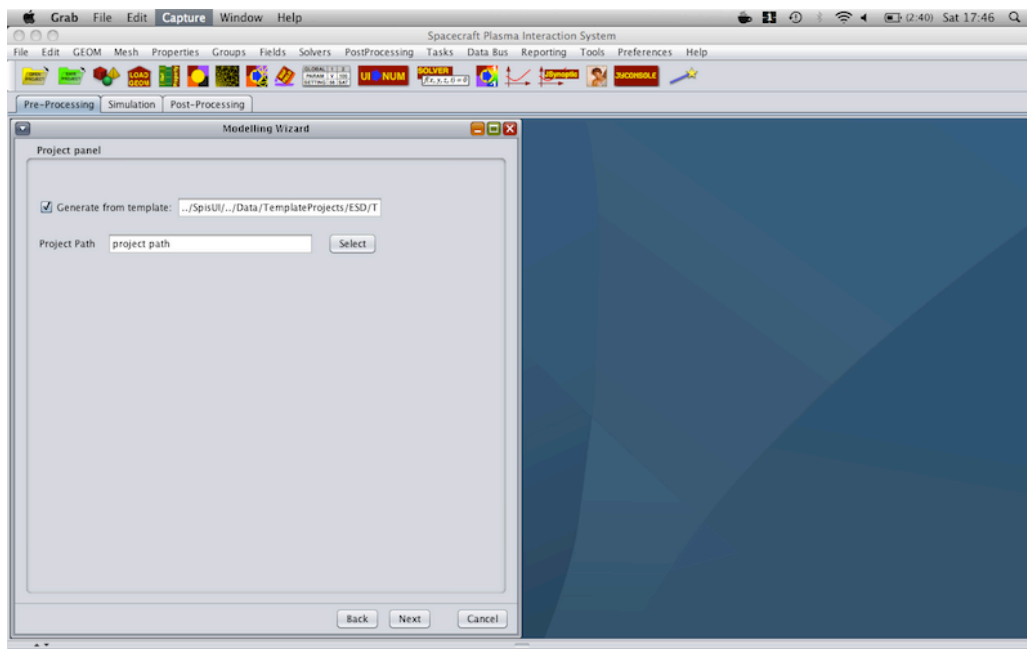


Figure 4: Generation of a new ESD project from the ESD template

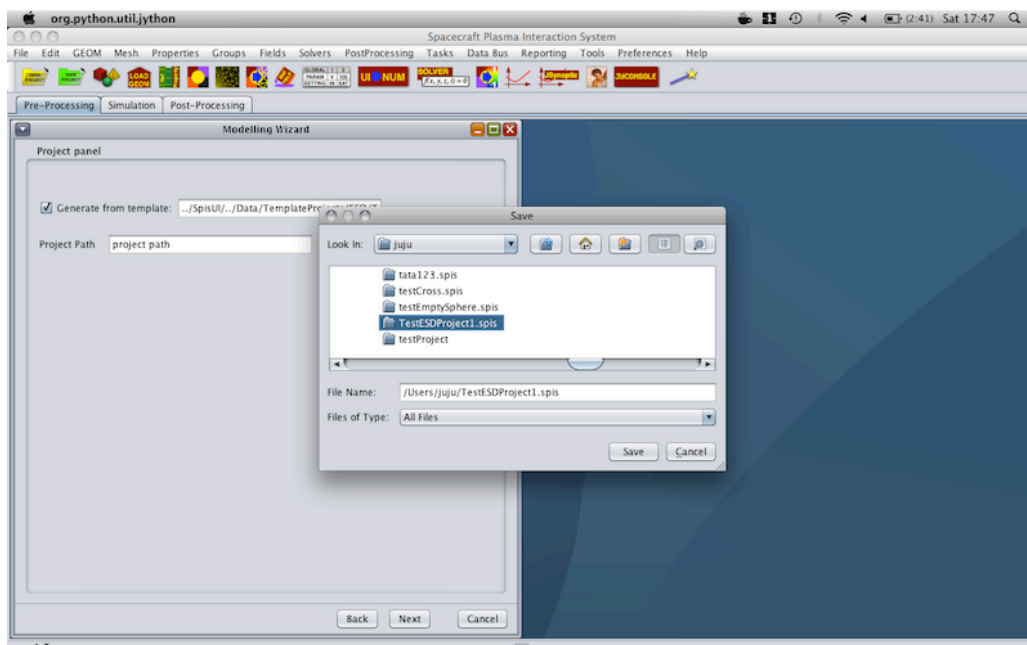


Figure 5: Selection/definition of the targeted ESD project.

NB: Currently, the targeted spis-project should be an existing and empty directory.

Reference: SPIS-TN-2010-10-001	Version: 1	Revision: 2
Status: Approved	Date: 2010/10/30	

4.4. Settings of the geometry configuration

The modelling of ESD effects induces very strong numerical constraints for both SPIS-NUM solver and the used mesher (i.e. Gmsh). Please see RD2 for further informations. For this reason and in order to simplify the most as possible, the modelling of the geometrical system is based on the adjustment of a predefined geometry.

Figure 6 shows this system, at different zoom levels and outlines the surface meshing. The last view focuses on the metal tip. These views outlines the very sever constraints regarding the meshing. Please see RD2 for further informations.

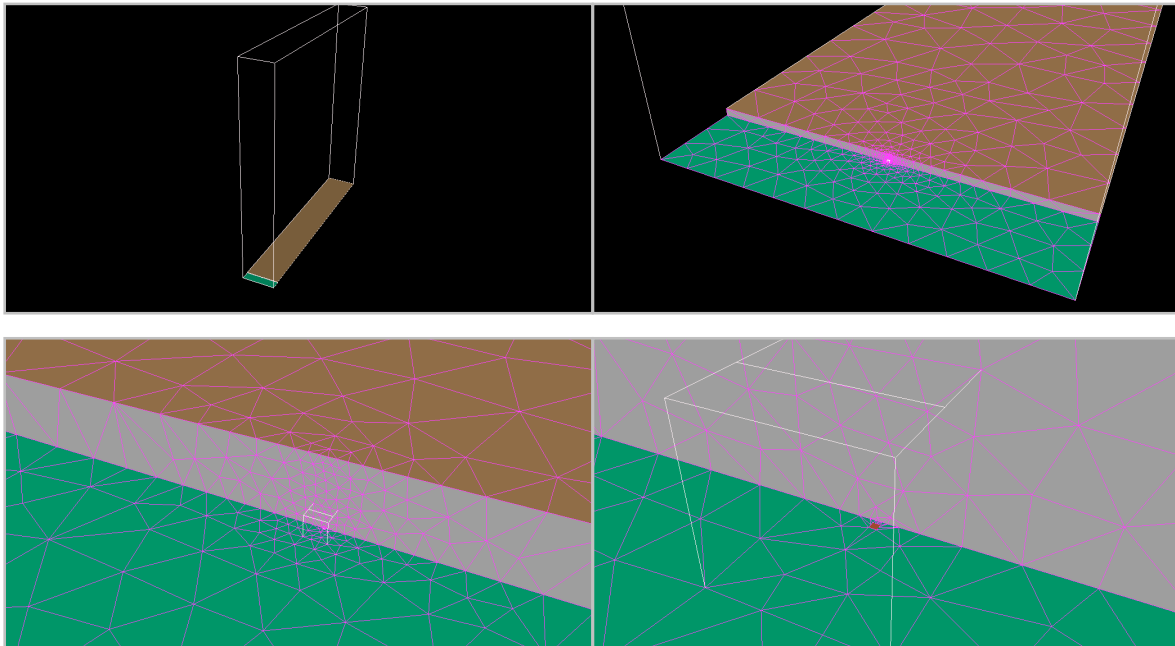


Figure 6: Views of the pre-defined geometrical model.

The wizard GUI allows only the settings of some dimensions of this system, like the box size, the metal length or the angle of the front of the dielectric. Technically, this is done by editing and updating the information set in the GEOM_PARAM_1.geo file, itself loaded as auxiliary file by the main CAD file (e.g. TP_ESD_v2.geo).

Currently, there is no checking / validation on the inputs parameters. Then it still remains of the responsibility of the user to check the relevance of his settings and if the mesh is still compliant with the SPIS-NUM constraints.

Figure 7, the after, display the geometrical panel, allowing these settings and remaining the main characteristics of the geometrical system.

The modifications are validated when the Next button is clicked.

Reference: SPIS-TN-2010-10-001	Version: 1	Revision: 2
Status: Approved	Date: 2010/10/30	

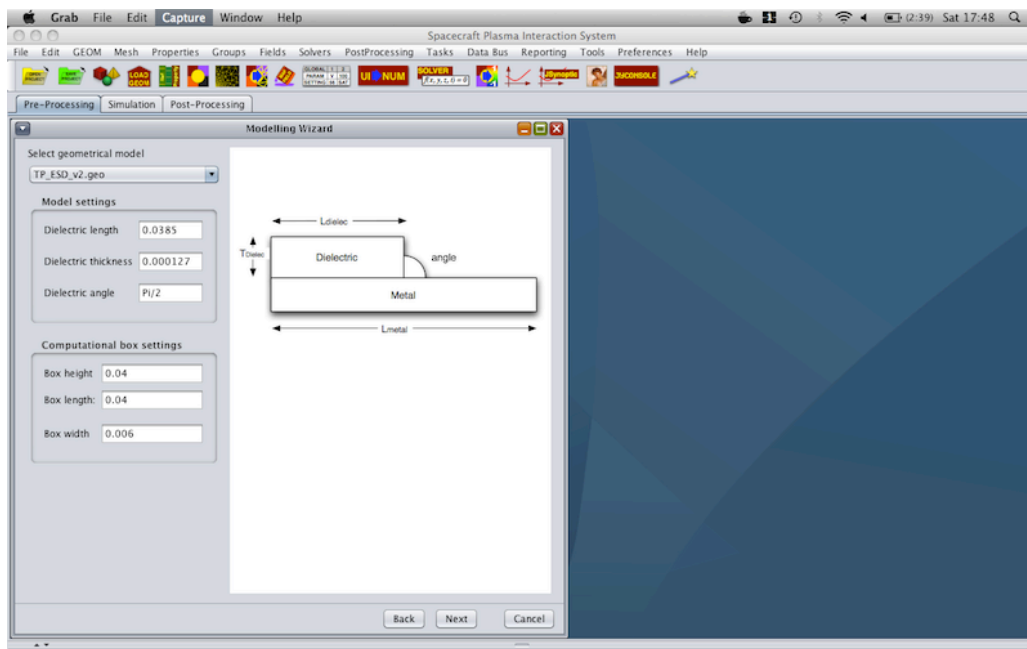


Figure 7: View of the geometrical model settings panel

4.5. Attribution of material properties

With respect to the previous versions of SPIS and the Groups Manager of the standard interface, the attribution of properties has been strongly simplified by both the introduction of meta-groups and the fact that here only material type should be attributed. Numerical conditions, defined through the Plasma Models and Electrical Nodes, are already defined.

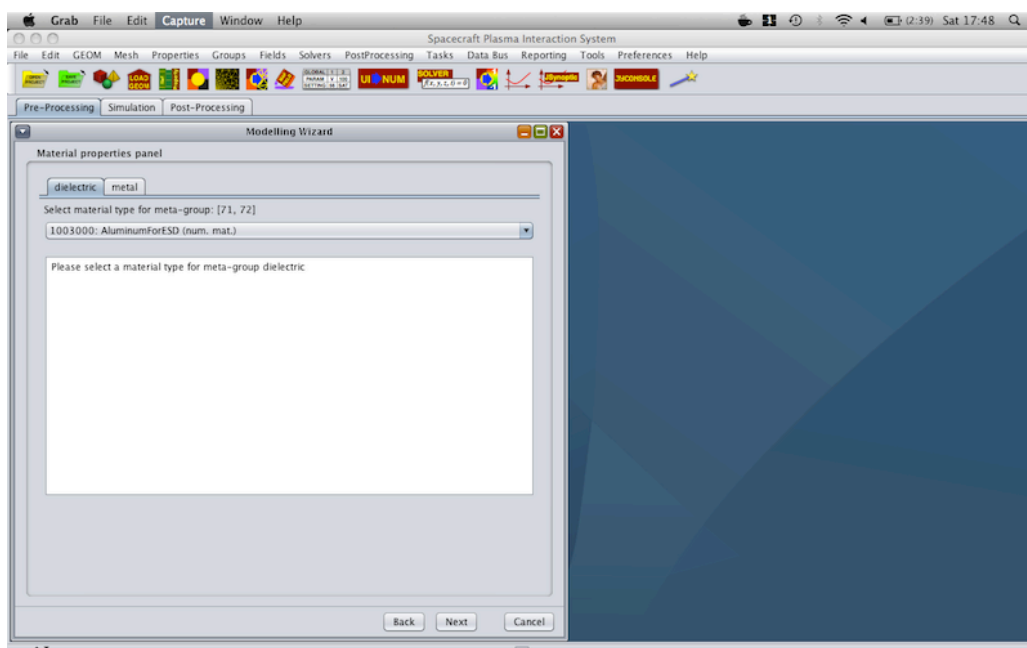


Figure 8: View of the groups/Properties editor.

Reference: SPIS-TN-2010-10-001	Version: 1	Revision: 2
Status: Approved	Date: 2010/10/30	

In the concept of meta-groups, groups are gathered in sub-set, in order to attribute the same property to several groups in one time, for instance for all metallic elements.

As illustrated in figures 9 and 10, for each meta-group the attribution of the material property is just done by selection of the right material the combo box. It is mandatory to attribute a material for each meta-group.

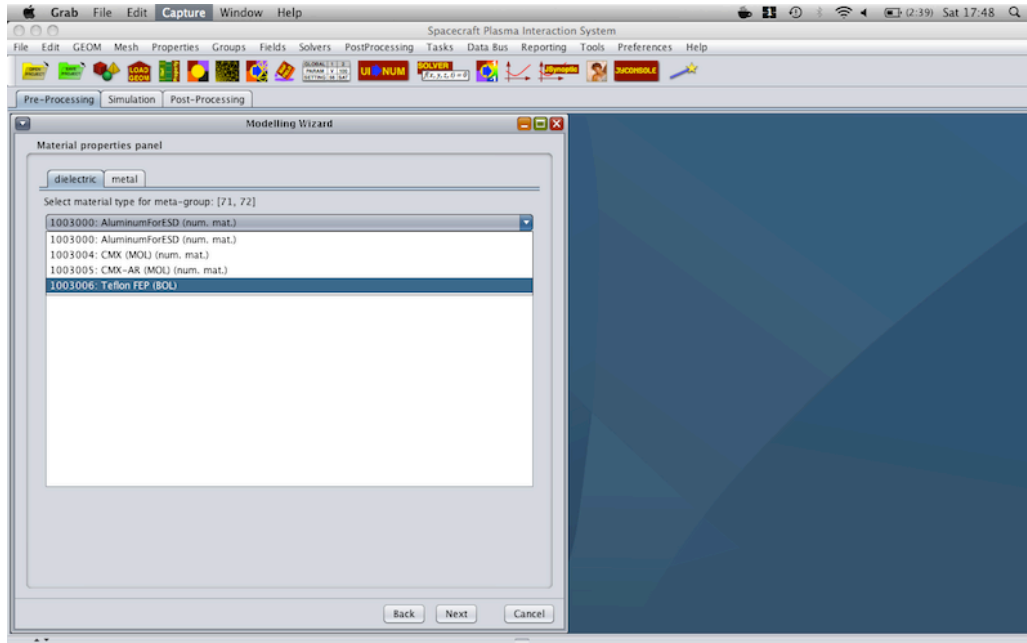


Figure 9: Selection of the material.

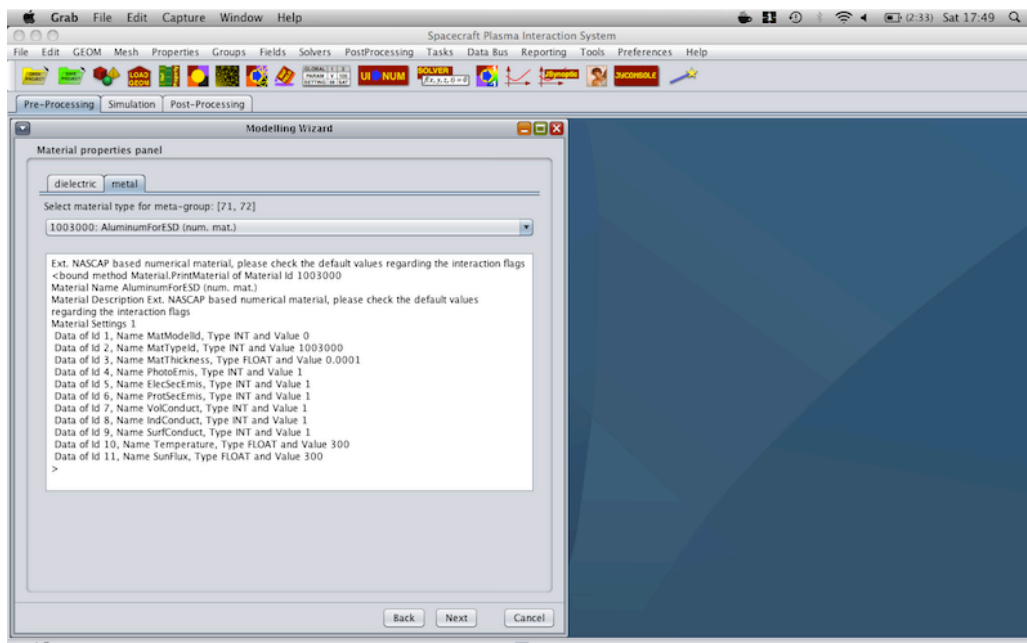


Figure 10: When the material is selected, its main characteristics are displayed.

Reference: SPIS-TN-2010-10-001	Version: 1	Revision: 2
Status: Approved	Date: 2010/10/30	

4.5.1. Settings of the space environment and plasma parameters

All parameters relative to the space environment and the plasma-surface interactions are set through a unique panel. In the specific case of ESD, please notice that ESD will occur only if a secondary emission is set (e.g. photo-electrons via the solar flux at on, or electrons secondary emission).

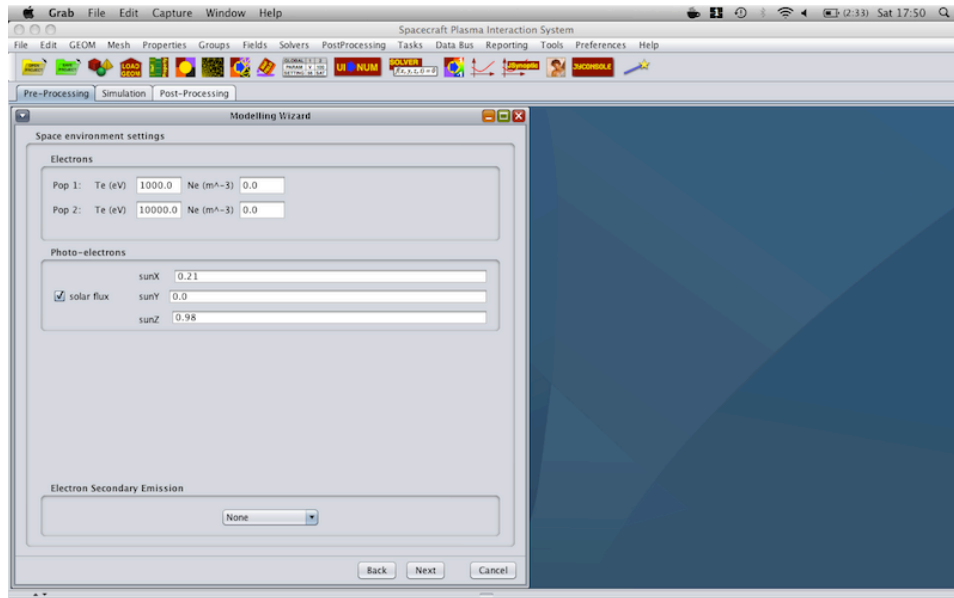



Figure 11: View of the environment panel

4.5.2. Settings of the simulation parameters

Parameters relative to the simulation control are set in the same manner, inside one panel. Please see [RD2] [RD3] for further details regarding the meaning of each fields and their relevant values. We strongly recommend to save the whole project at this stage, just by clicking on the on the save project icon .

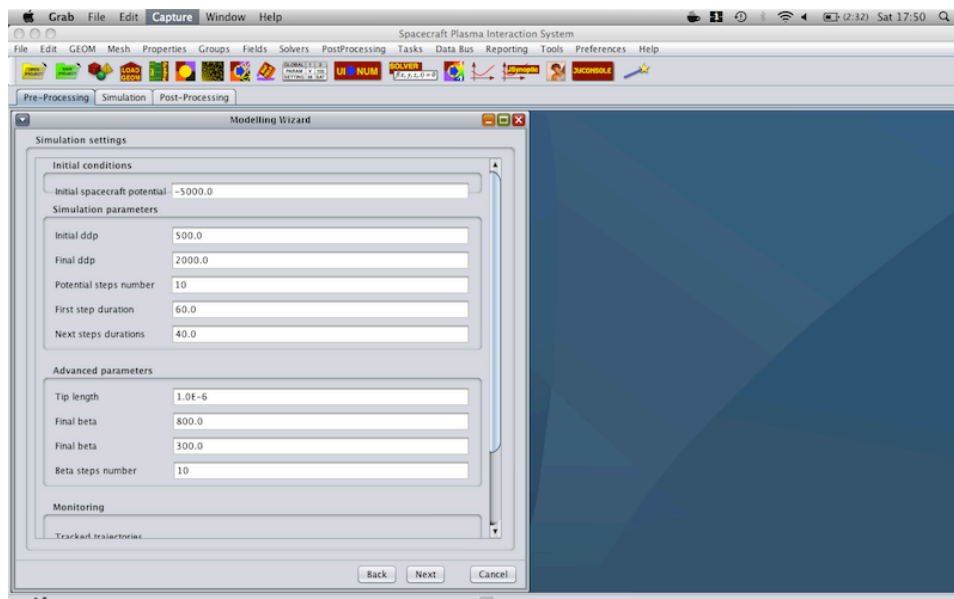


Figure 12: Setting of simulation control parameters.

Reference: SPIS-TN-2010-10-001	Version: 1	Revision: 2
Status: Approved	Date: 2010/10/30	

4.5.3. Performing the simulation

Figure 13 shows the simulation panel, with its two progress bars. The first one corresponds to the preprocessing phase, the second to the simulation run itself. Thanks to the SPIS-UI's Task Manager, the whole pre-processing (i.e. CAD loading, meshing, groups conversion and Data Fields mapping) is performed automatically.

Please notice that both, pre-processing and simulation run, may be very long tasks and the Next button, to switch to the post-processing panel, will be available only when the whole processing will be done.

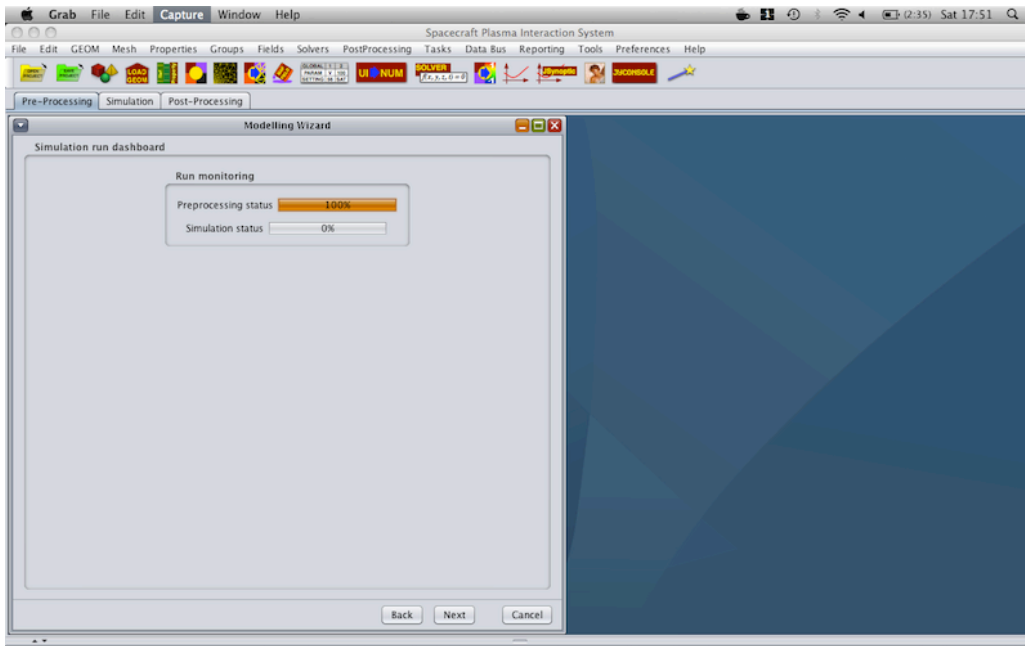


Figure 13: view of the simulation control panel.

Nb: Currently, only internal thread for the simulation phase is available.

4.5.4. Post-processing, data analysis and project saving

Key results are displayed through several plots and text areas inside one unique post-processing panel. The first index gathers the time evolutions of the Potential Difference between the tip and the potential barrier, on the left side, and the net emitted current, on the right side. The second plot, on the second index, displays the net collected current for all nodes and all populations of particles. Please notice that y-axis for currents is displayed in logarithmic scale (base 10) in order to display their whole dynamic. The third index displays an ASCII based report on ESD risks.

As for the standard 2D plots facility of SPIS-UI, it is possible to edit the plot characteristics, like scale, units or colours, just making a right-button click inside the plot to reach the contextual menu. In the same, it is possible to save the view into PNG or TIFF formats. The direct selection of a sub-area with the mouse allows to zoom-in the plot. The ESD risk report is saved when the project saving phase and is stored in the PROJECT_ROOT/Kernel/Output directory.

The bottom panel buttons allows to call the *DataField Manager* for deeper post-processing analysis, export results into ASCII Raw based format or save all results into the current project.

We strongly recommend to save all data by clicking on the Save Project button before to close the wizard.

Reference: SPIS-TN-2010-10-001	Version: 1	Revision: 2
Status: Approved	Date: 2010/10/30	

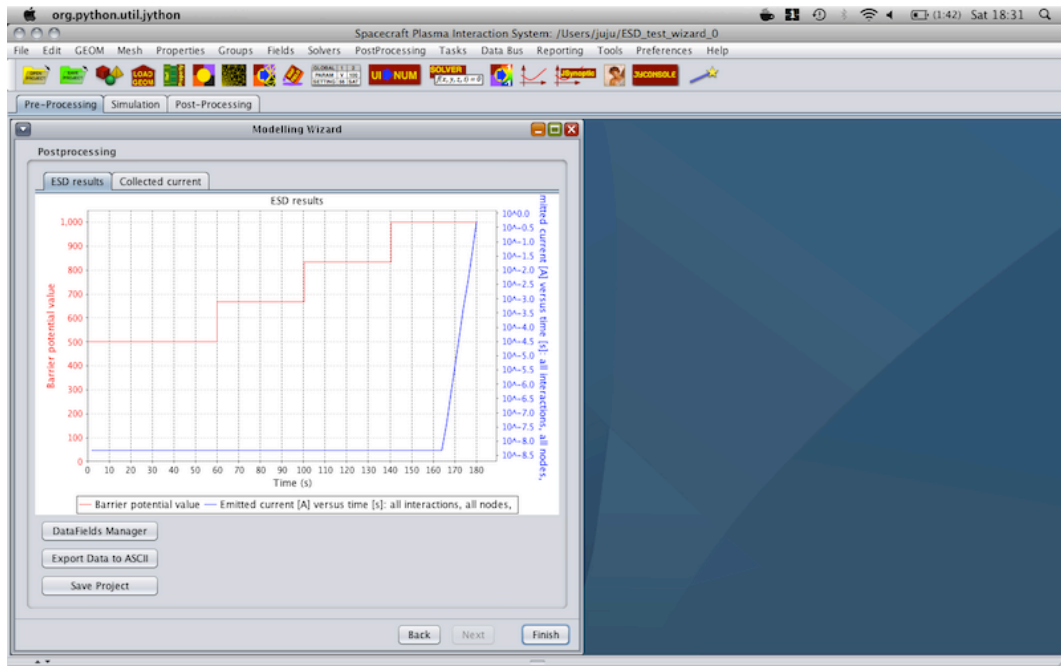


Figure 14: View of the post-processing panel. Currents on the right side axis have a logarithmic scale.

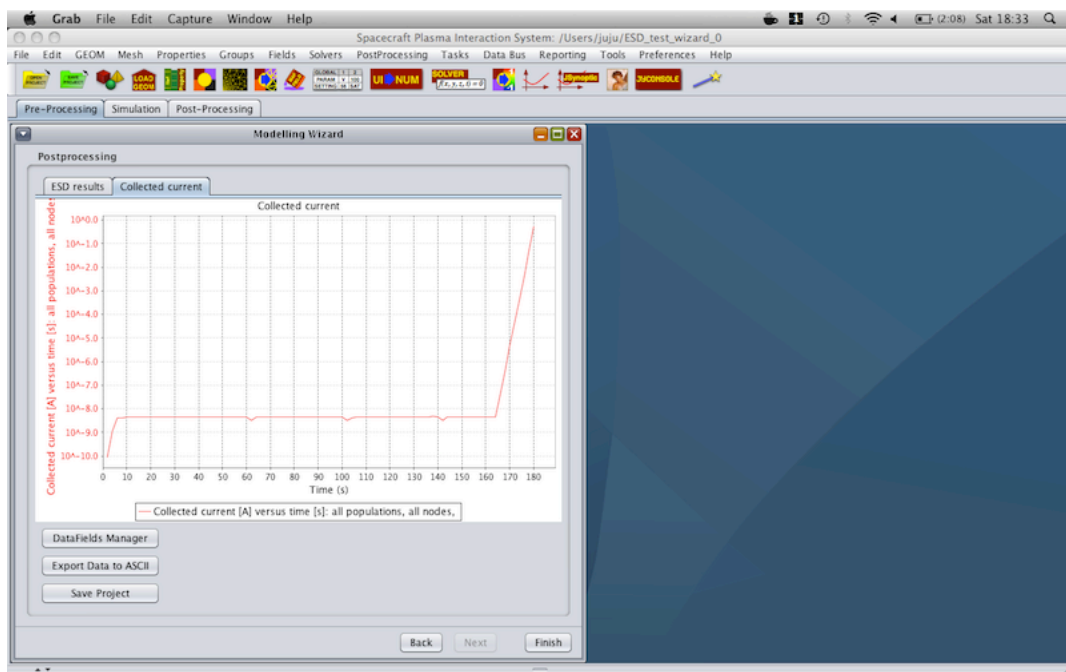


Figure 14: View of the post-processing panel

Reference: SPIS-TN-2010-10-001

Version: 1

Revision: 2

Status: Approved

Date: 2010/10/30

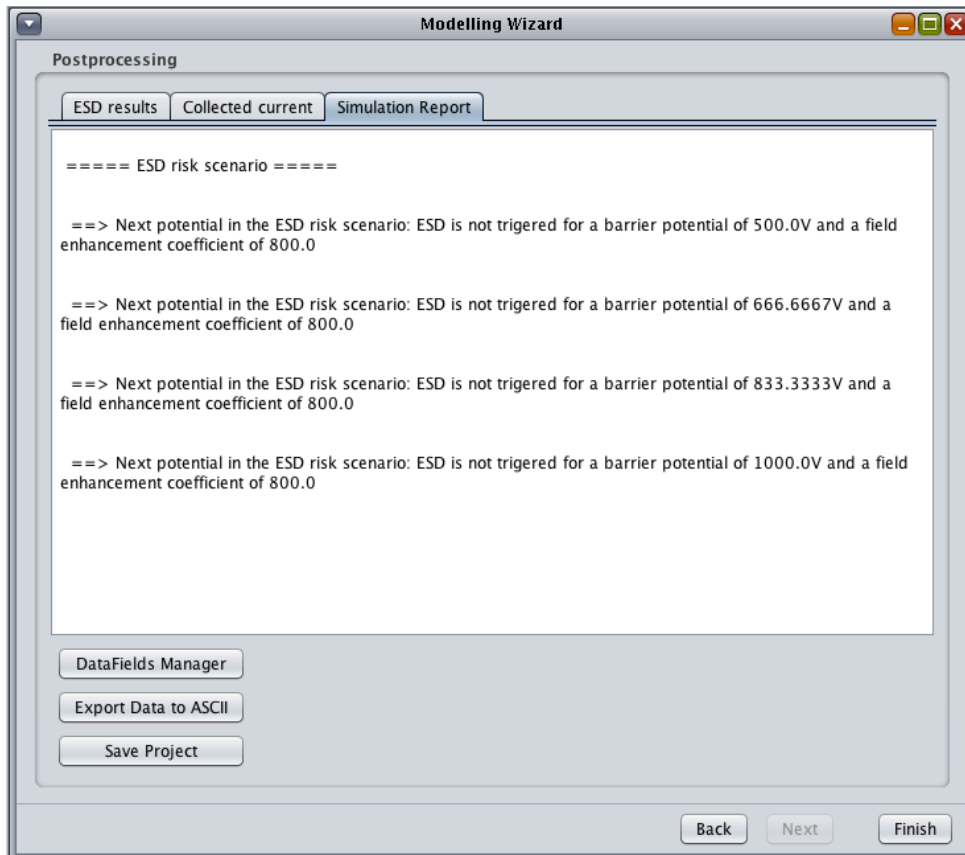


Figure 15: Simulation ESD risk report panel under ASCII format.

Reference: SPIS-TN-2010-10-001	Version: 1	Revision: 2
Status: Approved	Date: 2010/10/30	


5. Interaction with the “normal” and main SPIS-UI interface

5.1. Parameters settings and data consistency

One direct question is “Can I can edit or control parameters (for instance additional) outside the wizard in the classic GUI?”. In the absolute, yes, this is possible, the wizard being just another view of the same data model. For instance, it is possible to open in parallel the global parameters editors. But in this case, there is any guaranty on the final consistency of the input data and parameters, the control of the wizard being by-passed.

For this reason, we strongly recommend to do such operation very carefully.

5.2. Project persistency: Can save the project? And how to do it?

Yes of course ! the generated project is a classic spis-project, that can be saved as usual. The last panel of the wizard propose to save it at the end of the wizard only, to save the results of the simulation too, but you can save the project when you want just by clicking on the save project icon  .

5.3. Can I use additional post-processing tools like Cassandra?

Yes, of course! As already explained, the generated project is a classic spis-project fully compliant with most of the tools embedded in SPIS-UI. Through the Data Fields Manager, Cassandra, as well as other tools, like the 2D plot function or Paraview can be used at all time during the modeling process.

It is also possible to use the groups and mesh viewer, as usual, to control the global model.

5.4. Can I load and use the ESD template as usual for a classic SPIS project?

Yes, but...Templates are spis-projects and can be loaded directly, but in order to do not corrupt them we strongly recommend to copy them and/or save them into another name.

5.5. Can I reload and use the generated spis-project as usual for a deeper and more detailed study?

Yes of course! The generated project is a classic spis-project fully compliant with the classic GUI and can be freely reloaded for deeper and more detailed study using the classic approach.

5.6. Is the current project still present in the SPIS-UI framework after I have closed the wizard?

Yes absolutely, and all data remain available for deeper study as usual.

Reference: SPIS-TN-2010-10-001	Version: 1	Revision: 2
Status: Approved	Date: 2010/10/30	

	SPIS User Manual - Wizards	
	TN 2010/11-001: Wizard Based Modules	PAGE 20/22


6. Advanced uses and developments

6.1. For the developers: “Where the wizard is defined ? How to modify it ? ”

The ESD wizard is in fact defined at three levels, respecting the MVC pattern:

- In the XML based wizard scenario, defined in the file `$SPIS_ROOT/SpisUI/Templates/Wizards/ESDscenario1.xml`. This file is read dynamically at the runtime and can be modified without recompiling any source code. This file is directly read by the Keridwen’s Shaman Wizard Manager which itself plays the role of central controller for the wizard.
- In the `$SPIS_ROOT/SpisUI/AuxLibs/src/ESDPanels` Java based library for the definition of the views (i.e the panels). These panels are designed specifically for each application case, like for instance ESD modelling. Their modification requires to recompile the corresponding library. NB: Each panel should be embedded in a generic shamable component.
- In the `$SPIS_ROOT/SpisUI/Bin/Tasks/TaskWizardManager` Jython bases SPIS-UI task to make the link between the views (panel) and the SPIS-UI data model. This script-based module is processed at the runtime and is specific to each application case (e.g. ESD modelling).

Reference: SPIS-TN-2010-10-001	Version: 1	Revision: 2
Status: Approved	Date: 2010/10/30	

	SPIS User Manual - Wizards	
	TN 2010/11-001: Wizard Based Modules	PAGE 21/22

7. Conclusion

This Technical Note (TN) presents the UM specifically dedicated to the Wizard Based modules of SPIS. The present document focus on the ESD Wizard, but the global approach remains general and can be followed for other pre-defined modelling processes.

The main concepts of the wizard-based approach have been presented.

The specific actions and settings related to the ESD modelling detailed. However, we strongly recommend to the user to read the present document closely in parallel with the documentation of SPIS-NUM [RD2] [RD3].

Reference: SPIS-TN-2010-10-001	Version: 1	Revision: 2
Status: Approved	Date: 2010/10/30	

A. Annexe 1: XML ESD wizard scenario

```

<?xml version="1.0" encoding="UTF-8"?>

<Scenario>

    <Panel ID="id1" ClassName="org.spis.esd.shaman.ProjectShamanPanel"
Switcher="com.artenum.shaman.switcher.NextShamanSwitcher" >
        <Action Type="next" Target="id2" />
    </Panel>
    <Panel ID="id2" ClassName="org.spis.esd.shaman.GeometryShamanPanel"
Switcher="com.artenum.shaman.switcher.NextShamanSwitcher" >
        <Action Type="next" Target="id3" />
    </Panel>
    <Panel ID="id3" ClassName="org.spis.esd.shaman.MaterialShamanPanel"
Switcher="com.artenum.shaman.switcher.NextShamanSwitcher" >
        <Action Type="next" Target="id4" />
    </Panel>
    <Panel ID="id4" ClassName="org.spis.esd.shaman.EnvironmentShamanPanel"
Switcher="com.artenum.shaman.switcher.NextShamanSwitcher" >
        <Action Type="next" Target="id5" />
    </Panel>
    <Panel ID="id5" ClassName="org.spis.esd.shaman.EnvironmentShamanPanel"
Switcher="com.artenum.shaman.switcher.NextShamanSwitcher" >
        <Action Type="next" Target="id6" />
    </Panel>
    <Panel ID="id6" ClassName="org.spis.esd.shaman.SimulationSettingShamanPanel"
Switcher="com.artenum.shaman.switcher.NextShamanSwitcher" >
        <Action Type="next" Target="id7" />
    </Panel>
    <Panel ID="id7" ClassName="org.spis.esd.shaman.SimulationRunShamanPanel"
Switcher="org.spis.esd.shaman.SwitcherSimulationControl" >
        <Action Type="next" Target="id8" />
    </Panel>

    <Panel ID="id8" ClassName="org.spis.esd.shaman.PostProcessingShamanPanel"
Switcher="com.artenum.shaman.switcher.LeafShamanSwitcher" >
    </Panel>

    <Root ID="id1" />
</Scenario>
  
```

Reference: SPIS-TN-2010-10-001	Version: 1	Revision: 2
Status: Approved	Date: 2010/10/30	